UNIVERSITÀ DEGLI STUDI DI MILANO

PhD School in Physics, Astrophysics and Applied Physics

XXXIV Cycle

Astrophysical nuclear reactions on Neon isotopes at LUNA

Disciplinary Scientific Sector FIS/04

Director of the School: Prof. Matteo Paris

Supervisor of the Thesis: Prof. Alessandra Guglielmetti

Co-Supervisor of the Thesis: Prof. Antonio Caciolli

Candidate:

Eliana Masha

Academic year 2021/2022

Referee:

Dr. Chiara Mazzocchi
University of Warsaw (Poland)

Dr. Ronald Schwengner
Helmholtz Zentrum Dresden Rossendorf (Germany)

Commission of the final examination:

Prof. Antonio Caciolli
Università degli Studi di Padova (Italy)

Prof. Paola Marigo
Università degli Studi di Padova (Italy)

Prof. Paolo Prati
Università degli Studi di Genova (Italy)

Final examination:

Date: 21 January 2022

Università degli Studi di Milano, Dipartimento di Fisica, Milano, Italy

Contents

Abstract

This thesis reports the direct measurements of the ^{22}Ne$(\alpha,\gamma)^{26}$Mg and ^{20}Ne$(\mathrm{p},\gamma)^{21}$Na reactions at astrophysical energies of interest.

The ^{22}Ne$(\alpha,\gamma)^{26}$Mg reaction competes with the ^{22}Ne$(\alpha,\mathrm{n})^{25}$Mg reaction which is the main source of neutrons for the s-process in low-mass Asymptotic Giant Branch and massive stars. At temperatures T $<$ 300 MK where the (α,γ) channel becomes dominant, the rate of the ^{22}Ne$(\alpha,\gamma)^{26}$Mg reaction is influenced by several resonances studied only indirectly. The first part of this thesis concerns the direct measurement of one of these resonances, E_r = 334 keV, which so far was studied only indirectly leading to six orders of magnitude range of possible values for its resonance strength. The experiment has been performed at LUNA (Laboratory for Underground Nuclear Astrophysics) using the intense alpha beam of the LUNA 400 kV accelerator and a windowless gas target combined with a high-efficiency BGO detector. In the present study, an upper limit of $4.0 \cdot 10^{-11}$ eV has been determined for the resonance strength. Taking into account these results, an updated ^{22}Ne$(\alpha,\gamma)^{26}$Mg thermonuclear reaction rate was obtained and its role on the predicted ^{25}Mg/^{26}Mg ratio of a $5M_{\odot}$ AGBs was investigated. The data show a decrease by a factor of 15 of the intershell ^{25}Mg/^{26}Mg ratio.

The ^{20}Ne$(\mathrm{p},\gamma)^{21}$Na is the slowest reaction of the NeNa cycle. It determines the velocity of the cycle and defines the final abundances of the isotopes synthesized in this cycle. The uncertainties on the NeNa cycle are affected by the ^{20}Ne$(\mathrm{p},\gamma)^{21}$Na reaction rate.

The main goal of the second part of this thesis was the direct measurement of the E_{cm} = 366 keV resonance which dominates the total rate in the temperature range between 0.2 GK and 1 GK. The measurement has been performed at LUNA using the windowless gas target and two high-purity germanium detectors placed at different positions. This measurement allowed to reduce the uncertainty on the strengths of the 366 keV resonance from 18% to 7%. These results were used to update the ^{20}Ne$(\mathrm{p},\gamma)^{21}$Na reaction rate.

Introduction

The evolution of the Universe and the origin of the chemical elements have always been the subject of several experimental studies and theoretical models. Spectroscopic observations of radionuclides in the interstellar medium and stellar atmosphere have proved that stars are giant nuclear reactors that are constantly shaping and changing the chemical composition of the Universe. Theoretical models and supercomputers are trying to reproduce the observed abundances and compute detailed models of the evolution of stars and galaxies. To achieve the same level of accuracy as the observations, the theoretical models require high precision input parameters. A crucial input for these models is the thermonuclear reaction rate (cross-sections) for all the nuclear processes involved.

Measuring these nuclear cross-sections is very challenging and is the main goal of experimental nuclear astrophysics. In stellar environments, the energy of the interacting particles is usually much lower than the Coulomb repulsion between the nuclei. Under these conditions, the nuclear reactions can only proceed via the quantum tunneling effect. As a result, the reaction cross sections at relevant energies can be extremely low, and very difficult to measure since the signal can be lost in the natural background. Possible solutions to overcome this problem can be the use of indirect approaches or the use of high energy cross-section data which allow the extrapolation down to the energies of interest. Nevertheless, both these approaches might introduce several uncertainties on the reaction rate, and affect the predicted chemical abundances.

A turning point in this context has been the introduction of underground measurements performed for the first time at the Laboratory for Underground Nuclear Astrophysics (LUNA) laboratory located in Gran Sasso, Italy. The deep location of LUNA optimizes sensibly the signal-to-noise ratio for the nuclear reactions at astrophysical energies.

This thesis provides the direct measurements of the $^{22}\mathrm{Ne}(\alpha,\gamma)^{26}\mathrm{Mg}$ and $^{20}\mathrm{Ne}(\mathrm{p},\gamma)^{21}\mathrm{Na}$ reactions at LUNA. The first reaction plays an important role in the nucleosynthe-

sis of heavier elements through the slow neutron capture process AGB and massive stars. In particular, the ^{22}Ne$(\alpha,\gamma)^{26}$Mg reaction competes with the ^{22}Ne$(\alpha,\mathrm{n})^{25}$Mg reaction which is the main responsible for the production of the necessary neutrons for the s-process. To constrain the role of the ^{22}Ne$(\alpha,\mathrm{n})^{25}$Mg reaction in the s-process, the rate for both these reactions is required. The uncertainty of the ^{22}Ne$(\alpha,\gamma)^{26}$Mg reaction rate at astrophysical energies of interest ($0.1 \leq T \leq 0.4$) is governed by several low energy resonances which are measured only indirectly. To reduce these uncertainties, the first direct measurement of one of these resonances at 334 keV has been performed at LUNA.
The second reaction, ^{20}Ne$(\mathrm{p},\gamma)^{21}$Na governs the velocity of the NeNa cycle in several astrophysical scenarios and determine the final chemical abundances of the cycle. The rate of this reaction, depending on the temperature, is dominated by the high energy tail of a sub-threshold state at E_R = -6.7 keV, a direct capture component and a narrow resonance at E_R = 366 keV. To reduce the uncertainty of the reaction rate, the 366 keV resonance has been directly measured. Future measurements of cross-sections below 400 keV will follow the work presented here.

The thesis is organized into four chapters: Chapter 1 introduces some basic concepts related to stellar evolution and gives a general description of the nuclear reaction in stars. Chapter 2 describes the LUNA experiment, the accelerator, and common experimental details on the two reactions studied in this thesis. Chapter 3 is dedicated to the study of the ^{22}Ne$(\alpha,\gamma)^{26}$Mg reaction. This chapter provides a description of the astrophysical relevance and the current knowledge of the ^{22}Ne$(\alpha,\gamma)^{26}$Mg reaction, a description of the experimental setup, the measurements, analysis techniques, and the final results. Chapter 4 reports the study of ^{20}Ne$(\mathrm{p},\gamma)^{21}$Na reaction. This chapter provides the astrophysical motivation, the state of the art, the experimental setup, the measurements performed, data analysis, Monte Carlo simulations, and the final results.

This thesis is the outcome of my own analysis and the results shown in the text, especially the results related to the ^{20}Ne$(\mathrm{p},\gamma)^{21}$Na reaction should be considered as preliminary.

Chapter 1

Nuclear astrophysics in stars

I'm pretty sure, that the answers to the questions I grew up with can be found in stars, as if all their beauty weren't enough.

EM

What are we made of and how were the elements that we are made of formed after the Big Bang? The main elements that our body is made of are carbon (C), oxygen (O), and nitrogen (N), and all these elements are produced in stars via nuclear fusion reactions. Nuclear astrophysics studies nuclear-level processes that take place naturally in the Universe. As its name suggests, nuclear astrophysics is at the intersection of astrophysics and nuclear physics. Astrophysics applies the laws of physics to the study of celestial objects, from the Sun to much larger and more complicated objects. On the other hand, nuclear physics studies the interactions between the constituents of atomic nuclei, which are $\sim 10^{26}$ times smaller than the Sun. The combination of both fields can explain the formation of the chemical elements our universe is made of and how nuclear processes shape the cosmos.
This chapter aims to introduce some of the basic concepts in star evolution and in nuclear astrophysics. In the first section, a short overview on the life of stars, with major attention on post main sequence evolution, is given. Instead, the second section will focus on a general description of thermonuclear reactions in stars, emphasizing the particle induced reactions.

1.1 Stellar evolution

Stars are not eternal and their lives can be very different, depending on the mass and composition of the stars themselves. Their interiors are the main production sites of elements. Generations of stars have been formed and released their matter via mass-loss processes or explosions to the interstellar medium. This chemically enriched matter provides the building blocks of new stellar systems, planets, and

even life itself. The most crucial parameter in a star's life is its mass, more precisely, the mass it has when it starts the hydrogen fusion processes in its core (main-sequence mass). This process allows keeping the balance with gravity, preventing the star from collapsing toward its center. When the core of the star runs out of hydrogen it undergoes a series of changes until it dies, and all these changes and the way it dies depend on the mass of the star. The whole process from the main sequence to the end takes long, much longer than any living being's life, although how long the evolution takes also depends on the star's mass. One of the most powerful tools in astrophysics, to trace the evolutionary stage of a star, is the Hertzsprung-Russell diagram (H-R diagram). It allows us to study stars in different astrophysical sites and investigate their formation history. The H-R diagram shows the luminosity (or absolute magnitude) of stars as a function of the effective temperature (Figure 1.1).
Most of the stars, including our Sun, are found along a region called the Main Sequence. These stars are fusing hydrogen to helium in their cores. Main Sequence stars vary widely in effective temperature but the hotter they are, the more luminous they are, therefore the main sequence line follows a band going from the bottom-right of the diagram to the top-left. Other major groups of stars shown in the H-R diagram are the white dwarfs, located in the lower-left region, and the giants (and supergiants) in the upper-right region; luminous stars that have evolved off the main sequence.

1.1.1 Star formation

The light elements such as H, ^{2}H, ^{3}H, ^{3}He, ^{4}He and some amount of Li and Be were produced during the first 20 minutes after the Big Bang, in a process referred to as Big Bang Nucleosynthesis (BBN). After the BBN, the Universe expanded and cooled down without any change in terms of baryonic matter. Thereafter, about 380.000 years after the Big Bang, the charged electrons and protons combined to form neutral hydrogen atoms. This epoch is known as the recombination era. After recombination, the Universe entered a period called the "Dark Ages of the Universe", until gravitational attraction operated on very slight over-densities in the matter distribution, leading to the formation of stars and galaxies.
Our understanding of the star formation process is mainly based on observations. What is known until now indicates that stars are formed out of giant collapsing clouds of gas and can take place under a wide range of circumstances which result in stars being formed at a slow rate (star formation region in our galaxy) or hundreds to thousands of times faster (such as in the compressed gas clouds which result when galaxies are disturbed or actually collide). The gas clouds are in hydrostatic equilibrium with the surrounding interstellar medium, as long as the

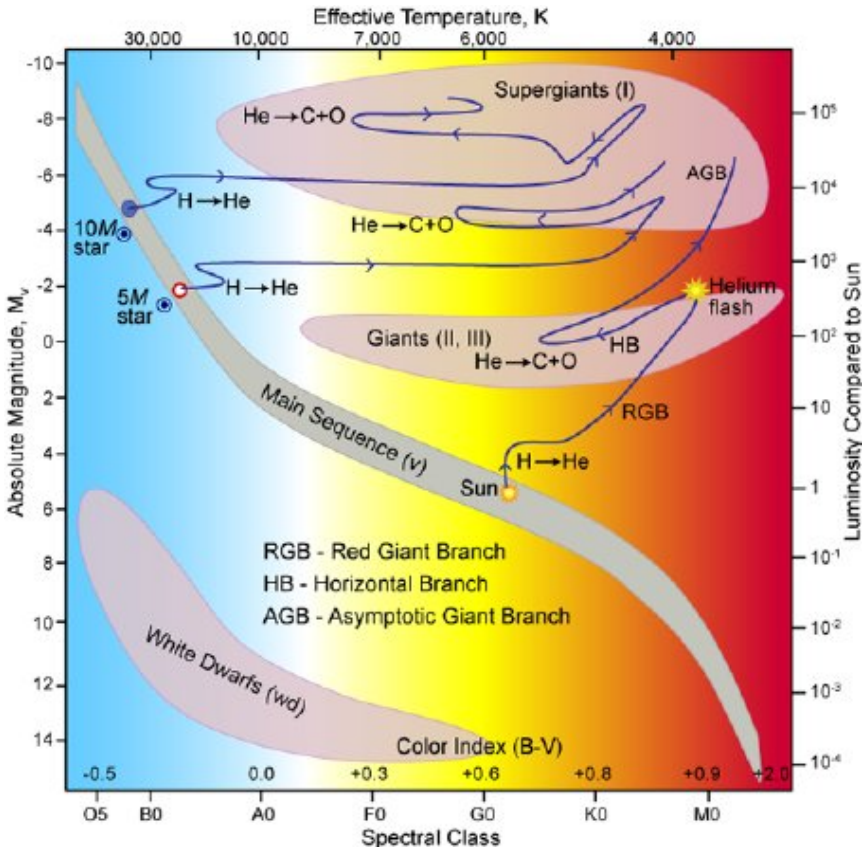

Figure 1.1: Hertzsprung-Russell (H-R) diagram which shows stars in terms of their luminosity (reported on the right axis, related to the stellar mass and size) and temperature (reported on the top axis). The colored background shows the spectral class reported on the lower axis. The blue lines show three different evolutionary scenarios for stars of 1 solar mass, 5 solar masses, and 10 solar masses. Illustration: Robert Hollow, Commonwealth Science and Indus- trial Research Organisation (CSIRO), Australia, adapted by Carin Cain.

thermal energy compensates the gravitational energy. For a cloud of a given radius and temperature, the equilibrium is given by Eq. 1.1:

$$\frac{3}{5}G\frac{M^2}{R} = 3\frac{M}{m}GkT \tag{1.1}$$

where M, m, and R are the total mass of the cloud, the average mass of the particles forming the cloud, and the radius of the clouds, respectively.
When the thermal energy becomes too low with respect to the gravitational energy, the gas cloud can become gravitationally unstable and start to collapse. The time scale of the cloud collapsing process is of several millions of years, due to the low densities involved. For a given gas cloud there is a critical mass, called the Jeans mass, which depends on the radius of the cloud, its temperature and the average mass of the particles in the cloud given by Eq. 1.2:

$$M_J = \left(\frac{5kT}{Gm}\right)^{3/2}\left(\frac{3}{4\pi\rho}\right)^{1/2} \tag{1.2}$$

with ρ the cloud density. If the Jeans mass is exceeded ($M_{cloud} \geq$M$_J$), the cloud becomes unstable to collapse. Since the Jeans mass decreases with increasing density, smaller fragments are formed and, therefore, clumps of different mass (typical initial mass of material $\sim 0.01M_\odot$, where $M_\odot$ refers to solar mass which is a standard unit of mass in astronomy equal to $\sim 2{\times}10^{30}$ kg) can form stars of different initial masses. As soon as the collapse slows down and the cloud core reaches hydrostatic equilibrium (beginning of the hydrogen-burning stage), a more stellar-like object, known as a protostar is formed. The rest of the cloud material keeps falling onto the protostar which forms an accretion disk that surrounds the protostar. During this process, together with the mass, the temperature of the material increases due to the heat generated by the gravitational compression. The increasing internal temperature (about 1 million kelvin) causes the protostar to be visible, radiating approximately 1.000 times the Sun's current luminosity. When mass accretion stops in the protostar, the stellar object is known as pre-main sequence star (pre-MS). This stage of stellar evolution towards the main sequence may last between 100.000 and 10 million years depending on the size of the pre-main sequence star being formed. Pre-MS stars with masses $0.01M_\odot \leq M \leq 0.08M_\odot$ don't have enough mass to ignite H burning and they become brown dwarfs. On the other hand, the gravitational compression for the pre-MS stars with masses above $0.08M_\odot$ continues and since the temperature in this stage is still too low for nuclear burning, the pre-MS star moves almost horizontally in the H-R diagram (following the so-called Hayashi line), increasing its temperature and slightly increasing its luminosity. The contraction continues until the central temperature becomes high enough to start H burning and a star is born. The energy released from the H fusion in the core

of the star stops the contraction and the stars lie on the zero-age main sequence. A more complete description of the stars formation and their evolution up to the death can be found in [1, 2, 3].

1.1.2 Main sequence

Stars on the zero-age main sequence are in thermal and hydrostatic equilibrium with an almost homogeneous composition (mainly hydrogen and some small traces of helium). On the main sequence phase, they will produce most of the energy converting hydrogen in helium through the proton-proton chain, the CNO cycle, or other catalytic cycles. The rate at which they do this and the amount of fuel available depends upon the mass of the star and the central temperature. The position on the main sequence and the spectral class they belong to is a function of the star's mass, this is so-called mass-luminosity relation given by:

$$L \propto M^{3.5} \tag{1.3}$$

where L is the luminosity of the star and M its mass. Main sequence stars vary in mass. More massive stars have a stronger gravitational force acting inwards so their core gets hotter. The higher temperatures mean that the nuclear reactions occur at a much greater rate in massive stars. They thus use up their fuel much quicker than lower mass stars and therefore their life is relatively short. On the other hand, the life of the low-mass star in the main sequence will be longer. A star with only half the mass of the Sun can spend 80 billion years on the main sequence, much longer than the age of the Universe which means that all the low-mass stars that have formed are still on the main sequence.

1.1.3 Beyond main sequence

When a main sequence star runs out of hydrogen in its core the energy production slows down and is not anymore sufficient to counteract the gravitational collapse. When this takes place, the radiation pushes the outer layers of the star far out into space, turning the star into a red giant. On the other side, the core of the star continues to collapse, and to heat up until it reaches high temperatures, high enough to fuse helium into carbon. Eventually, the helium will also run out and other elements as well. The exact post-main sequence and the fate of the star from the main sequence to its death depend on the mass. The point in which the star leaves the main sequence is called turnoff point and its position in the HR diagram can be used to evaluate the age of the cluster to which it belongs. Since the life and the death of the stars depend on their mass, it is difficult to make a precise classification. In general, there are four major categories.

Very low-mass stars

This category of stars includes stars with mass, $M \leq 0.4 M_{\odot}$. Their structure is made of a unique convection zone, with hydrogen and helium mixed throughout the star. The star fuses hydrogen slowly and will never build up a helium core or reach temperatures high enough for any other nuclear reaction to take place. These stars will spend about 100 Gyr in the main sequence and probably end up as Black Dwarfs. At the moment there are no very low-mass stars to run over all the hydrogen and end in Black Dwarfs.

Low-mass stars

The mass limit for low-mass stars depends on the development of an electron-degenerate structure which is a stellar application of the Pauli Exclusion Principle. These structures are generated in extremely high temperature and pressure conditions with atoms stripped of their electrons. At high densities the electrons are forced to close together but they are allowed to exist only at certain energy level. In dense gas conditions such as the stellar environment, all of the lower energy levels become filled with electrons and the gas itself is defined as degenerate matter.
Basically, all stars with masses $M \leq 2 M_{\odot}$ are classified low mass stars. All these stars, in the main-sequence phase, will fuse hydrogen into helium in their cores. The path they will follow after the hydrogen runs out depends on the mass of the star. Moreover, some differences exist also during the main-sequence phase.
In stars with masses $M \leq 1.5 M_{\odot}$, the hydrogen-burning proceeds via the pp chains, and the energy generated in the core is transported via radiation. More massive stars, instead, with masses above $1.5 M_{\odot}$ fuse hydrogen via the CNO cycles in their cores and the transportation of the energy from the core to the external layers is done through convection.
During the core H-burning phase, the amount of free particles decreases, and the core slightly contracts in order to stay in hydrostatic equilibrium. The change of mean weight and opacity during this phase slowly increases the luminosity and the star moves from the main sequence to the red giant branch (RGB) in the HR diagram. During the RGB phase, the contraction heats up the core until it becomes electron degenerated. The convective envelope deepens significantly, reducing the star's mass and dredges up the products of hydrogen burning from the outer core. The process is referred to as the first *dredge-up*.
In a normal gas, when the temperature reaches 0.1 GK, the helium in the core starts to fuse to carbon and oxygen and the star enters the helium-burning phase. Consequently, the temperature will slow down and generated energy will cause an expansion until the stability of the star is reached. However, because of degenerate

electrons in the RGB stars, helium ignites violently. As the nuclear He-burning progresses inwards, the degeneracy of the core is lifted. This thermonuclear runaway is also known as *core helium-flash* and determines the end of the RGB phase of low-mass stars.
After the degeneracy is lifted, the high core temperature makes the star expand and cool down. As a result, the luminosity decreases significantly and the star moves in the horizontal branch. During this stage, in the core of the star, the helium fusion goes on building up the C-O core, while hydrogen fusion is still active in a shell around the core, mainly through the CNO cycle. The nuclear energy produced in helium burning is considerably smaller with respect to hydrogen burning. Therefore, the helium-burning phase is relatively short compared with the hydrogen-burning phase.
When the amount of helium in the core is exhausted, the star is no longer in dynamic equilibrium. The thermal pressure is not able to balance the gravitational forces and the core starts to contract. Helium burning moves in a shell surrounding the C-O core, separated from the H burning shell by a He-rich intershell. The star enters the early asymptotic giant branch (E-AGB) phase and starts to move on towards higher luminosity which was stopped by core helium burning. Nuclear energy production is dominated by the He-shell that burns outward. Meanwhile, the H-layer around the He-shell expands and cools down until the H-shell burning extinguishes. The energy produced in the helium-burning shell can not be radiated away and a thermonuclear runaway takes place, known as *helium shell flash* or *thermal pulse*. The hydrogen-burning shell reignites and ultimately takes over as the dominant nuclear energy source until the next *thermal pulse* occurs. The cycle may repeat many times and the evolutionary phase is known as the thermally pulsing asymptotic giant branch (TP-AGB). During this stage the star moves horizontally to the left in the HR diagram.
Towards the end of the TP-AGB phase, the star undergoes a period of heavy mass loss. Pulsations with increasing amplitudes and dust-driven winds drive the matter out where it loses its gravitational bound to the star and merges with the interstellar medium. As soon as the whole envelope is gone, which marks the end of this stage, low-mass star turns for a very short time into planetary nebulae and then end their lives as cooling C-O white dwarfs.

Intermediate-mass stars

The intermediate-mass stars have masses in the range $2M_{\odot} \leq \mathrm{M} \leq 8M_{\odot}$. The lives and death of these stars are not so different from the low-mass stars. The main difference is that for stars with masses above $2M_{\odot}$, helium cores during the red giant branch phase do not become electron degenerate. These stars typically end

up as white dwarf. In the HR- diagram, the stars move to the left side, in the region of classical Cepheids, and then comes back to the right. In stars with mass above $4M_{\odot}$ the fusion of the He-shell causes a very strong expansion and cooling of the envelope, extinguishing the H-shell. Products of hydrogen burning are then convected to the surface, enhancing the abundance of ^{4}He, ^{14}N and ^{13}C in the so-called *second dredge-up*. Nuclear reactions in these stars make most of the carbon and nitrogen in the Universe. When they die, they blow off their atmospheres, dispersing such elements in the space. After the *second dredge-up*, the H shell is reignited and the star moves in the AGB phase.

Massive stars

Stars with masses a least $8M_{\odot}$ are called high-mass stars. These stars live only a short time of ∼10 million years on the Main Sequence. Still, they go through stages very similar to those of intermediate-mass stars. With respect to the intermediate-mass stars, which end their live by expelling their outer layers due to thermal pulses in a planetary nebula phase, the high mass stars have so much mass that they can survive this phase. Once the high mass stars start to run out of hydrogen in the core, and start burning hydrogen in the shell, they expand into a Red Giant stage just like low mass stars. In this case, there is no helium flash. The helium core is so hot that nuclear fusion begins and continues slowly over time, without any degeneracy pressure. During this phase, stars move back toward the MS, and fuse helium in their core in $\leq 10^5$ years. Once the high mass star reaches the Red Supergiant stage, and is burning helium in a shell around the inert carbon core, the core can reach temperatures able to fuse carbon into heavier elements. The carbon in its core is burned only for few hundred years, and the next stages such as neon burning, oxygen burning and silicon burning begin. Each stage is shorter than the previous one, partly because the reactions are less and less efficient: each of them produces less and less energy. Once silicon is fusing into iron, there are no reactions with iron able to generate energy and only degeneracy pressure can hold the star up against the gravity. When the pressure caused by the electron degenerated matter (degeneracy pressure) is overcome, the star has reached the final stage. While all of this is happening, the outer appearance of the star changes relatively slowly, with luminosity staying virtually the same. The stars tend to follow a zig-zag horizontal path in the HR diagram. The end of massive stars is determined from the initial mass of the star. Stars with masses $8\mathrm{M}_{\odot} \leq M \leq 11\mathrm{M}_{\odot}$ will end as an oxygen–neon white dwarf since they are not able to fuse elements higher then carbon in their core.
Stars with initial masses $M \leq 20$ - $30M_{\odot}$ explode as a type II Supernova and form a neutron star as a remnant, while stars above this limit can collapse directly to

form a black hole without a supernova explosion.

1.2 Thermonuclear reactions in stars

Different theoretical models have been developed to understand the evolution of stars and to reproduce the observed elemental abundances. A crucial input for these models is the thermonuclear reaction rate for all the nuclear reactions involved. The energy produced by the thermonuclear reactions depends on the energy released by the single reaction involved and on the number of reactions happened in the star. In general, thermonuclear reactions in stars are two body problems which can be schematically described as a + A→ B+b, with A the target nucleus, a the projectile and B, b the reaction products. The reaction rate is the number of reactions per unit volume per unit time [2]. It depends on the density of interacting particles ρ_a and ρ_A, their relative velocity v, and the nuclear cross-section $\sigma(v)$ and is given by Eq. 1.4:

$$r = \rho_a \rho_A v \sigma(v) \tag{1.4}$$

Inside the stars, nuclei are not moving at a unique and precise speed. They interact in a certain range of velocities following a probability distribution $\phi(v)$, known as Maxwell-Boltzmann distribution. The $\phi(v)$ describes the speed of particles in thermal equilibrium, and gives the probability for a particle to have a speed in a certain interval. This distribution is normalized to unity:

$$\int_0^\infty v\sigma(v)\phi(v)dv = 1 \tag{1.5}$$

The reaction rate in Eq. 1.4 becomes:

$$r = \rho_a \rho_A \int_0^\infty v\sigma(v)\phi(v)dv = \rho_a \rho_A \langle \sigma v \rangle \tag{1.6}$$

where the bracket quantity $\langle \sigma v \rangle$ refers to the reaction rate per particle pair. In a non-degenerate, non relativistic stellar environment, the velocity of the two nuclear species A and a, can be well described by the Maxwell-Boltzmann distribution Eq. 1.7 and Eq. 1.8:

$$\phi(v_a) = 4\pi v_a^2 \left(\frac{m_a}{2\pi k_B T}\right)^{3/2} e^{-m_a v_a^2/2k_B T} \tag{1.7}$$

$$\phi(v_A) = 4\pi v_A^2 \left(\frac{m_A}{2\pi k_B T}\right)^{3/2} e^{-m_A v_A^2/2k_B T} \tag{1.8}$$

where k_B is the Boltzmann constant and T is the gas temperature. Therefore, using Eq. 1.7 and Eq. 1.8, the reaction rate for particle pair (Eq. 1.6) involves a double integral over both velocity distributions:

$$\langle \sigma \upsilon \rangle = \int_0^{+\infty} \int_0^{+\infty} \phi(\upsilon_a)\phi(\upsilon_A)\sigma(\upsilon)\upsilon d\upsilon_a d\upsilon_A \tag{1.9}$$

The quantities υ_a and υ_A, are related to the relative velocity $\upsilon = \upsilon_a - \upsilon_a$ and the center of mass velocity $V = \frac{m_a}{m_a+m_A}\upsilon_a + \frac{m_A}{m_a+m_A}\upsilon_A$. Assuming the total mass $M = m_a + m_A$ and the reduced mass $\mu = \frac{m_a m_A}{m_a+m_A}$, the velocity distributions $\phi(\upsilon)$ and $\phi(V)$ are given by Eq. 1.10 and Eq. 1.11, respectively:

$$\phi(\upsilon) = 4\pi\upsilon^2 \left(\frac{\mu}{2\pi k_B T}\right)^{3/2} e^{-\mu\upsilon^2/2k_B T} \tag{1.10}$$

$$\phi(V) = 4\pi V^2 \left(\frac{M}{2\pi k_B T}\right)^{3/2} e^{-MV^2/2k_B T} \tag{1.11}$$

It is now possible to write Eq. 1.9 with the new variables:

$$\langle \sigma \upsilon \rangle = \int_0^{+\infty} \phi(V)dV \int_0^{+\infty} \phi(\upsilon)\sigma(\upsilon)\upsilon d\upsilon \tag{1.12}$$

Assuming the center of mass energy $E = \frac{1}{2}\mu\upsilon^2$ and knowing that the cross-section depends only on the relative velocity of interacting nuclei, Eq. 1.12 becomes:

$$\langle \sigma \upsilon \rangle = \left(\frac{8}{\pi\mu}\right)^{\frac{1}{2}} \frac{1}{(k_B T)^{\frac{3}{2}}} \int_0^{+\infty} E\sigma(E)e^{-E/k_B T}dE \tag{1.13}$$

The reaction rate influences different stellar items such as time scales, nucleosynthesis of elements and energy production. As described in Section 1.1.3, during the stellar evolution, the temperature changes and consequently the reaction rate will change. The energy dependence of the cross section, $\sigma(E)$, is related to the reaction mechanism that can be resonant or non-resonant.

1.2.1 Non-resonant reactions induced by charged particles

The interacting nuclei inside the stellar environment are positively charged and continuously repel each other. The potential energy associated to this repulsion is called the Coulomb potential and for two interacting particles A and a has the form of:

$$\begin{cases} E_C(r) = \frac{Z_a Z_A e^2}{r}, \ r \geq R_n \\ E_C(r) = -V_0, \ r \leq R_n \end{cases} . \tag{1.14}$$

where r is the distance of the interacting nuclei, R_n is the sum of interacting nuclei radii, and Z_a, Z_A the atomic numbers of the interacting nuclei, respectively. A qualitative behavior of the potential is shown in Figure 1.2.
At stellar temperatures (energies), the kinetic energy of the interacting particles is usually much lower than the Coulomb repulsion between the nuclei. Any classical approach requires energies higher than $E_C(r)$. Considering quantum mechanics, one finds that there is a finite probability to go through the Coulomb barrier even for particles with energies $E < E_c$ (Tunnel effect). The nuclear reactions in stars happen through quantum tunneling.
In quantum mechanics, the probability of finding the particle at position r is given

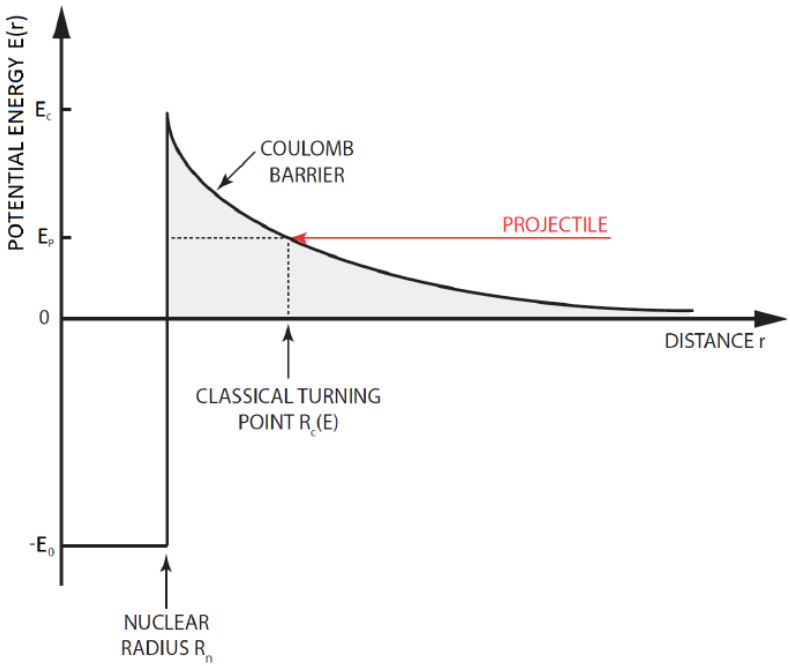

Figure 1.2: Schematic representation of the combined nuclear and Coulomb potentials. An incident projectile with energy $E < E_C$ will try to penetrate the Coulomb barrier. Classically the projectile would reach the minimum distance to the nucleus at a distance $R_C(E)$ called the classical turning point.

by the square of its wave function $|\psi(r)|^2$. Therefore, the tunneling probability to penetrate is given by:

$$P = \frac{|\psi(R_n)|^2}{|\psi(R_C)|^2} \tag{1.15}$$

where R_C is the classical turning point, the distance where the barrier is equal to the projectile energy. Considering projectile energies far below the Coulomb barrier and resolving the Schrödinger equation for the Coulomb potential, the tunneling probability in Eq. 1.15 can be approximated by the Gamow factor given in Eq. 1.17:

$$P = e^{-2\pi\eta} \tag{1.16}$$

where η is the so-called Sommerfeld parameter and is given by:

$$\eta = \frac{Z_a Z_A e^2}{\sqrt{2}\hbar}\sqrt{\frac{\mu}{E}} \tag{1.17}$$

with E the center of mass energy given in keV and μ the reduced mass in amu.
For charged particles, the nuclear the cross section, $\sigma(E)$, is proportional to the probability P given in Eq. 1.16 and drops rapidly for energies below the Coulomb barrier:

$$\sigma(E) \propto e^{-2\pi\eta} \tag{1.18}$$

On the other side, the cross section $\sigma(E)$, is also proportional to the squared De Broglie wavelength λ:

$$\sigma(E) \propto \pi\lambda^2 \propto \frac{1}{E} \tag{1.19}$$

with λ defined in Eq. 1.20:

$$\lambda = \frac{2\pi}{k} = \frac{m_a + m_A}{m_A}\frac{h}{\sqrt{2m_a E}} \tag{1.20}$$

where E is the energy in the laboratory frame.
Using both terms in Eq. 1.18 and Eq. 1.19, the cross section can be given as:

$$\sigma(E) \propto \frac{1}{E}e^{-2\pi\eta}S(E) \tag{1.21}$$

where $S(E)$ is the *astrophysical* $S-factor$ and includes all nuclear effects. For non-resonant reactions, the S-factor varies slowly. Therefore, $S(E)$ values measured at high energies can be extrapolated to lower energies where measurements are not possible.
Using the Eq. 1.21 in the Eq. 1.13 the reaction rate per particle pair becomes:

$$\langle\sigma\upsilon\rangle = \left(\frac{8}{\pi\mu}\right)^{1/2}\frac{1}{(k_B T)^{3/2}}\int_0^{+\infty} S(E)e^{-E/k_B T}e^{-2\pi\eta}dE \tag{1.22}$$

Since the $S(E)$ for non-resonant reactions varies smoothly with energy, it can be assumed constant and moved outside the integral:

$$\langle \sigma \upsilon \rangle = \left(\frac{8}{\pi \mu} \right)^{1/2} \frac{1}{(k_B T)^{3/2}} S(E_0) \int_0^{+\infty} e^{-E/k_B T} e^{-2\pi\eta} dE \tag{1.23}$$

The energy dependence in the Eq. 1.22 or (Eq. 1.23) is dominated by the exponential terms of the integrand. The first term, $e^{-E/k_B T}$, comes from the Maxwell-Boltzmann distribution and decreases with increasing energy. The second one, $e^{-2\pi\eta}$, represent the tunneling probability and decreases with decreasing energy. The convolution of the two terms gives rise to the so-called *Gamow peak* which defines the narrow energy window over which most of the stellar nuclear reactions happens.

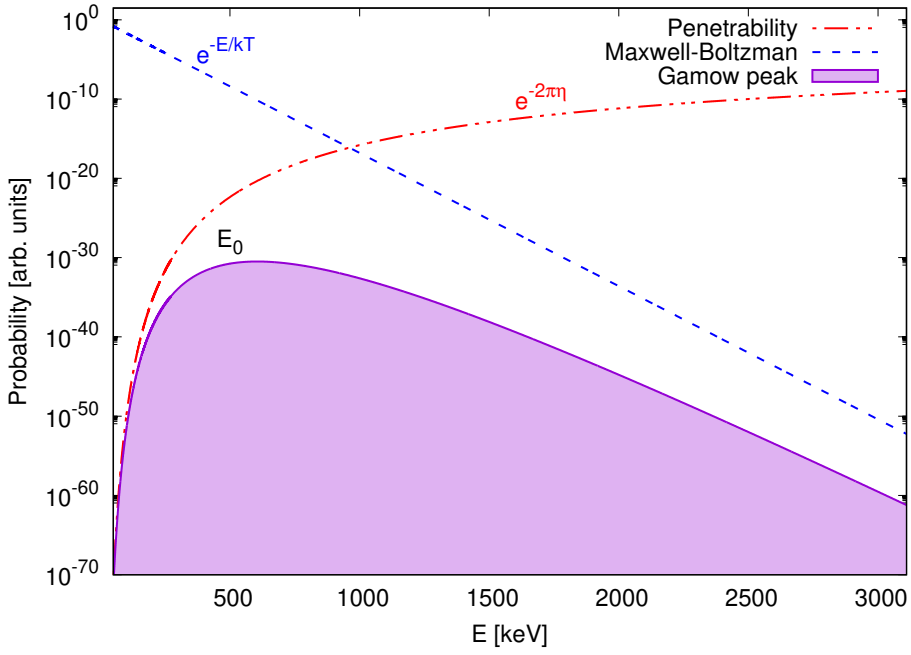

Figure 1.3: Gamow energy window for the $^{22}\mathrm{Ne}(\alpha,\gamma)^{26}\mathrm{Mg}$ *reaction at 0.3 GK. In red the tunneling probability, in blue the Maxwell-Boltzman distribution and in violet the Gamow function.*

Figure 1.3 shows both terms of the integrand in Eq. 1.23 as a function of the energy and their convolution as well. For a given stellar environment with temperature T, the energy of Gamow peak maximum E_0 is obtained from the first derivative of

the integrand:

$$E_0 = 0.1220 \left(Z_a^2 Z_A^2 \mu T\right)^{1/3} \tag{1.24}$$

where T is given in units of GK and μ in amu.
For non resonant reactions, the Gamow peak can be approximated with a Gaussian function:

$$exp\left(-\frac{2E_0^{3/2}}{\sqrt{E}k_BT} - \sqrt{\frac{E}{k_BT}}\right) \approx exp\left(-\frac{3E_0}{k_BT}\right) exp\left[-\left(\frac{E-E_0}{\Delta/2}\right)^2\right] \tag{1.25}$$

where Δ is the effective width of the peak:

$$\Delta = \frac{4}{\sqrt{3}}\sqrt{E_0 k_B T} \tag{1.26}$$

Nuclear reactions in stars take place in the energy range $E = E_0 \pm \Delta/2$.
Considering the approximation in Eq. 1.25, the reaction rate in Eq. 1.23 becomes:

$$\langle \sigma \upsilon \rangle = \left(\frac{8}{\mu}\right)^{1/2} \frac{\Delta}{(k_B T)^{3/2}} S(E_0) e^{-3E_0/k_B T} \tag{1.27}$$

where a constant S-factor, $S(E_0)$, is assumed.
If the S-factor cannot be assumed constant for certain energy regions, a second correction is required and can be performed through a Taylor series around $E = 0$:

$$S(E) \approx S(0) + S'(0)E + \frac{1}{2}S''(0)E^2 \tag{1.28}$$

where the primes indicate derivatives with respect to E. As a result of this expansion, the constant astrophysical S-factor $S(E_0)$ in Eq. 1.27 is replaced by an effective S-factor S_{eff} [4, 2]:

$$\begin{aligned} S_{eff}(E_0) = S(0) \Bigg[1 + \frac{5}{12\tau} + \frac{S'(0)}{S(0)} (E_0 + \\ \frac{35}{36}k_B T + \frac{1}{2}\frac{S''(0)}{S'(0)}\left(E_0^2 + \frac{89}{36}E_0 k_B T\right) \end{aligned} \tag{1.29}$$

where τ is a correction due to the asymmetry of the real Gamow peak with respect to the Gaussian approximation.

1.2.2 Direct capture

The radiative direct capture reaction is a particular case of non-resonant mechanism. This process is characterized by the complete absorption of the incident

projectile by the target and immediate ejection of one or more photons with energy E_γ:

$$E_\gamma = E_{cm} + Q_{value} - E_i \tag{1.30}$$

where E_i is the energy of the level populated in the nucleus B. The ejected photons are strongly peaked along the trajectory of the incident projectile. Figure 1.4 shows a schematic representation of a typical direct capture mechanism. Considering the transition from the entrance channel A+a to the the final nucleus B, the cross-section can be described by a single matrix element:

$$\sigma_\gamma \propto |\langle B|H_\gamma|A+a\rangle|^2 \tag{1.31}$$

where H_γ describes the γ-emission. The direct capture is a purely electromagnetic

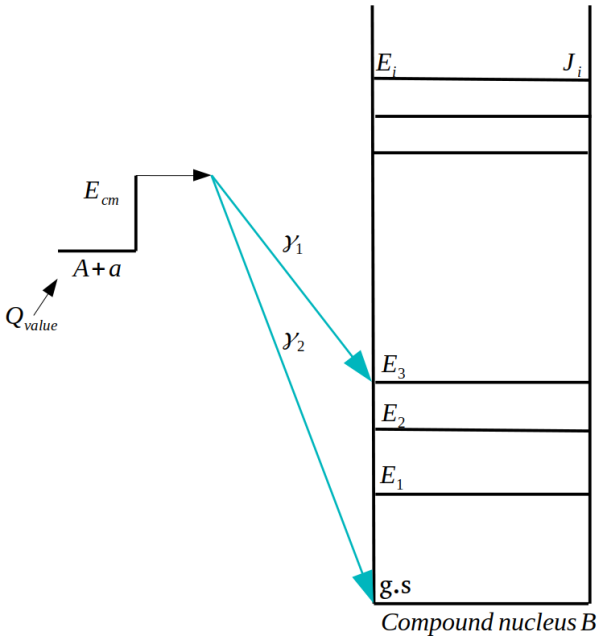

Figure 1.4: Schematic representation of a generic direct capture reaction A+a.

process which dominates at energies above 20 MeV, or when there are no strong resonances in or near the Gamow window. It is also particularly important at low energies in light nuclei reactions where the density of resonances is very low. The radiative capture reactions are involved in pp chain, CNO cycles, in the explosive conditions in novae, x-ray bursts, and supernovae. Compared to strong interactions, the direct capture progress slowly and often control the reaction process and

the rate of nucleosynthesis. It is important to directly measure the radiative capture cross-section at the relevant energies, but at the same time it is very difficult due to the low probability of these reactions. Thanks to their smooth $S(E)$-factor, it is possible to extrapolate the high energy data down to the relevant energies or to adopt indirect approaches.

1.2.3 Reactions through narrow and isolated resonances

In the resonant mechanism, the excited state E_r of the compound nucleus is populated in the entrance channel and then decays to a lower state. This process happens only when the energy $Q_{value} + E_R$ of the entrance channel coincides with the energy of the excited state in the compound nucleus:

$$E = E_r = Q_{value} + E_R \tag{1.32}$$

Figure 1.5 shows the transition from the entrance channel A + a to the excited state E_r of the compound nucleus B. If the exited state E_r decays by photon emission into a lower energy state E_f, the cross section σ_γ can be calculated as the product of two matrix elements:[1]:

$$\sigma_\gamma \propto |\langle E_f|H_\gamma|E_r\rangle|^2 |\langle E_r|H_f|A+a\rangle|^2 \tag{1.33}$$

where the matrix element H_f describes the formation of the compound state and H_γ the subsequent γ- emission of the state E_r.
Each matrix element is equivalent to a partial width Γ_i. Introducing Γ_i, the cross section in Eq. 1.33 can be rewritten in a simple way such as:

$$\sigma_\gamma \propto \Gamma_f \Gamma_\gamma \tag{1.34}$$

The resonance may decay or be excited in different ways. All different process involved are taken into account in the total width Γ, defined as:

$$\Gamma = \sum_i \Gamma_i \tag{1.35}$$

For $\Gamma \leq E_r$ the resonance is defined as narrow and it is isolated if the separation of nuclear levels is large compared to the width. The cross-section of a narrow isolated resonance can be described by the Breit-Wigner cross section:

$$\sigma_{BW}(E) = \frac{2J+1}{(2J_a+1)(2J_A+1)}\,(1+\delta_{aA})\,\pi\lambda^2 \frac{\Gamma_\gamma \Gamma_f}{(E-E_R)^2 + (\frac{\Gamma}{2})^2} \tag{1.36}$$

where

[1] Two matrix elements are due to the two-step process

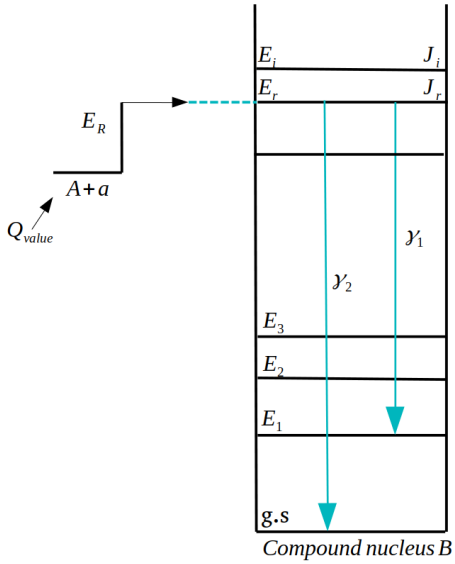

Figure 1.5: Resonant capture reaction A(a,γ)B.

- j_a, j_A are the spins of the interacting particles and J is the spin of the excited state of the compound nucleus
- $1+\delta_{aA}$ containing the Kronecker delta function (δ_{aA}), takes into account the increase in the cross section for the scattering of identical particles
- λ is the de Broglie wavelength of the projectile in the center of mass system defined in Eq. 1.20

Considering the Breit-Wigner cross section in Eq. 1.36, the stellar reaction rate in a resonant case is given by:

$$\langle \sigma v \rangle = \left(\frac{8}{\pi\mu}\right)^{\frac{1}{2}} \frac{1}{(k_B T)^{\frac{3}{2}}} \int_0^\infty \sigma_{BW}(E) E e^{-E/k_B T} dE \tag{1.37}$$

Since the $\Gamma \leq E_r$, the Maxwell-Boltzmann distribution varies slowly, it is almost equal to its value at the resonance energy and can be taken outside the integral:

$$\langle \sigma v \rangle = \left(\frac{8}{\pi\mu}\right)^{\frac{1}{2}} \frac{1}{(k_B T)^{\frac{3}{2}}} E_R e^{-E_R/k_B T} \int_0^\infty \sigma_{BW}(E) dE \tag{1.38}$$

Introducing the resonance strength $\omega\gamma$ defined as:

$$\omega\gamma = \frac{2J+1}{(2J_a+1)(2J_A+1)} (1+\delta_{12}) \frac{\Gamma_\gamma \Gamma_f}{\Gamma} = \omega \frac{\Gamma_\gamma \Gamma_f}{\Gamma} \tag{1.39}$$

the integral in Eq. 1.38 becomes:

$$\int_0^\infty \sigma_{BW}(E)dE = 2\pi^2\lambda^2\omega\gamma \tag{1.40}$$

while the reaction rate can be expressed as:

$$\langle\sigma\upsilon\rangle = \left(\frac{2\pi}{\mu k_B T}\right)^{\frac{3}{2}} \hbar^2(\omega\gamma)_R e^{-E_R/k_B T} \tag{1.41}$$

1.2.4 Reactions through broad and isolated resonances

A broad resonance is characterized by $\Gamma\ /E_R \geq 10$ %. In this case the energy dependence of the total and partial widths together with the de Broglie wavelength, are not negligible and the Breit-Wigner cross-section is expressed by:

$$\sigma_{BW}(E) = \sigma_R \frac{\Gamma_R}{E} \frac{\Gamma_\gamma(E)}{\Gamma_\gamma(E_R)} \frac{\Gamma_f(E)}{\Gamma_f(E_R)} \frac{(\Gamma_R/2)^2}{(E-E_R)^2 + (\Gamma(E))^2/4} \tag{1.42}$$

where σ_R is the cross section at the resonant energy. The stellar reaction rate can be given as:

$$\langle\sigma\upsilon\rangle = \frac{\sqrt{2\pi}\hbar^2\omega}{(\mu k_B T)^{3/2}} \int_0^\infty dE e^{-E/k_B T} \frac{\Gamma_f(E_R)\Gamma_\gamma(E)}{(E-E_R)^2 + (\Gamma(E))^2/4} \tag{1.43}$$

For energies lower than the resonance energy, the S-factor varies slowly with energy, therefore the reaction rate can be calculated in the same way as for non resonant reactions. Moreover, if there is no interference between resonant and non resonant mechanism, the reaction rate $\langle\sigma\upsilon\rangle$ can be obtained as the sum of the different contributions:

$$\langle\sigma\upsilon\rangle \quad = \quad \langle\sigma\upsilon\rangle_{NR} + \langle\sigma\upsilon\rangle_R \tag{1.44}$$

If resonances near the particles threshold are present, they can completely dominate the reaction rate at low stellar temperatures.

1.2.4.1 Sub-threshold resonances

When the excited state with energy E_r is lower than the Q_{value} of the reaction, the resonance energy given by $E_R = E_r - Q_{value}$ is negative. It is quite clear that the exited state E_r cannot be formed. This kind of resonance mechanism is known as sub-threshold resonance (or sub-threshold bound state) and plays a significant role in nuclear astrophysics. Indeed, the sub-threshold resonance tail can increase significantly the nuclear reaction rate at relevant energies. Like in the resonant case, the sub-threshold resonance peak structure can be modeled using a Breit-Wigner distribution. In particular, this kind of mechanism is relevant for the ^{20}Ne(p, γ)^{21}Na reaction studied in the present work. Further information is given in Chapter 4.

Chapter 2

The LUNA experiment

Some people are so crazy that they actually venture into deep mines to observe the stars in the sky.

Naturalis Historia-Plinio, 23-79 B.C.

The $^{22}Ne(\alpha,\gamma)^{26}Mg$ and $^{20}Ne(p,\gamma)^{21}Na$ experiments presented in this work were performed at LUNA (Laboratory for Underground Nuclear Astrophysics [5]). This chapter is dedicated to the description of the LUNA experiment. The accelerator and the details of the gas target setup, underlying the main aspects related to the two reactions under study are briefly described. The last section is focused on the background reduction in an underground laboratory.

2.1 LUNA

The LUNA laboratory is located at Gran Sasso National Laboratory, Italy (LNGS). The laboratories are covered by 1400 m of rocks, corresponding to 3800 m of water equivalent. Such natural shielding reduces the muon component of the cosmic background by a factor of 10^6 and the neutron component by a factor of 10^3 with respect to a laboratory on the Earth's surface [6],[7]. The LUNA experiment exploits deep underground location and the low-background environment to perform direct measurements of nuclear reactions at relevant astrophysical energies. Since 1991 two different accelerators have been used at LUNA: a 50kV [8] and a 400 kV accelerator [9]. The 50 kV machine was mainly used to study H-burning reactions relevant to the Sun, producing pioneering results. After the "solar" phase of LUNA, the installation of the LUNA 400 kV accelerator, which is still operating today, started a rich program devoted to the study of the Big Bang Nucleosynthesis (BBN) and the synthesis of the elements through the CNO, Ne-Na and Mg-Al cycles.

2.2 Accelerator

The LUNA 400 kV accelerator is a commercial single-ended electrostatic accelerator [9], built by High Voltage Engineering Europe (HVEE) (Netherlands), able to meet the requirements of the scientific program of LUNA. The accelerator is enclosed in a tank filled with a gas mixture composed of N_2 (75%), and CO_2 (25%) at 20 bar (Figure 2.1). An Inline-Cockroft-Walton power supply inside the tank generates the High Voltage (HV) which is stabilized by an RC filter located at the power supply module and an active feedback loop based on a chain of resistors. The long-term beam stability is a key parameter for nuclear astrophysics experiments, because measuring low cross-sections requires long data-taking periods.

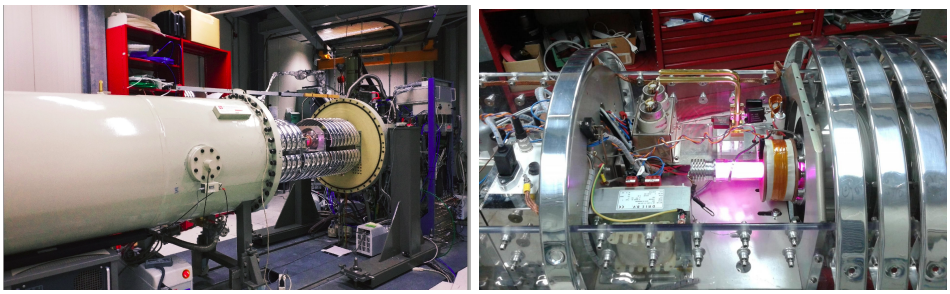

(a) *(b)*

Figure 2.1: LUNA 400kV machine. (a) Open tank of the LUNA 400 kV accelerator. The metallic rings keeping the ion source area free from electric fields, are visible. (b) Radio frequency ion source of the LUNA 400 kV accelerator. The pink light emitted by the hydrogen plasma is visible.

The radio-frequency ion source, mounted directly on the accelerator tube, provides proton and alpha beams with intensity up to 1mA and 500μA in the Faraday Cup (FC) at 0°, respectively (Figure 2.1b). A pumping system keeps the vacuum inside the accelerating tube at about 10^{-7} mbar. With a 45° analyzing magnet and a vertical steering magnet the ions produced by the LUNA 400 kV accelerator can be guided from FC0 to a windowless gas target (Section 2.3). Instead, using the 0° the ion beam is delivered to a solid target line. In Figure 2.2 both beamlines located at LUNA experimental hall are shown.
The beam current on the target depends on the ion. In the energy range 150–400 keV, the machine provides a proton beam current on target of up to 500 μA and an alpha beam current of up to 250 μA. Going down with the energy, the current on the target drops as well. To improve the focusing at lower energies, a manual shorting device allows to short-circuits some of the rings of the accelerator column,

limiting the number of active elements.
The controls of the beamline gate valves and Faraday cups, together with the computer which controls the accelerator itself, are located in the control room. The HVEE software allows to continuously monitor the status of all accelerator parameters and to choose the ion beam settings. The actual beam energy is a

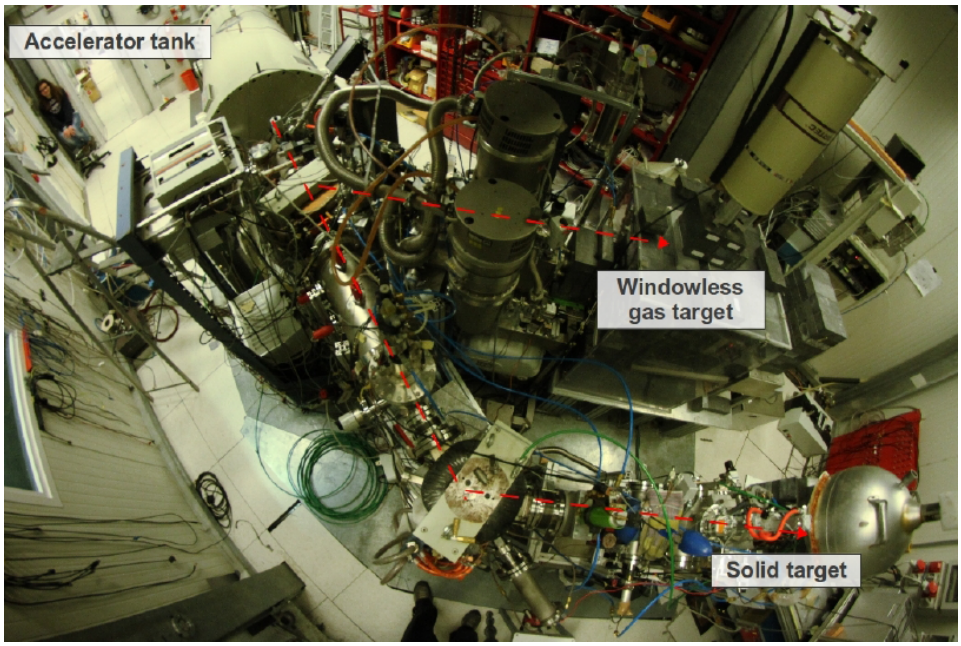

Figure 2.2: The two beam lines at LUNA: solid (foreground) and gas (background) target setups.

function of the accelerator terminal voltage (TV) and the ion source probe voltage (PV). The energy calibration of the machine over a wide energy range has been done using the radiative capture reaction $^{12}\mathrm{C}(\mathrm{p},\gamma)^{13}\mathrm{N}$ [9]. Furthermore, some well-known resonances in $^{23}\mathrm{N}(\mathrm{p},\gamma)^{24}\mathrm{Mg}$, $^{25}\mathrm{Mg}(\mathrm{p},\gamma)^{26}\mathrm{Al}$ and $^{26}\mathrm{Mg}(\mathrm{p},\gamma)^{27}\mathrm{Al}$ have been used for the determination of the beam energy spread and long term stability. The calibration function obtained is given in Eq. (2.1):

$$E = (0.9933 \pm 0.0002)\frac{\mathrm{keV}}{\mathrm{kV}} \cdot (TV + PV) - (0.41 \pm 0.05)\mathrm{keV} \qquad (2.1)$$

with E the calibrated beam energy. The uncertainty on the proton beam energy is 0.3 keV, while the beam energy spread was found to be lower than 100 eV. The proton beam stability has been measured to be 5 eV/h. In addition to the measures with solid target beamline, the accelerator energy calibration has been

also checked using resonances in the ^{20}Ne(p, γ)^{21}Na and ^{21}Ne(p, γ)^{22}Na reactions during the ^{22}Ne(p, γ)^{23}Na.

2.3 Gas target

Nuclear astrophysics experiments require to measure very small nuclear cross-sections. Therefore, targets need to grant high stability over long irradiation times with intense ion beams. The two experiments presented in this thesis involve noble gases as targets. Therefore, the use of the extended gas target grants ideal working conditions in terms of stability. Moreover, gas targets can achieve very high isotopic purity which may significantly reduce the possible beam-induced background. The use of the gas target without any entrance window to confine the gas, like the one used at LUNA, is important since it avoids any beam energy loss and energy straggling due to solid objects along the beam path. The LUNA gas target system consists of three differential pumping stages, the interaction chamber, a gas distribution line, and a gas recycling system (Figure 2.3). In the following sections, each component is described in detail.

2.3.1 Pumping system and gas recycling

A drawing of the LUNA gas target is shown in Figure 2.3. The beam direction is displayed as a red arrow and the gas flows from the target chamber towards the pumping stages. Before reaching the gas target, the beam is collimated by three water-cooled apertures: AP3 (25 mm diameter), AP2 (15 mm diameter), and AP1 (5 mm diameter). Each of these apertures is provided with an ammeter in order to check the current loss during the beam focusing.
The gas is injected into the target chamber through an inlet copper tube located at the end of the chamber flange when the VT valve is open. The gas, coming from the gas bottle located outside (VHe4 open) or inside (VHe3 open, used for more expensive gases, since the line is shorter) the experimental room, reaches the VT valve passing through a distribution line. Such line is split in two branches: one with a needle valve providing a constant flux, the other equipped with a feedback-controlled valve (model MKS 248A) that adjusts the gas flow to keep a constant target pressure. The gas is continuously pumped out from the chamber via the three pumping stages. First, the gas flows inside the AP1 collimator (l=40 mm long) and enters the first pumping stage, where 99.5% of the gas is pumped out by a RUVAC WS 2001 (2050 m^3/h) pump backed by a RUVAC WS 501 (505 m^3/h) pump. Then, the remaining gas reaches the second stage by crossing the AP2 collimator (l= 80 mm long). Here the gas is pumped out through three TMP1000C (3600 m^3/h) turbopumps (TP2L, TP2M, TP2R). Finally, a small amount of residual gas

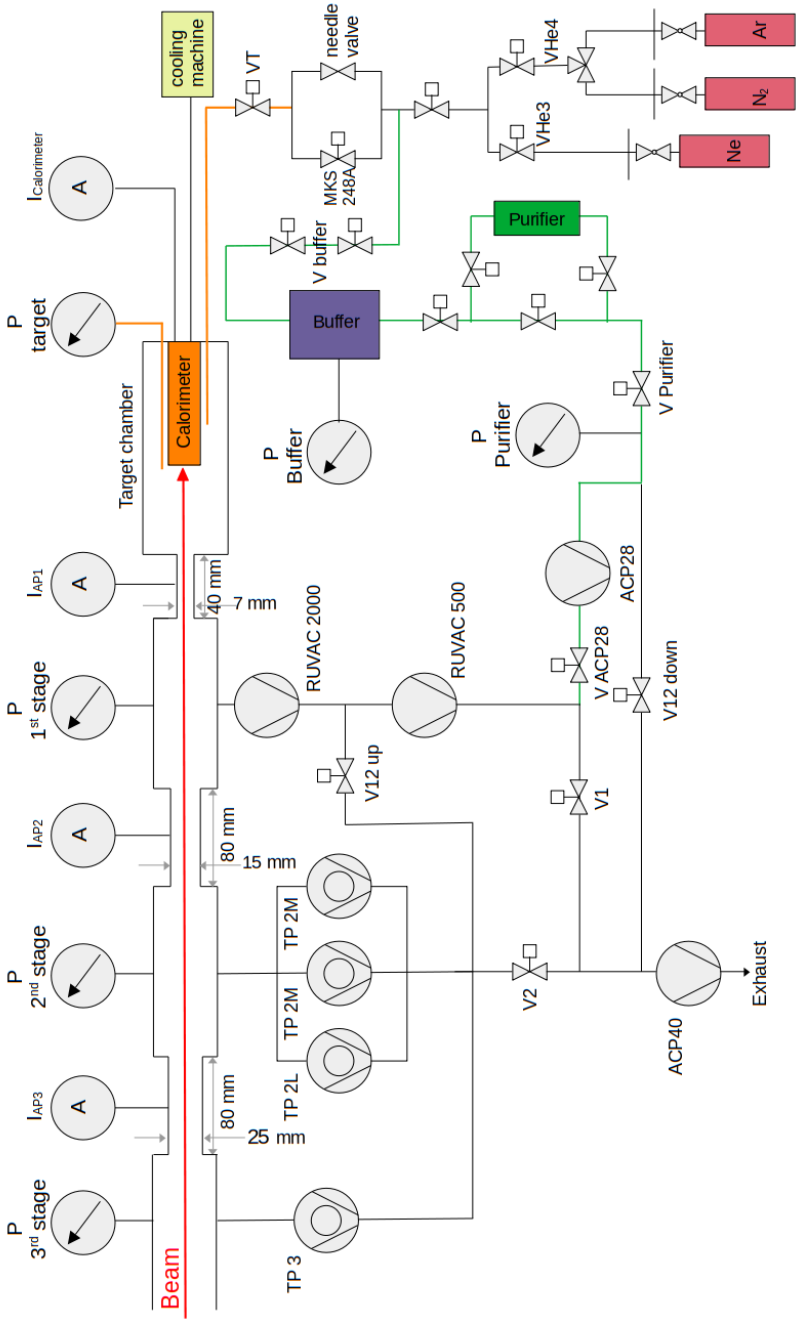

Figure 2.3: Sketch of the gas target differential pumping system. The beam path is highlighted with a red arrow.

from the second stage flows via the AP3 collimator (l= 80 mm long) path in the third pumping stage. In this last stage, the gas is pumped by a TURBOVAC 361 (1250 m^3/h) turbopump.
The typical pressures along the gas path for 2 mbar of neon gas in the chamber are of $\sim 6 \cdot 10^{-3}$ mbar in the first stage, $\sim 10^{-6}$ mbar in the second stage, and $\sim 10^{-7}$ mbar in the third stage.
Depending on the valve configuration, the gas from the first two pumping stages can either be flushed out of the system or collected for reuse, which is fundamental when dealing with very expensive enriched or rare gases. When the recycling mode is enabled, V1, V2 and V12down are closed, while V12up and VACP28 are open and the gas flows through the green path in Figure 2.3. Along this line, the gas coming from the different pumping stages is collected by an ACP28 pump and sent to a Monotorr PS4-MT3-R-2 purifier (Vpurifier open) with a PS4-C3-R-2 chemical getter, designed to remove hydrocarbons, oxygen and nitrogen from noble gases. From the purifier the cleaned gas is stored in a buffer volume (Vbuffer open) at $\sim$ 800 mbar and then re-injected in the chamber through the inlet path. The pressure of the buffer is continuously monitored so that if the pressure rises abnormally and a test with ion beam indicates that the concentration of contaminants is increased, the gas is flushed and replaced. The slow control of the gas target is provided by LabVIEW software and an NI FieldPoint based system. The software is used to remotely operate the gas target system and monitor the status of the pumps and valves. Moreover, the software allows to monitor and log (every 1 second) the pressures in the different pumping stages, the target chamber, purifier, and buffer.

2.3.2 Calorimeter

The interaction of the ion beam with the gas target and the beam stop generates many secondary electrons, and many low-energy protons can be neutralized as well. Therefore, using the classical Faraday cup approach for the current measurement is not effective. To work around this issue, the current intensity is measured using a constant temperature gradient calorimeter [10]. The calorimeter is made up of a hot side (beam stop), and a cold side in thermal contact to each other (Figure 2.4). A cooling machine keeps the cold side of the calorimeter at a constant temperature called T_{cold} (usually T_{cold}= -5°C), while the hot side temperature is adjusted by heating resistors. A feedback system reads the hot side temperature through PT100 thermoresistors and adjusts the resistors power (the so-called zero power, W_0) to keep the beam stop at a constant temperature T_{hot} (usually T_{hot}= 70°-75°C). The W_0 depends on the gas type and pressure on the chamber. When the beam impinges on the hot side, the latter is heated up both by the beam and the thermoresistors. In this case, the power provided by the resistors to keep the hot side at T_{hot} will be

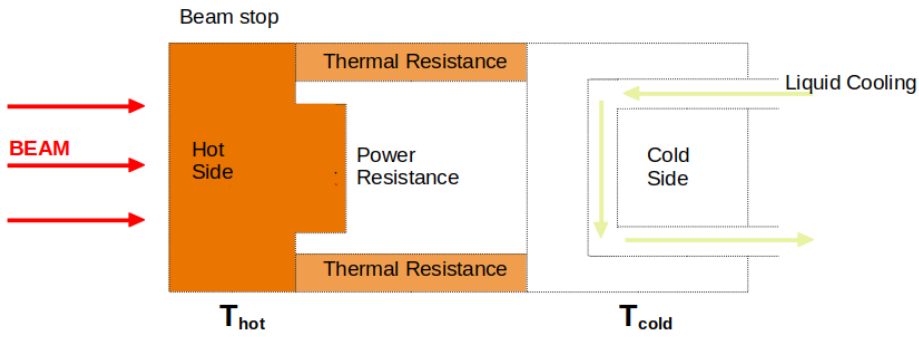

Figure 2.4: A schematic draw of the beam calorimeter. The beam comes from the left to the right where is stopped at the hot side of beam stop site of the calorimeter.

lower. If W_0 is the power provided by resistors while the beam is off and W_{beam} the power when the beam is on, the calorimetric power W_{calo} is given by the difference of these quantities: W_{calo}= W_0-W_{beam}. The beam intensity I, is given by Eq. 2.2:

$$I = \frac{W_{calo}}{E_{beam} - \Delta E_{beam}} \cdot e \tag{2.2}$$

where E_{beam} and ΔE_{beam}, are the beam energy and beam energy loss passing through the gas target, respectively. The calorimetric power was calculated by measuring the heating resistors voltage (V) and current (I). The outputs are measured by a NI cRIO 9207 module and logged every second by a LabVIEW control software. The software is made of two parts: the controller software which runs on the NI cRIO-9075 in the experimental room as a standalone application and the PC software. The software allows the operation of the calorimeter as well as the monitoring of all parameters (temperatures, current, voltage, power). Moreover, an automatic interlock system prevents the calorimeter from overheating, and only if the measured temperature is in the correct range the system allows to send the beam on target. More details can be found in [11],[12]. The calorimeter calibration is checked comparing the calorimetric beam current with the electrical reading obtained in vacuum using the calorimeter and the chamber as a Faraday cup. More details on the calorimeter calibration used for the different reactions will be given in Chapters 3 and 4.

2.4 Background at LUNA

A crucial parameter when measuring small nuclear cross-sections is the signal to background ratio. The main sources of background can be classified into two categories:

- natural background
- beam-induced background (BIB)

Their contribution depends on the type and size of the detector, its location, different shielding adopted, the purity of the target, and the beam energy.

2.4.1 Natural background

The underground location of the LUNA experiment provides a significant reduction in the typical background in a gamma-ray spectrum above 3 MeV [13, 14]. At lower energies, the LUNA laboratory background contains radiation from ^{40}K, the isotopes of the ^{232}Th and ^{238}U chains present in the Gran Sasso rocks, affecting especially the energy region below 2.6 MeV. This component of the background can be suppressed by means of passive shieldings working much more efficiently at LNGS compared to Earth's surface. Indeed, on the Earth's surface, the thickness of passive shieldings is limited by the interaction of cosmic rays with the shielding material, producing background. On the other hand, much thicker shieldings can be adopted underground, where the cosmic ray flux is suppressed by orders of magnitude. In Figure 2.5 a typical γ-ray background spectrum taken with HPGe detector in the surface laboratory and underground at Gran Sasso laboratory with and without shielding is shown.
Since the natural background depends also on the natural radioactivity of the constituent materials of the detector itself, more details related to the background of the two setups adopted for the study of ^{22}Ne$(\alpha,\gamma)^{26}$Mg (BGO) and ^{20}Ne$(\mathrm{p},\gamma)^{21}$Na (HPGe) reactions will be given in Chap. 3 and Chap. 4, respectively.

2.4.2 Beam induced background

If contaminant elements are present inside the target chamber, the beam can induce unexpected nuclear reactions both in the target and in the surrounding materials which produce unwanted signals. The beam-induced background depends on the beam energy and on the position of the contaminants along the beam path. The yield and the exact interaction position of the contaminants are in general hardly determined. According to the energy of the emitted products of interest, the beam-induced background may cause a meaningful background, limiting significantly the

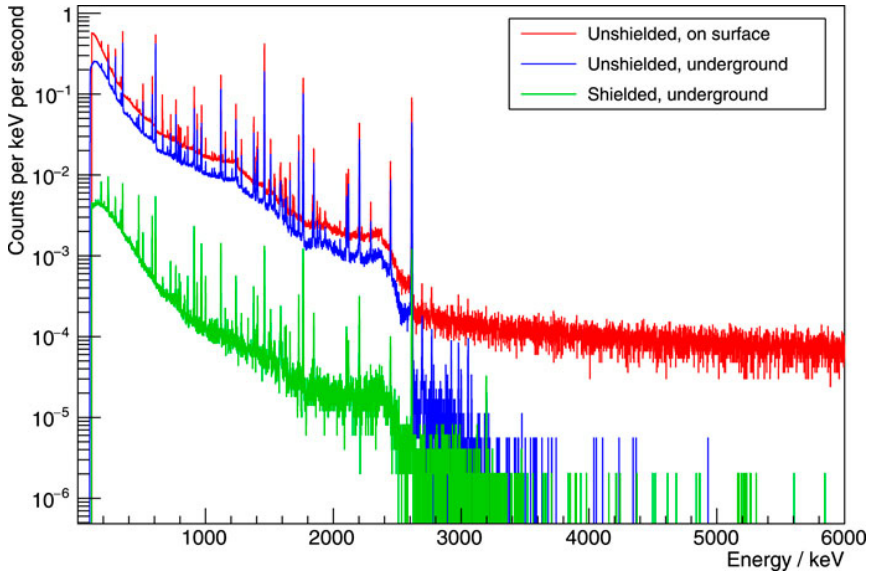

Figure 2.5: Typical γ-ray background taken with a HPGe detector in the surface laboratory (red), at LUNA experimental hall (blue) and at LUNA with 15 cm lead shielding (green).

overall measurement. The typical beam-induced background sources at LUNA are listed in the following:

- ^{12}C(p,γ)^{13}N (Q_{value} = 1943 keV) reaction. The ^{12}C may originate from the hydrocarbons present in the pumping system oil and then adsorbed onto metallic surfaces. The ^{12}C contaminants in the target gives rise to γ-rays at $E_\gamma = E_{cm} + Q_{value}$. ^{12}C can be easily implanted on the collimator and calorimeter, therefore two different γ-rays can be visible, depending on the position (and therefore the beam energy) at which the reaction has occurred.

- ^{11}B(p,γ)^{12}C (Q_{value} = 15957 keV) reaction. ^{11}B is a know contaminant at LUNA, giving rise to γ-rays at $E_\gamma = (E_{cm} + 15957)$ keV, $E_\gamma = (E_{cm} + 11518)$ keV and $E_\gamma = 4439$ keV. In particular the boron contamination can play a significant role close to the resonance at 163 keV of the ^{11}B(p,γ)^{12}C reaction.

- ^{15}N(p,$\alpha\gamma$)^{12}C reaction ($Q_{value} = 4965$ keV) and ^{15}N(p,γ)^{16}O reaction (Q_{value} = 12126 keV). The first one give rise to photons at $E_\gamma = 4439$ keV, while the second one produces photons at $E_\gamma = (E_{cm} + 12126)$ keV. The nitrogen might originate from air entering through leaks into the target chamber or

from implanted nitrogen contamination during different test with nitrogen gas.

- ^{13}C(p,γ)^{14}N (Q_{value} = 7551 keV) reaction emitting γ-rays at E_γ =(E_{cm} +7551) keV.
- ^{19}F(p,$\alpha\gamma$)^{16}O (Q_{value} = 8114 keV) reaction becomes dominant near its resonances at E_{res} = 223 and 340 keV. The presence of ^{19}F in the target is identified by a particular structure due to the stopped and doppler shifted γ-rays from the decay of 6130 keV state into the ^{16}O. The first and second escape peaks are also visible. The flourine is assumed to be an ingredient in the heat-conducting paste used in the calorimeter and Viton O-rings present in several parts of the gas target system.
- ^{14}N(p,γ)^{15}O (Q_{value} = 7297 keV) reaction close to the E_{res} = 273 keV resonance which produces γ-rays at 5181, 5241, 6172, 6792, 6859, 7275, 7556, 2373 and 1380 keV.

More specific details regarding the beam induced background observed during the ^{22}Ne(α,γ)^{26}Mg and ^{20}Ne(p,γ)^{21}Na measurements will be given in Chap. 3 and Chap. 4, respectively.

Chapter 3

Study of the $^{22}Ne(\alpha,\gamma)^{26}Mg$ reaction

If your experiment needs a statistician, you need a better experiment.

Ernest Rutherford

This chapter will focus on the direct measurement of the 334 keV resonance of the $^{22}Ne(\alpha,\gamma)^{26}Mg$ reaction. The first part will be dedicated to the astrophysical motivations. Here an introduction to the astrophysical scenarios where the $^{22}Ne(\alpha,\gamma)^{26}Mg$ reaction plays a significant role will be discussed. The second section will focus on the previous measurements. The experimental setup will be described in the third part. Both data analysis and results will be described in the last part.

3.1 Astrophysical motivation

Neon-22 isotope is synthesized during He-burning in massive [15] and Asymptotic Giant Branch (AGB) [16] stars via the reaction sequence given in Eq. 3.1:

$$^{14}N(\alpha,\gamma)^{18}F(\beta^+,\nu)^{18}O(\alpha,\gamma)^{22}Ne \tag{3.1}$$

Its destruction proceeds through two different reactions given in Eq. 3.2 and Eq. 3.3:

$$^{22}Ne(\alpha,n)^{25}Mg \quad Q_{value} = -478 \text{ keV} \tag{3.2}$$

$$^{22}Ne(\alpha,\gamma)^{26}Mg \quad Q_{value} = 10.6 \text{ MeV} \tag{3.3}$$

In particular, the $^{22}Ne(\alpha,n)^{25}Mg$ reaction is one of the two main neutron sources for the slow, neutron process (s-process) in low-mass AGB stars and in massive stars. Due to the negative Q_{value}, this reaction is activated at high temperatures ($T \geq$ 300 MK). The role of the $^{22}Ne(\alpha,n)^{25}Mg$ reaction as a neutron source is affected by the $^{22}Ne(\alpha,\gamma)^{26}Mg$ reaction. This last one, can be active during the entire

He-burning phase, reducing the amount of the ^{22}Ne before the $^{22}\mathrm{Ne}(\alpha,\mathrm{n})^{25}\mathrm{Mg}$ reaction is activated. Which of these reaction dominates depends on trend of their reaction rates as a function of the temperature. Furthermore, it has been observed that the $^{22}\mathrm{Ne}(\alpha,\gamma)^{26}\mathrm{Mg}$ reaction rate affects also the nucleosynthesis of isotopes between ^{26}Mg and ^{31}P in intermediate-mass AGB stars [17]. An overview of the nuclear s-process and the conditions where the $^{22}\mathrm{Ne}(\alpha,\mathrm{n})^{25}\mathrm{Mg}$ becomes dominant are given in the following subsections.

3.1.1 Slow neutron capture process

It is known from the pioneering work by Burbidge, Burbidge, Fowler, and Hoyle ($\mathrm{B^2FH}$) [18], that the nucleosynthesis of the elements heavier than iron proceed through the slow (s)- or rapid (r)-neutron capture reactions. The s-process is responsible for the production of half of all elements heavier than iron. It is characterized by typical neutron densities of about $\rho_\mathrm{n} \sim 10^{11}$ cm^{-3} and a neutron capture time much larger than the β-decay lifetime. Figure 3.1 shows a schematic overview of the s-process paths which is located close to the valley of stability [19].

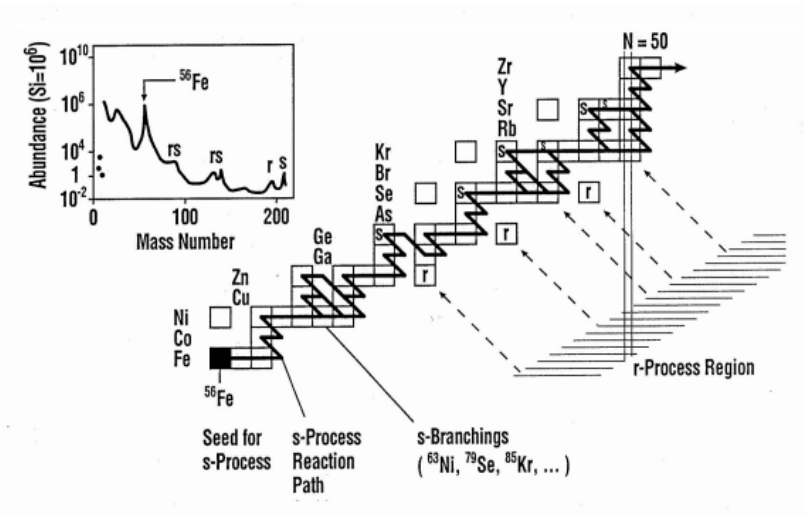

Figure 3.1: S-process path for elements between iron and the actinides [19].

The s-process nucleosynthesis chain starts with ^{56}Fe as a seed nucleus and terminates with the production of ^{209}Bi. It is known that there are at least two slow components, the *main* and the *weak* s-process. Each of them dominates in specific phases of stellar evolution.

In particular, the main component of the s-process is responsible for the nucleosynthesis of nuclei between ^{90}Zr and ^{209}Bi. This process takes place in the He-rich intershell of low-mass AGB stars [20, 21] and the energy production occurs by alternate stages of radiative hydrogen burning and convective helium burning in a thin shell around the inert CO core. The main neutron sources for the main s-process is the $^{13}C(\alpha,n)^{16}O$ reaction activated at temperatures of $\sim$ 0.09 GK [22] during the low-mass TP-AGB phase. During this phase, the ratio of free neutron/seed nuclei is high enough to allow the s-process operates efficiently for a long time. A second stage happens during the subsequent convective He flashes. The material previously produced is mixed with the helium intershell and is again exposed to neutrons produced by the $^{22}Ne(\alpha,n)^{25}Mg$ reaction, activated when temperatures exceed 0.25 GK. This second neutron exposure is weaker, but strong enough to define the isotope ratios of s-process branchings[1].
The weak s-process component is responsible for the synthesis of nuclei between ^{56}Fe and ^{90}Y and in general is less understood compared with the main s-process. It takes place at the end of the convective core He-burning, and at the beginning of carbon (shell) burning in massive stars (Section 1.1.3). At these environments, the temperatures reach (0.22 - 0.35) GK, high enough to activate the $^{22}Ne(\alpha,n)^{25}Mg$ reaction which is the main neutron source for this s-process component. The amount of neutrons produced in the core helium burning is relatively low, hence, the s-process cannot get through the isotopes with closed neutron shells at N = 50. On the other side, in the shell carbon burning, the neutron flux is produced by the $^{22}Ne(\alpha,n)^{25}Mg$, the $^{17}Ne(\alpha,n)^{20}Ne$, and$^{13}C(\alpha,n)^{16}O$ reactions. In particular the role of the $^{22}Ne(\alpha,n)^{25}Mg$ reaction depends on the amount of ^{22}Ne present, and on the rate of $^{12}C(^{12}C,p)^{23}Na$ reaction able to produce protons which can interact with ^{22}Ne nuclei.

3.1.2 s-process in AGB stars

As described in Section 1.1.3, AGB stars are the dying phase of low-mass and intermediate-mass star before their degenerate CO or NeO cores are left as cooling white dwarves. Every observed star which presents enrichment with heavier elements is related with this type of stars, in both direct or indirect ways. A precise model of these stars would significantly improve the understanding of the processes occurring in these stars, and the isotopic abundances in the Galaxy. A schematic representation of the internal structure of these stars is shown in Figure 3.2. Briefly, they consist of an inert core of carbon and oxygen, then a helium burning shell, the helium intershell, and at the end a radiative hydrogen burning shell followed by

[1] Branching in the s-process happens when an unstable isotope with long half-lives come across where neutron capture competes with β-decay [23]

the convective envelope. In the AGB phase, thermal pulses (TP) are generated in

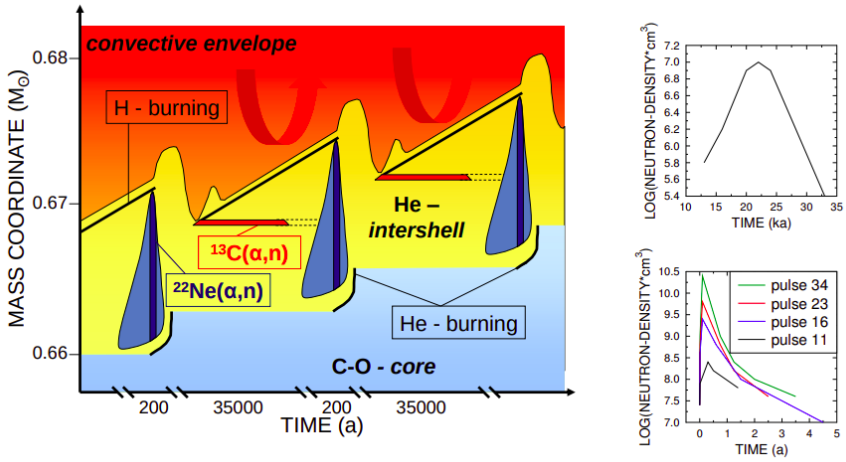

Figure 3.2: Schematic structure and evolution of AGB stars, showing recurrent H and He burning episodes with indications for the related s-process environments (left). Right: Strength and time-dependence of the neutron density in thermally pulsing low-mass AGB stars contributed by $^{13}\mathrm{C}(\alpha,\mathrm{n})^{16}\mathrm{O}$ *reaction (top right) and* $^{22}\mathrm{Ne}(\alpha,\mathrm{n})^{25}\mathrm{Mg}$ *(bottom right) [19].*

the He-rich intershell region located between the hydrogen and the helium-burning shells. During TP, the He fusion produces a large amount of energy and drives the convection zone of the entire interlayer. The outer layer of the star continuously expand and the H-burning is powered down. The convective envelope sink out in mass reaching the intershell and brings the products of partial He burning to the stellar surface (third dredge-up, TDU). This cycle where the hydrogen and helium burning shell alternate will be repeated as much as possible according to the initial properties of the star.During this processes the star losses mass, affecting the star properties, the duration of the AGB phase, the strength of the pulse and the efficiency of the third dredge-up. Both the main neutron sources for the s-process occur in the intershell. The $^{13}\mathrm{C}(\alpha,\mathrm{n})^{16}\mathrm{O}$ reaction takes place during the hydrogen burning phase and can release neutrons very smoothly for about 10^4 years. The neutron densities involved in this phase are of the order of 10^7 cm^{-3}, low enough to make the s-process highly slow. Instead, the $^{22}\mathrm{Ne}(\alpha,\mathrm{n})^{25}\mathrm{Mg}$ reaction, that requires higher temperatures, takes place only in the thermal pulses. Compared to the $^{13}\mathrm{C}(\alpha,\mathrm{n})^{16}\mathrm{O}$ case, it only lasts for 10 years and basically follows the burst of the thermal pulse and proceeds with higher neutron densities ($\sim 10^{13}$ cm^{-3}). In

particular, $^{22}Ne(\alpha,n)^{25}Mg$ reaction occurs only at the bottom of the pulse-driven convection zone (PDCZ) developed during the thermal pulses in the He-burning, while the $^{22}Ne(\alpha,\gamma)^{26}Mg$ is active even at lower temperatures. Their reaction rate ratio determines the neutron flux.
As already discussed in Section 1.1.3, the evolution of low-mass and intermediate-mass stars is mainly the same. Nevertheless, because of the mass-dependence of the TP AGB stars evolution, small differences should be taken into account. On one hand, the s-process can take place only in low-mass AGB stars. One the other one, the intermediate-mass AGB stars can reach higher temperatures, able to activate the Hot Bottom Burning (HBB) mechanism where the outer part of the shell is mixed in the convective envelope. During this mechanism, the temperatures at the bottom of the convective envelopes are higher than 60 MK depending on the stellar mass and metallicity. The high temperatures of the HBB alters the surface chemistry of the star though proton captures processes. In general, at these conditions both the NeNa and the MgAl cycles are activated. The second one is responsible for the destruction of the ^{24}Mg isotope, which is the most abundant isotope among Mg isotopes. In general, the abundance of magnesium and its isotopic ratio in the interstellar medium, are important quantities for the study of star formation processes in cosmological timescales.
The observed isotopic abundances of magnesium are presented in different works [24, 25, 26] and what is interesting is that they are produced in different stellar environments. The ^{24}Mg s mainly produced by massive stars in star-forming galaxies during core carbon and neon burning before the supernova explosion [27]. Instead, the ^{25}Mg and ^{26}Mg isotopes are mainly produced through α-capture processes (Eq. 3.2 and Eq. 3.3) in different sites of AGB stars. Therefore, these isotopes begin to contribute later in the galactic chemical evolution. For what concerns the s-process, the ^{25}Mg and ^{26}Mg isotopes are the most important neutron poisons because of neutron capture on magnesium stable isotopes, in competition with neutron capture on ^{56}Fe (seed nucleus for s-process).
Different chemical evolution models and theoretical studies stress out the importance of high precision data for a better understanding of the nuclear processing in the AGB phase of low and intermediate mass stars and the chemical enrichment of galaxies [28, 29].

3.2 State of the art

Different experiments were performed for an overall investigation of $^{22}Ne + \alpha$ reactions and the energy levels of ^{26}Mg which play a crucial role in the thermonuclear reaction rate calculation in the energy range relevant to astrophysical scenarios.

In this energy range, between 250 keV and 900 keV (excited levels between E_x = 11.0865 MeV and E_x = 11.515 MeV) the rate is affected by different resonances (a recent summary is given in [30]). For several excited states of ^{26}Mg both excitation energies and spin parity assignments are still under debate and hence also their contribution to the rate. In particular, for what concerns the ^{22}Ne$(\alpha,\gamma)^{26}$Mg reaction, some crucial resonances that significantly contributes to the reaction rate correspond to the excited states of E_x = 10.949.1(1) MeV ($E_{r,cm}$= 334.4(8)) and E_x=11.084(1) MeV ($E_{r,cm}$= 469(1)). Both of them were studied several times and the results show large discrepancies. Most of the data present in literature were studied using indirect approaches, especially for the low-energy region. Previous experiments performed at LUNA [31, 32, 11] showed that the assumptions made by indirect methods on poorly-known excited states can lead to inaccurate results. In the following, the previous measurements on the 334 keV resonance investigated during this work are presented, as well as the previous studies on the ^{26}Mg states.

Wolke et al., 1989 [33]

Both the ^{22}Ne$(\alpha,\gamma)^{26}$Mg and ^{22}Ne$(\alpha,\mathrm{n})^{25}$Mg reactions were studied in the energy range between 0.71 MeV and 2.25 MeV. An alpha beam delivered by the 4MV Dynamitron accelerator at Insitut fur Strahlenphysik in Stuttgart impinged onto a windowless gas target system filled with ^{22}Ne gas (99% enrichment). The composition of the gas was continuously monitored with a Q 200 mass spectrometer and α elastic scattering observed in surface barrier Si detectors placed at 30°, 90° and 120° with respect to the beam direction. The emitted gammas were observed with three different germanium detectors of 85 cm^3, 80 cm^{33}, and 123 cm^3 shielded with 5 to 10 cm of lead. The neutron emission was studied with a ^{3}He ionization chamber. As a result, the well-known resonance at 2.05 MeV was confirmed and 15 new resonances were found. The $^{22}\mathrm{Ne}+\alpha$ reaction rate including the new resonances was evaluated in the temperature range between 0.2 and 1.6 GK. In the energy region important for the s-process (0.2 - 0.6 GK), the efficiency of the ^{22}Ne$(\alpha,\mathrm{n})^{25}$Mg neutron source relative to the ^{22}Ne$(\alpha,\gamma)^{26}$Mg competitor was significantly reduced, mainly due to the 828 keV resonance in the ^{22}Ne$(\alpha,\gamma)^{26}$Mg reaction.

Giesen et al., 1993 [34]

In this paper the authors show both α-transfer and α-capture studies. The α-unbound levels in ^{26}Mg have been studied using the ^{22}Ne$(^6\mathrm{Li},\mathrm{d})\alpha$-transfer reaction. Based on the selection rules, the ^{22}Ne$(^6\mathrm{Li},\mathrm{d})^{26}$Mg direct α-transfer reaction populates natural-parity states in ^{26}Mg. Therefore, any observed α-bound states

($E_x \geq$10.612 MeV) should correspond to ^{22}Ne + α resonances. The α-transfer experiment was performed at FN-Tandem accelerator, University of Notre Dame, using a ^{6}Li beam of 32 MeV on 99% enriched ^{22}Ne gas. The reaction products were detected at the focal plane using a position-sensitive proportional counter system backed by a scintillator. The excitation energies between 9.3 and 12.1 MeV were measured at different angles and the final results were determined averaging the values taken at all angles.

The ^{22}Ne α-capture reaction was studied between 0.60 MeV and 0.93 MeV. The measurement was performed by using the ion beam delivered by the JN Van de Graaff accelerator impinging on an implanted ^{22}Ne target mounted at an angle of 90° with respect to the beam direction. The target stability was determined using the well-known resonances of ^{22}Ne$(\mathrm{p},\gamma)^{23}$Na at 640 keV and 850 keV detected with a large volume (35%) Ge detector in a close geometry. The emitted neutrons were detected by an array of 31 ^{3}He proportional counters. To keep under control the beam-induced background neutrons from the ^{22}Ne(α,n) reaction, the detectors were shielded with paraffin.

Two low-energy resonances, at 825 keV and 633 keV were measured. For the first one, a resonance strength of $\omega\gamma = (234 \pm 77)$ μeV was obtained, while for the second one significantly affected by the beam-induced background, only an upper limit of $\omega\gamma \leq 5\mu$eV was reached. The ^{22}Ne$(\alpha,\mathrm{n})^{25}$Mg and ^{22}Ne$(\alpha,\gamma)^{26}$Mg reaction rates at low-temperatures (0.01 - 1.0 GK) were calculated using the newly introduced low energy resonances. The ^{22}Ne$(\alpha,\mathrm{n})^{25}$Mg reaction rate was completely dominated by the 825 keV resonance. In the ^{22}Ne$(\alpha,\gamma)^{26}$Mg reaction rate, the contribution of the 825 keV resonance was significant for temperatures above 0.4 GK while at lower temperatures the reaction rate was affected by the 400 keV and 633 keV resonances.

Ugalde et al., 2007 [35]

The ^{22}Ne$(^6\mathrm{Li},\mathrm{d})^{26}$Mg reaction was used to study natural parity states in ^{26}Mg between 10.615 and 11.093 MeV and their implication on the reaction rate.

The experiment was performed at Yale University with a 30 MeV ^{6}Li beam impinging an implanted ^{22}Ne target produced at Yale as well. The products of the reaction were separated with an Edge split-pole spectrometer and detected at the focal plane with a position-sensitive gas ionization chamber and a scintillator.

Four ^{26}Mg states were identified and J^π assignments to different states were given as well. Thanks to a better resolution compared to the one in [36], it was found that the $E_x = 10.949(25)$ MeV state observed in [34] corresponds to two states in ^{26}Mg: $E_x = 10.808(20)$ MeV and $E_x = 10.953(25)$ MeV. The other two states observed, $E_x = 9.32(6)$ MeV and $E_x = 9.57(4)$ MeV correspond to the $E_x = 9.404(20)$ MeV

and $E_x = 9.586(20)$ MeV state in [34], respectively. The contribution of the two resolved states to the (α, γ) rate has been calculated taking the total differential cross-section in [34] for the 19.949 (25) MeV state and splitting it into two parts. The upper limit of the reaction rate has been calculated by assigning the states at 10.808(20) MeV and 10.953(25) MeV as $J^\pi = 0^+$ and $J^\pi = 5^-$, respectively. The lower limit was calculated by assigning $J^\pi = 4^+$ and $J^\pi = 7^-$ respectively. The rate was compared with the one given in [37] and [38] showing a significant reduction for temperatures below 0.3 GK.

Longland et al., 2009 [39]

The energy and quantum numbers of excited states between $E_x = 10.8$ MeV and $E_x = 11.4$ MeV in ^{26}Mg were studied via the ^{26}Mg$(\gamma, \gamma')^{26}$Mg reaction. The measurements were performed at the TUNL HI$_\gamma$S facility. The monoenergetic γ-ray beam of 10.8, 11.0, 11.2 and 11.4 MeV delivered by the HI$_\gamma$S impinged on a solid target of magnesium-oxide (MgO) powder enriched to 99.41(6)% in ^{26}Mg. The emitted γ-rays were detected with four high-purity germanium (HPGe) detectors (60% relative efficiencies), three were located perpendicular to the incident beam whereas one of the detectors outside the vertical plane (out of plane). The location of the detectors was chosen in order to unambiguously determine the spins and parities of ^{26}Mg states.
Five excited states were observed and spin parities were assigned to $E_x = 10573.3(8)$ keV ($J^\pi = 1^-$), $E_x = 10647.3(8)$ keV ($J^\pi = 1^+$), $E_x = 10805.7(7))$ keV ($J^\pi = 1^-$), $E_x = 10949.1(8)$ keV ($J^\pi = 1^-$), and $E_x = 11153.5(10)$ keV ($J^\pi = 1^+$). The E_x=10 647.3 keV and $E_x = 11153.5(10)$ keV states were identified also in previous experiments, in [40] ($E_x = 10647(2)$ keV) and [41] (E_x=11153.8(12) keV), respectively. For this last one no spin-parity assignment was provided. The absolute ground-state-transition partial widths for the five observed states are discussed in [42]. The rate calculated using the new data showed that the natural parity states have a significant impact on the reaction rate of the ^{22}Ne$(\alpha, \mathrm{n})^{25}$Mg reaction, while the $E_x = 11153.5(10)$ keV state with unnatural parity has no impact in any of the $^{22}\mathrm{Ne} + \alpha$ channels.

Massimi et al., 2012 [43]

The neutron capture cross-sections of the stable magnesium isotopes ^{24,25,26}Mg in the energy range of interest for the s-process were measured using the time-of-flight technique. The experiment was performed at the n_TOF facility at CERN. Neutrons were produced by a proton beam of 20 GeV delivered by the CERN/PS accelerator complex, impinging on a massive lead target. The neutrons produced

and continuously analyzed reached the enriched samples of ^{24}Mg, ^{25}Mg and ^{26}Mg, produced by magnesium oxide powder(MgO) which was sealed in very thin aluminum cans with total masses of 350 mg. The ^{24,25,26}Mg + n capture yields have been measured with an array of $C_6^2H_6$ liquid scintillators. The data were analyzed using a simultaneous resonance shape analysis of capture and transmission data and updated (n,γ) cross-sections for the ^{24,25,26}Mg isotopes were given. For the ^{26}Mg + n cross-section, a possible underestimation of 20% due to the target features, should be taken into account. Moreover, the use of highly enriched samples allowed to assign doubtful resonances; the 68.5 keV resonance assigned to ^{24}Mg in literature belongs to ^{26}Mg. The authors updated the (n,γ) cross-sections of ^{24,25,26}Mg for thermal energies between kT= 5 and 100 keV, including the specific values for the common s-process astrophysical sites; kT= 8 and 23 keV related to the He shell burning in low-mass AGB stars and kT= 25 and 90 keV for core He and shell C burning in massive stars. Furthermore, the resonances and excited state parameters for ^{25,26}Mg were used for an update of the $^{22}Ne(\alpha,n)^{26}Mg$ reaction rate in the temperature range between 0.05 GK and 1 GK.

Talwar et al., 2016 [44]

Resonance energies and the α-widths of the ^{26}Mg exited states were studied through α-inelastic scattering $^{26}Mg(\alpha,\alpha')^{26}Mg$ and α-transfer $^{22}Ne(^6Li,d)^{26}Mg$ measurements. The experiments were performed using the high resolution Grand Raiden (GR) Spectrometer at the Research Center for Nuclear Physics (RCNP) in Japan. For the $^{26}Mg(\alpha,\alpha')^{26}Mg$ reaction, the authors were able to measure the excited states between E_x = 7.69 MeV and E_x = 12.06 MeV using a self-supporting ^{26}Mg solid target (enriched at 99.4%). Instead, in the case of the α-transfer reaction, a ^{22}Ne gas target (enriched at 99%) allowed the study of the ^{26}Mg exited states in the region between E_x = 7.36 MeV and E_x = 11.32 MeV. The scattered α particles and deuterons were detected at the focal plane detection system consisting of multiwire drift chambers (MWDCs) and 10 mm thick plastic scintillators along with a 2 mm thick aluminum absorber placed between the scintillators. Six energy levels were observed: E_x = 10.717, 10.822, 10.951, 11.085, 11.167, and 11.317 MeV above α threshold. For these states, spin-parity, excitation energy and α width were determined. The results were used to re-calculate the $^{22}Ne + \alpha$ reaction rates which was compared with previous rates given in [37, 45]. Moreover, significant α-clusters were observed for the 10.951, 11.167, and 11.317 MeV states which significantly dominated the overall reaction rate. In particular the 11.167 MeV state increased the $^{22}Ne(\alpha,\gamma)^{26}Mg$ reaction rate by $\sim$ 2 orders of magnitude with respect to the rate given in [45], and almost by a factor of 3 with respect to the reaction rate adopted in [37] for temperatures below 0.2 GK.

Adsley et al., 2017 [46]

Information on the existence, spin, and parity of levels in ^{26}Mg were determined through α-inelastic scattering $^{26}\mathrm{Mg}(\alpha,\alpha')^{26}\mathrm{Mg}$ measurements. The α-particle beam of 200 MeV was scattered off an enriched ^{26}Mg target. Scattered particles were momentum-analyzed in the K600 Q2D magnetic spectrometer at iThemba LABS in South Africa. A plastic scintillator was located at the focal plane in order to trigger the data acquisition and to measure the energy deposited by the particles hitting the focal plane. The time between the focal plane hit and the accelerator RF pulse was recorded, giving a measure of the time-of-flight of the scattered particles through the spectrometer. Particle identification was performed using the energy deposited at the focal plane and the time-of-flight through the spectrometer. Two vertical drift chambers were used for the particle positions and trajectories at the focal plane.
The complete set of data were acquired in two experiments. The first experiment was in the 0° of the K600 using 99.94 % enriched ^{26}Mg target of areal density 1.33 mg/cm^2. This configuration was limited to a full acceptance of θ_{lab} <2°. Instead, the second experiment was performed in the configuration in which the spectrometer aperture was placed at θ_{lab}= 2°, covering θ_{lab}=2°-6°. In this case the target had a 99.94 % enrichment and an areal density 0.6 mg/cm^2. Spins and parities of the measured states were deduced from the differential cross-section of scattered α particles. Some discrepancies were observed with respect to the states assigned in [44]. In particular, a 0^+ state at 10.82 MeV was assigned in addition to the 1^- state at 10.805 MeV [44], and a new state with J>1 at 10.89 MeV was observed. Taking into account the new data, a new reaction rate for the $^{22}\mathrm{Ne}(\alpha,\gamma)^{26}\mathrm{Mg}$ reaction was calculated using the STARLIB tool in the temperature range between 0.01 and 1 GK. The new rate shows a significant increase between 0.04 and 0.1 GK.

Massimi et al., 2017 [47]

The authors report accurate, high-resolution measurements of $^{25}\mathrm{Mg}(\mathrm{n},\gamma)^{26}\mathrm{Mg}$ and $^{25}\mathrm{Mg}(\mathrm{n},\mathrm{tot})$ reaction cross sections providing accurate information on ^{26}Mg levels. The measurements were carried out combining two time-of-flight experiments; n_TOF facility at CERN for (α,γ) channel and GELINA facility of the Institute for Reference Materials and Measurements (IRMM) in Geel for the total cross-section. For both measurements, 97.87% enriched ^{25}Mg metallic targets were used. The emitted γ-rays were detected by two deuterated benzene C_6D_6 scintillation detectors, placed on either sides of the neutron beam. The total cross-section was measured with a ^{6}Li-glass detector at GELINA. The authors provided new information on the resonance parameters, spin parities, and excitation energies

for ^{26}Mg states between 11.112 and 11.344 MeV. In particular, five natural-parity states, which are thought to dominate the reaction rate, have been identified corresponding to energies E_r = 589, 649, 656, 779 and 786 keV. An uncertainty of 0.1 keV has been associated to the excitation and resonance energies. The uncertainty on the cross-section data was reduced by a factor of three compared to previous data available. The results were used to calculate the $^{22}Ne(\alpha,n)^{25}Mg$ and $^{22}Ne(\alpha,\gamma)^{26}Mg$ reaction rates resulting in a significantly higher (α,n) /(α,γ) ration than the literature data.

Adsley et al., 2018 [48]

In this paper the authors present a high-resolution study of levels of the ^{26}Mg through the $^{26}Mg(p,p')^{26}Mg$ and $^{26}Mg(d,d')^{26}Mg$ reactions. The measurements were performed using 18 MeV proton and deuteron beams impinging on an enriched (94% enrichment) ^{26}MgO target at the tandem accelerator at the Maier-Leibnitz Laboratorium at Garching, Munich. Reaction products were momentum-analyzed in the MLL Q3D magnetic spectrograph. Focal-plane particle identification was attained using the energy deposited in the two gas detectors and a plastic scintillator at the focal plane of the spectrograph.
In this work the authors confirmed states around E_x= 10.8-10.83 MeV in ^{26}Mg suggested in previous works. Moreover, four new states at 10.943, 11.074, 11.102, and 11.119 MeV were observed in ^{26}Mg. The 11.102 and 11.119 MeV states resulted above the neutron threshold but were not observed in ^{25}Mg + n reactions, implying small neutron widths. Since there was no information about the spin parities of these states, the authors were not able to determine whether these levels contribute to α-particle-induced reactions on ^{22}Ne.
In addition, other six potential states, all above the neutron threshold, at 11.209, 11.216, 11.266, 11.414, 11.426, and 11.481 MeV were observed ^{26}Mg but not confirmed.

Hunt et al., 2019 [49]

The authors show the study of the $E_{r,lab}$= 830 keV resonance in the $^{22}Ne(\alpha,\gamma)^{26}Mg$ reaction. The measurement was performed at the Laboratory for Experimental Nuclear Astrophysics (LENA). The α-bean from the JN Van de Graaff accelerator reached ^{22}Ne implanted targets through a liquid nitrogen-cooled copper tube. The emitted γ-rays were detected with the LENA γ γ coincidence system composed by a coaxial HPGe detector (135% relative efficiency) located at 0° with respect to the beam direction, a NaI(Tl) annulus and a veto scintillator shielding the HPGe detector. The authors determined a resonance energy and resonance strength of

$E_{r,lab}$ = 835.2(3.0) keV and $\omega\gamma = 4.6(1.2)\text{x}10^{-5}$ eV, respectively. Both mean values turned out higher than previous measurements (the resonance energy ∼7 keV higher with respect to the value given in [33]) but the results agree within uncertainties. Based on their experimental results and the literature data for this resonance, the authors assigned spin parities of $J^\pi = 0^+, 1^-, 2^+ 3^-$.

Lotay et al., 2019 [50]

In Lotay et al., the resonant states in ^{26}Mg were studied through the $^{11}\text{B}(^{16}\text{O}, \text{p})^{26}\text{Mg}$ fusion-evaporation reaction. The measurement was performed at the Argonne ATLAS accelerator. The 19 MeV ^{16}O beam bombarded a thick target of ^{11}B ($300\mu\text{g/cm}^2$) for 100 hours in order to produce the ^{26}Mg nuclei through the one proton evaporation channel. The emitted γ-rays were detected using 90 Compton-suppressed HPGe detectors (Gammasphere array) and analyzed with the γ-γ coincidence technique. Due to the type of reaction used in the measurement, no J= 0 and J=1 levels were strongly populated. For the observed γ-ray transitions the authors considered only $E1$, $M1$, and $E2$ multipolarities. The excitation energies obtained resulted in agreement with previous data. The authors evaluated the reaction rate for the $^{22}\text{Ne}(\alpha,\gamma)^{26}\text{Mg}$ reaction considering their resonances and spin-parity of states that have been previously observed and confirmed in direct measurements, (^{6}Li, d) transfer reaction studies, and α-scattering experiments. The uncertainties in the adopted (α,γ) reaction rate have been reduced by a factor of ∼10-20 for temperatures between 0.16 and 0.20 GK.

Ota et al., 2020 [51]

The $^{22}\text{Ne}(^6\text{Li}, \text{d})^{26}\text{Mg}$ reaction in inverse kinematics has been measured to study the excited states in ^{26}Mg. The measurement was performed at the Texas AM University Cyclotron Institute. A ^{22}Ne beam of 154 MeV delivered by the K150 cyclotron impinged on a 30 $\mu\text{g/cm}^2$ ^{6}LiF target (95%^{6}Li purity). The products of the reaction were detected with a quasi-4π position-sensitive Si array, TIARA, four HPGe clovers, and a Multipole-Dipole-Multipole spectrometer. The detection of both d and ^{25,26}Mg in coincidence is sensitive to the decay modes of observed states, and thus to the $\Gamma_\text{n}/\Gamma_\gamma$ branching ratio. The authors determined a new n/γ = 1.14(26) for the E_x= 11.32 MeV resonance in ^{26}Mg ($\omega\gamma$= 42(11)μeV). Moreover, new upper limits on the α-partial width of neutron unbound resonances at E_x= 11.112, 11.163, 11.169, and 11.171 MeV are given. Using the new results on the excited states of ^{25}Mg and ^{26}Mg, the new reaction rates for the $^{22}\text{Ne}(\alpha,\text{n})^{25}\text{Mg}$ and $^{22}\text{Ne}(\alpha,\gamma)^{26}\text{Mg}$ reactions are determined. The reaction rates are significantly lower than previous rates in the temperature range between 0.2 and 0.4 GK. A crucial

role on the uncertainties of the rate is given by the 557 keV resonance which has a large effect for almost the entire temperature range of He-burning in massive stars and IM-AGB stars.

Jayatissa et al., 2020 [52]

The authors presented new constraints on the $^{22}Ne(\alpha,n)^{25}Mg$ and $^{22}Ne(\alpha,\gamma)^{26}Mg$ reaction rates by measuring the partial α- widths of resonances in ^{26}Mg through $^{22}Ne(^{6}Li,d)^{26}Mg$ and $^{22}Ne(^{7}Li,t)^{26}Mg$ reactions at energies near the Coulomb barrier.
The $^{22}Ne(^{6}Li,d)^{26}Mg$ and $^{22}Ne(^{7}Li,t)^{26}Mg$ reactions have been studied in the center of mass energies of 4.7 MeV and 5.3 MeV, respectively. The ^{22}Ne beam delivered by the K150 cyclotron at the Texas AM University Cyclotron Institute bombarded the LiF target (30 $\mu g/cm^2$ thickness on 10$\mu g/cm^2$ carbon backing).
The detection and identification of the deuterons and tritons scattered at 5° through a Multipole-Dipole-Multipole (MDM) spectrometer was obtained by a gas-filled gridded ionization chamber with 4 resistive avalanche counters (ACs) and 3 aluminum anodes combined with CsI (Tl) scintillator array. The efficiency of the MDM and the target degradation was continuously monitored.
The authors observed four states (E_x = 11.08(2), 11.30(2), 11.8(2) and 11.95(2) MeV) in the deuteron spectra from the $^{22}Ne(^{6}Li,d)^{26}Mg$ reaction which were also confirmed from the comparison with $^{22}Ne(^{7}Li,t)^{26}Mg$ reaction. Among these states, only the state E_x = 11.32 MeV is above the neutron decay threshold in agreement with [44]. Instead, there was no evidence for the E_x = 11.17 MeV state given in [44], therefore only a restricted upper limit has been given for its partial α-width. The $^{22}Ne(\alpha,n)^{25}Mg$ and $^{22}Ne(\alpha,\gamma)^{26}Mg$ reaction rates are proportional to the resonance strengths determined by the partial α-width, spin parities and branching ratios of the resonances.
The authors calculated the reaction rate for both (α,n) and (α,γ) channels using the adopted resonance parameters for the observed states. They show the ratio of their rate to the reaction rate adopted in [45]. The reaction rate given showed a significant difference with respect to the previous reaction rates, especially in the temperature range between 0.1 and 0.27GK.

More work is needed for a precise knowledge of the ^{26}Mg excited states and their contribution to the reaction rate of $^{22}Ne + \alpha$ channels. A simplified level scheme of ^{26}Mg is given in Figure 3.3. The present work focuses on the direct investigation of the $E_{r,cm}$ = 334 keV resonance corresponding to the excited state E_x = 10.9491(1) MeV [53] which decays emitting different γ-rays. The decay scheme for the 10.9491(1) MeV excited state, together with the corresponding branching ratio

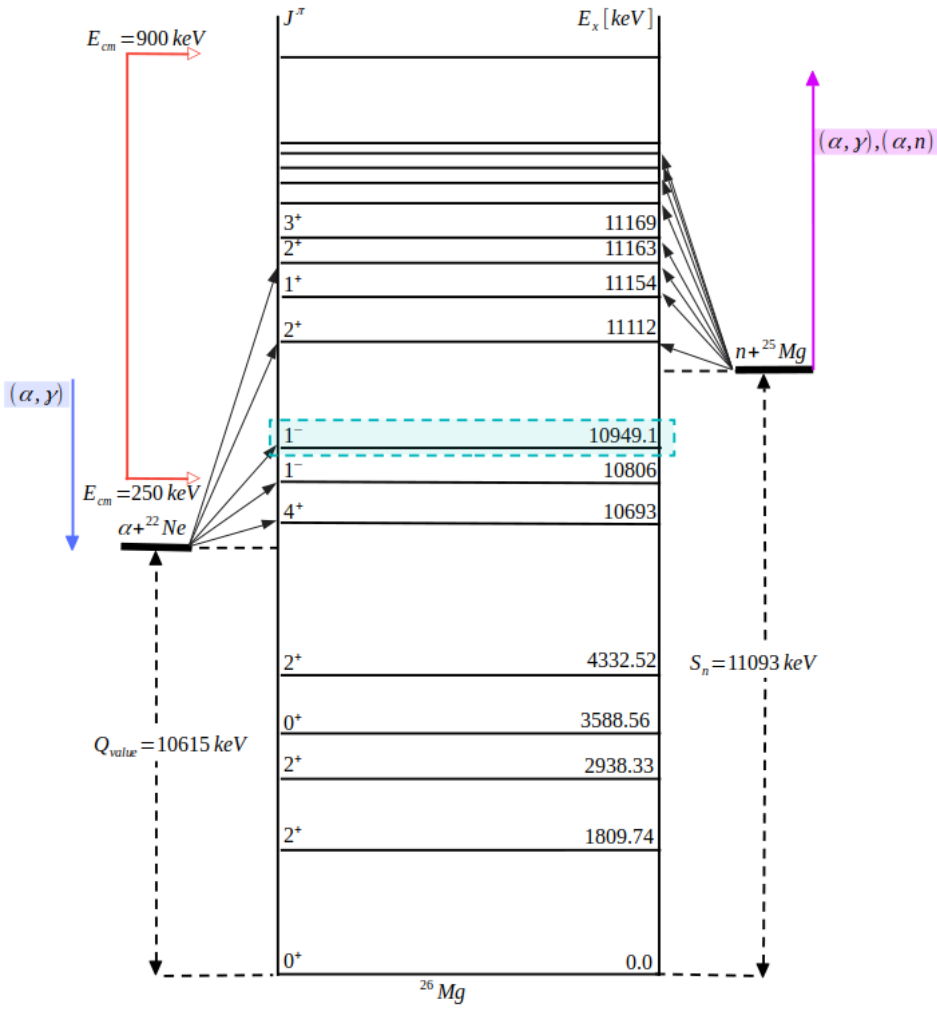

Figure 3.3: Part of a simplified level scheme of ^{26}Mg. *The turquoise region corresponds to the* $E_{cm} = 334$ *keV resonance region. The region indicated by red arrows corresponds to the energy region relevant for astrophysical scenarios discussed in the text. The* (α,γ) *channel region is given by the blue arrow while the region where both* (α,γ) *and* (α,n) *channels are opened is given by the violet arrow.*

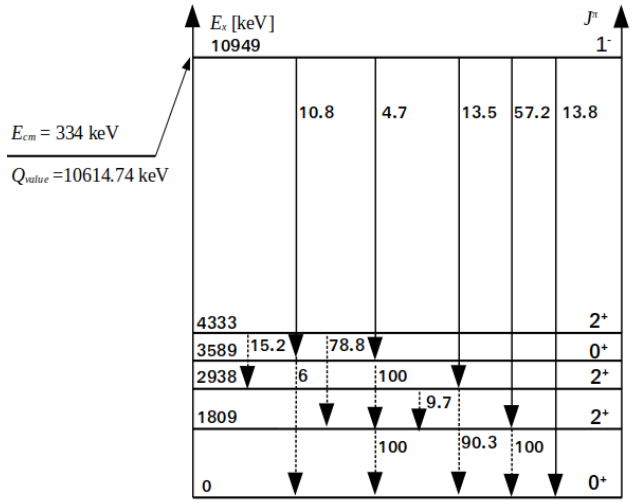

Figure 3.4: Decay scheme of ^{26}Mg *10.9491(1) MeV excited state. Branching ratios are taken from [39].*

Low. Limit [eV]	Adopt. $\omega\gamma[eV]$	Upp. Limit [eV]	Reference
1.4 10^{-14}	1.7 10^{-13}	1.6 10^{-12}	Giesen et al. 1993 [36]
-	4.7 10^{-13}	-	Giesen et al. corrected
-	1.4 10^{-13}	1.3 10^{-12}	NACRE 1999 [37]
-	-	3.6 10^{-9}	Iliadis et al. 2010 [54]
-	-	8.7 10^{-15}	Longland et al. 2012 [45]
-	-	3.6 10^{-9}	STARLIB 2013 [55]
-	-	2.0 10^{-13}	Talwar et al. 2016 [44]
-	-	8.7 10^{-14}	Lotay et al. 2019 [50]
-	-	9.0 10^{-14}	Jayatissa et al. 2020 [52]
-	-	9.0 10^{-14}	Ota et al. 2020 [51]
-	-	8.7 10^{-14}	Adsley et al. 2021 [30]

Table 3.1: Summary of the literature on the E_α = *334 keV resonance strength in the* ^{22}Ne$(\alpha,\gamma)^{26}$Mg *reaction. More information on excitation energies and spin parities for each reference are given in Table A.1.*

are shown in Figure 3.4. The 334 keV resonance has been studied only indirectly and all current results lead to a wide range of reported values for its resonance strength (10^{-14} - 10^{-9} eV). A summary of the literature data for the discussed

resonance is given in Table 3.1.
For a better understanding of the role of the 334 keV resonance on the ^{22}Ne$(\alpha,\gamma)^{26}$Mg reaction rate new constraints are needed. The large discrepancies on the resonance parameters are even more evident in terms of thermonuclear reaction rates. Different evaluations of the reaction rate were performed until now [37, 54, 45, 44, 47, 51, 30]. According to the excited state parameters adopted, the total reaction rate leads to different results. In Table 3.2 and Table 3.3 the properties of resonances used for the ^{22}Ne$(\alpha,\gamma)^{26}$Mg reaction rate evaluation given in [45] are shown.

E_x [keV]	E_r^{cm} [keV]	E_r^{lab} [keV]	J^π	$\omega\gamma$ [eV]
10693	79	93 (2)	4^+	-
11315	701	828 (5)	2^+	$3.6(4)\cdot10^{-5}$
11441	826	976.39 (23)	4^+	-
11465	851	1005.23 (25)	5^-	-
11508	893	1055.9 (11)	1^-	-
11526	910	1075.5 (18)	1^-	-
11630	1017	1202.3 (17)	1^-	-
11748	1138	1345 (7)	1^-	-
11787	1173	1386 (3)	1^-	-
11828	1213	1433.7 (12)	2^+	$2.5(3)\cdot10^{-4}$
11895	1280	1513 (5)	1^-	$2.0(2)\cdot10^{-3}$
11912	1297	1533 (3)	1^-, 2^+	$3.4(4)\cdot10^{-3}$
11953	1339	1582 (3)	2^+, 3^-, 4^+	$3.4(4)\cdot10^{-3}$
12051	1437	1698 (3)	2^+, 3^-	$6.0(7)\cdot10^{-3}$
12140	1525	1802 (3)	1^-	$1.0(2)\cdot10^{-3}$
12184	1570	1855 (8)	(0^+)	$1.1(2)\cdot10^{-3}$
12273	1658	1960 (8)	(0^+)	$8.9(1)\cdot10^{-3}$
12343	1729	2043 (5)	0^+	$5.4(7)\cdot10^{-2}$

Table 3.2: Properties of known resonances adopted in [45] for the evaluation of the ^{22}Ne$(\alpha,\gamma)^{26}$Mg *reaction rate. Ambiguous spin-parities are shown in parentheses. More detailed information on level properties are given in [56].*

Instead, information on the total and partial widths are given in Appendix A. In [45] the evaluation of the reaction rate was performed using the STARLIB Monte Carlo code RATESMC [57] accessible online [58]. Differently from the NACRE reaction rate evaluation [37] where the total widths were assumed from the upper limit values, in [45] the total widths have been adopted from measured values. Moreover, an improved treatment of upper limits for reduced α-particle widths

E_x [keV]	E_r^{cm} [keV]	E_r^{lab} [keV]	J^π	$\omega\gamma_{UL}$ [eV]
10806	191	225.9 (5)	1^-	-
10943	328	388 (2)	5^--7^-	-
10949	334	395.15 (18)	1^-	-
11112	497	587.90 (10)	2^+	$3.7{\cdot}10^{-8}$
11163	548	647.93 (11)	2^+	$4.3{\cdot}10^{-7}$
11171	556	657.53 (19)	2^+	$6.2{\cdot}10^{-7}$
11183	568	671.70 (21)	1^-	$1.0{\cdot}10^{-6}$
11243	629	742.81 (12)	$2(^-)$	$4.7{\cdot}10^{-6}$
11274	659	779.32 (14)	$(2)^+$	$4.9{\cdot}10^{-6}$
11280	665	786.17 (13)	$4(^-)$	$8.2{\cdot}10^{-7}$
11286	671	792.90 (15)	1^-	$5.0{\cdot}10^{-6}$
11286	672	793.83 (14)	(2^+)	$5.0{\cdot}10^{-6}$
11289	674	797.10 (29)	(2^-)	$5.1{\cdot}10^{-6}$
11296	681	805.19 (16)	(3^-)	$5.1{\cdot}10^{-6}$
11311	696	822.6 (4)	(1^+)	$5.2{\cdot}10^{-6}$
11326	711	840.8 (6)	(1^-)	$5.4{\cdot}10^{-6}$
11328	714	843.24 (17)	1^-	$5.4{\cdot}10^{-6}$
11329	714	844.4 (6)	(1^-)	$5.4{\cdot}10^{-6}$
11337	722	853.6 (7)	(1^-)	$5.4{\cdot}10^{-6}$
11344	729	861.86 (18)	(2^+)	$5.5{\cdot}10^{-6}$
11345	730	862.91 (19)	$4(^-)$	$5.5{\cdot}10^{-6}$
11393	778	919.34 (19)	$5(^+)$	$1.6{\cdot}10^{-6}$

Table 3.3: Upper limit resonances adopted [45] for the evaluation of the ^{22}Ne$(\alpha,\gamma)^{26}$Mg reaction rate. Ambiguous spin-parities are shown in parentheses. More detailed information on level properties are given in [56].

was adopted and new nuclear data as well. The same calculation methodology used in [45] was adopted in the most recent evaluation by Adsley et al. 2021 [30]. This was done to guarantee that the only variations observed in the reaction rates were due to improvements in the nuclear data. To show the effect of the changes in the nuclear data for the $E_r = 706$ keV resonance in [30] the reaction rates were calculated with and without including the results in [52]. In this work, the new ^{22}Ne$(\alpha,\gamma)^{26}$Mg reaction rate evaluation will be done using the nuclear data given in [45] except fot the 334 keV resonance strength which will be replaced with the new LUNA value. A brief summary of the latest ^{22}Ne$(\alpha,\gamma)^{26}$Mg thermonuclear reaction rate evaluations as a function of temperature is given in Figure 3.5. The

rates are normalized to the NACRE reaction rate [37].

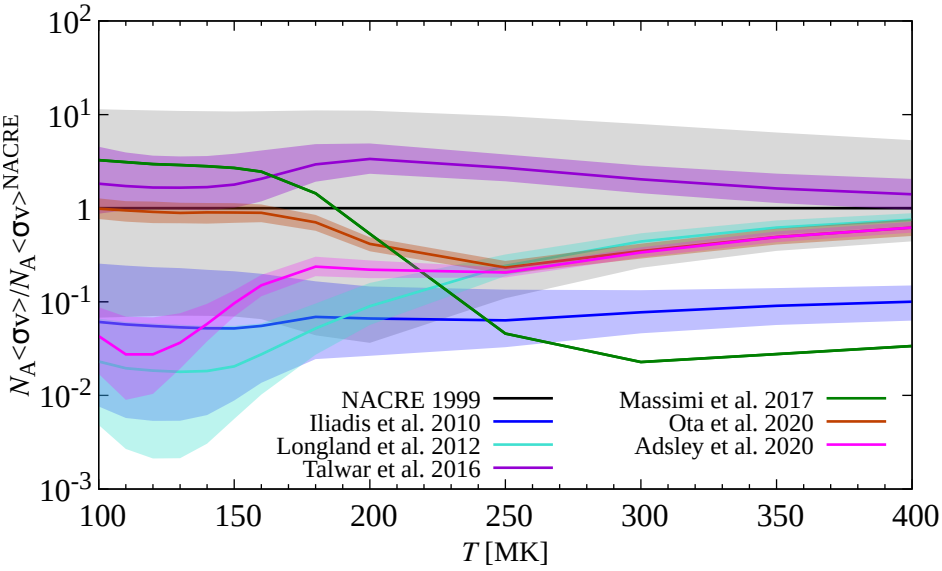

Figure 3.5: State of the art for the thermonuclear reaction rate of $^{22}\mathrm{Ne}(\alpha,\gamma)^{26}\mathrm{Mg}$ *reaction as a function of temperature* T*. Shaded bands represent the uncertainties [37, 54, 45, 44, 47, 51, 30].*

3.3 Experimental setup

The study of the 334 keV resonance of $^{22}Ne(\alpha,\gamma)^{26}Mg$ reaction was performed exploiting the gas target beamline (Section 2.3) combined with a high-efficiency BGO detection system. The data taking was completed in two subsequent campaigns:

- Campaign I, Summer 2016
- Campaign II, Spring - Summer 2019

Specific details from Campaign I can be found in [59]. The present work on the $^{22}Ne(\alpha,\gamma)^{26}Mg$ reaction is dedicated to the data taking in Campaign II and the final results obtained. The setup used in both campaigns was the same, except for some small improvements in Campaign II which allowed to refine the results of Campaign I. The high intensity α beam was delivered to a dedicated target chamber, filled with 1 mbar enriched ^{22}Ne (99.9%). The target chamber was partially occupied by the calorimeter for the beam intensity measurement. Both the target chamber and the calorimeter were located inside the borehole of the detector which consists of six optically independent BGO crystals.
The setup used here for the study of the $^{22}Ne(\alpha,\gamma)^{26}Mg$ reaction was mainly the same used in [12, 11].

3.3.1 Target chamber

The target chamber was located inside the detector borehole (60 mm diameter). It consists of several parts: connecting tube between the 1st stage and the collimator, interaction chamber, calorimeter. In Figure 3.6), a drawing of the target chamber is given.
The interaction chamber consists of a stainless steel tube of 475 mm in length, 56 mm of inner diameter, and 59 mm outer diameter, large enough to allow the calorimeter on the right side, small enough to fit on the detector. The interaction chamber is wrapped in a Kapton sheet to guarantee the electrical insulation with the BGO detector. On the beam direction side, the interaction chamber is provided with two copper tubes, one used for the gas inlet, and the other one is connected to an MKS baratron type 626 pressure gauge to constantly monitor the pressure in the chamber. On the same side of the copper tubes, the interaction chamber is connected to the first PEEK insulating ring which is connected to a water-cooled beam collimator made from copper (AP1). The collimator is insulated from the interaction chamber by two PEEK rings. When the calorimeter is mounted inside the chamber, an active chamber length of 108 mm is measured from the collimator to the beam stop surface (Figure 3.7). The other side of the collimator is connected to the connecting tube (allowing the connection between the 1st pumping stage and

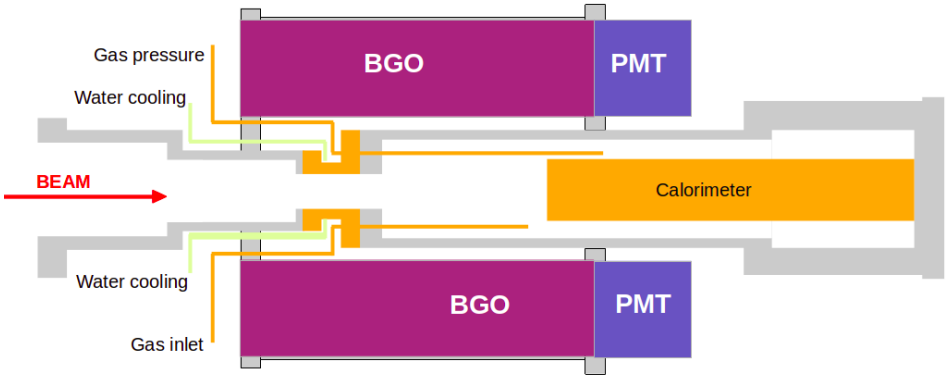

Figure 3.6: Design of the target chamber and the BGO detector. The α beam comes from the left, where the target chamber is connected to the first pumping stage.

the collimator) through the second PEEK insulating ring. The connecting tube diameter has to be large enough to keep the high-pressure gradient, sufficiently small to allow the gas and water tubes to pass through the BGO borehole, and long enough to place the interaction volume in the maximum BGO detection efficiency. Both connecting tube and its flange were designed to be electrically disconnected from all of the other pieces. A cross-section of the interaction chamber and the connection with the collimator and connecting tube is given in Figure 3.7.

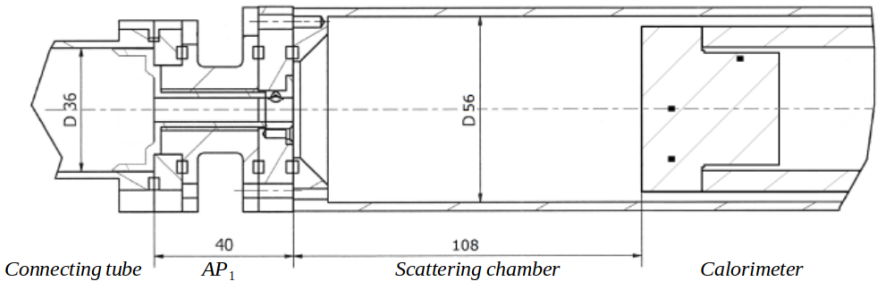

Figure 3.7: Drawing of the target chamber parts; the beam comes from the connecting tube on the left, goes through the AP1 collimator and enters the interaction chamber. On the right side of the interaction chamber is mounted the beam calorimeter.

3.3.2 BGO detector

To face the low count rate of the $^{22}Ne(\alpha,\gamma)^{26}Mg$ reaction, a high detection efficiency is required [60, 11]. For this reason, a large optically segmented Bismuth Germanate (BGO) detector produced by Scionix was used to detect the γ-rays emitted from $^{22}Ne(\alpha,\gamma)^{26}Mg$ reaction.
The BGO is an inorganic scintillator ($Bi_4Ge_3O_{12}$) characterized by large atomic number and high density (7.13 g/cm^3). These characteristics make the BGO detector the scintillator with the highest probability of gamma-ray absorption per unit volume.

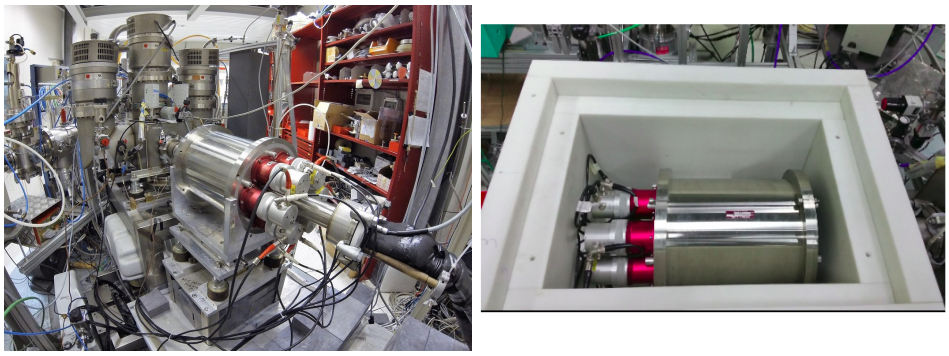

(a) Setup adopted for Campaign I. *(b) Setup improved for Campaign II.*

Figure 3.8: Experimental setup used for the study of $^{22}Ne(\alpha,\gamma)^{26}Mg$ *reaction.*

However, the high refractive index of the BGO and the relatively low light yield affect the collection of scintillation light, therefore decreasing the energy resolution. Furthermore, the light yield of the BGO strongly depends on the temperature. For temperatures of about 20°C the light yield decreases by 1% every 1°C increase in temperature [61]. The analyses presented in this work take into account this effect (Section 3.4.1). The detector is composed of six scintillating crystals arranged in a hexagonal configuration to surround the interaction chamber. The BGO was housed on a frame that can move along the beamline if necessary. The crystal is a cylinder 28 cm long, with a coaxial hole of 6 cm in diameter and a radial thickness of 7 cm. It is read out by photomultiplier tubes located at one end of the bar, with the other end covered by plastic light reflectors (Figure 3.8a). The BGO detector used without external shielding as shown in Figure 3.8a was the setup adopted for Campaign I. In the preliminary analysis of Campaign I [59] no direct observation of the resonance was shown. However, the results showed a 0.4σ excess in the net counting rate. To confirm if this excess is due to a possible resonance detection it was necessary to have under control any source of background. In particular,

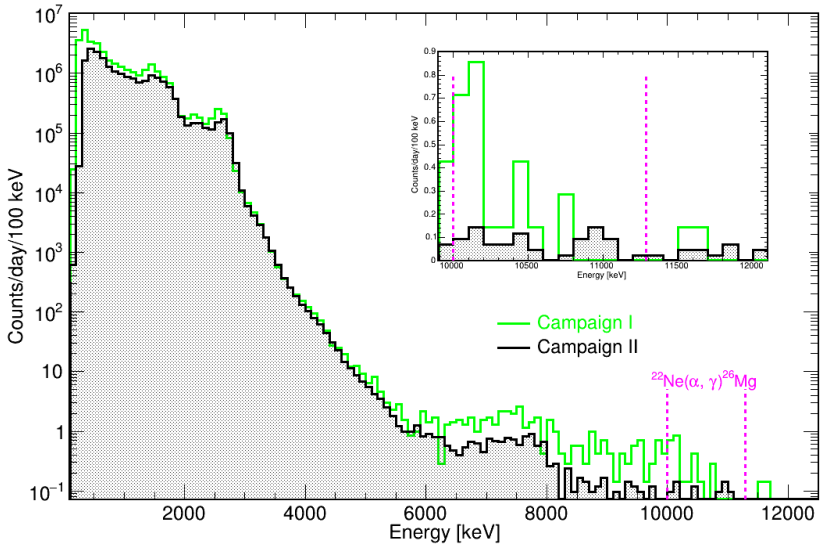

Figure 3.9: Laboratory background taken during Campaign I (green line) and Campaign II (black line). The dashed magenta lines define the ROI for the 334 keV resonance.

at the energy range of interest for the 395 keV resonance, the background in the BGO detector at LUNA was mainly dominated by neutron-induced effects ([62]). To reduce these effects, a 10 cm thick borated (5%) polyethylene (PE-HMW 500 BOR5 by Profilan Kunstofiwerk) shield surrounded the BGO in Campaign II (Figure 3.8b).
Figure 3.9 shows the comparison of the laboratory background taken with (Campaign II) and without (Campaign I) shielding. The shielding reduced the counting rate in the region of interest for the 334 keV resonance by a factor of 3.3 ±0.3, and by a factor of 3.8±0.4 considering the neutron-induced background ROI (∼ 6-13 MeV).

3.3.3 Electronics and DAQ

The adopted data acquisition chain is shown in Figure 3.10. For each crystal, a devoted digital acquisition chain and independent power supply were provided. The high voltage power supply was given by a CAEN V6533P HVPS which was controlled via GECO2020 software. Typical voltages of about 900 V are needed for the PMTs, with differences up to 50 V among the six PMTs in order to match the gain. The anode output coming from the six PMTs was independently amplified

by ORTEC 113 scintillation preamplifiers. The stability of the electronics and the dead time of the acquisition were evaluated by a pulse generator connected to the preamplifiers. The preamplifier output of the six sectors was then acquired by a

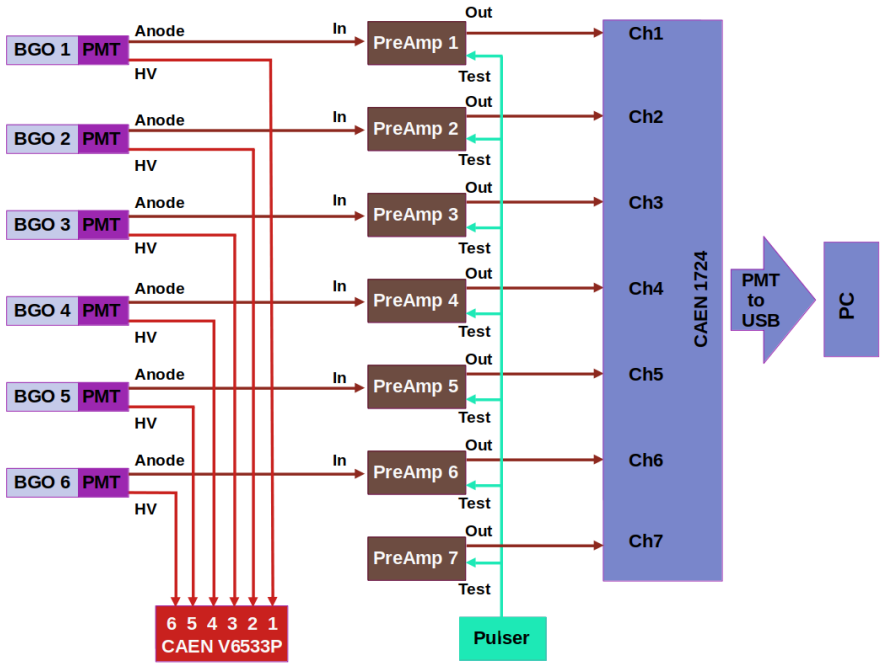

Figure 3.10: Data acquisition scheme. Each crystal sector has independent power supply and digital acquisition chain.

CAEN V1724 (8 channel, 14 bit, 100 MS/s) digitizer, connected to the acquisition PC through a CAEN VME-USB bridge and read out by the MC2 Digital MCA Data Acquisition and Analysis Software (*MC*^{2} *Analyzer*). The threshold and triggers of each channel were independently fixed from *MC*^{2} *Analyzer* software. In order to choose the best parameters for the data acquisition, different tests were performed using the *MC*^{2} software in oscilloscope mode. The *MC*^{2} *Analyzer* allows to visualize online each channel and make some online analysis of the data. Moreover, for each acquired event, the trigger timestamp, the energy were saved in the binary files for subsequent offline analysis. A homemade C++ software was written to convert the binary files into ROOT files based on the Object Oriented Data Analysis Framework developed by CERN [63, 64]. The software was able to build the spectra for each channel with and without calibration. Moreover, the program builds both the singles sum spectrum, obtained by simply summing the individual spectra for each crystal and the addback spectrum, which contains the

sum of the coincident signals in two or more crystals. Thanks to the high-efficiency of the BGO detector, it is possible to detect multiple emitted radiations in the same nuclear decay. In the present work, a 3.5 μs wide window was chosen to group the coincident events. Their energies were summed and recorded in the addback spectrum. In addition, timestamp and energy data for every single event, allow to recover coincidence information and perform coincidence analysis which was not completely useful in this work due to the very low rate of 334 keV resonance.

3.4 Data analysis

3.4.1 Energy calibration

Using the BGO detector in add-back mode, the expected gamma-ray peak from the 334 keV resonance has an energy of $E_\gamma = Q_{value} + E_{cm}$ = (10614 + 334) keV = 10950 keV. The region of interest (ROI) depends on the energy calibration of the acquired spectra. A nominal ROI width of 1256 keV was calculated using simulations and the experimental approach given in [2].
As discussed in Section 3.3.2, the light yield of the BGO is strongly temperature dependent, hence the energy calibration of the detector might change over time. To take into account this effect, the data were daily saved and all the spectra of the six BGO sectors acquired were self-calibrated. Once the spectrum of each BGO segment is calibrated, the sum and the addback spectra can be obtained as well. Each channel was calibrated in energy using the low energy peaks from the natural background. The calibration is based on the γ-lines from ^{40}K (E_γ= 1460 keV), ^{214}Bi (E_γ= 2204 keV), and ^{208}Tl decays (E_γ= 2614 keV). These peaks, in particular the ^{40}K and ^{204}Tl lines, are visible and distinguishable in all of the ^{22}Ne$(\alpha,\gamma)^{26}$Mg runs, in the beam-induced background runs with Ar gas as target and in the natural background measurements. Instead, the ^{214}Bi γ-line is not perfectly distinguishable in some short runs. Therefore, to adopt a standard approach some very preliminary tests were performed. For some runs where all three peaks are well visible, the energy calibration is done using both two peaks and three peaks. The effect of using two or three γ-lines resulted negligible and the calibration of all acquired spectra is done using a linear relation between channel and the γ-lines of ^{40}K and ^{208}Tl:

$$E_\gamma[keV] = a_0 + a_1 \cdot Ch \tag{3.4}$$

where Ch is the channel, a_0 the intercept and a_1 the slope. A typical BGO spectrum with the relevant peaks for the calibration, and the linear calibration curves, are shown in Figure 3.11 and Figure 3.12, respectively. The energy calibration with the natural background peaks can cover only the energy region up to E_γ = 2614

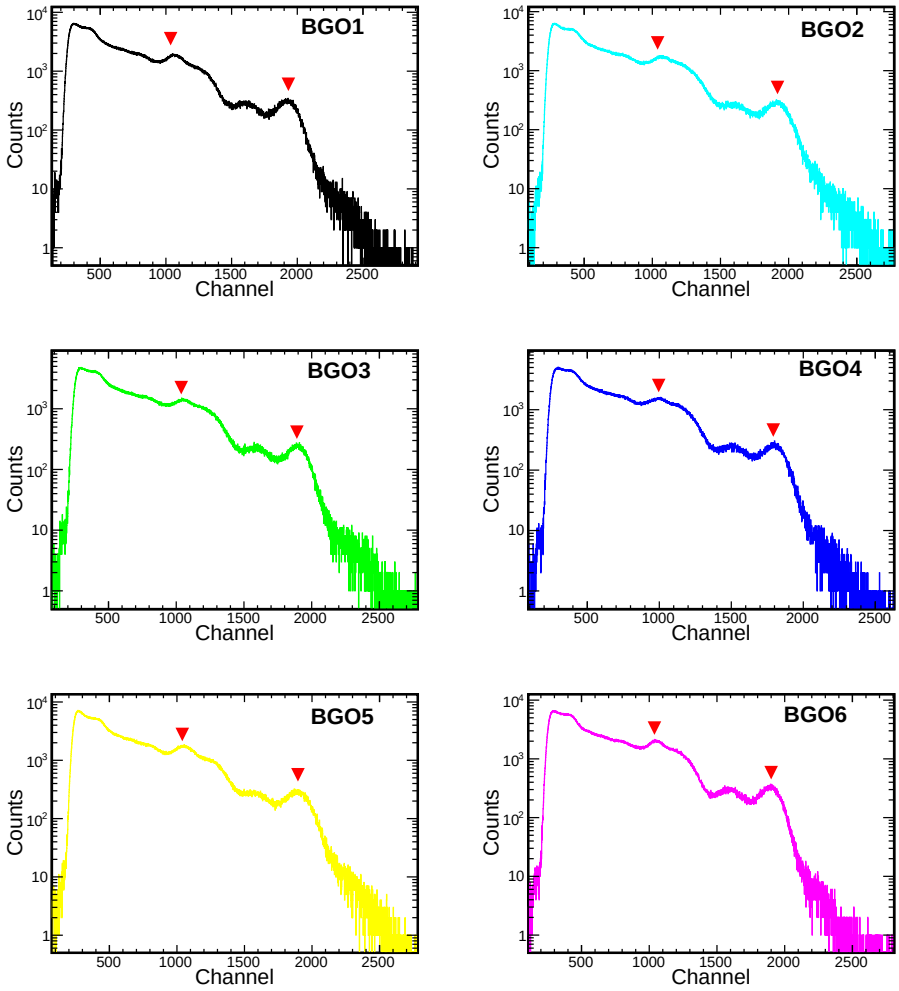

Figure 3.11: Spectra of the BGO segments for a given $^{22}\mathrm{Ne}+\alpha$ *run. The peaks used for the energy calibration are shown with red markers.*

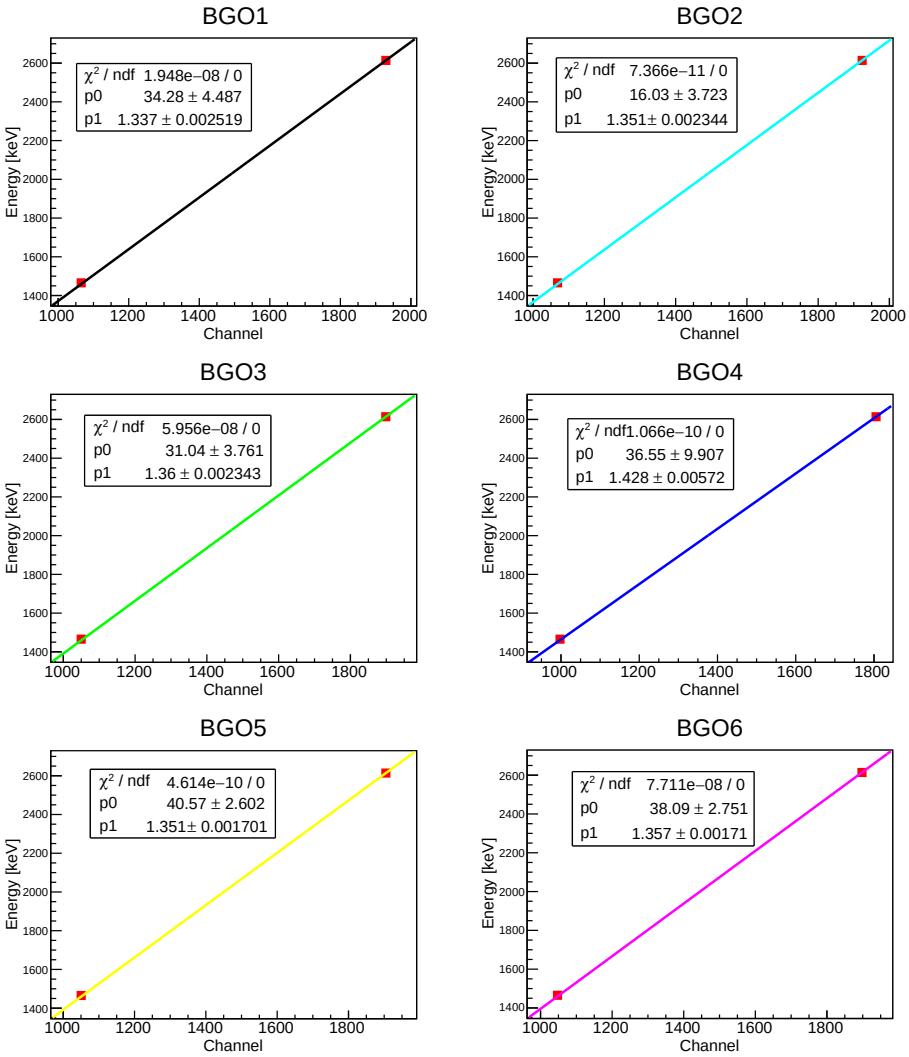

Figure 3.12: Energy calibration curve of the BGO segments for the run given in Figure 3.11.

keV, quite away from the region of interest for the ^{22}Ne$(\alpha,\gamma)^{26}$Mg reaction. The linearity of the energy calibrations, up to $\sim$ 8 MeV, is confirmed using γ-lines originated by the ^{14}N(p,γ)^{15}O reaction, E_r = 278 keV resonance , Q_{value} = 7297 keV, Table 3.4. In this context, a few measurements for the 278 keV resonance using either the nitrogen present in the chamber as a contaminant or directly nitrogen gas at a fixed pressure were performed. Since the count rate for the ^{14}N(p,γ)^{15}O reaction at the resonance energy is high, short runs of 10-20 minutes are enough for sufficient statistic. The procedure for the validation of the energy calibration linearity up to 8 MeV can be summarized as follows:

1. Background run
2. p + ^{14}N run at E_r = 278 keV
3. Background run

The background runs were long enough to clearly distinguish the ^{40}K and ^{208}Tl peaks, short enough to avoid changes in energy calibration due to the BGO temperature effects. For the same reason, the background measurements were done both before and after the measurement at the E_r = 278 keV resonance energy.
As a first step, the background runs were calibrated using the ^{40}K and ^{208}Tl peaks, and no discrepancies were found between the first and the last run. Thereafter, the calibration curves obtained from the background runs are applied to the nitrogen run[2]. Moreover, the nitrogen run is also calibrated separately using peaks from the ^{14}N(p,γ)^{15}O reaction with a both linear and quadratic functions. In all

E_{in} [MeV]	E_{fin} [MeV]	E_γ [MeV]	BR [%]
7.556	6.791	0.765	22.9
	6.172	1.384	57.8
	5.241	2.315	0.6
	0	7.556	1.6
6.791	0	6.791	100
6.172	0	6.172	100
5.241	0	5.241	100
5.181	0	5.181	100

Table 3.4: Excited state levels of ^{15}O *populated in the* ^{14}N(p,γ)^{15}O *reaction [65].*

cases, for all BGO sectors, the discrepancies between the nominal energies and the

[2]Since it takes some time to put the gas in the chamber at a fixed pressure, for this test was considered the beam-induced background measurement at the E_r = 278 keV resonance energy.

centroid of the peaks are less than 5 keV, caused by the peak fitting uncertainty. The above discussion confirms the BGO linearity up to 8 MeV. If the random coincidences between the γ-rays from the different ^{16}O decays are also considered, the add-back spectra generated from the nitrogen run can extend the energy region up to 15 MeV (Figure 3.13), covering the region of interest for the ^{22}Ne$(\alpha,\gamma)^{26}$Mg reaction. However, the peak at 15 MeV generated in the add-back spectra is very broad increasing the uncertainty of its centroid. Moreover, this peak can be used only for the add-back spectra and not for the single BGO. Therefore, since it is needed to calibrate each single BGO, the ^{14}N$(\mathrm{p},\gamma)^{15}$O run is not sufficient for the non-linearity check in the ^{22}Ne$(\alpha,\gamma)^{26}$Mg region of interest.

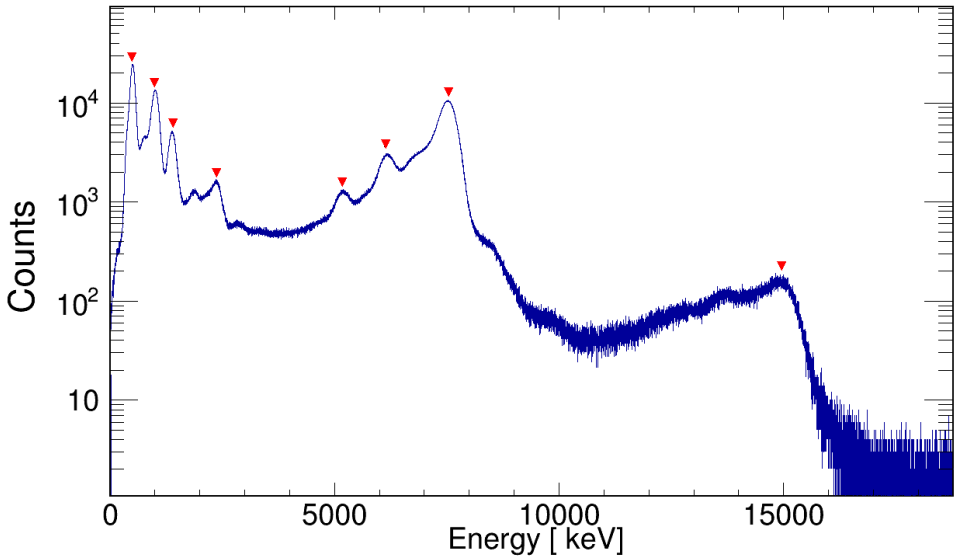

Figure 3.13: ^{14}N$(\mathrm{p},\gamma)^{15}$O *add-back spectrum at the resonance energy* E_r = *278 keV. Red markers indicate the gammas emitted from* ^{15}O.

In order to estimate the deviation from the linearity, two different spectra acquired during the previous ^{22}Ne$(\mathrm{p},\gamma)^{23}$Na experiment with the same BGO setup are analyzed:

- p + ^{22}Ne run at the resonance energy E_p = 196.4 keV (Q_{value}= 8794 keV, measurement time $\sim$ 15 h, $\mathrm{P}_{^{22}\mathrm{Ne}}$ = 2 mbar).

- p + ^{11}B run at at the resonance energy E_p = 163.9 keV (Q_{value}= 11518 keV, measurement time $\sim$ 12 h, $\mathrm{P}_{^{22}\mathrm{Ne}}$ = 2 mbar). In this case ^{11}B is a contaminant present in the chamber.

In these two spectra, the γ-lines from the natural background (E_γ= 1460 keV, E_γ= 2614 keV), the peak from the ^{22}Ne$(p,\gamma)^{23}$Na resonance (E_γ= 8975.3 keV), and peaks from 163.5 keV resonance of ^{11}B$(p,\gamma)^{12}$C reaction (E_γ= 4439 keV,E_γ = 11668 keV and E_γ= 16107 keV) are well visible. The adopted procedure to check the BGO linearity and to define the region of interest for the 334 keV resonance measurement can be summarized as follows:

1. Each BGO sector was calibrated with a linear function (Eq. 3.4), using the ^{40}K and ^{204}Tl γ-lines. Figures A.1 and A.2 show the relevant peaks for the calibration, and the linear calibration curves, respectively.

2. The calibrated spectra in 1 were used to calculate the deviation of the observed peaks from the nominal energies. The γ- line from ^{22}N$(p,\gamma)^{23}$Na reaction was shifted of about 60-65 keV from the nominal position, while the peaks at $\sim$ 11.5 MeV and $\sim$16 MeV produced from ^{11}B$(p,\gamma)^{12}$C reaction were shifted up to 170 keV and 270-300 keV, respectively (Figure 3.14).

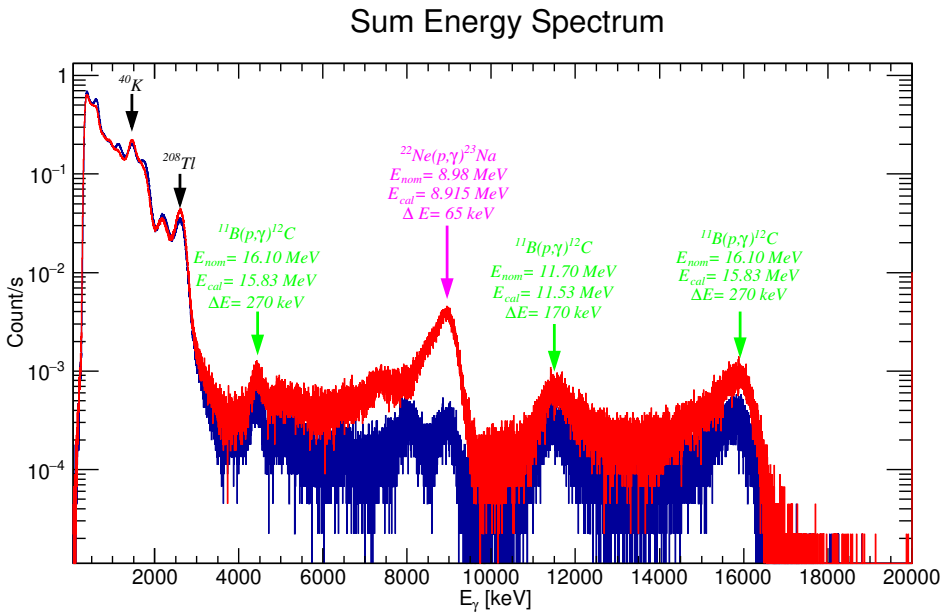

Figure 3.14: ^{22}N$(p,\gamma)^{23}$Na *spectrum for the test linearity of the BGO. In red the spectrum taken at* E_p= *196.4 keV, in blue the spectrum taken at* E_p= *163.9 keV*

3. The BGO calibration was repeated using a quadratic calibration (Eq. 3.5) based on all peaks visible in the above spectra.

$$E_\gamma[keV] = a_0 + a_1 \cdot Ch + a_2 \cdot Ch^2 \tag{3.5}$$

Figure show the quadratic calibration curves for the different BGO segments. Taking into account the deviation of the observed peaks obtained with linear calibration with the expected one (2), the BGO resolution, and the nominal ^{22}Ne$(\alpha,\gamma)^{26}$Mg ROI, a 1210 keV ROI at $[E_{min} - E_{max}]$ =[10055 - 11265] keV was determined. This approach is the same used in Campaign I ([59]).
In the present work, to define the ROI of interest taking into account the non-linearity of the BGO, another approach was developed. Considering the above runs where both quadratic and linear calibration can be applied, it is possible to move from the quadratic-calibrated ROI to the linear-calibrated ROI. The approach is summarized in the following:

1. The minimum and maximum energy, E_{min}, E_{max} from the nominal ROI for the 334 keV resonance is defined.

2. Eq. 3.5 is resolved for $E = E_{min}$, E_{max}. The solutions, Ch_{minQ} and Ch_{maxQ} are obtained for $E = E_{min}$ and $E = E_{max}$, respectively

3. Eq. 3.4 is resolved for $Ch = Ch_{minQ}$, Ch_{maxQ} obtained in 2. The solutions E_{minL} and E_{maxL} are obtained from $Ch = Ch_{minQ}$ and $Ch = Ch_{maxQ}$, respectively. E_{minL} and E_{maxL} define the minimum and maximum energy of the ROI in the linear-calibrated spectra.

Using this alternative approach to consider the non-linearity of the BGO, a ROI of $[E_{minL} - E_{maxL}]$ =[9998 - 11286] keV is obtained.

3.4.2 Detection efficiency

The detection efficiency was studied during the ^{22}N$(p,\gamma)^{23}$Na BGO campaign [12], combining the experimental measurements with Monte Carlo simulations (Geant3 and Geant4). The efficiency depends not only on the γ-energy but also on the position along the beam path. For this setup, the detection efficiency was measured using the standard radioactive sources ^{7}Be ^{60}Co, ^{88}Y, and ^{137}Cs for the low energy region and the 278 keV resonance in ^{14}N$(p,\gamma)^{15}$O for higher energies. A more detailed efficiency determination is given in Chapter 4 (the setup is different but the approach is similar). The detection efficiency for the single BGO channels was directly determined by the experimental data of standard sources and the ^{14}N$(p,\gamma)^{15}$O reaction while for the addback mode further improvements were needed. In the energy and target region not accessible by the experimental data, the detection efficiency was determined by Monte Carlo simulations using the Geant4 code. The Geant4 simulations were fine-tuned with the experimental data. Furthermore, the setup was also described using the well-tested LUNA Geant3 code [10], with consistent results. The Geant3 code provides a full de-

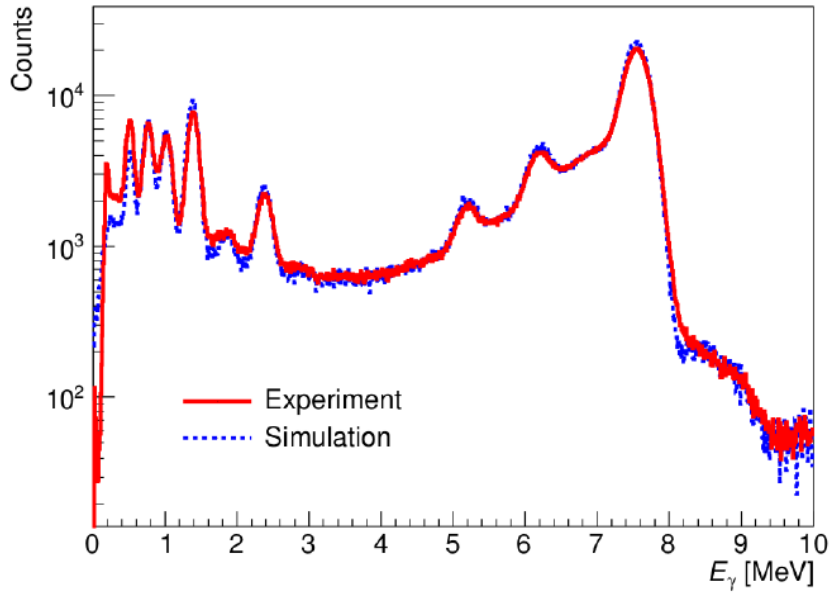

Figure 3.15: Comparison of experimental and Monte Carlo simulations for the ^{14}N$(p,\gamma)^{15}$O *addback spectrum at the resonance Ep = 278 keV [11].*

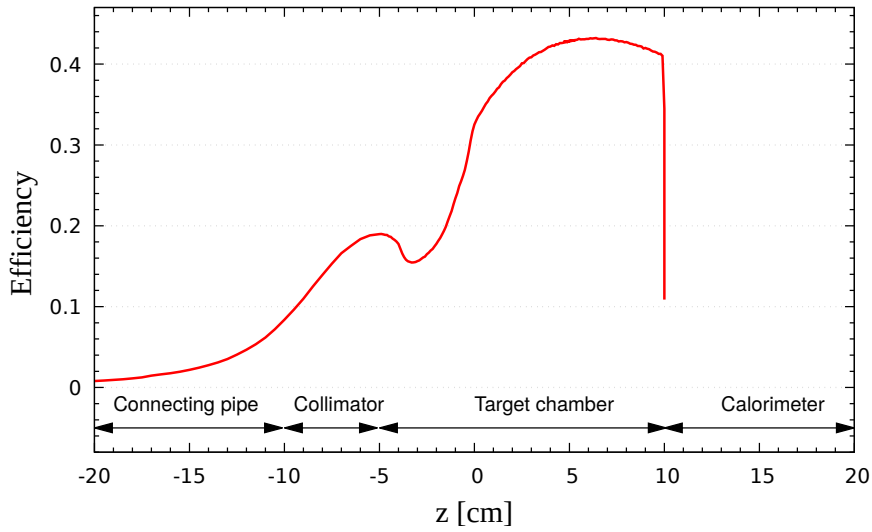

Figure 3.16: Simulated detection efficiency for E_γ *= 10950 keV as a function of position z along the beam path.*

scription of the physical effects given by the beam going through the gas target. Figure 3.15 shows the experimental addback spectra for the $^{14}N(p,\gamma)^{15}O$ reaction together with Monte Carlo simulations addback spectra [11]. The simulation was found to match the experimental efficiency for the radioactive sources within 4%, without any re-scaling. Figure 3.16 shows the simulated detection efficiency for E_γ= 10950 keV. The adopted detection efficiency in the region of interest for the $^{22}Ne(\alpha,\gamma)^{26}Mg$ was of $\sim$ 45%.

3.4.3 Gas target density

When the beam entered into the target chamber, due to collision with gas of the target, it looses energy. The beam intensity depends on the energy lost in the target and the gas density $\rho(z)$ along the beam path. This last one depends on the pressure and the temperature of the gas in the chamber. The pressure is kept constant thanks to the feedback system, while the hot side of the calorimeter together with the water cooled collimator introduce a temperature gradient along the target chamber. The density profile is given by the equation of state for an ideal gas:

$$\rho(z) = \frac{p(z)}{k_B T(z)} \tag{3.6}$$

where $p(z)$ and $T(z)$ are respectively pressure and temperature along the beam path. The proton beam energy loss over the beam path is given by:

$$\Delta E = \int_{L_{eff}} \frac{dE}{d(\rho z)}(z)dz \tag{3.7}$$

where $dE/d(\rho z)$ is the stopping power in eV/(atoms/cm^2) taken from SRIM [66], $\rho(z)$ the gas density in atoms/cm^3 and L_{eff} is the effective beam path length defined as:

$$L_{eff} = \frac{1}{\rho_0}\int_{z_{in}}^{z_{fin}} \rho(z)dz \tag{3.8}$$

where ρ_0 is the nominal density in the middle of the target chamber. To study the gas density profile without beam on target, dedicated measurements of the pressure and temperature profiles were performed.

Study of the gas density without beam

The gas density studies were performed during the study of $^{22}N(p,\gamma)^{23}Na$ reaction using the same chamber equipped with several flanges to connect pressure or temperature gauges [12] (Figure 3.17). The pressure profile was measured with four capacitance pressure gauges: two MKS Baratron type 626A and two Pfeiffer CMR 363. The nominal pressure in the middle of the target chamber was continuously

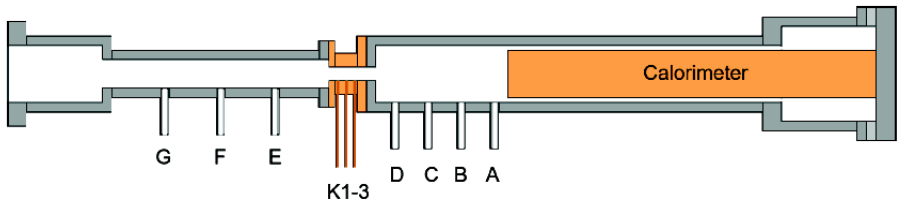

Figure 3.17: Schematic view of the target chamber used for the pressure and temperature profiles measurement.

measured by one of the two MKS Baratron and the other pressure gauges were calibrated with respect to the reference one. The pressure profile was studied in the connecting tube and in the target chamber considering using several ^{22}Ne pressures in the chamber, from 0.5 to 5 mbar with steps of 0.5 mbar. The pressure (as well as density) values on the edges of the collimator were extrapolated from the trend in the interaction chamber and the connecting tube. Figure 3.18 shows the pressure

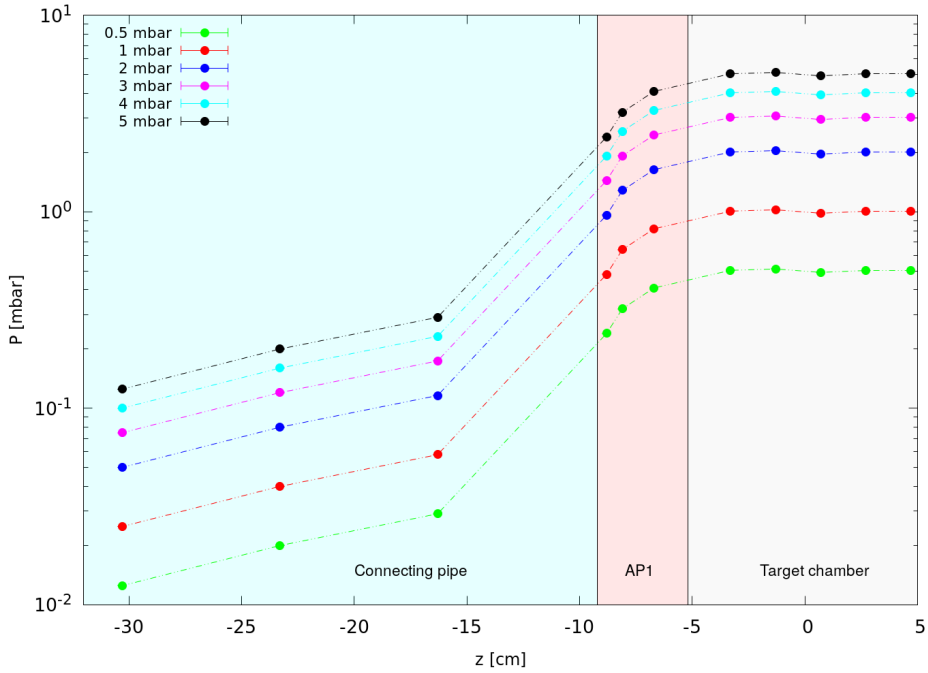

Figure 3.18: Pressure inside the gas target chamber as a function of the distance z. z=0 corresponds to the center of effective target chamber.

as a function of the position in the chamber, for different nominal pressures in the chamber. The pressure profile inside the chamber is typically flat with a drop of 1 order of magnitude in the AP_1 collimator. The total uncertainty for the pressure profile was estimated to be 1%.
For the temperature profile, four Pt100 RTDs (Resistance Temperature Detectors) were mounted inside the chamber and the measurements were done for different nominal pressures in the chamber, from 0.5 to 5 mbar with steps of 0.5 mbar. Differently from the pressure profile, which have a flat behaviour inside the chamber, the temperature profile is affected by the calorimeter hot side and the water cooling on the other side. Furthermore, the temperature at the beam spot position coincides with the temperature of the calorimeter hot side (343 K), the temperature inside the collimator is assumed to be the same as the cooling water (287 K). Moreover, the pipe connecting the target chamber to the first pumping stage is assumed to be at ambient temperature (295 K, measuredwith PT100 located in the accelerator room). Figure 3.19 shows the temperature as a function of the beam path for 1 mbar (working pressure for the $^{22}Ne(\alpha,\gamma)^{26}Mg$ measurements). The overall temperature profile in the interaction chamber is determined with 0.34 % uncertainty (1 K).

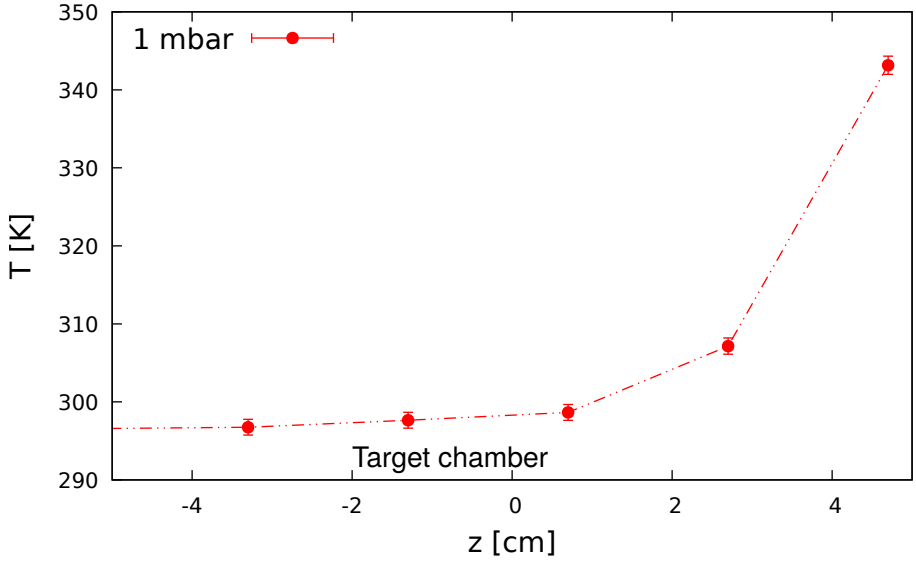

Figure 3.19: Temperature profile for 1 mbar ^{22}Ne.

The density profile was estimated using Eq. 3.6 and combining the pressure and temperature profiles given in Figure 3.18 and Figure 3.19. Figure 3.20 shows the density profile for 1 mbar ^{22}Ne (red points).

As expected from the equation of state for an ideal gas, the density profile shows an inverse behavior with respect to the temperature profile. It increases slowly in the connecting tube, then there is a strong rise in the collimator followed by a decreasing trend until it reaches the calorimeter. At different z in the chamber, not measured experimentally, the density profile is obtained using extrapolations. The gas density profile without beam has been determined with an uncertainty of 0.9% inside the target chamber, 1.5% inside the collimator, and 1.7% in the connecting tube. These results include also the uncertainties due to the extrapolations.
The density profile is used in Eq. 3.8 to determine the effective target length L_{eff} in 1 mbar ^{22}Ne, which results in L_{eff} = (13.9±0.5) cm.

Beam heating effect

The interaction with the intense ion beam increases the temperature, the gas density along the beam path may decrease. This effect, known as the beam heating effect has been studied in different gases [67, 68] and should be taken into account in the energy loss determination. The beam heating correction in neon was studied during the ^{22}Ne$(p,\gamma)^{23}$Na HPGe campaign at LUNA [69, 70] using the resonance scan technique. The effect was studied scanning the well known narrow resonance at $E_{p,res}$= 271.56 keV, of ^{21}Ne$(p,\gamma)^{22}$Na reaction. For this purpose, the experimental setup consisted of a collimated NaI detector placed perpendicularly to the beam path close to the target chamber which was the same used for the ^{22}Ne$(p,\gamma)^{23}$Na reaction. The resonance scan was done using natural neon gas which contains only a small quantity of ^{20}Ne (90.48% ^{20}Ne, 0.27% ^{21}Ne, 9.25% ^{22}Ne) with beam energy steps between 0.5 keV and 2 keV. The scans were repeated for different pressures in the chamber and different values of beam intensity. The maximum yield of the resonance scan is obtained when the reaction is populated in front of the detector and the energy loss is given as the difference between the energy of maximum yield and the resonance scan energy:

$$\Delta E_p = E_{p,Ymax} - E_{p,res} \tag{3.9}$$

Considering all the different resonance scans performed, several values of the energy loss in Eq. 3.9 as a function of the beam current and the pressure in the target chamber were determined. The energy loss without beam was obtained by extrapolating this function down to current I = 0. The ratio between the energy loss at a certain current (ΔE_I)and the energy loss at I = 0 (ΔE_0)gives the ratio between the density with the beam on target ρ and the density without beam ρ_0, i.e the density reduction factor:

$$\frac{\rho}{\rho_0} = \frac{\Delta E_I}{\Delta E_0} \tag{3.10}$$

From previous studies [67, 71], is known that the beam-heating effect is proportional to the specific power dissipation of the beam in the target gas given as:

$$\frac{dW}{dz} = \frac{dE}{d(\rho z)}\rho I \tag{3.11}$$

therefore the density reduction function (beam heating function) can be parameterized as:

$$\frac{\rho}{\rho_0} = 1 - \alpha_{BH}\frac{dW}{dz} \tag{3.12}$$

where α_{BH}= $(0.44 \pm 0.05)10^{-3}$cm/mWatt [72]. Since the geometry of the target chamber for the study of the ^{22}N(p, γ)^{23}Na reaction is not the same used for the beam heating correction presented above, some other correction should be considered. Moreover, the use of the α beam instead of the proton beam should also be taken into account. The role of the target geometry on the beam heating effect is studied in [73]. The ΔT caused by the beam heating depends on the dimension of the chamber following the relation given in Eq. 3.13:

$$\Delta T = \frac{H}{2\pi K} ln\left(\frac{r_{chamber}}{r_{beam}}\right) \tag{3.13}$$

where H is the heat flow, K is the thermal conductivity of the gas, $r_{chamber}$ is the inner radius of the target chamber, and r_{beam} the beam radius. Using Eq. 3.13 with the geometry of the target chambers used in ^{22}Ne(p, γ)^{23}Na HPGe campaign and ^{22}Ne(α, γ)^{26}Mg BGO campaign it is possible to determine how much the beam-heating in the new chamber differs from the previous one. The beam heating coefficient with the ^{22}Ne(α, γ)^{26}Mg BGO target chamber, α_{BH}^{BGO} is given by:

$$\alpha_{BH}^{BGO} = \alpha_{BH}\frac{\ln\left(r_{chamberBGO}/r_{beam}\right)}{\ln\left(r_{chamber}/r_{beam}\right)} \tag{3.14}$$

where $r_{chamberBGO}$ is the inner radius of the BGO target chamber given in Section 3.3.1. The result in Eq. 3.14 refers to the proton beam, and are corrected for α-beam taking into account that the dissipated power along the beam path depends on the stopping power of the ion beam:

$$\alpha_{BH}^{\alpha} = \alpha_{BH}^{p}\frac{(dE/dx)_\alpha}{(dE/dx)_p} = 0.85 \text{ cm/Watt} \tag{3.15}$$

with $(dE/dx)_\alpha$ and $(dE/dx)_p$ the energy loss of α and proton beam in the gas, respectively. As a result, for the beam heating of the present setup, an uncertainty of 50% was associated. Figure 3.20 shows the density profile, with and without the beam heating correction.

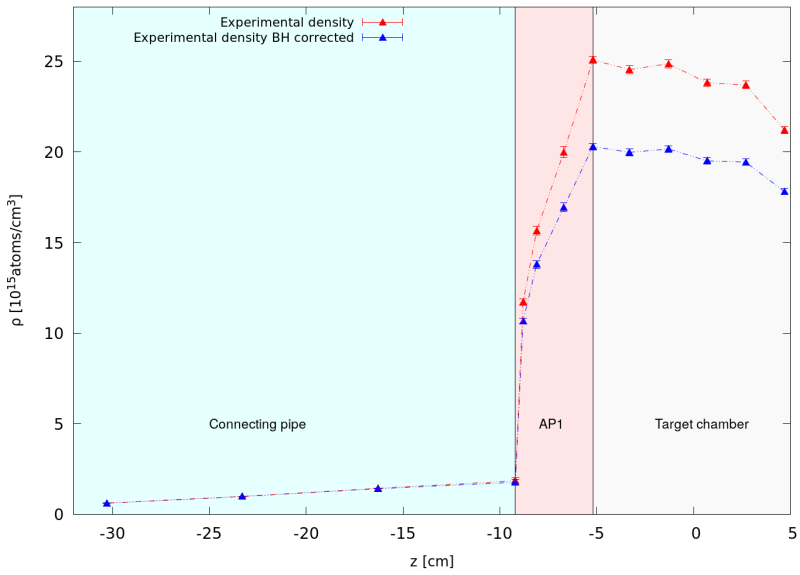

Figure 3.20: Density profile in 1 mbar ^{22}Ne. In red the density profile without taking into account the beam heating effect, in blue the one corrected for the beam heating.

3.4.4 Energy straggling

When a charged particle penetrates through matter, it interacts via inelastic collisions with the bound electrons in the atoms of the stopping material, transferring part of the energy to the electrons. Every interaction with the electrons of the target material makes the projectile lose part of its energy, causing the projectile to slow down. This process is made up of small but finite losses in a large number of collisions. Therefore, there will be a statistical fluctuation in the total energy lost by particles with the same incident energy traveling through the same path length. As a consequence, there will also be fluctuations in the distance the incident particles will travel before being stopped. These fluctuations are known as *energy straggling* and *range straggling*, respectively. They give rise to an energy distribution of the beam, f(E,x) centered at E=E_0-ΔE, where E_0 is the incident energy and ΔE the mean energy loss. A schematic representation of energy distribution of the beam passing through the target is shown in Figure 3.21 where x is the path length of the beam.

In different studies, [75, 76], is shown that the experimental straggling effect is well in agreement with the theory developed by Bohr [77]. For small energy losses, the energy distribution of the beam is well described by a Gaussian probability density

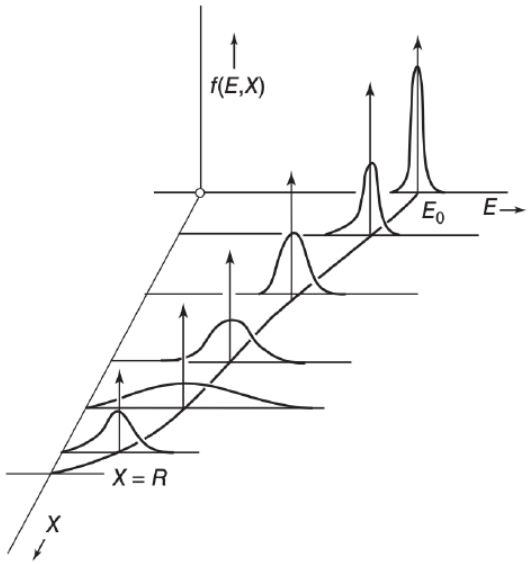

Figure 3.21: Schematic representation of energy distribution functions f(E, x) for charged particles beam with a small initial energy spread as they move through an absorber along a path of length x [74].

function and its width, referred to as the energy straggling σ_{stragg}, is given by Bohr approximation:

$$\sigma_{stragg} = \sqrt{4\pi e^2 Z_p^2 Z_t \rho d} \tag{3.16}$$

where Z_p is the atomic number of the projectile, Z_t is the atomic number of the target, d the thickness, and ρ the density of the target.

The energy straggling affects the position inside the chamber where nuclear reactions take place. In the particular case of a resonant reactions, if the straggling is negligible, the reaction would take place in a thin slice of the target. Instead, for a large energy straggling, the resonance is populated in a thicker slice of the target, causing a reduction of the maximum resonance yield (Section 3.4.5).

In the present study of the ^{22}Ne$(\alpha,\gamma)^{26}$Mg reaction, the effect of the energy straggling on the total resonance yield is studied adopting the approach given in [78]. Assuming a constant stopping power[3] over the total resonance width, σ_{stragg} in Eq. 3.16 can be given by Eq. 3.17 taken from [4]:

$$\sigma_{stragg} = 1.210^{-9}\sqrt{Z_p^2 Z_t \Delta E/\epsilon} \tag{3.17}$$

[3]In very thin targets the energy lost is relatively small and the stopping power is approximately constant over the target thickness.

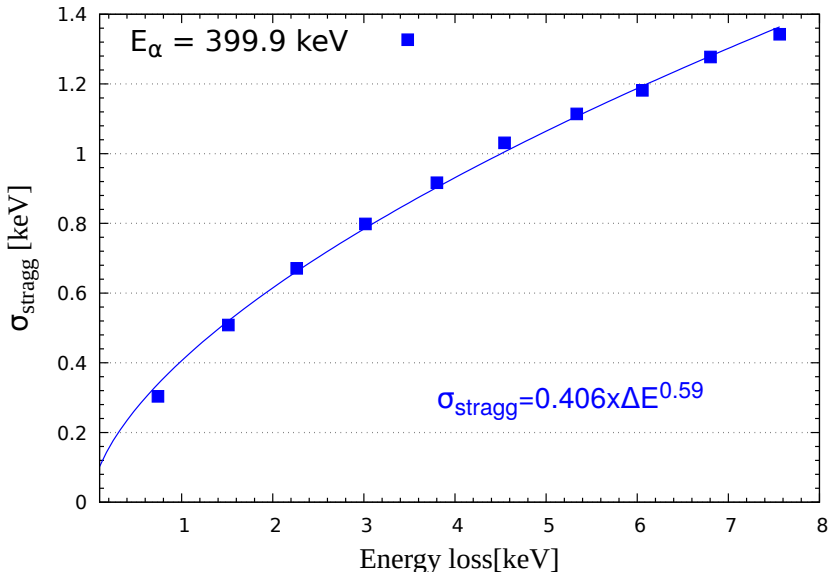

Figure 3.22: Energy straggling as a function of the energy loss in the target for 399.9 keV α beam. The line is the parametrization obtained using the approach in [78].

where ΔE is the energy loss and ϵ the stopping power in eV/(atoms/cm^2). Eq. 3.17 can be parametrized by the relation given in Eq. 3.18:

$$\sigma_{stragg} = a\Delta E^b \tag{3.18}$$

The parameters a = 0.406±0.009 and b = 0.59± 0.01, are derived by fitting the energy straggling data which are obtained by running many TRIM Monte carlo simulations of α ions at different depths in 1 mbar neon gas. Figure 3.22 shows the data obtained by TRIM together with their fit for the ^{22}Ne$(\alpha,\gamma)^{26}$Mg reaction. Taking into account this parametrization, the density profile and the efficiency for the γ emitted from the ^{22}Ne$(\alpha,\gamma)^{26}$Mg reaction, a Root script can calculate the energy straggling correction of the experimental yield curve. In this correction the lateral straggling is negligible and not taken into account. The correction is applied in Section 3.4.5.

3.4.5 Data taking and results

The study of the 334 keV resonance was carried out by performing long runs at the beam energy where the maximum yield was expected. The beam energy was chosen to take into account the literature resonance energy, the position of the maximum

detection efficiency, and the energy loss in 1 mbar ^{22}Ne. The laboratory and beam-induced background were deeply investigated. In particular long background runs before and after the α + ^{22}Ne measurements were performed. Instead, to investigate the beam-induced background (BIB), at the same beam energy used for the α + ^{22}Ne, long runs in 0.468 mbar argon gas were performed. The pressure was chosen in order to have the same energy loss like the one given in 1 mbar ^{22}Ne. Briefly the experimental data taking procedure for the 334 keV resonances study can be summarized as follows:

- long laboratory background runs taken immediately after the borated polyethylene shielding mounting
- beam induced background runs in 0.468 mbar Ar at the nominal energy.
- on resonance runs in 1.0 mbar ^{22}Ne at the nominal energy.
- long laboratory background runs after the ^{22}Ne data taking

Based on the low values of the 334 keV resonance strength, and the results of Campaign I [59] which showed a very low count rate in the region of interest the precise estimation of the contributions from the laboratory and beam-induced background are crucial for the final results. Table 3.5 summarize the total time and charge for each contribution.

Run type	E_α[keV]	P [mbar]	t[days]	Q[C]
Laboratory background (before)	no beam	no gas	9.5	
α + Ar	399.9	0.468	7.2	84.4
α + ^{22}Ne	399.9	1.0	23.6	430.4
Laboratory background (after)	no beam	no gas	40.3	

Table 3.5: Running time, and accumulated charge for each contribution considered during Campaign II.

The first set of laboratory background data was acquired during August - September 2018. To check the effect of the shielding, each laboratory background run, saved daily or at the most every three days, is separately analyzed in different ROIs with focus on the 334 keV resonance ROI. Figure 3.23 shows the count rate of the laboratory background over time. The count rate is calculated in the ROI of ^{22}Ne$(\alpha,\gamma)^{26}$Mg reaction, and in the region from 6 to 13 MeV to check the neutron induced background. The fluctuations of the count rate over time, in the ROI for 334 keV resonance, are less then 1.8σ. The main contribution of incompatibility is due to the long runs (2 - 3 days) where the energy calibration might shift on time.

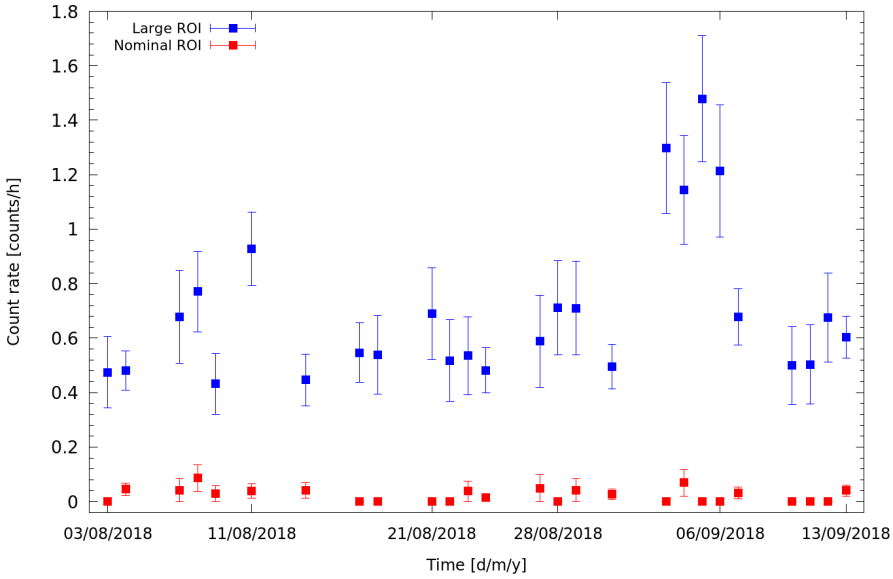

Figure 3.23: Laboratory background with 10 cm borated polyethylene shielding taken before Campaign II. In blue the count rate in a large ROI = (6 - 13) MeV, in red the count rate in the nominal ROI = (9.998 - 11.286) MeV.

Experimental yield calculation

The measured reaction yield is defined as:

$$Y = \frac{N_R}{Np} = \frac{N}{\eta}\frac{e}{Q} \tag{3.19}$$

where N_R is the total number of nuclear reactions, N_p is the total number of incident particles, N is the number of net counts in the sum peak, η is the detection efficiency for the emitted γ, e is the is the elementary charge, and Q the total accumulated charge. The charge calculation is done by using the average live time of the BGO segments which are stopped and saved simultaneously. For each run, the dead time of each segment, calculated using the pulser channel, resulted 1%. The experimental yield at a given beam energy E_0 is related to the nuclear cross-section by the relation:

$$Y(E_0) = \int_{E_0-\Delta E}^{E_0} \frac{\sigma(E)}{\epsilon(E)} dE \tag{3.20}$$

where ΔE and $\epsilon(E)$ are the total energy loss in the target and effective stopping power, respectively. As described in Section 1.2.3, the 334 keV resonance with ΔE

$\geq \Gamma_\alpha + \Gamma_\gamma$, can be defined as a narrow resonance. Therefore, the nuclear cross-section is well described by the Breit-Wigner cross-section given in Eq. 1.36, and the integral in Eq. 3.20 becomes:

$$Y(E_0) = \frac{\lambda_r^2}{2\pi}\frac{\omega\gamma}{\epsilon_r}\frac{M+m}{M}\left[\arctan\left(\frac{E_0 - E_r}{\Gamma/2}\right) - \arctan\left(\frac{E_0 - E_r - \Delta E}{\Gamma/2}\right)\right] \quad (3.21)$$

where λ_r and ϵ_r are respectively the De Broglie wavelength and the effective stopping power evaluated at the resonance energy. The coefficient $(M+m)/M$, with M the mass of the target and m the projectile mass, takes into account that the stopping power is given in the laboratory system.
Moreover, since the target thickness in units of keV, $\Delta E \sim 8$ keV is much larger than the 334 keV resonance width ($\Delta E \geq \Gamma$), the maximum reaction yield is given by:

$$Y = \frac{\lambda_r^2}{2}\frac{\omega\gamma}{\epsilon_r}\frac{M+m}{M} \quad (3.22)$$

and still in Eq. 3.22 some experimental phenomena have to be taken into account to correctly determine the reaction yield. The energy resolution of the beam and its energy straggling (Section 3.4.4) inside the target, play a significant role in the yield determination. Therefore,the experimental yield relation given in Eq. 3.21 has to be replaced with a more general relation (Eq (4.111) Iliadis textbook [4]):

$$Y(E_0) = \frac{1}{\epsilon_r}\int_{E_0-\Delta E}^{E_0} dE' \int_{E_i=0}^{\infty} dE_i \int_{E=0}^{E_i} \sigma(E) g(E_0, E_i) f(E_i, E, E') dE \quad (3.23)$$

where $g(E_0, E_i)$ describes the energy distribution of the beam and $f(E_i, E, E')$ is the probability distribution related to the energy straggling. Assuming the approach in [32], the energy spread of the alpha beam from the accelerator, σ_{beam}= 0.1 keV, and the considerations discussed in Section 3.4.4, an approximate energy distribution related to the energy straggling has been derived. Moreover, the changes in the target density, $\rho(z)$, and efficiency, η_z, are also taken into account. Therefore, Eq. 3.23, with some simplifications, i.e, integrating over the target depth z instead of the energy E' becomes:

$$Y(E_0) = \frac{1}{\epsilon_r}\int_0^{z_{max}} dz \int_{E=E_0}^{E=0} f(E, E(z)) dE \sigma_{BW} \eta(z) \rho(z) \quad (3.24)$$

with $f(E, E(z))$ given as:

$$f(E, E(z)) = \exp\left[-\frac{(E - E(z))^2}{2\left[\sigma_{beam}^2 + \sigma_{straggle}^2(E(z))\right]}\right] \quad (3.25)$$

The computation of the predicted yield curve (Eq. 3.24) under the ^{22}Ne$(\alpha,\gamma)^{26}$Mg experimental conditions shows a correction factor of $C_{straggle}$= 0.93 due to the

energy straggling. This result no longer allows using the thick target yield approximation given in Eq. 3.22. Therefore, to take into account this correction, the modified thick-target yield equation is then given by:

$$Y_{max} = C_{straggle}\frac{\lambda_r^2}{2}\frac{1}{\epsilon_r}\omega\gamma \tag{3.26}$$

Net count calculation

For each of the contributions: the laboratory background, BIB, and ^{22}Ne + α measurements, all addback spectra are used. Then, the counts (N) for each of the contributions are calculated using the full statistics from the total addback spectra. Moreover, based on the results of Campaign I, and on the online analysis of the present data, which didn't show any evident peak in the region of interest, several offline analysis and test are done. In particular, the counts are calculated in several ROIs which takes into account both the ROI width from Campaign I and the ROI width estimated in the preset work. For each of them both energy calibration approaches are considered:

- ROI_L= [8000 - 13000], ROI_width = 1256 keV, energy calibration approach II
- ROI_1= [10116 - 11161], ROI_width = 1000 keV, energy calibration approach II
- ROI_2= [10187 - 11143], ROI_width = 1000 keV, energy calibration approach I
- ROI_3= [9998 - 11286], ROI_width = 1256 keV, energy calibration approach II
- ROI_4= [10055 - 11265], ROI_width = 1256 keV, energy calibration approach I

Moreover, in addition to the counts in the addback spectra, the counts for the singleSum spectra, sum of single crystal[4], are calculated. The net counts in the region of interest for the reaction, $N_{R,net}$ are calculated by Eq. 3.27:

$$N_{R,net}^{BIB} = N_{^{22}Ne} - c_{BIB}\cdot N_{Ar} \tag{3.27}$$

where $N_{^{22}Ne}$ and N_{Ar} are the counts in the region of interest for the ^{22}Ne and Ar spectra, respectively. c_{BIB} is the ratio between the total charge in ^{22}Ne and the total charge in Ar spectra. The net counts are also calculated subtracting, instead of the beam induced backgrounds, the laboratory background given as:

$$N_{R,net}^{NB} = N_{^{22}Ne} - c_{NB}\cdot N_{NB} \tag{3.28}$$

where $N_{^{22}Ne}$ and N_{NB} are the counts in the region of interest for the ^{22}Ne and laboratory background spectra, respectively. c_{NB} is the ratio between the total time

[4]Counts of the single crystal were calculated only for the α+ ^{22}Ne spectra.

in ^{22}Ne and the total time in laboratory background spectra. Both measurement campaigns showed that the beam induced background is compatible with the laboratory background (Figure 3.24). As a result, to increase the background statistics, a test where the net counts are determined subtracting the total background (BIB + NB) is also considered.

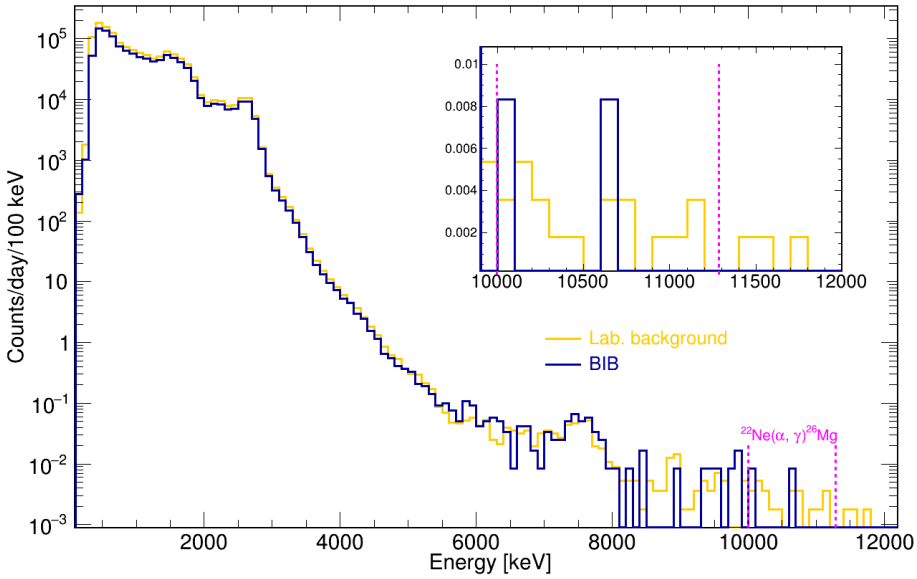

Figure 3.24: Addback mode spectra. Comparison of laboratory background (blue) and beam induce background (orange) measured during Campaign II. The spectra are normalized to the total measurement time. The dashed magenta lines define the ROI for the 334 keV resonance.

The sum of all the corresponding addback spectra for the α + ^{22}Ne runs, together with a zoom in the identified region of interest are given in Figure 3.25.
In order to understand if the net count is significant it must be compared with the critical limit (L_C) at 95 % confidence level.
The critical limit defines the number of counts below which the measured net area is compatible with the background fluctuations [79], and hence, the uncertainty of the background must be taken into account. If it is considered a non-radioactive sample measured a significant number of times, a series of background counts would be obtained. In this case the mean net count above background would be zero but following a Gaussian distribution with a standard deviation σ_0:

$$\sigma_0 = \sqrt{2B} \tag{3.29}$$

where B are the background counts.

- If $N \geq k_\alpha \sigma_0$: N is statistically significant
- If $N \leq k_\alpha \sigma_0$: N is not significant

where the constant k_α defines the degree of confidence in the conclusion and $k_\alpha \sigma_0$ is the critical limit L_C. For 95% confidence limit, $k_\alpha = 1.645$, therefore the critical limit is given as:

$$L_C = k_\alpha \sigma_0 = 1.645\sqrt{2B} \tag{3.30}$$

Using the counts found in the sum of all addback spectra in Neon, $N_{Ne} = 8 \pm 3$,

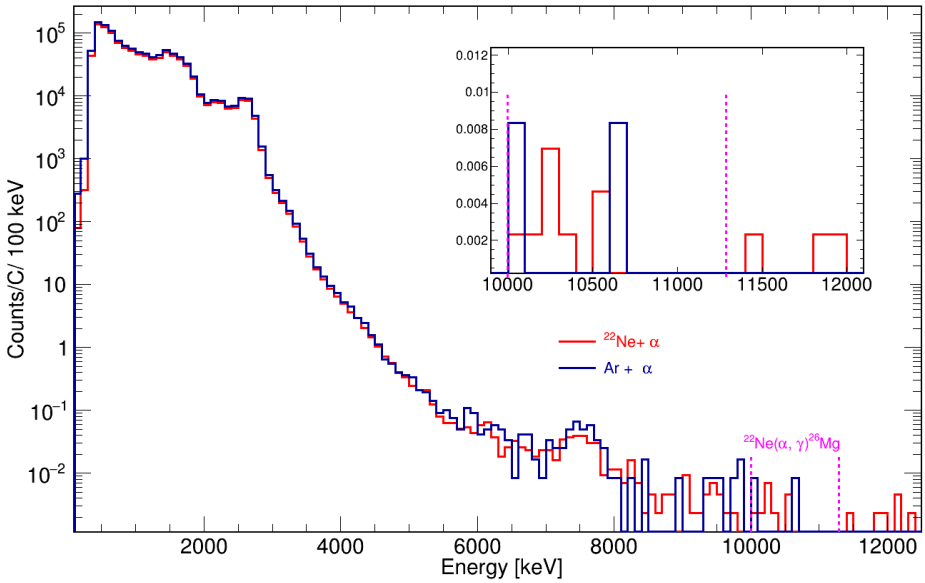

Figure 3.25: Addback mode spectra. In red the sum of all addback spectra in α+ ^{22}Ne *obtained during Campaign II. In blue the sum of the spectra in Ar used for the study of the beam induced background. The dashed magenta lines define the ROI for the 334 keV resonance.*

the net counts with the different background subtractions are estimated and are given in Table 3.6, together with the corresponding critical limit.
Since the net count are below the critical limit, from the present data is possible to give an *upper limit*, L_U, which defines what is the maximum statistically reasonable count for net counts below the critical limit.
The upper limit for the 334 keV resonance strength is estimated using Monte Carlo sampling technique based on the model given by Rolke (2001)[80]. This method is

Background contribution	Counts	Net count	L_C
BIB	2±1	-2.2 ±0.7	7.4
Lab. background	18±4	-2.5±0.3	7.6
Lab. background+ BIB	20±4	-1.9±0.2	7.3

Table 3.6: Net count and critical limit for different background contributions.

based on the likelihood ratio test statistic, together with improvements for those cases where there is no signal observed as in the present work. In this method, the background can be estimated either from Monte Carlo simulations or experimental data. Moreover, it can be extended to those cases where different background sources are present in the data. In the present work both laboratory and beam induced background sources are estimated considering the experimental count rates. The Rolke method, already implemented in the TRolke class in Root, uses the profile likelihood and quotes upper limits for small signals and two-sided confidence intervals for larger samples.
In the present work, for the Rolke Monte Carlo sampling technique the signal and the background are assumed to follow a Poisson distribution.

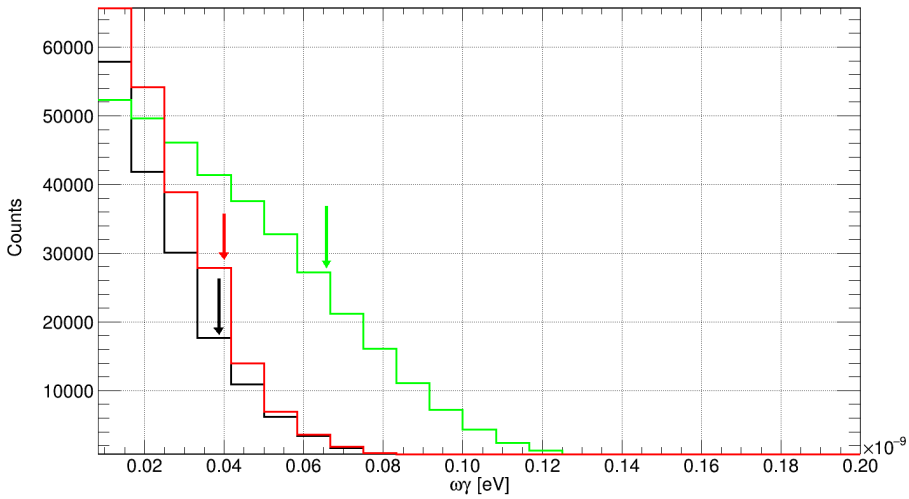

Figure 3.26: Probability density functions of the resonance strength for campaign II. In black line the PDF assuming the laboratory background, in green the beam induced background and in red considering both BIB and laboratory background. The arrows indicate the upper limits obtained at 90% confidence level for each case.

The calculations assume 10^6 samples for each case for both campaigns.
The probability density functions of the resonance strength for the different background subtractions in Campaign II are shown in Figure 3.26 while the comparison of the probability density functions of Campaign I and II is given in Figure 3.27.

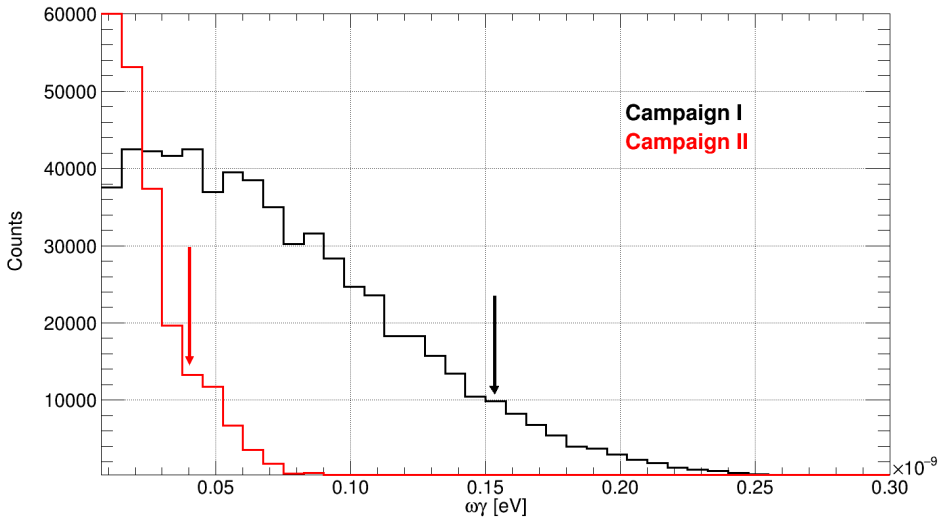

Figure 3.27: Probability density functions of the resonance strength for campaign I assuming the laboratory background (black) and campaign II assuming laboratory and BIB (red). The arrows indicate the upper limits obtained at 90% confidence level.

Background subtraction	$\omega\gamma$ [eV]
BIB	$\leq 6.6{\cdot}10^{-11}$
Lab. background	$\leq 3.8{\cdot}10^{-11}$
Lab. background+ BIB	$\leq 4.0{\cdot}10^{-11}$
Campaign I	$\leq 1.5{\cdot}10^{-10}$

Table 3.7: Upper limits for the resonance strength of the 334 keV resonance. In the upper part of the Table are shown the results obtained during Campaign II while the last line shows the result from Campaign I.

The upper limits of the resonance strength obtained in Campaigns I and II are given in Table 3.7. In particular, the upper limit for Campaign I has been calculated considering the laboratory background for the net counts while the results for Campaign II consider laboratory background, BIB and both of them together.

3.4.6 Thermonuclear reaction rate

The total thermonuclear reaction rate is calculated in the temperature range between 100 MK and 600 MK using the present upper limits reported in Table 3.7 for the 334 keV resonance and Eq. 1.41. All other resonances are assumed as in [45]. Substituting the constants, the reaction rate in Eq 1.41 becomes:

$$N_A\langle\sigma\upsilon\rangle = \frac{1.5394 \cdot 10^{11}}{(\mu T)^{3/2}}(\omega\gamma)_R e^{-11.605 E_R/T} \tag{3.31}$$

where N_A is the Avogadro constant (N_A = 6.022 141 29(27) $10^{23}\mathrm{mol}^{-1}$). The resonance strength $\omega\gamma$ and energy (E_R) of the resonance are expressed in MeV. The behavior of the new LUNA upper limit on the $^{22}\mathrm{Ne}(\alpha,\gamma)^{26}\mathrm{Mg}$ reaction rate as a function of the temperature, for the different upper limits considered, is given in Figure 3.28. The rates are normalized to the so-defined LUNA tot rate which is the

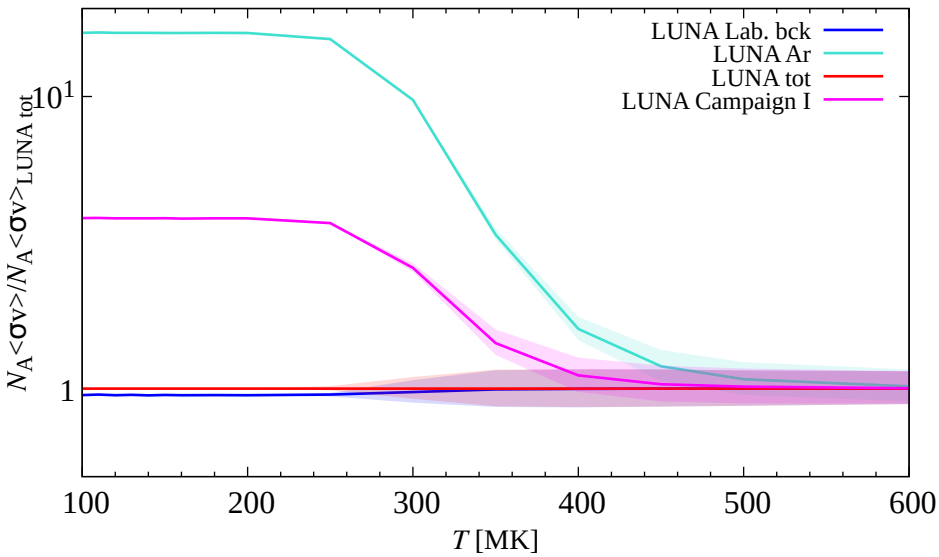

Figure 3.28: LUNA thermonuclear reaction rate of $^{22}\mathrm{Ne}(\alpha,\gamma)^{26}\mathrm{Mg}$ reaction as a function of temperature T.

reaction rate calculated by taking into account the 334 keV upper limit obtained subtracting the total background. The rate below 500 MK becomes very sensitive to the 334 keV resonance while there is a good agreement above 500 MK. For the upcoming discussion the rate calculated using the upper limit obtained with total background subtraction is considered. Furthermore, the new LUNA upper limit on the reaction rate is calculated also based on the most recent $^{22}\mathrm{Ne}(\alpha,\gamma)^{26}\mathrm{Mg}$ reaction rate available in literature [30]. The LUNA rates are given in Table 3.8.

T_9 [GK]	LUNA L12[$cm^3mol^{-1}s^{-1}$]	LUNA A21[$cm^3mol^{-1}s^{-1}$]
0.01	2.14E-77	5.52E-79
11	7.28E-74	2.58E-75
12	6.34E-71	2.93E-72
13	1.90E-68	1.12E-69
14	2.52E-66	1.81E-67
15	1.73E-64	1.48E-65
16	6.96E-63	6.93E-64
18	3.26E-60	4.16E-61
0.02	4.34E-58	6.83E-59
25	3.14E-54	9.65E-55
0.03	3.35E-49	3.94E-49
0.04	2.31E-41	4.00E-41
0.05	1.10E-36	2.76E-36
0.06	6.98E-33	5.91E-33
0.07	4.61E-29	1.18E-29
0.08	3.83E-26	1.03E-26
0.09	7.02E-24	2.12E-24
0.1	4.46E-22	1.50E-22
0.11	1.31E-20	4.86E-21
0.12	2.18E-19	8.80E-20
0.13	2.32E-18	1.02E-18
0.14	1.75E-17	8.26E-18
0.15	1.00E-16	5.06E-17
0.16	4.58E-16	2.47E-16
0.18	5.67E-15	3.45E-15
0.2	4.18E-14	2.83E-14
0.25	1.52E-12	1.28E-12
0.3	2.59E-11	2.34E-11
0.35	4.81E-10	4.10E-10
0.4	6.19E-09	5.21E-09
0.45	4.78E-08	4.08E-08
0.5	2.45E-07	2.13E-07
0.6	2.79E-06	2.49E-06
0.7	1.57E-05	1.42E-05
0.8	5.77E-05	5.31E-05
0.9	1.66E-04	1.54E-04
1	4.11E-04	3.85E-04

Table 3.8: New LUNA $^{22}Ne(\alpha,\gamma)^{26}Mg$ *reaction rates (LUNA L12 and LUNA A21) calculated taking into account the other resonances from [45] and [30], respectively.*

The LUNA rates, Longland 2012 (LUNA L12) and Adsley 2021 (LUNA A21) based, together with the previous rates given in the literature are shown in Figure 3.29. Above 250MK the LUNA rates based on the two literature data are perfectly in agreement. Below 250 MK the discrepancies between the two rates increase up to 40% at 100 MK. For temperatures below $\sim$ 250 MK the LUNA upper limit is higher

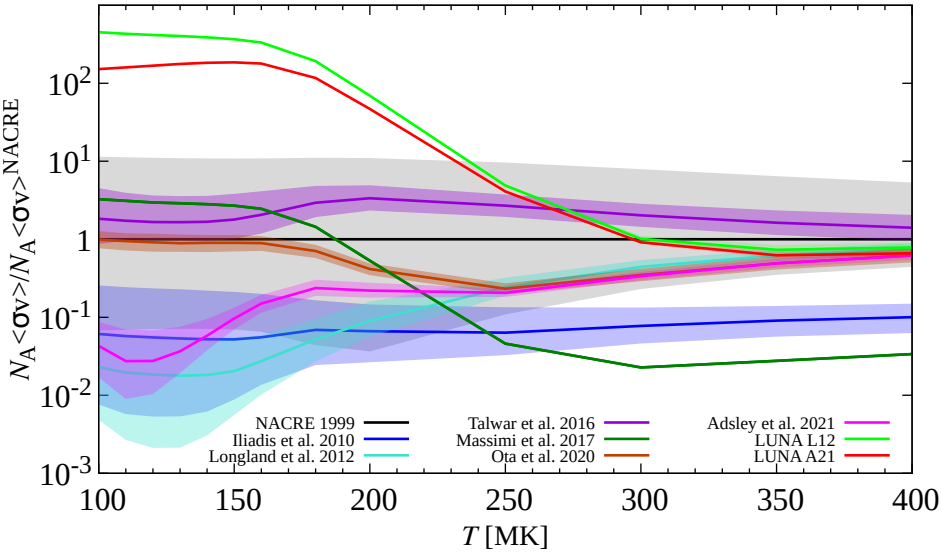

Figure 3.29: LUNA thermonuclear reaction rates of ^{22}Ne$(\alpha,\gamma)^{26}$Mg *reaction as a function of temperature T normalized to the previous NACRE rate [37]. The present results are shown in green (LUNA L12) and red (LUNA A21).*

than all previous literature reaction rates. These discrepancies slow down with increasing temperatures. For temperatures $\sim$ 400 MK, there is a good agreement with several present rates. Using the LUNA rate, the upper limit on the cross-over temperature is estimated. The cross-over temperature corresponds to the temperature where the ^{22}Ne$(\alpha,\mathrm{n})^{25}$Mg reaction dominates the ^{22}Ne$(\alpha,\gamma)^{26}$Mg one. With the present results, the upper limit for the cross-over temperature is 300 MK, higher than the previous values of 200 MK ([45]) and 210 MK ([30]) given in literature. The LUNA result is expected to affect the predicted nucleosynthesis in intermediate-mass AGB stars at temperatures below 250MK.

3.4.7 Astrophysical implications

As described in the previous section, in the present work the LUNA reaction rate based on the Longland 2012 rate [45] and Adsley 2021 [30] are considered. However,

since the last one is very recent and not well included in present stellar models, the astrophysical impact of the $^{22}Ne(\alpha,\gamma)^{26}Mg$ rate, is studied considering the LUNA rate based on the Longland rate [45], hereafter labeled as LUNA UL.
The role of the new LUNA $^{22}Ne(\alpha,\gamma)^{26}Mg$ rate on the synthesis of the neutron-rich magnesium isotopes (^{25}Mg, ^{26}Mg) is studied for a TP-AGB phase intermediate-mass star. In this particular phase, all involved nuclei, ^{22}Ne, ^{26}Mg, ^{25}Mg, ^{26}Mg are produced inside the PDZC developed during the TP He-burning shell. The astrophysical abundance evolution is calculated with the COLIBRI code ([81]) developed to compute the evolution of stars along the thermally pulsing asymptotic giant branch (TP-AGB) phase, starting from the first thermal pulse up to the complete ejection of the stellar mantle by stellar winds.

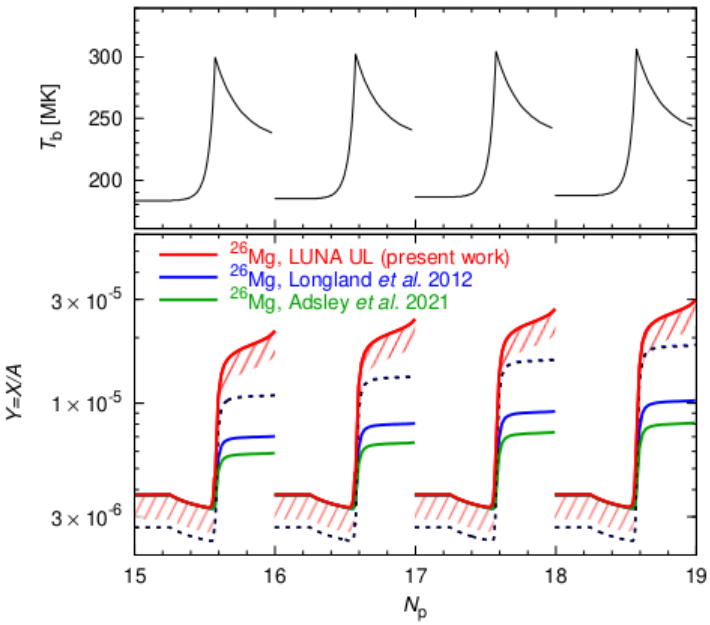

Figure 3.30: Temperature and abundances in the pulse driven convective zone (PDCZ) during thermal pulses of a TP-AGB with initial mass $M = 5M_\odot$ *and metallicity* $Z = 0.014$*. The evolution of the temperature at the base of the PDCZ (top) and the abundances of* ^{25}Mg, ^{26}Mg *during four consecutive thermal pulses (bottom). The dashed line shows the* ^{25}Mg *abundance. Abundances are given as molar fraction* $Y = X/A$*, where* X *is the abundance in mass fraction and* A *the mass number of the nuclide. Red lines are used to clarify that the new LUNA results is an upper limit.*

The calculation has been done considering a star with mass M = 5M$_\odot$ and metallicity z = 0.014. For the same ^{22}Ne$(\alpha, \mathrm{n})^{25}$Mg reaction rate ([82]), the evolution results obtained with the new LUNA ^{22}Ne$(\alpha, \gamma)^{26}$Mg upper limit and the literature rates given in [45] and [30] are compared. In Figure 3.30 the temperature and abundances in the pulse driven convective zone (PDCZ) during four consecutive thermal pulses for the adopted star, for the three ^{22}Ne$(\alpha, \gamma)^{26}$Mg rates are given. The ^{25}Mg, ^{26}Mg abundance shows a decreasing trend at the beginning of the thermal pulse when the temperature is not enough (T_b ∼180 MK) to produce significant Mg. When the $\alpha + ^{22}$ Ne channels are activated ($T_b \sim 300$ MK), the Mg abundances rise rapidly. Using the Longland rate, the ^{26}Mg abundance remains always below the ^{25}Mg abundance. Instead, with the LUNA upper limit the ^{26}Mg abundance exceeds the ^{25}Mg and increases until the end of a thermal pulse. In

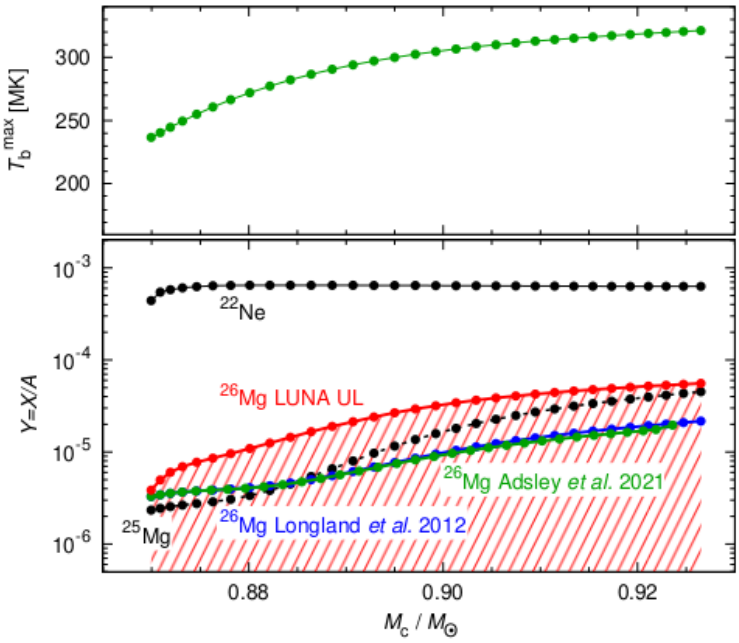

Figure 3.31: Temperature and abundances in the pulse driven convective zone (PDCZ) during thermal pulses of a TP-AGB with initial mass M = 5M$_\odot$ and metallicity Z = 0.014. Maximum temperature at the base of the PDCZ (top) and intershell abundances left at the quenching of each thermal pulses (bottom) as a function of the core mass, over the whole TP-AGB phase (31 TPs). Each point corresponds to one TP. Red lines are used to clarify that the new LUNA results is an upper limit.

the case of the abundance evolution during all 31 thermal pulses given in Figure 3.31, is observed that with the increasing temperature, after $\sim$ 10 thermal pulses the amount of ^{25}Mg obtained using the Longland rate, overcome the initial large amount of ^{26}Mg. With the LUNA UL, the ^{25}Mg remains below the ^{26}Mg until the end of the 31 TPs when they get close. Therefore, it must be taken into account that the choice of the ^{22}Ne$(\alpha,\mathrm{n})^{25}$Mg rate significantly changes the isotope ratio Y(^{25}Mg)/Y(^{26}Mg). The evolution computed with the Longland rate gives an isotopic ratio of $\sim$2 while the one obtained with the new LUNA UL $\sim$0.3.

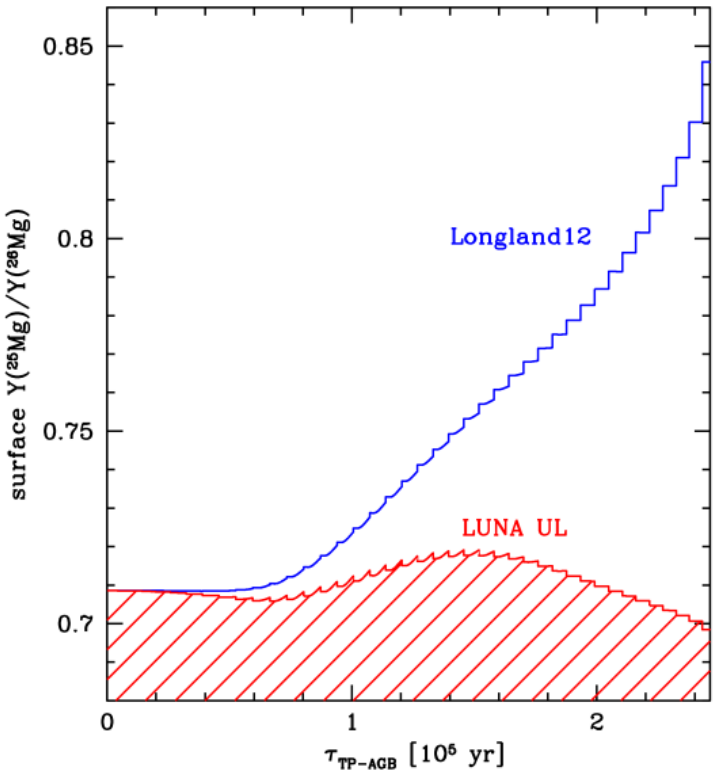

Figure 3.32: Temperature and abundances in the pulse driven convective zone (PDCZ) during thermal pulses of a TP-AGB with initial mass $M = 5M_{\odot}$ and metallicity $Z = 0.014$. Maximum temperature at the base of the PDCZ (top) and intershell abundances left at the quenching of each thermal pulses (bottom) as a function of the core mass, over the whole TP-AGB phase (31 TPs). Each point corresponds to one TP. Red lines are used to clarify that the new LUNA results is an upper limit.

Moreover, with the same star model, the impact of the magnesium isotopes on the surface for both Longland and the new LUNA $^{22}Ne(\alpha,\gamma)^{26}Mg$ rates is studied. Figure 3.32 shows the comparison of the isotopic ratio $Y(^{25}Mg)/Y(^{26}Mg)$ at the surface for Longland and LUNA rate. The TP-AGB model assumed undergoes a moderate third dredge-up and hot bottom burning during the quiescent stages. The different abundances of the ^{25}Mg and ^{26}Mg in the PDCZ affect the surface abundances behavior. On one side the Mg-Al reactions contribute to increase the surface ratio during the interpulses, on the other one during the mixing events the ratio increases (decreases) assuming Longland (LUNA) rate. The isotopic ratio $Y(^{25}Mg)/Y(^{26}Mg)$ obtained with Longland rate rises faster over time since both hot-bottom burning and third dredge-up effect the ratio in the same positive direction.

At the end of the TP-AGB phase, the role of the hot bottom burning is negligible and the isotopic ratio is influenced by the last dredge-up. Therefore, at the end of the TP-AGB phase, the ratio with the Longland rate keeps increasing while the one calculated with LUNA rate decreases. These results show that the isotopic magnesium abundances at the TP-AGBs surface are significantly affected by the $^{22}Ne(\alpha,\gamma)^{26}Mg$ rate which might influence the chemical ejecta from AGB stars as well.

Chapter 4

Study of the $^{20}\mathrm{Ne}(\mathrm{p},\gamma)^{21}\mathrm{Na}$ reaction

What works for one artist doesn't necessarily work for another - try anything and everything and go with what works for you.

Paul Dixon

This chapter reports the study of the 366 keV resonance of $^{20}\mathrm{Ne}(\mathrm{p},\gamma)^{21}\mathrm{Na}$ reaction. The first part introduces the astrophysical motivation. The second summarizes the previous measurements. The experimental apparatus and data acquisition system are given in the third section. In the last part, Monte Carlo simulation, data analysis, and the results are discussed.

4.1 Astrophysical motivations

4.1.1 Neon-Sodium (NeNa) cycle

In stars similar to our Sun, hydrogen fusion proceeds mainly through the pp-chain, which is not affected by the presence of heavier elements. Moving to more massive stars that contain heavier elements and burn at higher temperatures, the heavier elements can catalyse the hydrogen burning. Both carbon-nitrogen-oxygen (CNO) and neon-sodium (NeNa) cycles convert hydrogen into helium in these stellar environments. The CNO is the main responsible for the energy generation in these environments and also opens the possibility of further nucleosynthesis on heavier nuclei. In addition, when hydrogen burning takes place in much hotter environments (T $>$ 0.1 - 1 GK such as in supermassive stars, Novae, RGBs, supernovae outbursts, and accreting neutron stars), the CNO cycle can proceed through the hot - CNO (HCNO) cycle.
On the other hand, the NeNa cycle requires higher temperatures and is characterized by slower reaction rates with respect to the CNO cycle, hence it is less important as an energy production source. However, the NeNa cycle has a crucial

role in the nucleosythesis of elements from ^{20}Ne to ^{24}Mg and opens the nucleosynthetic paths to higher mass isotopes. Both HCNO and NeNa cycles are shown schematically in Figure 4.1. The NeNa cycle begins with ^{20}Ne which can be produced in stellar sites through several phases of burning. As shown in Figure 4.1 the ^{20}Ne isotope can be produced through proton capture on ^{19}F or decay of ^{20}Na isotope, during the HCNO cycle. Furthermore, ^{20}Ne can be produced during helium

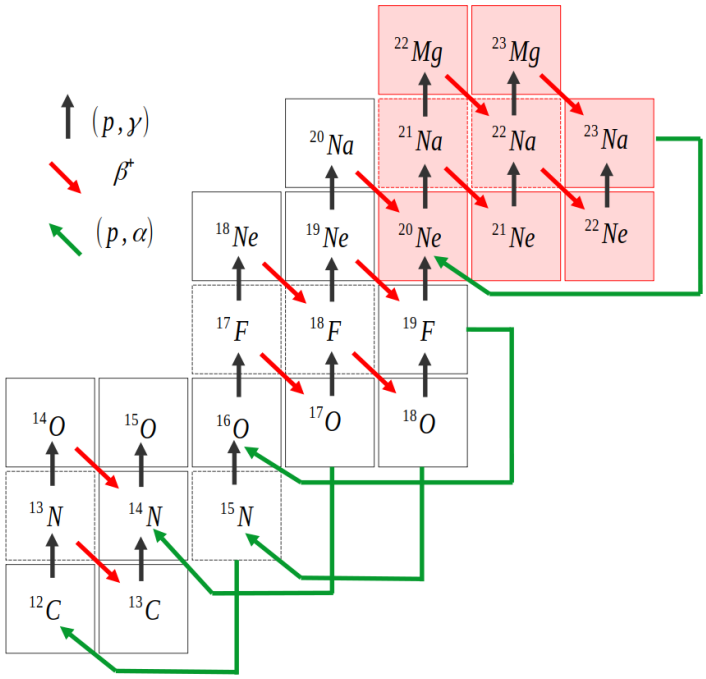

Figure 4.1: Reaction network of HCNO and NeNa cycles. Stable nuclides are represented with solid line boxes, radioactive nuclides by dashed lines. Red boxes indicate the NeNa cycle while the white boxes the HCNO cycle which ends with ^{20}Ne isotope.

burning stages via alpha capture processes in ^{12}C nuclei (^{12}C$(\alpha,\gamma)^{16}$O$(\alpha,\gamma)^{20}$Ne) as well as during carbon burning through ^{12}C$(^{12}$C$,\alpha)^{20}$Ne reaction. However, it should be considered that these last two scenarios have a smaller impact since happen in more extreme stellar conditions with very low reaction rates.
Starting with proton captures on ^{20}Ne isotopes, all NeNa reactions are activated in stellar scenarios characterized different temperature range of interest. To constrain the role of the NeNa cycle, a precise knowledge of the reaction rates of all nuclear reactions involved is required.

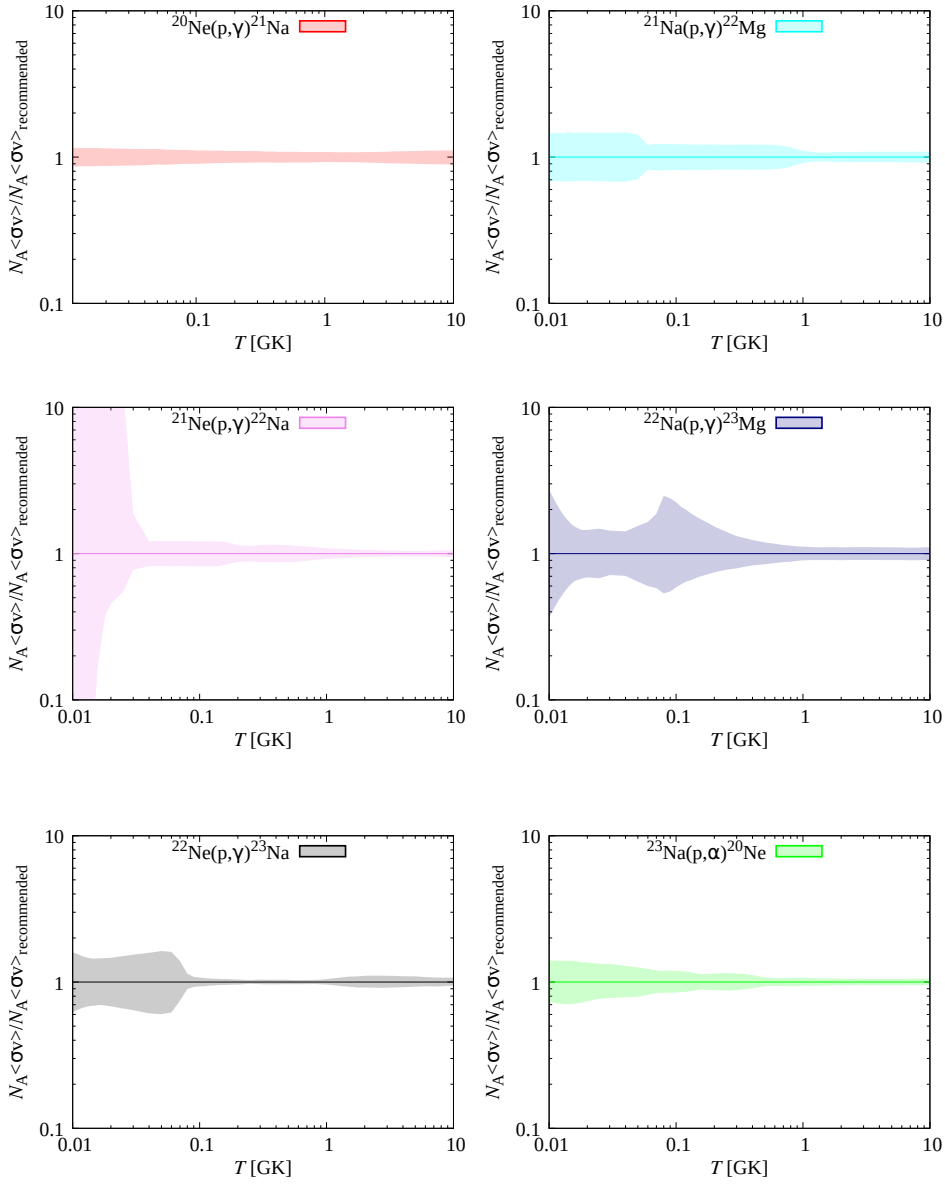

Figure 4.2: Thermonuclear reaction rates for all nuclear reactions involved in the NeNa cycle. The ^{20}Ne(p, γ)^{21}Na *reaction rate was taken from the most recent [83], the* ^{22}Ne(p, γ)^{23}Na *from [84] while the* ^{21}Ne(p, γ)^{22}Na, ^{21}Na(p, γ)^{22}Mg, ^{22}Na(p, γ)^{23}Mg *and* ^{23}Na(p, α)^{20}Ne *rates are taken from [54].*

Figure 4.2 shows the thermonuclear reaction rates involved in the NeNa cycle considering the available literature data [54, 83, 84]. The ^{20}Ne(p,γ)^{21}Na is the slowest reaction of the neon-sodium (NeNa) cycle (total cycle time is about 1.8x10^5 years), and hence it sets the velocity of the entire cycle and constitutes as a bottleneck for the production of ^{22}Na and ^{22}Ne isotopes. Table 4.1 gives a summary of the reaction rates, at a temperature $T = 0.2$ GK, of the reactions involved in the NeNa cycle. The β^+ decay half-lives of the radioactive involved isotopes are also given.

Reaction	β^+ Decay	$T_{1/2}$	$N_A < \sigma v >$ [cm$^3 mol^{-1} s^{-1}$]
^{20}Ne(p,γ)^{21}Na	^{21}Na	22.5 s	4.57x10^{-06} [83]
^{21}Na(p,γ)^{22}Mg	^{22}Mg	3.9 s	1.99x10^{-02} [85]
^{21}Ne(p,γ)^{22}Na	^{22}Na	2.6 y	2.01x10^{-04} [84]
^{22}Na(p,γ)^{23}Mg	^{23}Mg	11.3 s	2.76x10^{-02} [85]
^{22}Ne(p,γ)^{23}Na			3.68x10^{-02} [85]
^{23}Ne(p,α)^{20}Ne			1.47x10^{-02} [85]

Table 4.1: Reaction rates at a temperature $T = 0.2$ GK and half lives of the NeNa cycle. Half lives are from NNDC.

Until a short while ago, the uncertainty of the NeNa cycle was governed by the ^{22}Ne(p,γ)^{23}Na reaction. This reaction was deeply studied at LUNA [70, 31, 69, 86]. Thanks to the LUNA results, together with recent results given in [87, 84], the uncertainties associated with the ^{22}Ne(p,γ)^{23}Na reaction were significantly reduced. Presently the ^{20}Ne(p,γ)^{21}Na and the ^{23}Ne(p,α)^{20}Ne reactions represent the major source of uncertainty. This work is focused on the ^{20}Ne(p,γ)^{21}Na reaction that takes place in several stellar environments such as red giants stars (during H shell-burning), asymptotic giant branch stars, novae, and massive stars, where temperatures can reach $T = 0.5$ GK [88]. An improvement of the knowledge on this reaction can increase the understanding of several astrophysical scenarios.
At the state of the art, the modeling of the O-Na anti-correlation without sodium destruction is still difficult and incomplete [89]. In [90] it was shown that the proton capture on ^{20}Ne nuclei at low energies could explain the observed oxygen-sodium (O-Na) abundance anti-correlation in globular cluster (GC) member stars. On the other hand, a reduction of about a factor of 2-4 in the ^{23}Na(p,α)^{20}Ne reaction cross-section might limit the sodium destruction and solve the observed abundances [91]. Recently, in [87] it was shown that the exit (^{23}Na(p,α)^{20}Ne) and entrance (^{20}Ne(p,γ)^{21}Na) reactions for the NeNa cycle are the least known and the competition between their rates dictates the final abundances of ^{23}Na and hence a better knowledge of both can fix the abundance issues.

4.1.2 Classical novae

The most simple theory of classical novae involves a close binary system where a white dwarf of carbon-oxygen (CO) or oxygen-neon (ONe) composition and a main-sequence star orbit around each other with a period of generally less than 12 hours.
Their close geometry and the extreme gravity of the white dwarf make the hydrogen from the companion star being sucked into an accretion disk and eventually deposited as a hydrogen layer on the surface of the white dwarf. With the matter accreting onto the surface of the white dwarf under degenerate conditions, the temperature and the pressure at the innermost layer of the accretion disk increase enough to ignite nuclear fusion reactions. These reactions rapidly convert the hydrogen into heavier elements and thanks to the quick rise of the temperature, advanced H-burning cycles are ignited as well. The result is a runaway thermonuclear reaction which in turn drives up the rate of hydrogen burning. This process is not instantaneous, hence at some point the temperature rises rapidly without being balanced by an increase in external pressure. During this small amount of time, the matter is violently expelled into the interstellar medium without touching the underlying white dwarf star which remains intact [92].
The classical novae events constitute a natural laboratory where different scientific disciplines merge. Some observations in the nova systems can be explained only by assuming that matter from the outer layers of the underlying white dwarf is mixed with the accumulated matter during or prior to the thermonuclear runaway. This mixing ensures the role of the CNO cycle. Moreover, spectroscopic observations of large neon abundances for the most energetic classical novae, also known as neon novae, confirm these theories.
Their spectra are a fundamental source of information for chemical abundances in the ejecta. The merging of data from optical, UV, and IR spectra has been used to determine the chemical abundances of many elements produced in the novae. The chemical abundances of some elements present in the novae can be used as thermometers for the explosion since the ratios show a strong monotonic dependence on the peak temperature. Several studies ([93, 94]) show that the peak temperature during the H-burning in classical novae is less than 400 MK. The nuclear reactions involved in the CNO cycle are very slow at these temperatures, hence the final abundances stay approximately unchanged during the explosion.
The ^{20}Ne isotope produced during the HCNO remains approximately unchanged as well. Since the ^{20}Ne(p,γ)^{21}Na reaction is very slow at novae temperatures (close to the surface of ONe novae the temperatures are between 0.1 GK and 0.4 GK, E_{cm} = (80 - 300) keV), all initial ^{20}Ne nuclei mixed from the white dwarf into the accreted envelope are not strongly affected during the thermonuclear runaway.

Actually, the large neon abundance observed in the ejecta of neon novae is mainly due to the low proton capture rate on ^{20}Ne and was also the reason that enabled the discovery of ONe novae via emission of the Ne II line.

4.1.3 The O-Na anti-correlation in Globular Clusters

Globular clusters (GCs) are dense, spherical collections of stars, orbiting mostly in the extended star halos surrounding most spiral galaxies. The GCs studies have been of crucial importance for the development of stellar theories since they contain some or the oldest stars in a galaxy. Their age can be determined by their almost complete absence of metals, elements heavier than hydrogen and helium present in the early universe. The estimation of the GCs age provide an evaluation for the age of the galaxy to which the cluster belongs and a lower limit on the age of the Universe as well. Moreover, observations of GCs can constrain stellar evolution models since it is generally assumed that all stars belonging to the cluster formed during a single massive star formation event with the same initial gas composition. There is still work to be done for a better understanding of GCs formation and evolution. Several studies show disagreements between stellar models and observations of GCs. The most classical example of these disagreements is the anti-correlation between elemental O-Na, Mg-Al abundances which have been observed in every GC studied [95]. However, stellar models can not reproduce this situation. This might be explained with a wrong or incomplete astrophysical theory or a lack in the nuclear reaction database required for this particular stellar environment.
The observations suggest that the interstellar medium during the younger cluster star formation was contaminated with the material produced by older stars which evolved and pushed back the synthesized material into interstellar medium ($self - enrichment$). Nevertheless, $self - enrichment$ alone can not describe the stellar objects. Several progenitor models have been proposed to explain GC generations which includes different environments such as massive stars, binary system, rapidly rotating stars and AGB stars. The most suitable sites today seems to be massive AGB stars undergoing hot bottom burning and fast rotating massive stars [97, 98].
To determine which reactions need to be measured for understanding the O-Na anti-correlation, different Monte Carlo post processing nucleosynthesis calculations for TP-AGBs are performed. In [96] a total of 176 nuclear species and 1657 nuclear reactions in their calculations is considered.
In Figure 4.3 the correlation between the final ^{23}Na abundance and the rate of the main reactions that determine the abundance are shown. It can be observed that $^{20}\mathrm{Ne}(\mathrm{p},\gamma)^{21}\mathrm{Na}$, $^{22}\mathrm{Ne}(\mathrm{p},\gamma)^{23}\mathrm{Na}$ and $^{23}\mathrm{Ne}(\mathrm{p},\alpha)^{20}\mathrm{Ne}$ reactions have the largest impact on the final abundance of the ^{23}Na. Since the $^{22}\mathrm{Ne}(\mathrm{p},\gamma)^{23}\mathrm{Na}$ reaction is

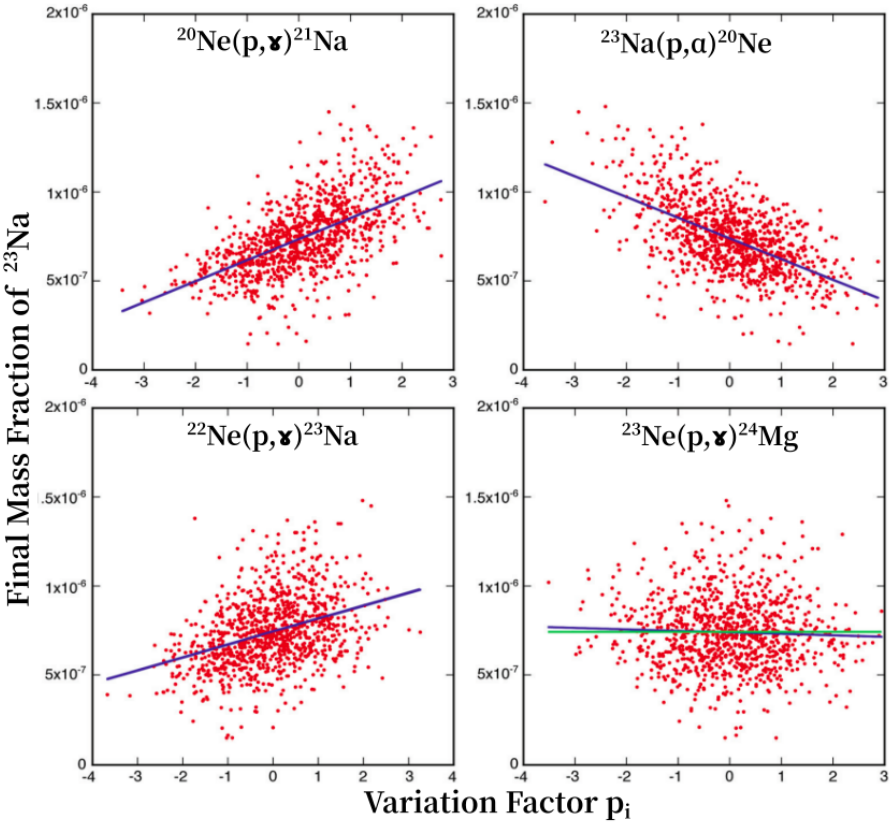

Figure 4.3: Correlations between the final abundance of ^{23}Na *and the rate-variation factor* p_i *for each of the 1000 samples of the reaction network. The blue lines are linear fits to the correlations. Figure taken from [96].*

well constrained with the recent results in [70, 31, 69, 86, 87, 84], the exit and the entrance NeNa cycle reactions become the bottlenecks.

4.2 State of the art

It should be clear at this point that the NeNa cycle as well as ^{20}Ne(p, γ)^{21}Na reaction is of importance to understand better the stellar objects previously described. This work focuses on the the ^{20}Ne(p, γ)^{21}Na reaction with the aim of clarifying its role in the different astrophysical scenarios involved.
In the literature, there are only a few measurements of the ^{20}Ne(p, γ)^{21}Na reaction using both direct and indirect approaches. All these studies cover only the energy region above 370 keV. In the following, the previous studies for the resonance and the non - resonant component are presented.

Tanner et al., 1959 [99]

The ^{20}Ne(p, γ)^{21}Na reaction was measured at E_{cm}= 600 and 1050 keV. The yield of the reaction was observed by delayed counting of ^{21}Na(τ = 23s) positron activities after proton bombardment. The measurements were performed delivering a proton beam onto a solid neon target prepared by bombarding a water-cooled aluminum sheet with 50 keV neon ions. The target was mounted off-axis in order to allow the rotation of the target out of the proton beam and close to the β counter. The detection of the positrons was done through a plastic scintillator mounted in a close-fitting cylinder. The two direct capture cross-sections observed are given in Table 4.2.

E_{cm}[keV]	σ [μb]	S-factor [keV b]
600	$<$0.14	$<$25
1050	1.3$\pm$0.2	17$\pm$3

Table 4.2: Cross section and S-factor for ^{20}Ne(p, γ)^{21}Na at E_{cm} = 600, 1050 keV.

Based on the experimental cross-section at 1050 keV, the extrapolated S_0 reported was about 66 keVb with an uncertainty of a factor of three. In the S_0, the contribution of the resonant capture tail of 2.43 MeV resonance should be considered.

Van der Leun et al., 1964 [100]

The ^{20}Ne(p, γ)^{21}Na reaction was studied at three different resonant energies, 1169, 1955, and 2138 keV. The measurements were performed using the proton beam

coming from the 3.2 MV Van de Graaff accelerator of the Utrecht University and thin ^{20}Ne targets adsorbed on tantalum backing. The emitted γ-rays were detected with 10x10 cm NaI crystals both surrounded by 10 cm of lead shielding.
The ^{20}Ne(p, γ)^{21}Na resonance curve was measured in the energy range between 1.1 MeV and 2.2 MeV with 2-6 keV energy steps, and with the detector located at 55° with respect to the proton beam at 1 cm from the target. Moreover, only transitions from the resonant levels to the ground state and first excited state were considered. Coincidence spectra were also acquired to complete the analysis. The widths and strengths of the resonances are summarized in Table 4.3 For each resonance, γ-ray

E_p [keV]	Γ [keV]	$\omega\gamma$ [eV]
1169 ±2	3.5	1.13 ±0.07
1955 ±4	5.3 ±1.0	4.0
2138 ±5	21 ±3	1.6

Table 4.3: Widths and resonance strengths for the three discussed resonances. The resonance strengths normalized to the resonance strength of 1.13 ± 0.07 eV for the 1169 keV resonance reported in [101].

transitions together with their intensity were determined. In addition to the single and coincidence spectra, the angular distributions at four different angles were determined. For these measurements, one counter-rotated in a horizontal plane around the beam at 10 cm from the target (measuring at different angles), while a second one had a fixed position in a plane perpendicular to the beam either in the horizontal plane or vertically above the target.

Rolfs et al., 1975 [102]

The ^{20}Ne(p, γ)^{21}Na reaction has been studied in the energy range E_p= 0.37 - 2.10 MeV. The measurements were performed using the proton beam delivered by the Van de Graaff accelerator at California State University in an extended windowless gas target with high-purity natural neon gas. The beam current was not measured, but a collimated silicon particle detector was placed at 135° to detect protons elastically scattered. The elastic scattering was used to continuously monitor the combined beam intensity and target density as well as any possible contamination of the target. The recirculating neon gas was purified using an LN_2 trap.
The emitted γ-rays were detected with two Ge(Li) detectors placed at 0° and 90°. Information on excitation energies and branching ratios for states in ^{21}Na were determined. For direct capture transitions, the associated cross-sections, and spectroscopic factors observed are given in Table 4.4 while a summary of several

Transitions [MeV]	$\sigma[\mu b]$	C^2S
DC→ 0	<0.012	<0.04
DC→ 0.33	0.32±0.05	0.77±0.13
DC→ 1.71	<0.007	<0.03
DC→ 2.43	0.63±0.07	0.90±0.10
DC→ 2.80	<0.012	<0.05
DC→ 2.83	<0.006	<0.5

Table 4.4: Direct capture (DC) transitions, cross sections and spectroscopic factors (C^2S) for the $^{20}Ne(p,\gamma)^{21}Na$ at E = 1050 keV [102].

Exitation energy [keV]
332.0±1.0
1716.3±1.3
2425.2±0.4
2797.6±1.4
2829.4±1.4
3544.8±0.6
4175±15
4295±2
2432.3±0.5

Table 4.5: Excitation energies in ^{21}Na and the Q_{value} (last line) for the $^{20}Ne(p,\gamma)^{21}Na$ reaction.

re-measured states is given in Table 4.5. A Q_{value} = (2432.3 ± 0.5) keV and a new resonance at E_p = 384±5 keV (corresponding to 2797.6 keV state) was measured. Based on their experimental results, the authors estimate an astrophysical S-factor of $S(0)$ = 3500 keVb. Instead, assuming the binding energy of E_r = 7.1 keV for the 2425 keV state from their results and using the relation given in [88] for the S-factor ($S(0)= 1.3E_r^{-2}\cdot 10^{14}$ eVb), the astrophysical S-factor resulted $S(0)$ = 2600 keVb. Therefore, the data show fast hydrogen burning of ^{20}Ne into ^{21}Na which decays rapidly in ^{21}Ne.

Keinonen et al., 1977 [103]

The $^{20,21,22}Ne(p,\gamma)^{21,22,23}Na$ reactions have been studied in the energy range E_p = 0.5 - 2.0 MeV. The measurements were performed at the Helsinki University using the proton beam delivered from the 2.5 MV Van de Graaff accelerator on

implanted neon targets.
The emitted γ-rays were detected with a 110 cm^3 Ge(Li) detector (3.2 keV resolution) placed at 55° with respect to the beam direction. The efficiency of the detector was determined using standard sources and ^{27}Al(p, γ)^{28}Si reaction. The targets were prepared by implanting ^{20}Ne$^+$, ^{21}Ne$^+$ and ^{22}Ne$^+$ ions at different energies in the range between 5 and 50 keV into 1.0 mm thick carbon backings. Their composition has been determined using the back-scattered α-particles detected by an annular silicon surface barrier detector (50 mm^2). The ratio Ne/C atoms were about 0.1. With the same technique, the content of the ^{16}O contamination was determined. The relative yields were measured using neon ions implanted on Ta backings. The strengths of the resonances at E$_p$= 1169, 1205 and 1278 keV in ^{20,21,22}Ne(p, γ)^{21,22,23}Na reactions, were determined. In particular, for the ^{20}Ne(p, γ)^{21}Na reaction, a resonance strength of 1.6± 0.3 eV with branching ratio of 95% was adopted. Considering this result, the S-factor extrapolation down to zero energies become $S(0) = 2500$ keVb which resulted in good agreement with the value $S(0) = 2600$ keVb in [104]. The high S(0) indicates fast hydrogen burning of ^{20}Ne.

Mukhamedzhanov et al., 2006 [105]

The ^{20}Ne(p, γ)^{21}Na reaction was studied indirectly using the ^{20}Ne(^{3}He, d)^{21}Na reaction. Both partial width of subthreshold resonance state at an excitation energy of 2425 keV in ^{21}Na and direct capture spectroscopic factor were calculated using the asymptotic normalization coefficient (ANC) formalism [106]. The experiment was performed using 25.83 MeV ^{3}He beam from the U-120M isochronous cyclotron at the Nuclear Physics Institute (Czech Academy of Sciences) impinging on high-purity isotopic ^{20}Ne (99.99%).
The differential cross-section was measured with two ΔE - E telescopes consisting of 220 μm Si surface barrier detectors and 4-mm-thick Si(Li) detectors.
The ANC calculations were extracted from comparison with distorted-wave Born approximation calculation on the experimental cross-section data. The obtained ANC was then used to calculate the DC contribution to the astrophysical S-factor, together with the subthreshold resonance width. The results show an agreement with the previous results in [102].

Lyons et al., 2018 [83]

The direct cross-section of ^{20}Ne(p, γ)^{21}Na reaction was measured in a wide energy range between 500 keV and 2000 keV. The measurements were performed using the 5U-4 accelerator at the Nuclear Science Laboratory at the University of Notre

Dame and a differentially pumped gas target of isotopically enriched ^{20}Ne gas. The emitted γ-rays (transitions to the ground state and to the 332 and 2425 keV excited states were observed) were detected with an HPGe detector (100%), placed at 90°, with respect to the beam, facing the target area.
To determine the contribution of the direct capture and the subthreshold resonance to the total cross-section, an R-matrix analysis on the experimental data was performed. The experimental data, together with the R-matrix results link the direct measurements given in [102] and the indirect measurements in [105]. The improved ^{20}Ne(p, γ)^{21}Na total reaction rate based on these new data showed an overall reduction of 20% with respect to the previous reaction rate libraries [107].

A.L. Cooper, PhD thesis, 2019 [108]

The 384 keV resonance of ^{20}Ne(p, γ)^{21}Na reaction and the direct capture at E_p = 330 keV has been studied at Laboratory for Experimental Nuclear Astrophysics (LENA). The resonance was measured using the proton beam coming from the JN accelerator with energies of 380 - 404 keV impinged on neon targets implanted on tantalum backings.
The measurement of the 384 keV resonance was made both for its astrophysical impact by reducing the uncertainty of the resonance strength with respect to the one given in [102], and to characterize the targets produced.
At each proton energy, the yield of the 373 keV peak was measured through the $\gamma\gamma$ Coincidence Spectrometer of LENA which consists of three detector clusters:

- the HPGe crystal closely positioned at 0° behind the target
- a segmented, angular array of 16 thallium-doped sodium iodide (NaI(Tl)) scintillating detectors
- five plastic scintillator panels that encase the HPGe and NaI(Tl) array on the sides and top

The 384 keV resonant strength was estimated for several targets and a weighted average value of $\omega\gamma = (7.22 \pm 0.68) \cdot 10^{-5}$ eV which disagrees with the value in [102] within 5.5σ was obtained.
The adopted branching ratios compared with previous data are given in Table 4.7. A significant disagreement for the weakest branch (res $\rightarrow$ 331.9 keV transition) is present. Moreover, a dedicated measurement campaign was devoted to the ^{20}Ne(p, γ)^{21}Na total cross-section at 330 keV. At this energy both the direct capture into the 2425 keV resonance and the subthreshold resonant capture into the 2425 keV state contribute to the total cross-section. Due to several background

sources, it was not possible to clearly distinguish the two contributions in the total cross-section. Nevertheless, an upper limit on the contribution of the capture process was given. In conclusion, an average S-factor of $S_{tot}(E^{lab}_{eff}) = (2.84 \pm 0.37)$ keV·b was given at 334 keV proton energy.

J.Karpesky, PhD thesis, 2020[109]

The ^{20}Ne(p, γ)^{21}Na reaction was studied in the inverse kinematics at the DRAGON facility (TRIUMF) in the center of mass energy range 265.5 - 519.6 keV.
The measurement was performed using the ^{20}Ne beam impinging into a windowless gas target. The reaction products were detected with a BGO scintillator array consisting of 30 closely packed scintillation detectors. This array, with an approximately 90% coverage of the total solid angle, allowed the measurement of the prompt γ-rays emitted during radiative capture reactions produced either from emissions from excited recoil nuclei or from the direct capture emissions.

$E_{cm}[keV]$	S-factor [keV·b]
265.5	21.9 (47)
319.0	13.5 (35)
441.9	13.4 (16)
519.6	12.7 (14)

Table 4.6: Total S-factor measurements for the four reaction energies measured at DRAGON [109].

The cross-section and S-factor for the transitions R/DC→0 keV, R/DC→332 keV and R/DC→2425 keV together with the total capture S-factor (Table 4.6) were determined for four different energies. The notation R/DC considers both the resonance and the direct capture component which are not distinguishable. The S-factor extrapolation to zero energies S(0) for the R/DC→0 keV transition resulted in disagreement with the flat behavior given in [102] but in line with the R - matrix results given in [83]. The results suggested a higher than originally expected contribution of the direct capture to the ground state at lower energies.
The S-factor for the different transitions obtained in [109], together with the previous data reported in [110, 83] are shown in Figures 4.4, 4.5, 4.6.

As was previously pointed out, the ^{20}Ne(p, γ)^{21}Na reaction sets the timescale of the NeNa cycle and defines the final abundances of the isotopes synthesized in this cycle. Therefore, precise data on the ^{20}Ne(p, γ)^{21}Na cross-sections together with a deep knowledge of the energy states in ^{21}Na (studied in several works [111,

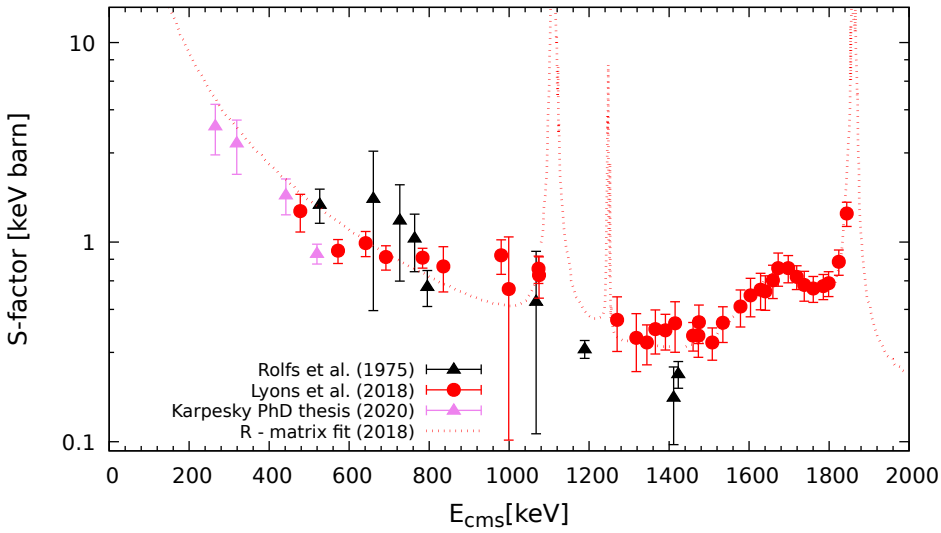

Figure 4.4: S-factor for the $^{20}\mathrm{Ne}(\mathrm{p},\gamma)^{21}\mathrm{Na}$ reaction using the literature data [102, 83, 109]. The data refers to the DC→0 keV transition and are extrapolated from [109].

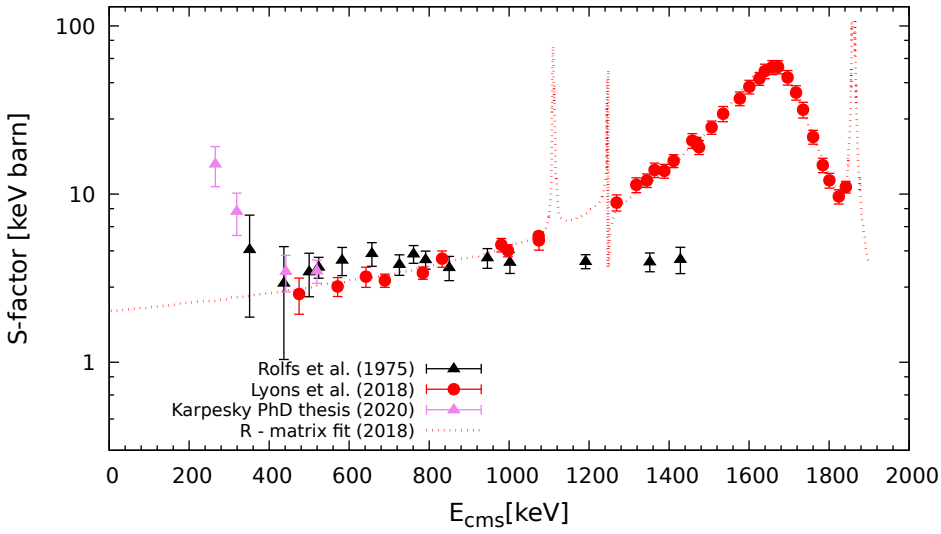

Figure 4.5: S-factor for the $^{20}\mathrm{Ne}(\mathrm{p},\gamma)^{21}\mathrm{Na}$ reaction using the literature data [102, 83, 109]. The data refers to the DC→332 keV transition and are extrapolated from [109].

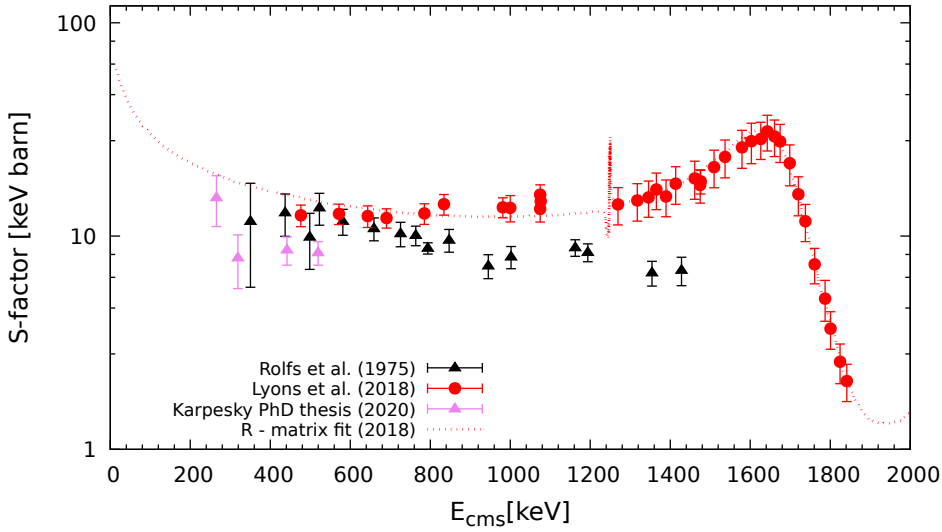

Figure 4.6: S-factor for the ^{20}Ne(p,γ)^{21}Na *reaction using the literature data [102, 83, 109]. The data refers to the DC→2425 keV transition and are extrapolated from [109].*

112, 113, 114, 115]), are crucial for the total reaction rate determination and for a better understanding of the NeNa cycle. Figure 4.7 shows the level scheme for ^{21}Na while Figure 4.8 shows a comparison of the two reaction rates present in literature [37, 83]. The new experimental data given in [83] result in a lower rate at low temperatures and in overall reduction of the rate uncertainty.

Figure 4.9 reports the different contributions to the total reaction rate as a function of the temperature. For temperatures below 0.1 GK, the reaction rate is dominated by the high energy tail of a sub-threshold state at E_R = -6.7 keV and by direct capture component. For temperatures between 0.1 GK and 1 GK, the rate is influenced by the direct capture component and a narrow resonance at E_R = 366 keV which is accessible with the LUNA 400 kV accelerator.

The main goal of this work is the direct measurement of the E_{cm} = 366 keV (E_{lab} = 384 keV) resonance followed by the direct capture [1] measurements below 400 keV where experimental data are not consistent and complete. The E_{cm} = 366 keV resonance corresponds to the exited state E_x = 2797.5 keV which decays emitting different γ-rays.

This resonance was studied in [102] and recently in [108]. A summary of the

[1] During this work only some very preliminary test on the direct capture are performed during Campaign II.

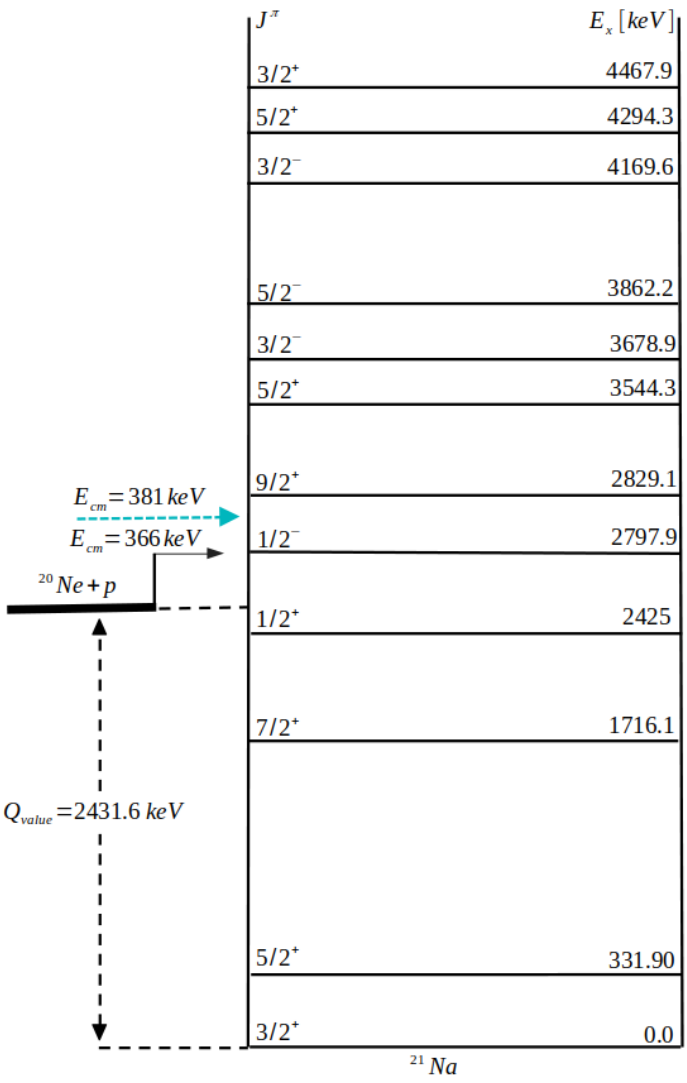

Figure 4.7: Level scheme for ^{21}Na *adopted from NNDC. Turquoise arrow indicates the maximum state achievable with the LUNA 400 kV accelerator.*

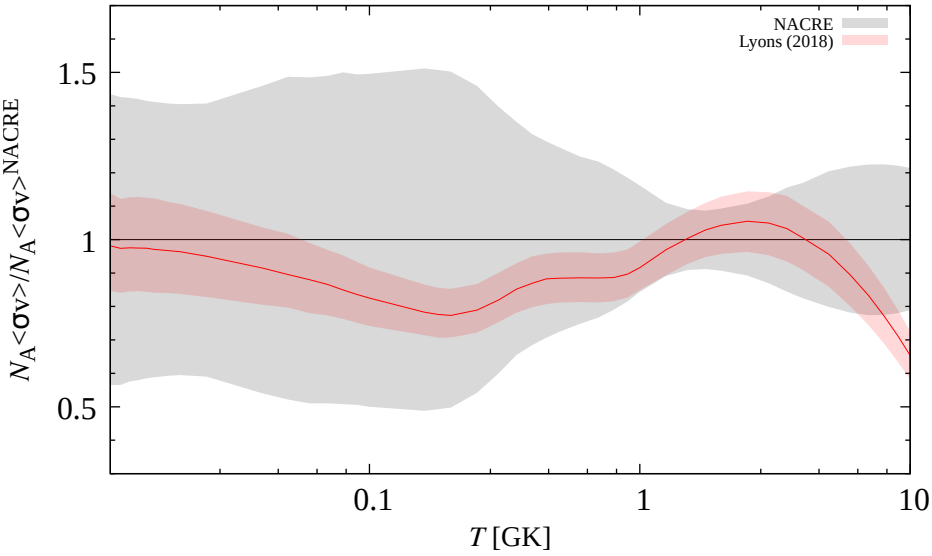

Figure 4.8: Literature ^{20}Ne(p, γ)^{21}Na *reaction rate as a function of the temperature, normalized to the NACRE reaction rate [37]. The shadow region is given by the lower and upper limits.*

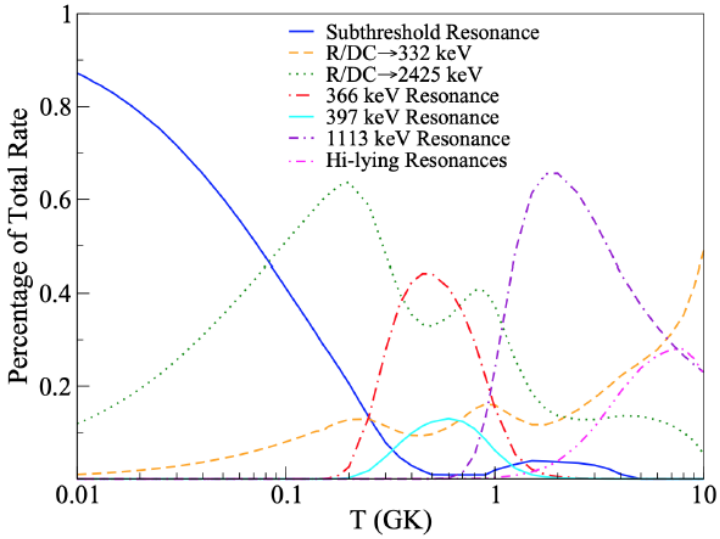

Figure 4.9: Different contributions to the total ^{20}Ne(p, γ)^{21}Na *reaction rate. Figure taken from [83].*

branching ratios and resonance strengths of the two works is given in Table 4.7.

E_i [keV]	E_f [keV]	Br. [%] (Rolfs et al. [102])	Br. [%] (Cooper [108])
2797.5	2425.9	56±4	61.5±7.3
	331.9	11±4	1.6±1.1
	0	33±4	35.9±5.3
$\omega\gamma$ [10^{-4}eV]		1.1±0.2	0.722±0.068

Table 4.7: Comparison between branching ratios for the 366 keV resonance (upper part) and resonance strengths (lower part) [102, 108].

For what concern the resonance energy, a value of $E_{lab} = (384 \pm 5)$ keV was measured in [102] and an evaluation of $E_{lab} = (384.5 \pm 0.5)$ keV was given in [85]. The role of the 366 keV resonance to the total reaction rate in high-temperature environments of oxygen-neon novae (0.1 GK - 0.45 GK) is very important. Discrepancies among different measurements and large uncertainties present in the literature lead to the necessity of new measurements.

4.3 Experimental setup

The study of the 366 keV resonance of ^{20}Ne(p, γ)^{21}Na reaction was performed exploiting the gas target beamline (Section 2.3) combined with a high-resolution HPGe detection system. Two different campaigns of data taking are already completed:

- Campaign I, September - October 2020
- Campaign II, May - July 2021

The experimental setup adopted is similar to the one adopted for the study of the ^{22}Ne(p, γ)^{23}Na reaction [70, 69]. The proton beam from the LUNA 400 keV accelerator was delivered to a dedicated target chamber filled with 2 mbar natural neon gas, through three differential pumping stages as explained in Section 2.3.
The setup used to study the ^{20}Ne(p, γ)^{21}Na is illustrated in Figure 4.10.
It consists of two high-purity germanium detectors: an Ortec low background detector with 90% relative efficiency (shown here also as GeDD) and a Canberra low background detector with 130% relative efficiency (shown here also as GePD). The GePD detector, located below the interaction chamber at 13.9 cm from AP1 collimator, is surrounded by a 4 cm thick copper shielding (in Appendix B a photo of the setup which shows the copper is visible) and a 25 cm thick lead shielding. The copper shielding is needed to reduce the bremsstrahlung γ-rays produced by the

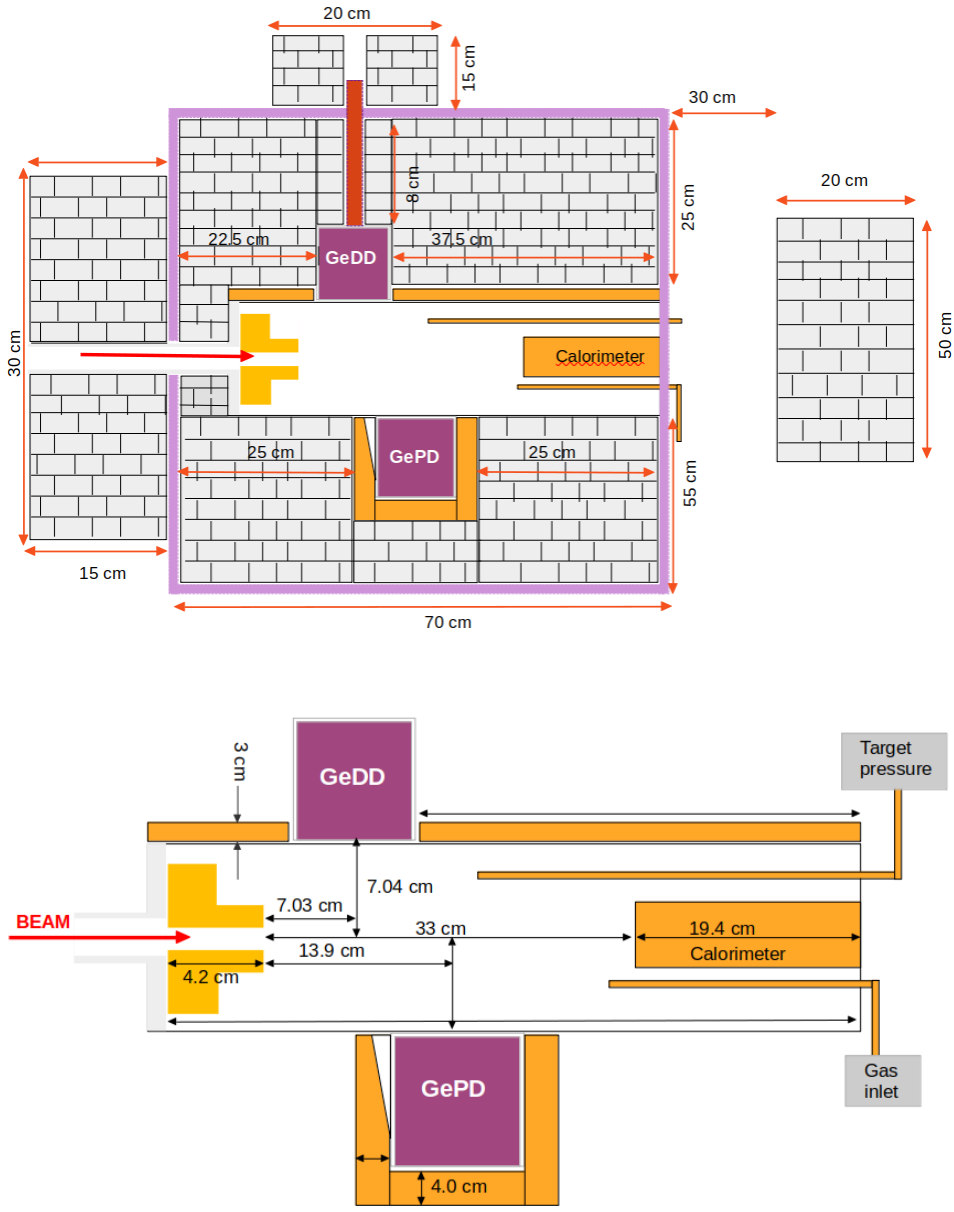

Figure 4.10: Drawing of the experimental setup used for the $^{20}\mathrm{Ne}(\mathrm{p},\gamma)^{21}\mathrm{Na}$ *reaction. The lead bricks and copper shielding (yellow) used are shown. The Radon box is shown by the light-violet box surroundig the lead castle.*

interaction of the electrons emitted in the β-decay of ^{210}Bi inside the lead shielding[2].
The GeDD detector, located on top of the interaction chamber at 7.03 cm from AP_1 collimator, is surrounded only by the lead shielding. Between the lead shielding above the chamber and the chamber, a 3 cm thick copper shielding is used.
The setup enclosed in the lead castle is itself enclosed in a plexiglass radon box shown by the violet line in Figure 4.10, upper part. The radon box establishes an N_2 overpressure around the lead castle and avoids radon gas flushing inside. It also prevents radon gas build-up around the detectors flushing inside the castle the nitrogen exhaust from the GePD detector dewar. Moreover, to avoid the γ-rays produced from the interaction of the beam with the AP_2 collimator, a 15 cm lead shielding between the pumping first stage and the chamber is used. Instead, on the right side, the external lead wall located behind the chamber prevents the detectors from the γ-rays which can reach the chamber through the end-flange.

4.3.1 Electronics and DAQ

For the measurements of the ^{20}Ne(p,γ)^{21}Na reaction, two independent data acquisition systems are adopted: CAEN digital acquisition and the analog multichannel acquisition. The CAEN digital acquisition allows the storage of the single events recorded by the two detectors in list mode configuration. For each event, times-

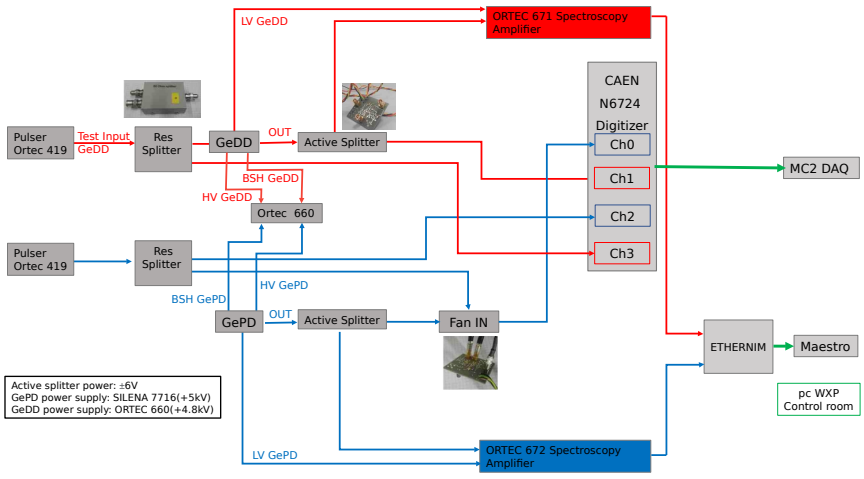

Figure 4.11: Data acquisition scheme for the study of the ^{20}Ne(p,γ)^{21}Na reaction. The signal of GeDD is given in red color while the GPD signal in blue.

[2]It is common to find the radioactive isotope of ^{210}Pb and therefore its daughter ^{210}Bi in the lead shielding.

tamp, energy, and pileup are saved and can be sorted offline according to the required analysis. Instead, the EtherNIM provides directly the detector's spectrum which is useful for a preliminary analysis. A scheme is shown in Figure 4.11.
The signals of the two detectors go to the preamplifiers. Thereafter, the amplified signals are sent to two active splitters (multiple distribution modules) which split the signals in order to link them to each other and to different signal processors. One of the two split signals is sent to an ORTEC Spettroscopy Amplifier (671 for GePD and 672 for GeDD). Spectroscopy Amplifier signals of the two detectors are then sent to an EtherNIM analog multichannel analyzer (4 channels) and ready by Maestro software. The other split signal is sent to a homemade adder to be summed to the pulser signal and then the output of the adder, together with pulser signal alone, is sent to CAEN N6724 digitizer module (4 channels, 14 bit, 100 MS/s) and read by the MC2Analyzer software.
The high voltage of both detectors is given by Ortec 660 module. All the DAQ chain is connected to a crate in the accelerator room which is electrically isolated from their support to avoid mass loops. The Caen module is connected via USB to a computer in the accelerator room which is accessible remotely from the control room. Instead, a second converter connects the Ortec BNC network with the laboratory ethernet which is then accessible from a computer in the control room.

4.3.2 Calorimeter calibration

In Section 2.3.2 the calorimeter and the determination of the beam intensity was introduced. A first preliminary calorimeter calibration for the study of the ^{20}Ne(p, γ)^{21}Na reaction was performed in February 2020, where the setup was not fully completed. Thereafter, before the first measurement campaign in October 2020, a precise calorimeter calibration was performed.
The experimental procedure is the same in both cases. Here a comparison of the calibration curve and the adopted one for the following analysis is given.
The calibration has been done evacuating the target chamber and using the calorimeter as a Faraday cup. During the measurements, the calorimeter and the target chamber were electrically insulated from the upstream. Several runs have been performed varying the proton energy from 50 keV to 380 keV using a current integrator and a counter unit collecting the total charge reaching the calorimeter and the chamber. The calorimetric measurement of the power delivered by the beam is given by

$$W_{cal} = W_0 - W_{beam} \tag{4.1}$$

where W_0 is the average value of the zero power, acquired before and after each run, while W_{beam} is the power delivered when the beam is on. The calorimetric

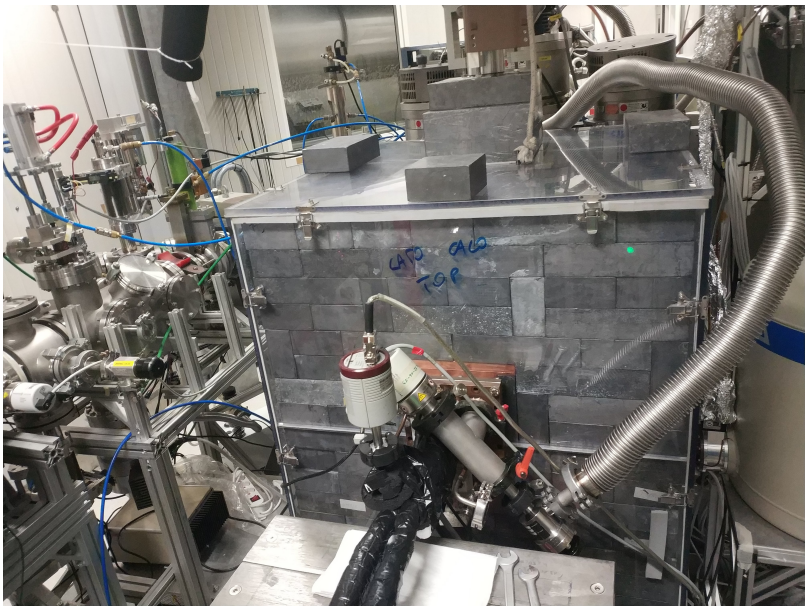

Figure 4.12: Improved setup for the calorimeter calibration. The valve mounted at the calorimeter which allows the evacuation of the gas from the first stage can also be observed.

electric power is calculated for each run as:

$$W_{el} = \frac{E_{beam} I_{target}}{q_e} \tag{4.2}$$

The W_{el} as a function of W_{cal} were fitted with the linear function given in Equation 4.3:

$$W_{el} = mW_{cal} + q \tag{4.3}$$

where m is the calibration function slope and q is the intercept.
Compared to the calorimeter calibration performed in February 2020, in October an additional valve mounted directly to the calorimeter (Figure 4.12) and connected to the first stage allows a 10^{-5}mbar vacuum in the chamber. To improve even more the vacuum in the chamber, during the calibration the collimator was dismounted. In October 2020 an energy range from from 50 to 390 keV was covered. The beam current was stable and higher (I>450μA) with respect to the beam intensity achieved in February. To allow the calorimeter to work properly with higher current, the hot side was keept at 80 °C and the cold side at -15°C. For the zero power long runs before and after the measurements were taken.
The same linear function given in Equation 4.3 was used to fit the W_{el} data as

a function of W_{cal}. The fit of the results of both calibrations are given in Figure 4.13, together with the residuals less than 1% (less than 1.5 %) for the data set in October 2020 (February 2020), while the calibration coefficients are given in Table 4.8 Moreover, together with the calibrations above, an additional calibration using

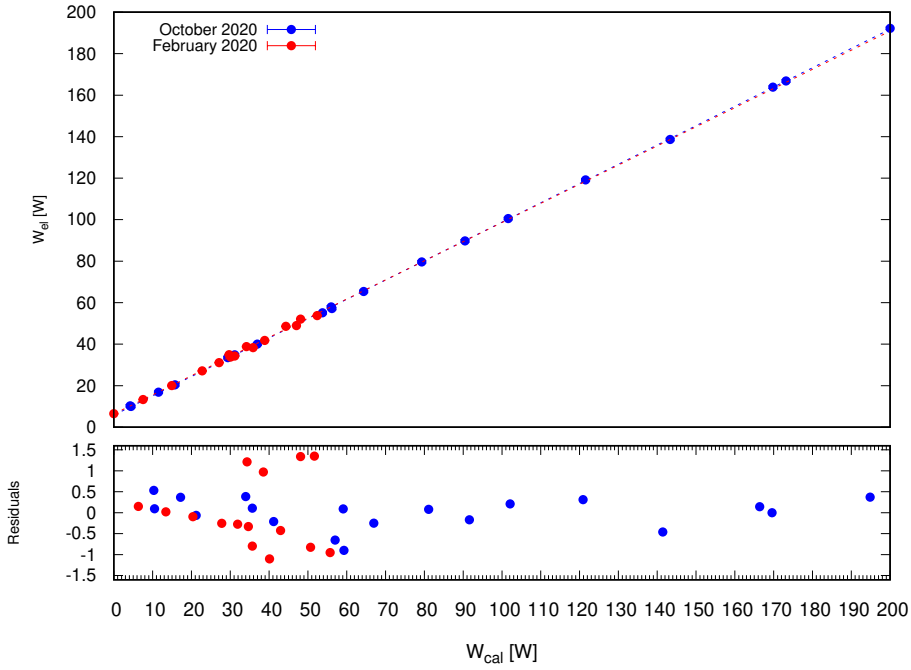

Figure 4.13: Comparison of two different calorimeter calibrations: February 2020 and October 2020. Calorimeter calibration function (top) and relative residuals (bottom). The error bars are smaller than the point dimension.

together the data in February and October was also performed. The results are given in Table 4.8 while the data are given in Appendix B.2

Data set	Calibration slope	Calibration offset	χ^2/ndf
February 2020	0.98±0.02	0.14±0.6	1.626/13
October 2020	0.988 ±0.003	-0.4±0.3	2.835/19
Feb. + Oct. 2020	0.986 ±0.002	-0.2±0.1	0.738/34

Table 4.8: Calorimeter calibration coefficients for different data-set.

The data analysis for the ^{20}Ne(p,γ)^{21}Na reaction has been done using the calibration curve obtained in October 2020.

4.4 Data analysis

4.4.1 Detection efficiency

In an extended gas target, the interaction with the beam takes place in different positions along the beam axis and the emitted γ-rays are seen at different angles from the detectors. The γ-energy region of interest for the ^{20}Ne(p,γ)^{21}Na reaction is up to ∼3 MeV. Therefore, taking into account that the detection efficiency depends on the γ energy and on the position of the emission, the detection efficiency has been measured at several positions along the beam axis, in a wide energy range with uncertainties of less than 1% at the top of the detectors. After Campaign I the setup was dismounted for several tests on the GePD detector and other technical issues, hence, the efficiency has been calculated separately for each campaign. For simplicity, the efficiency approach shown here considers the data from Campaign II and then a summary of the final efficiency needed for the ^{20}Ne(p,γ)^{21}Na analysis in the different campaigns will be given. The experimental data are combined with Geant3 simulations which will be described in Section 4.4.2. The detection efficiency at low energies has been measured with standard calibrated sources and thereafter the detection efficiency is extended to higher energies using the ^{14}N(p,γ)^{15}O reaction at the well-known E$_p$= 278 keV resonance. A guideline of the approach used for efficiency determination is described in the following:

1. Mount the sources (^{60}Co, ^{137}Cs, ^{133}Ba) one by one in the source holder which allows to have the same physical conditions as during the ^{20}N(p,γ)^{21}Na measurements.

2. Measure the efficiency $\eta(z)$ as a function of the distance from the collimator reaching ∼ 1% statistical uncertainty.

3. Apply summing corrections for ^{60}Co and ^{133}Ba sources (Paragraph 4.4.1). For this purpose is required the total efficiency which depends from the ratio between the counts in the peak and the total number of counts in the spectrum. The peak-to-total is deduced from Geant 3 simulations.

4. Perform a fit in the ln − ln scale(energy, efficiency) with the experimental points measured. In the general case the function is given by:

$$\ln\eta(E) = \sum_{i=0}^{n} a_i \left(\ln E\right)^i \tag{4.4}$$

the a_i coefficients are determined using χ^2 fitting method. The polynomial degree depends on the number of the experimental data.

5. Measure the scan for the ^{14}N(p,γ)^{15}O resonant reaction at E_p= 278 keV and determine the beam energy which corresponds to the maximum yield.

6. Perform two high statistic measurements at the maximum yield for each detector

7. Calculate the ratio between primary (1384 keV, 765 keV) and secondary (6171 keV, 6790 ke) γ-ray and apply summing corrections.

8. Derive the detection efficiency for the 765 keV and 1384 keV from the fit function obtained with sources.

9. Determine the efficiency for the 6171 keV and 6790 keV γ ray

10. Perform a fit in log-log scale (energy, efficiency) with low and high energy data derived from the ^{15}N(p,γ)^{15}O reaction.

11. Use the obtained function to calculate the efficiency for γ of interest.

Low energy efficiency

The low energy efficiency is measured using three point-like radioactive sources: ^{60}Co, ^{137}Cs and ^{133}Ba. For each source, the efficiency along the beam axes with steps of 0.5 - 1 cm has been measured. The main properties of the sources are summarized in Table 4.9. For these measurements, dedicated source holders consisting of central PVC frame were designed. The source holders were able to hold the sources at the same height as the center of the AP1 collimator. Since the geometry of the ^{60}Co (^{137}Cs) and the ^{133}Ba is different, the ^{133}Ba source holder was designed in a such way to have the center of the sources at the same position in the chamber. Figure 4.14 shows the source holder mounted in the long movable flange which allows the positioning of the source in different positions along the chamber. The absolute full-energy peak efficiency is obtained as the ratio between the measured net peak area and the number of γ-rays emitted at the same energy in the whole solid angle by a radioactive source. The efficiency is given by Eq. 4.5:

$$\eta_\gamma = \frac{N_\gamma}{A(t^*)\Delta t Br} \tag{4.5}$$

where N_γ is the number of detected γs in the time period Δt, Br is the branching ratio of the emitted γ and $A(t^*)$ the source activity at the time of measurement t*. The $A(t^*)$ is determined using the reference data of the activity given in Table 4.9 and the decay law:

$$A(t) = A_0 e^{\frac{t-t_0}{\tau}} \tag{4.6}$$

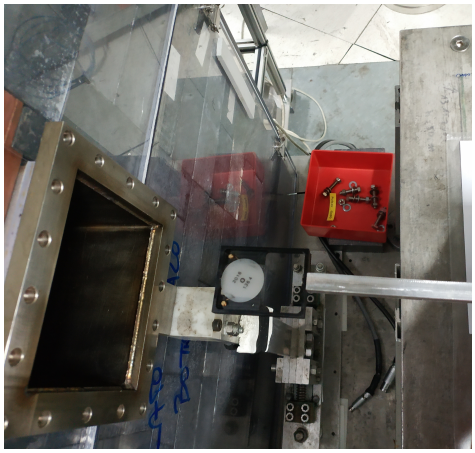
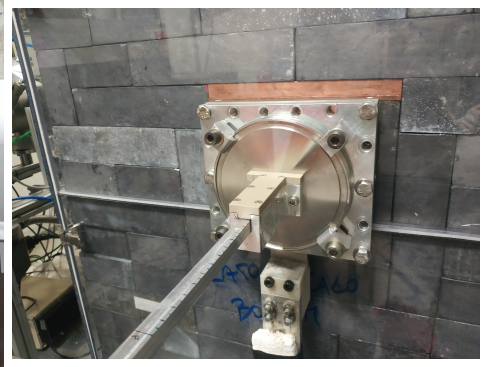

Figure 4.14: Left panel: ^{60}Co source mounted on the dedicated source which is fixed to a long movable flange. Right panel: movable holder fixed to the back flange of the chamber as in the final measurement configuration.

Source	Ref. date	A_0 [kBq]	$T_{1/2}$ [year]	E_γ [keV]	Br %
^{137}Cs	1/7/16	6.46 ± 0.04	30.08 ± 0.09	661.66	85.10
^{60}Co	1/7/16	9.001±0.04	5.2711± 0.0004	1173.23	99.85
				1332.49	99.9
^{133}Ba	4/11/19	28.36±0.03	10.55±0.1	276	7.16
				302	18.33
				356	62.05
				383	8.94

Table 4.9: List of most intense γ-rays emitted in the decay of the radioactive sources used for the low energy efficiency measurement. For ^{133}Ba source only the γ-lines used for the efficiency has been reported.

where A_0 is the certified activity at time t_0 and τ is the isotopic mean life time.

Figure 4.15 shows the experimental detection efficiency as a function of the source distance from the AP1 collimator for GePD and GeDD detector. For a fixed position in the chamber, corresponding to the maximum efficiency for each detector, the efficiency as a function of the γ energy measured with radioactive sources has

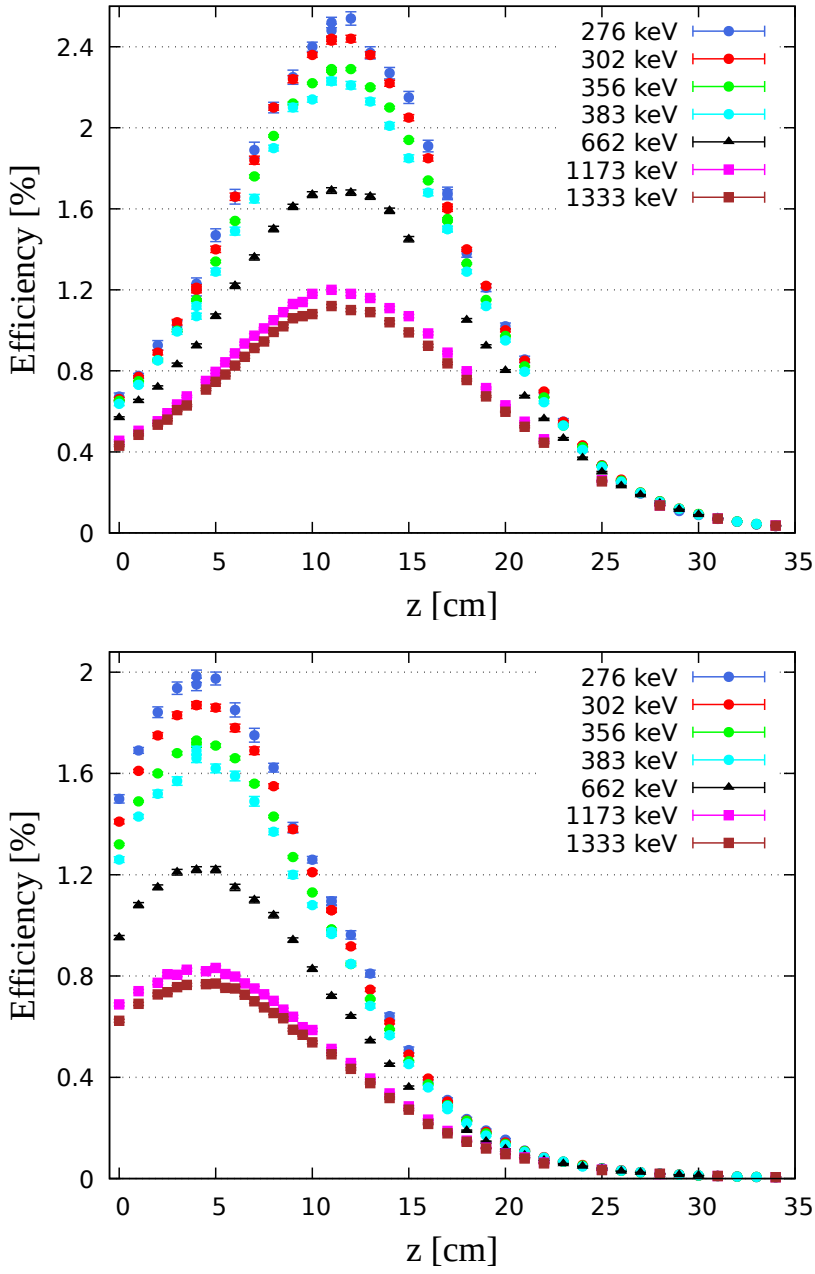

Figure 4.15: Efficiency as a function of the distance from the AP1 collimator measured moving the three sources along the beam axis. Top: GePD. Bottom: GeDD.

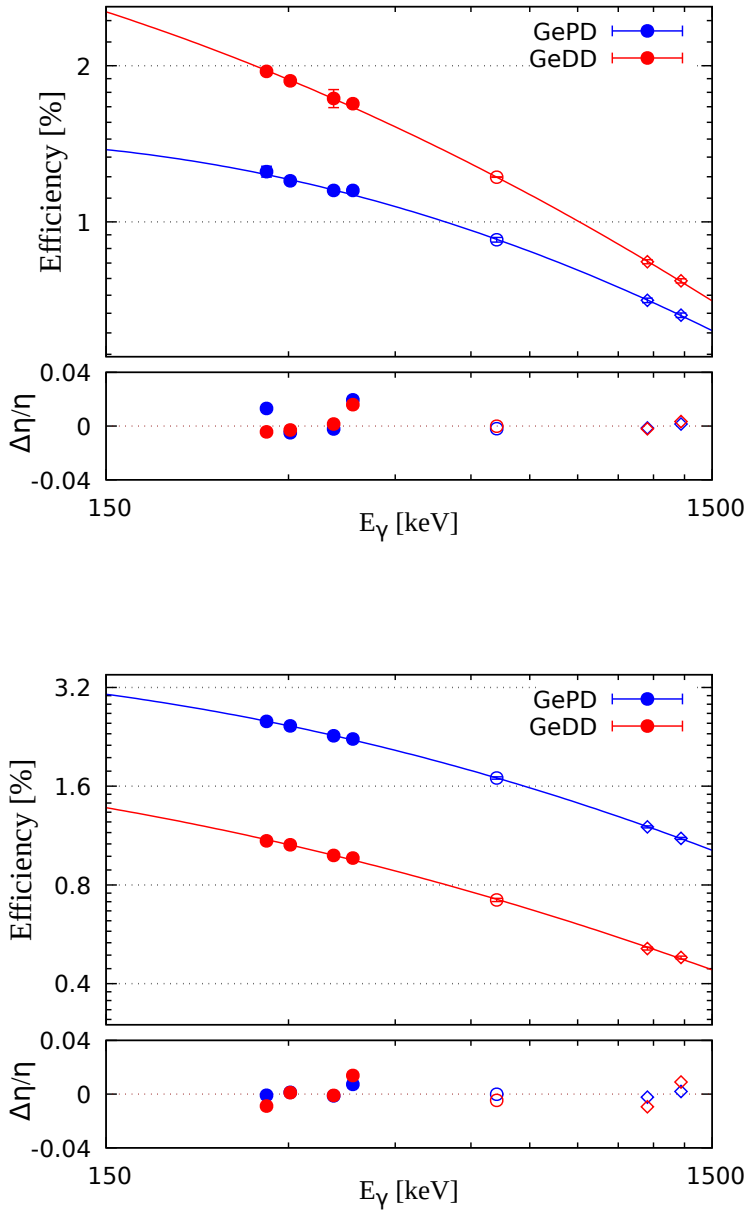

Figure 4.16: Efficiency as a function of the γ-ray energy for both detectors at z = 6 cm from the AP_1 collimator (top) and z = 11 cm (bottom). Full circles, empty circles and empty squares represents the ^{133}Ba, ^{137}Cs and ^{60}Co data, respectively. Error bars are within the points.

been reported. The efficiency versus energy is fitted with the function in Eq. 4.7:

$$\ln(\eta_\gamma) = a + b \cdot \ln(E_\gamma) + c \cdot \ln^2(E_\gamma) \tag{4.7}$$

Figure 4.16 shows the efficiency data versus energy together with the fit function and the residuals for both detectors. The fit parameters for each detector at two different position in the chamber are reported in Table 4.10.

	GePD detector		GeDD detector	
Par.	z = 6 cm	z = 11 cm	z = 6	z = 11 cm
a	-1.54±0.03	-0.08±0.02	0.9±0.1	0.06±0.03
b	0.866±0.008	0.727±0.005	0.391±0.002	0.427±0.007
c	-0.0986±0.0008	-0.0976±0.0005	-0.0769±0.0003	-0.0748±0.0007

Table 4.10: Fitting parameters for the efficiency curve measured with radioactive sources.

High energy efficiency

The detection efficiency was extended to the high energy region using a relative approach through the measurement of ^{14}N(p,γ)^{15}O reaction at E_p= 278 keV resonance. The resonance is characterized by a well-know resonance strength of $\omega\gamma$ = (12.8 ± 0.5) meV, a width Γ = (0.99 ± 0.3) keV and decays through different cascades reported in Table 3.4.

To achieve a point-like source configuration as much as possible, the ^{14}N(p,γ)^{15}O reaction was measured with a target pressure of 4 mbar[3]. Under these conditions, the energy loss of the proton beam is ∼1.3 keV/cm and the resonance width became ∼0.8 cm. The resonance was measured by changing the proton beam energy in 1-2 keV steps to populate the resonance at different positions in the target. Thereafter, a long run at the maximum detection efficiency for each detector has been measured. Figure 4.17 shows the measured resonance scan for the different γ-rays emitted in the ^{14}N(p,γ)^{15}O reaction. The resonance is characterized by two high energy γ-rays (6171 keV, 6790 keV) accompanied by two γ-rays in the low energy range covered by the radioactive sources (1384 keV, 765 keV).

Using the 1:1 ratio between primaries and secondaries γ-rays, the detection efficiency for the high energy gammas can then be determined by Eq. 4.8:

$$\eta(E_\gamma^h) = \eta^{fit}(E_\gamma^l) \cdot \frac{N_{E_\gamma^h}}{N_{E_\gamma^l}} \tag{4.8}$$

[3]This pressure still allows the pumping system to work safely.

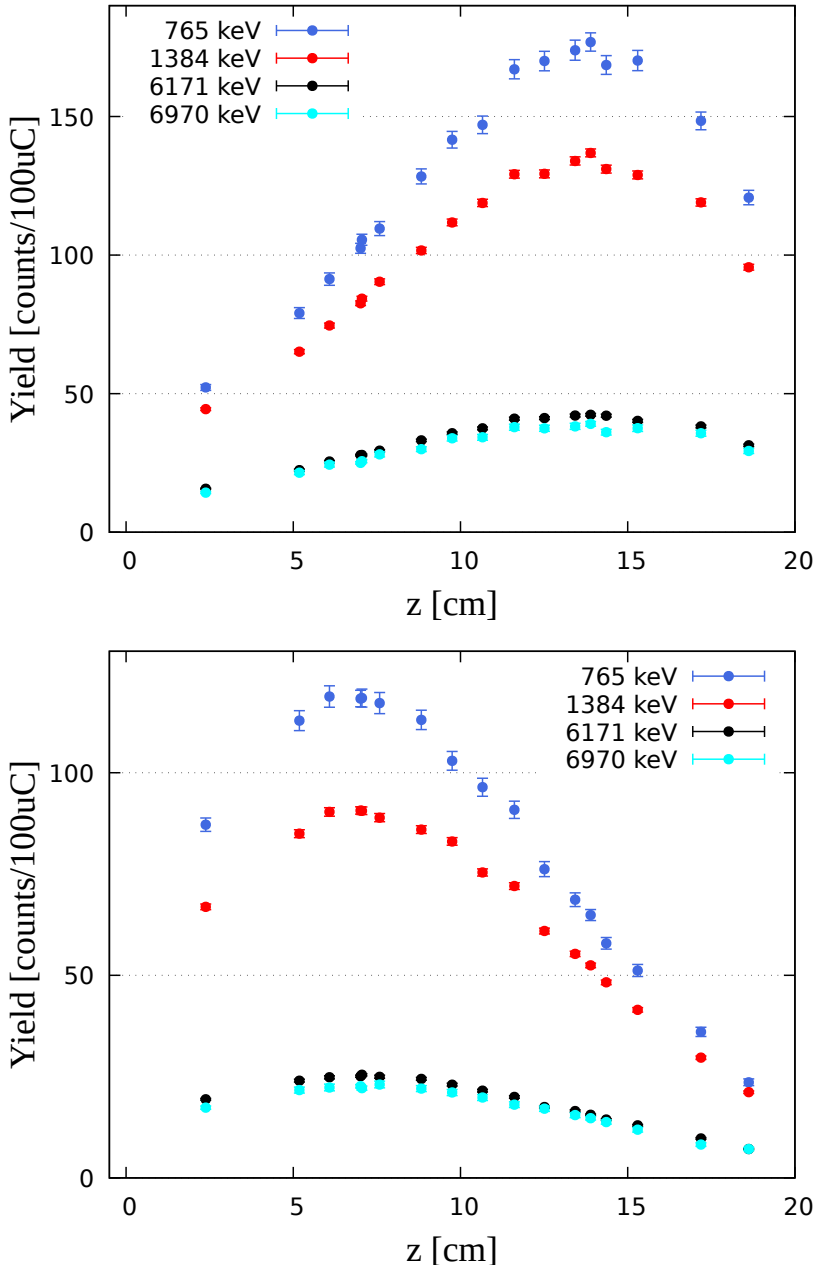

Figure 4.17: $^{14}\mathrm{N}(\mathrm{p},\gamma)^{15}\mathrm{O}$ *resonance scan as a function of the distance from the* AP_1 *collimator for GePD (top) and GeDD (bottom) detectors.*

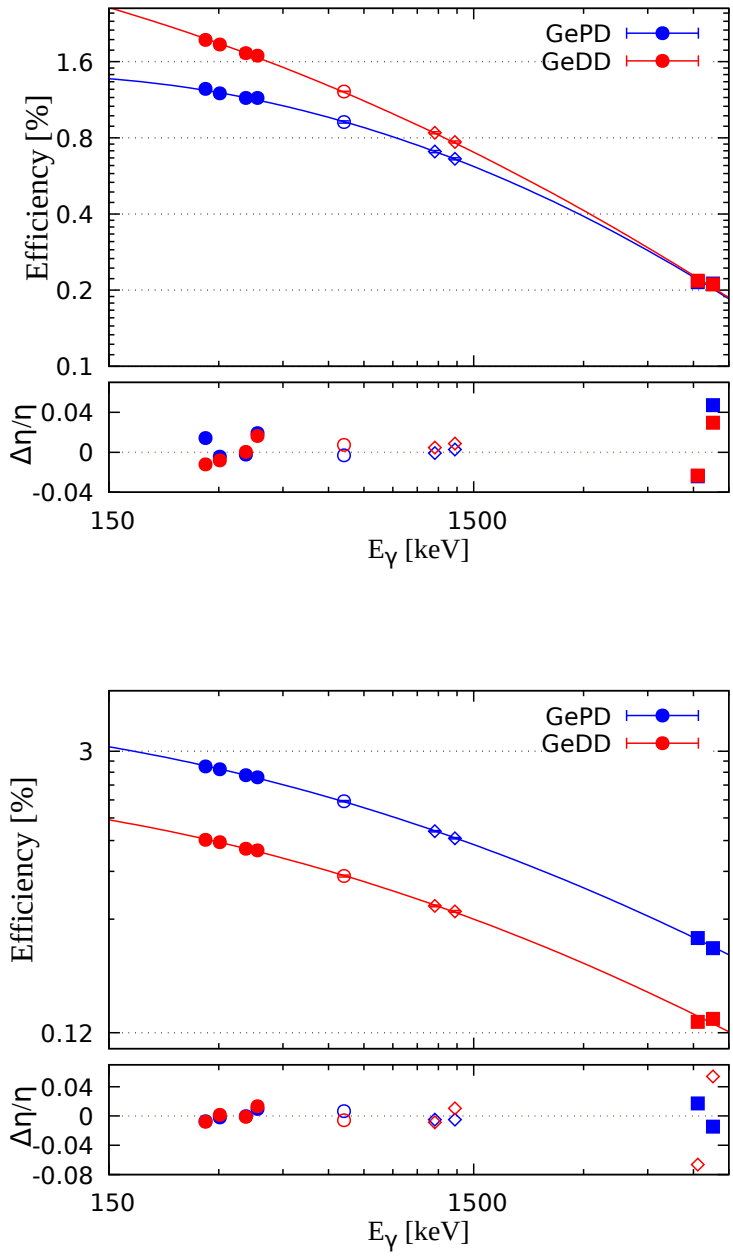

Figure 4.18: High-energy detection efficiency at z = 6 cm from the AP_1 collimator (top) and z = 11 cm (bottom). Full circles, empty circles, empty squares and full squares represents the ^{133}Ba, ^{137}Cs, ^{60}Co *and* ^{14}N(p,γ)^{15}O *data, respectively.*

where $\eta(E_\gamma^h)$ is the detection efficiency for the high energy gamma (6171 keV, 6790 keV), $\eta^{fit}(E_\gamma^l)$ is the efficiency for the corresponding low energy gamma which is calculated from the low energy fit function, and $N_{E_\gamma^l}$, $N_{E_\gamma^h}$ are the net counts for the low and high energy γ-rays. The efficiency function is obtained by using in Eq. 4.7 the two high energy γ efficiency ($\eta(6171)$, $\eta(6171)$) calculated from relation given in Eq. 4.8. Figure 4.18 shows the data and the fit of the total efficiency up to ∼7 MeV while Table 4.11 report the fit parameters.

	GePD detector		GeDD detector	
Par.	z = 6 cm	z = 11 cm	z = 6	z = 11 cm
a	-1.7±0.3	0.8±0.1	1.5±0.2	-0.09±0.3
b	0.92±0.07	0.45±0.04	0.22±0.05	0.5±0.1
c	-0.102±0.005	-0.076±0.003	-0.064±0.003	-0.078±0.007

Table 4.11: Fitting parameters for the efficiency curve up to ∼ 7 MeV.

Summing-out corrections

In the case of ^{60}Co and ^{133}Ba sources, the decay is characterized by two or several γ-rays. The same behaviour is present in the decay of 7.555 MeV level of ^{14}N(p, γ)^{15}O reaction. In all these cases (i.e emitted γ-ray is part of a cascade), if the lifetime of the intermediate excited state is shorter than the time resolution of the detector, the photons are detected as a single photon with energy the sum of the energies of the two individual photons. This effect, known as true coincidence summing effect causes loss of counts in the full energy peak of interest and a loss of efficiency. The summing effect depends on the probability that two (or more) photons emitted simultaneously will be detected simultaneously which is a function of the geometry. The further the source is from the detector, the less probable it is that the two γ-rays will be detected together. Taking into account the summing effect, the detection efficiency can be expressed by Eq.4.9:

$$\eta_1 = \frac{N_{net1}}{A \cdot Br_1(1 - \eta_{2,T} W(0))} \tag{4.9}$$

where η_1 is the full energy peak efficiency for γ_1, N_{net1} is the net peak area for γ_1, Br_1 is the branching, $\eta_{2,T}$ the total efficiency for the second γ-ray to be detected and $W(0)$ the angular correlation, the probability of the two gamma rays being emitted in the same direction.
The probability W(θ) is fixed by the conservation of the angular momentum and

can be shown as the sum of Legendre polynomials:

$$W(\theta) = P_0(\cos\theta) + a_2 P_2(\cos\theta) + a_4 P_4(\cos\theta) \tag{4.10}$$

where a_2 and a_4 are the angular distribution parameters, specific for each photon emitted by sources or reactions, P_0, P_2 and P_4 are the first three even-order Legendre polynomials determined by Eq. 4.11

$$\begin{cases} P_0(\cos\theta) = 1 \\ P_2(\cos\theta) = \frac{1}{3}(\cos^2\theta - 1) \\ P_4(\cos\theta) = \frac{1}{8}(35\cos^4\theta - 30\cos^2\theta + 3) \end{cases} \tag{4.11}$$

The theoretical angular correlation coefficients for ^{60}Co have been adopted from [116], the ^{15}O coefficients from [117] and the ^{133}Ba correction has been calculated using the a_2 and a_4 coefficients from [118]. The resulting angular corrections are given in Table 4.12.

Source	$W(0)$
^{60}Co	1.167
^{133}Ba	0.96
6.17	1.11
6.79	1.13

Table 4.12: Angular correlation used for the summing-out corrections.

The total detection efficiency $\eta_{2,T}$ ($\eta_{i,T}$) has been determined using Geant 3 Monte Carlo simulations. For this purpose, the experimental setup shown in Figure 4.10 has been implemented in Geant 3 in order to study the detection efficiency and further analysis on the reaction. (More details in Section 4.4.2). First, the Monte Carlo simulation was tuned to match sources data (^{60}Co, ^{137}Cs) at different position in the chamber, and high detection efficiency data (^{14}N(p,γ)^{15}O reaction).
Thereafter, the experimental and simulated peak-to-total ratios for all radioactive sources and the relative discrepancy between the two have been determined. For non monochromatic sources, the peak-to-total is calculated as the sum of the two peak areas divided by the total area under the spectrum.
Once verified that the experimental spectrum was correctly reproduced by the MC simulation and that the simulated peak-to-total ratio was comparable with the experimental one, individual point-like sources emitting a single gamma ray of the energy of interest has been simulated. An uncertainty of 20% to the peak-to-total ratio has been considered.

The total detection efficiency has been determined as the ratio between the experimental photopeak efficiency and the simulated peak-to-total ratio (Eq. 4.12):

$$\eta_{2,T} = \frac{\eta_2^{exp}}{(P/T)^{sim}} \tag{4.12}$$

The experimental photopeak efficiency corrected for the summing-out is determined by using Eq. 4.12 and Eq. 4.9. Table 4.13 shows the efficiency curve parameters using the data corrected by summing effect.

	GePD detector		GeDD detector	
Par.	z = 6 cm	z = 11 cm	z = 6	z = 11 cm
a	-1.8±0.3	0.7±0.1	1.5±0.2	-0.2±0.3
b	0.93±0.07	0.48±0.03	0.22±0.05	0.4±0.1
c	-0.102±0.005	-0.077±0.002	-0.063±0.004	-0.074±0.009

Table 4.13: Fitting parameters for the efficiency curve up to ∼ 7 MeV corrected by summing effect.

4.4.2 Monte Carlo simulations

The experimental setup has been implemented in the Geant 3 simulation written in FORTRAN in order to complete the detection efficiency and to better define the experimental conditions for the study of the ^{20}Ne(p, γ)^{21}Na reaction. In particular I choice this old version of Geant since various effects due to the beam passing through the target gas, such as the beam energy spread, have been implemented and already validated in several LUNA experiments [119, 11, 120]. The nuclear case of the ^{20}Ne(p, γ)^{21}Na reaction was implemented as well.
A side view from the Geant 3 geometry of the ^{20}Ne(p, γ)^{21}Na setup is shown in Figure 4.19. Instead in Figures B.2 and B.3 (Appendix B) a perspective and beam view of the geometry is given. Since there is a slight margin in the position of the individual pieces of the setup, a preliminary tuning of the geometry implemented in Geant 3 code was needed. The implemented geometry was fined-tuned with the standard sources: ^{60}Co and ^{137}Cs. To achieve this, the sources have been simulated inside the chamber at fixed positions along the beam line reproducing the experimental spectra. For each position the simulated efficiency given by Eq. 4.13 was compared with the experimental efficiency calculated in Eq. 4.5.

$$\eta_{sim}(E) = \frac{N_{net}}{N_{events}} \tag{4.13}$$

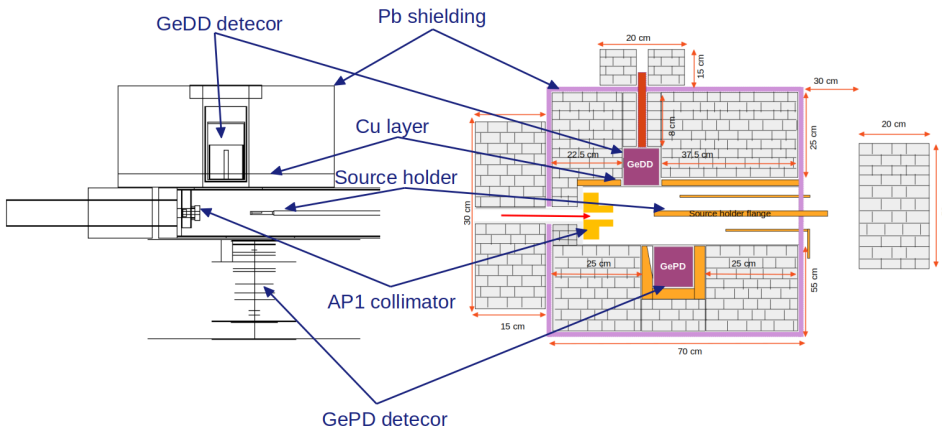

Figure 4.19: Side view of Geant3 geometry (left) and a drawing of the adopted for the ^{20}Ne(p,γ)^{21}Na *setup (right).*

where N_{net} and N_{events} are the net counts in the full energy peak and the total number of simulated events, respectively. The best agreement between the simulations and the experiment is obtained by adjusting reasonably the following parameters in the code:

- Position of the detectors along the beam line
- The distance of the detectors from the beam line axis
- The distance of the Cu and Pb shielding from the chamber and from the detectors
- The dead layers of the detectors

In Figure 4.20 a comparison of the experimental and simulated efficiency for both detectors are shown. Except for the far distances where the efficiency itself is very low, the simulations are in a good agreement with the experimental data. For both detectors the discrepancies between simulations and experiment are below 3%. A comparison of the experimental and simulated spectra for the standard sources and the ^{14}N(p,γ)^{15}O reaction are shown in Figure 4.21. Once validated, the Monte Carlo simulations were used to determine the peak-to-total ratio necessary for the summing corrections needed for the detection efficiency (Section 4.4.1).

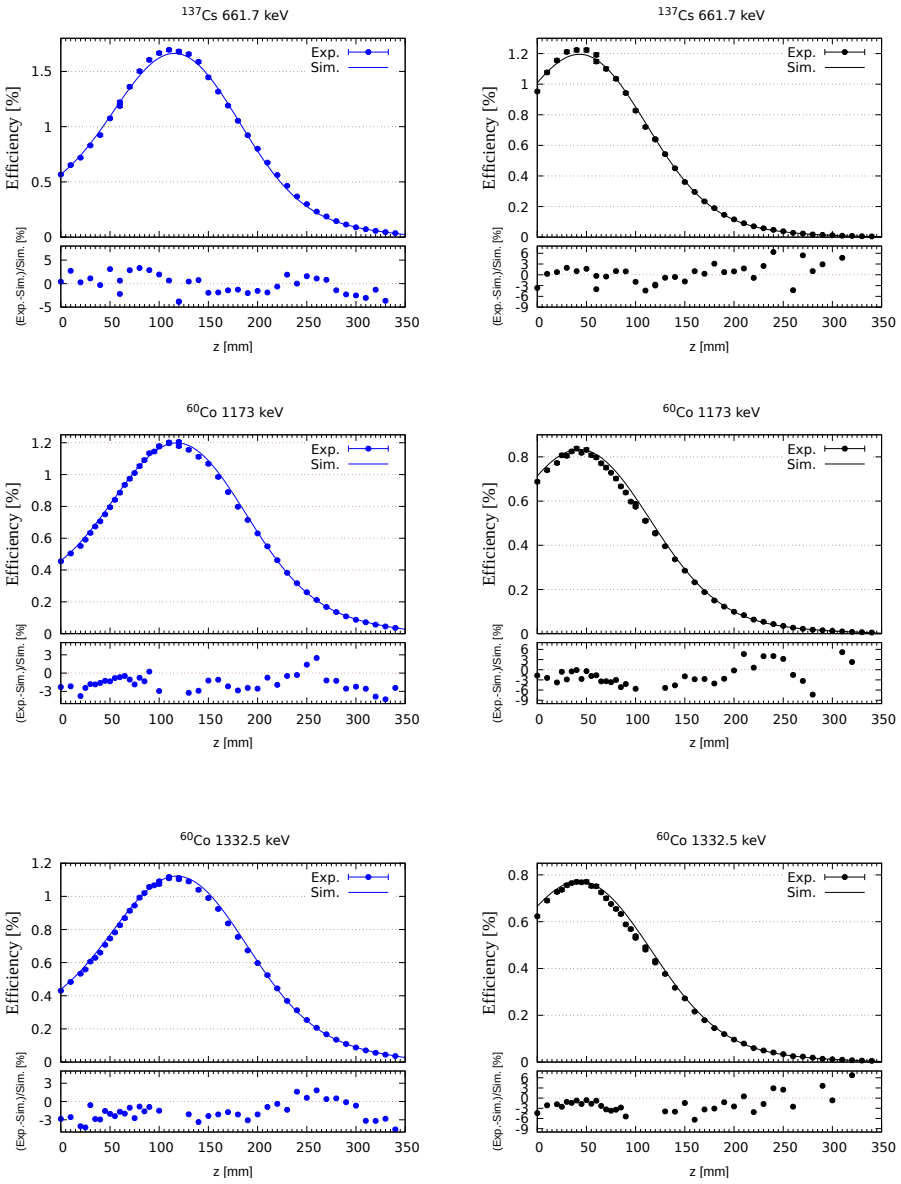

Figure 4.20: Comparison of experimental efficiency with the fit of the simulated one for GePD (blue) and GeDD (black). The residuals are shown as well.

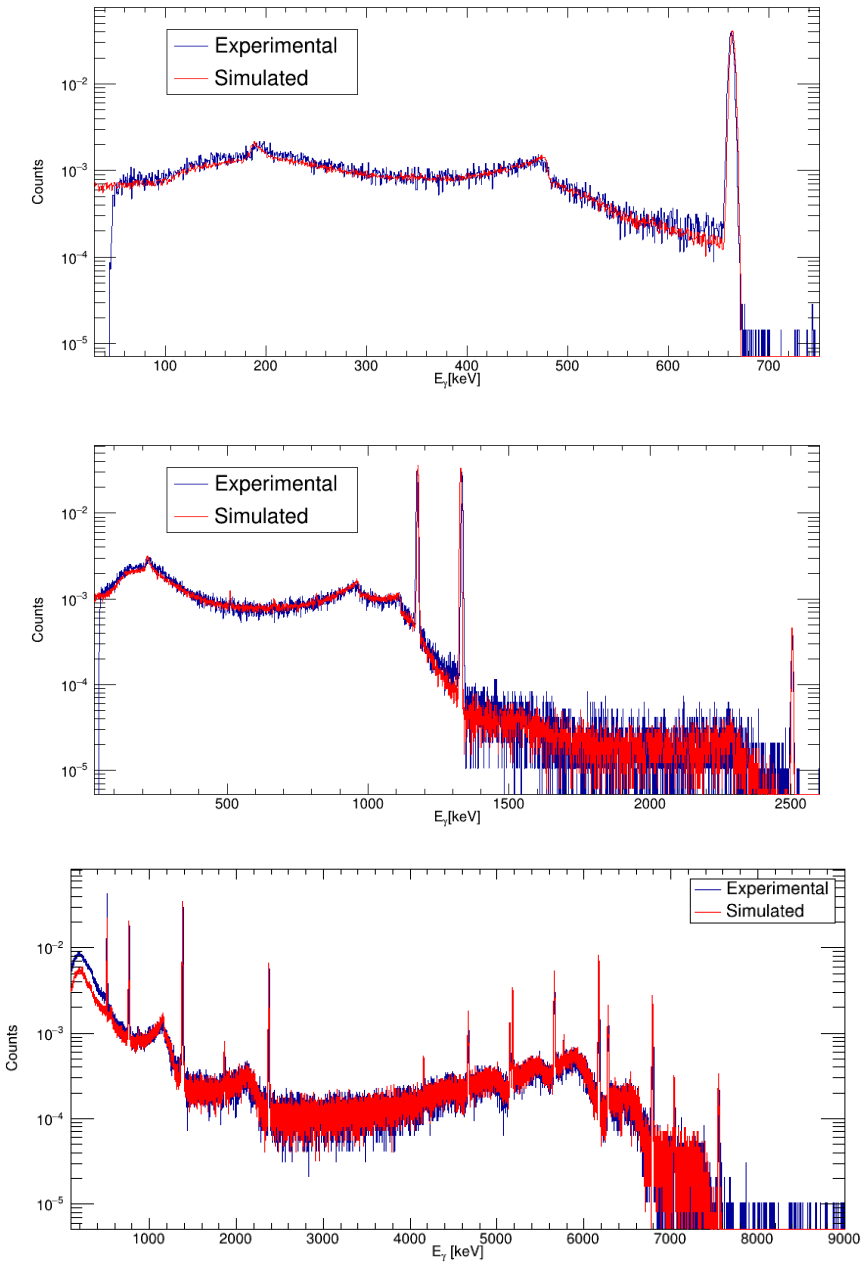

Figure 4.21: Comparison between simulated and experimental $^{137}\mathrm{Cs}$ *(up),* $^{60}\mathrm{Co}$ *(middle) and* $^{14}\mathrm{N}(\mathrm{p},\gamma)^{15}\mathrm{O}$ *reaction (down). The three spectra are normalized to the total area.*

4.5 366 keV resonance measurements

The measurements on the $E_{r,cm}$ = 366 keV resonance were performed filling the target with natural neon gas at 2 mbar. The nominal pressure was chosen as the best compromise taking into account the beam energy spread through the target and the count rate estimations [4]. The resonance was studied both in Campaign I and Campaign II through several data-taking runs in the energy interval from 386 keV to 400 keV, in steps of 1-2 keV. During Campaign I, a long run at the beam energy of maximum yield for the two detectors was performed. Thereafter, for each long run, beam-induced background runs with argon gas were performed as well. For technical reasons, this approach was not adopted in Campaign II where the available beam intensity and hence the total integrated charge was lower with respect to the data-taking in Campaign I. Therefore the final results here presented are determined considering information from both campaigns. In particular, the branching ratios were calculated only from the Campaign I at the high statistic runs, while the estimation of the resonance strength was determined in both campaigns.

Typical spectra taken at the maximum detection efficiency for GePD detector during Campaign I and Campaign II are show separately in Figure 4.22 and Figure 4.23, respectively. In Campaign I (Figure 4.22), all primary transitions are well visible while in Campaign II, due to low statistics, the weaker transitions (332 keV $\rightarrow$ g.s and 2798 $\rightarrow$ 332 keV transitions) are not observed in neither of the two detectors.

The experimental yield was calculated using Eq. 3.19 for each proton energy and for each detector considering all observed transitions. The beam intensity, and hence the total charge has been evaluated using the approach given in Section 3.4.3. The necessary corrections on the gas density are estimated from measurements performed during ^{22}Ne(p,γ)^{23}Na HPGe campaign at LUNA [69, 70] for the present experimental conditions.

In more details, during Campaign I the yield curve for 2798 $\rightarrow$ 332 keV, 2798 $\rightarrow$ 2425 keV, 2425 keV $\rightarrow$ g.s and 2798 keV $\rightarrow$ g.s transitions were obtained while in Campaign II the transition 2798 $\rightarrow$ 332 keV is not observed. Figure 4.24 shows the excitation function determined from the data of Campaign I, for all observed transitions and for each detector.

The fluctuations observed in the yield curve are mainly due to the pressure instabilities (variation between 1.9 to 2.3 mbar from run to run) during the resonance scan measurements. These fluctuations are even more pronounced in the weaker transition (2798 $\rightarrow$ 332 keV) yield curve where the count rate is lower. Neverthe-

[4] A dedicated Monte Carlo study was performed before the experimental campaign in order to better define the experimental conditions.

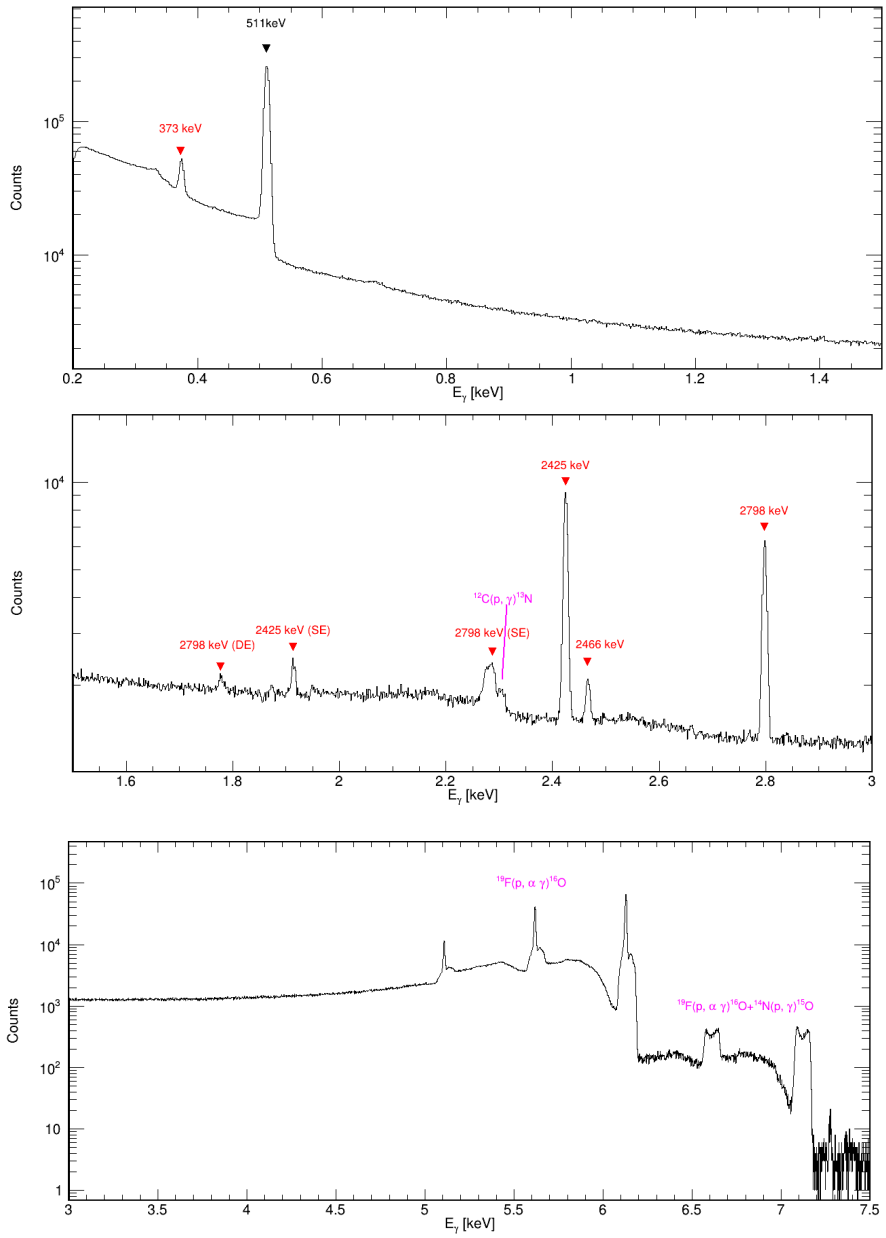

Figure 4.22: Typical $^{20}\mathrm{Ne}(\mathrm{p},\gamma)^{21}\mathrm{Na}$ *spectrum taken at* $E_p = 395$ *keV with GePD detector during Campaign I. The gamma transitions of the reaction are marked in red, while in magenta the main beam induced background sources. (SE) indicate the single escape peak for some of the transitions while (DE) the double escape.*

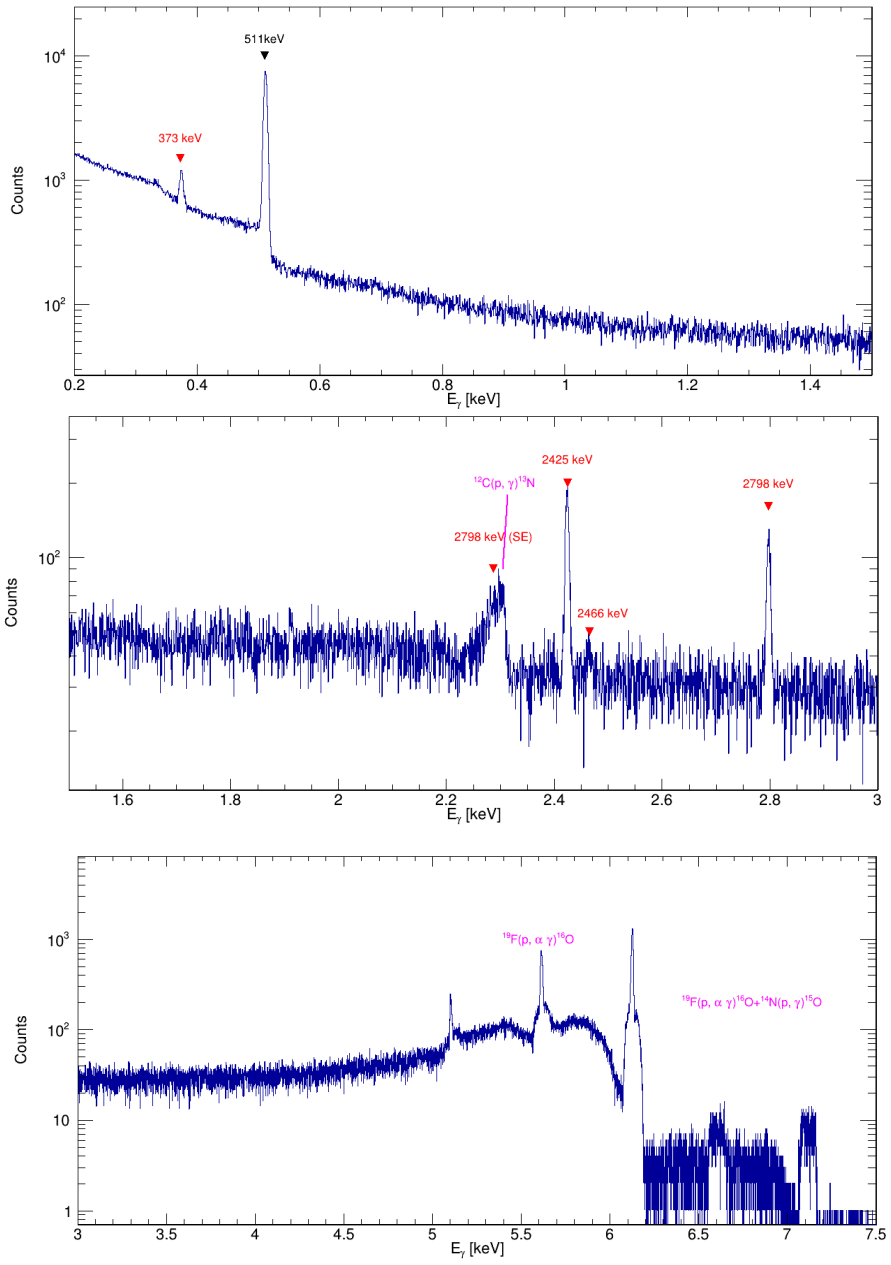

Figure 4.23: Typical $^{20}\mathrm{Ne}(\mathrm{p},\gamma)^{21}\mathrm{Na}$ *spectrum taken at* $E_p = 394$ *keV with GePD detector during Campaign I. The gamma transitions of the reaction are identified in red, while in magenta the main beam-induced background sources. (SE) indicates the single escape peak for some of the transitions.*

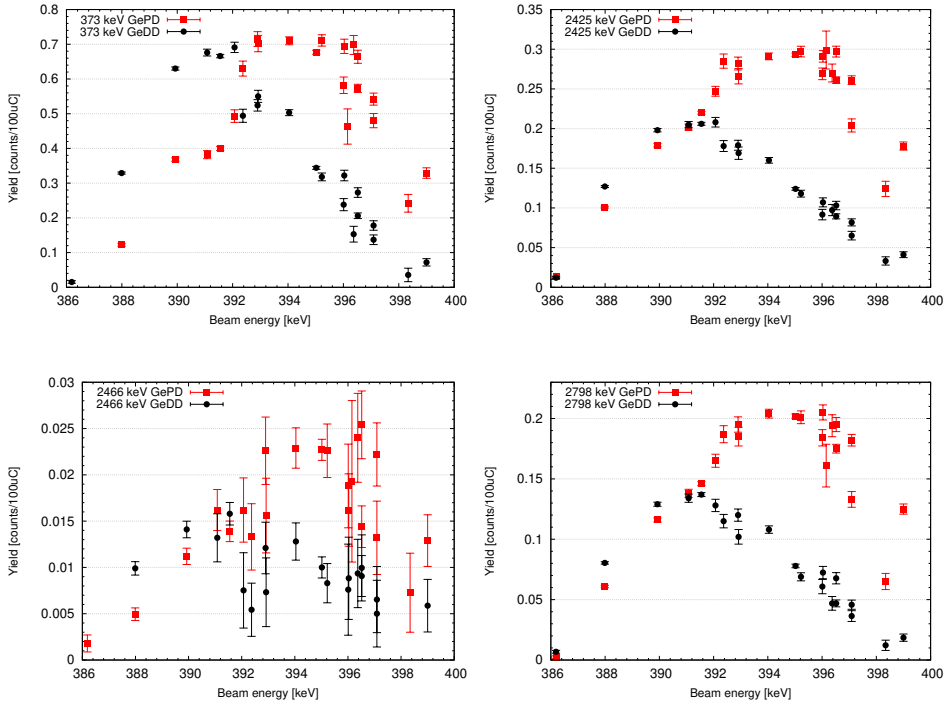

Figure 4.24: Yield curve for the observed transitions measured during Campaign I with GePD (blue) and GeDD (red).

less, the yield functions from Campaign I allowed to define the resonance plateau energy region. At this region, two long runs corresponding to the maximum detection efficiency for the GePD (E_p= 395 keV) and GeDD (E_p= 391 keV) detector have been performed. At the same energies, additional beam-induced background measurements were performed as well. To avoid all these fluctuation effects on the analysis, from Campaign I, only the high statistic data complemented by the BIB measurements were considered. After some improvements in the setup during

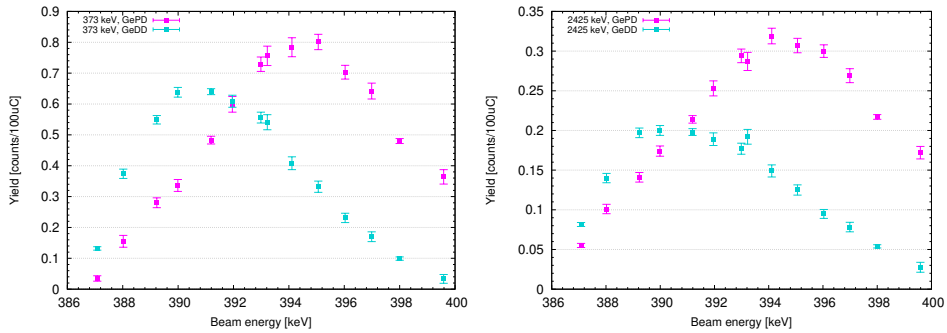

Figure 4.25: Yield curve for the 2798 → 2425 keV, 2425 keV → g.s transitions measured during Campaign II with GePD (magenta) and GeDD (turquoise).

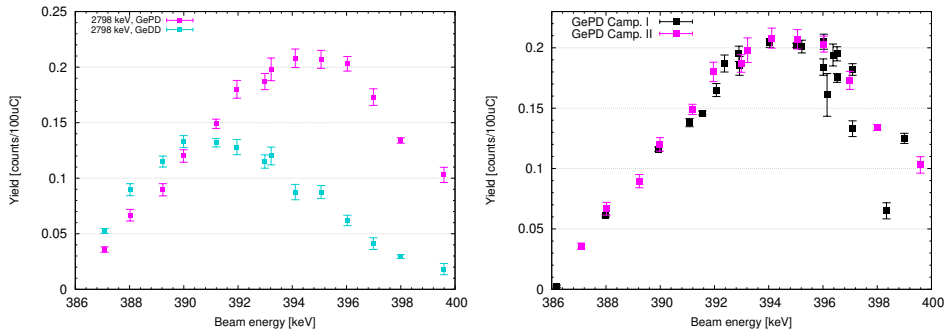

Figure 4.26: Yield curve for the 2798 keV → g.s transition measured during Campaign II with GePD (magenta) and GeDD (turquoise) (left). Comparison between yield function for 2798 keV → g.s transition measured in Campaign I (black) and Campaign II (magenta) with GePD detector.

Campaign II the pressure instabilities were totally reduced (reaching $\leq 0.1\%$ pressure variation). The 366 keV resonance scan was measured with steps of (1 - 2)

keV and the excitation function for all observed transitions is given in Figures 4.25 and 4.26.

4.5.1 Resonance energy determination

The energy of the resonance has been determined by using the yield profile of the observed decay modes compared with the efficiency profiles for each detector. The maximum of the resonance yield and the efficiency profile is expected to be in the same position along the target chamber for similar energies.
Figure 4.27 shows a comparison between the resonance scan yield and the efficiency curve as a function of the distance from the collimator for the 2798 keV $\rightarrow$ 2425 keV transition for both detectors. The resonance energy has been determined considering the energy loss of the beam through the beam path given by the following relation:

$$E_{R,lab} = E_p - \Delta E^{'} - (z - z_{coll})\frac{dE}{dz} \tag{4.14}$$

where E_R is the energy of the resonance, E_p the proton energy corresponding to the maximum resonance yield profile (determined by fitting the yield profile curve), $\Delta E^{'}$ is the energy loss from the first pumping stage to the target chamber, z is the distance between the source AP_1 collimator, z_{coll} is the effective AP_1 collimator length and $\frac{dE}{dz}$ is the proton energy loss per unit length in 2 mbar neon gas.
Due to the non stability of the resonance scans taken during Campaign I, the energy of the resonance has been determined using the resonance yield curve for all observable transitions in Campaign II. Nevertheless, a tentative resonance energy from Campaign I data was estimated as well.
The results on the resonance energy from the Campaign II data are reported in Table 4.14.

Transition	$E_{R,lab}$ GePD [keV]	$E_{R,lab}$ GeDD [keV]
2798 $\rightarrow$2425	385.9$\pm$0.5	386.4$\pm$0.6
2425 $\rightarrow$ g.s	385.7$\pm$0.5	386.4$\pm$0.7
2798 $\rightarrow$0	385.7$\pm$0.5	386.3$\pm$0.7

Table 4.14: Results on the resonance energies obtained during Campaign II.

Instead, Table 4.15 summarizes the results of resonance energy (the average value of the two detectors) determined during both campaigns compared with literature data. The present resonance energy results in agreement within 1σ with the value given in [102] and 2σ with [85].

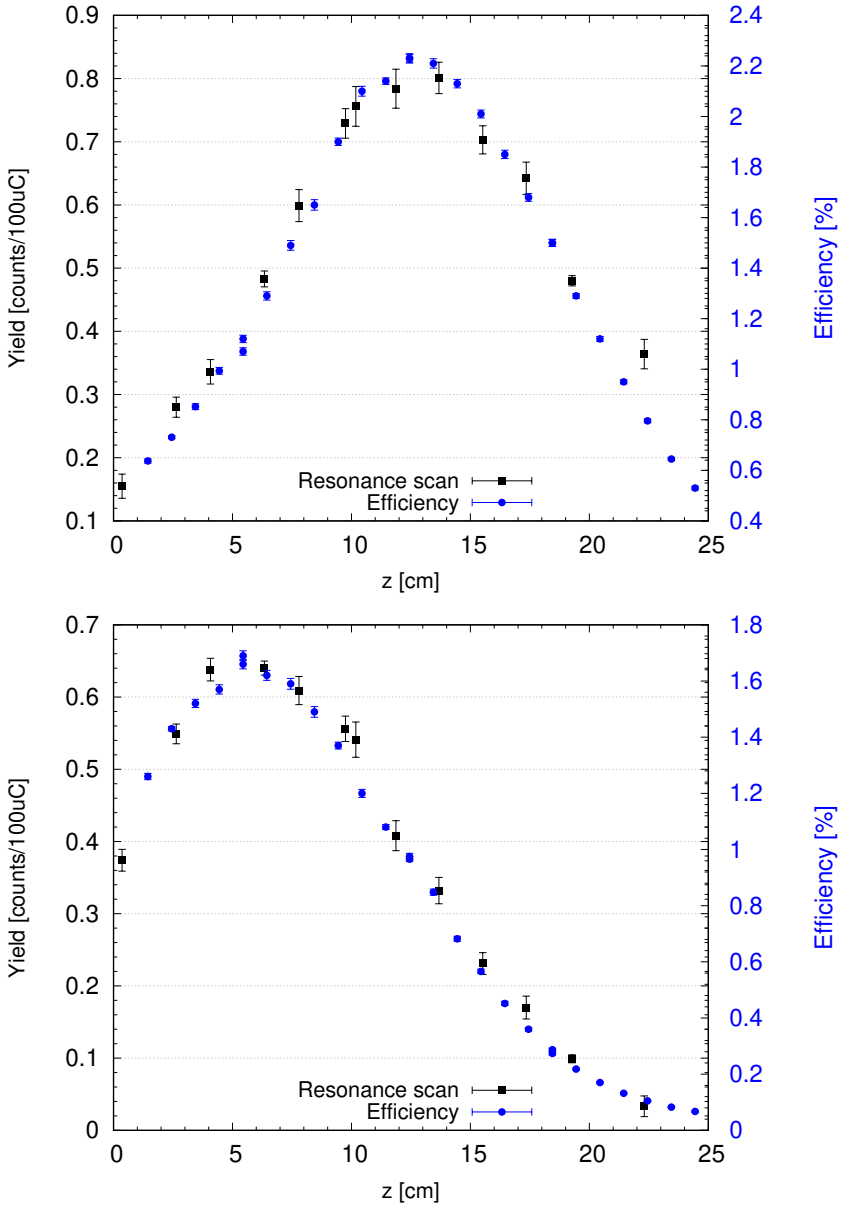

Figure 4.27: Comparison between resonance scan (black) for E_γ = 373 keV and efficiency curve (blue) for the E_γ = 383 keV (^{133}Ba source). Top panel shows the data from GePD detector while bottom the GeDD detector.

$E_{R,lab}$ LUNA II [keV]	$E_{R,lab}$ LUNA I [keV]	Rolfs et al. [102] [keV]	Iliadis et al. [85] [keV]
386.0±0.6	386.5 ±1.1	384±5	384.5 ±0.5

Table 4.15: Summary of results on the resonance energy obtained during Campaign I and Campaign II compared with the literature data.

4.5.2 Branching ratios

The branching ratios for the observed decay modes of the 2798 keV level have been calculated using the long run statistics acquired at 395 keV beam energy (Q = 15.7 C) where the resonance is populated in front of GePD detector, and at 391 keV proton energy (Q = 13 C) where the resonance is populated in front of GeDD detector. The intensities of the resonance primary peaks in these spectra were corrected for the summing-effect using Geant 3 simulations (Section 4.4.2).
The resonance γ-ray branching ratios are determined assuming that all possible decay modes are observed using the following relation:

$$Br_i = \frac{1}{\sum_j (N_j/\eta(E_j))} \frac{N_i}{\eta(E_i)} \tag{4.15}$$

where N_i and $\eta(E_i)$ are the net peak area and detection efficiency for transition i. Since the primary transition, 2798 $\rightarrow$ 2425 keV, is strongly affected by the Compton continuum, the branching results determined from the primary peaks has been checked by considering the 2425 keV $\rightarrow$ g.s transition.
The results of the branching ratios obtained in Campaign I for each detector are reported in Table 4.16:

	Br. GePD detector [%]		Br. GeDD detector [%]		
Transition	z = 6 cm	z = 11 cm	z = 6 cm	z = 11 cm	Rolfs et al. [102]
2425 $\rightarrow$ g.s	57.5±0.8	57.1±0.7	56.6±0.9	57±1	56±4
2798 $\rightarrow$332	3.5±0.4	4.5±0.3	4.6±0.4	5.0±0.7	11±4
2798 $\rightarrow$0	39.0±0.6	38.4±0.5	38.8±0.6	38±1	33±4

Table 4.16: Summary of Campaign I primary transition branching ratios (%) for the 366 keV resonance. Positions z = 6 and 11 cm correspond to the locations where the resonance is populated in front of the GePD and GeDD detector, respectively. The literature data in [102] are also given.

4.5.3 Energy straggling corrections

In section 3.4.4 the effects of a charged particle going through matter in terms of energy straggling were described. In the case of the 334 keV resonance, the contribution of the beam energy straggling was estimated considering the approach given in [13].
For the study of the ^{20}Ne(p, γ)^{21}Na reaction, the energy straggling corrections have been done using Geant3 Monte Carlo simulations. In Geant3 code, the energy loss and beam energy straggling are well described. The straggling effect is implemented based on the results given by TRIM simulations which can be parametrized using Eq. 3.18. The TRIM simulations were performed assuming the ^{20}Ne(p, γ)^{21}Na experimental conditions (pressure, resonance energy, position in the target). As a cross-check, assuming the same experimental, some LISE++ simulations were also performed. Figure 4.28 shows a comparison of the energy straggling as a function of the energy loss in the chamber for different approaches. In the present study,

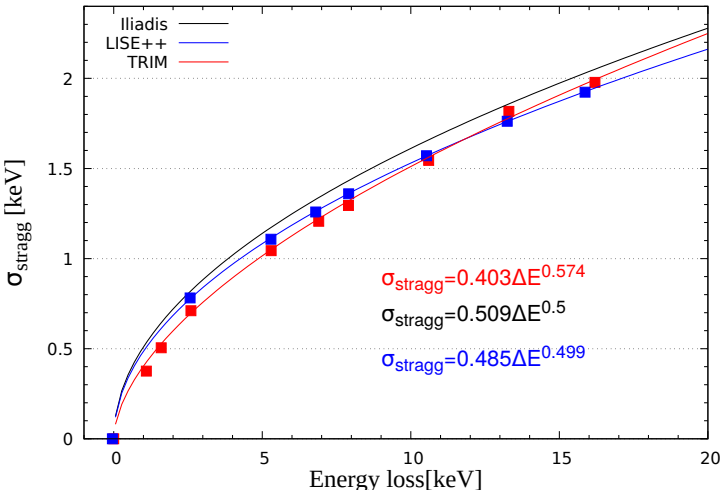

Figure 4.28: Energy straggling as a function of the energy loss in neon gas at 2 mbar for E_p = 395 keV beam. The line is the straggling parametrization obtained with TRIM (red), LISE++ (blue) the one determined with Eq. 3.17 (black).

Monte Carlo simulations assume the straggling parametrization given by the TRIM calculations (red curve in Figure 4.28).
The corrections for the energy straggling have been performed considering the following approach: Fixed the beam energy corresponding to the maximum yield curve for the two detectors, and hence the energy loss, the energy straggling (σ_{stragg}) has determined by the above parametrization given by TRIM simulations.

Then, monoenergetic sources following a Gaussian distribution of $\sigma = \sigma_{stragg}$ corresponding to the observed transitions have been simulated. After that, the two different decay levels(Figure 4.29), each with a Gaussian distribution of $\sigma = \sigma_{stragg}$ were also simulated. The corrected experimental counts for each transition are

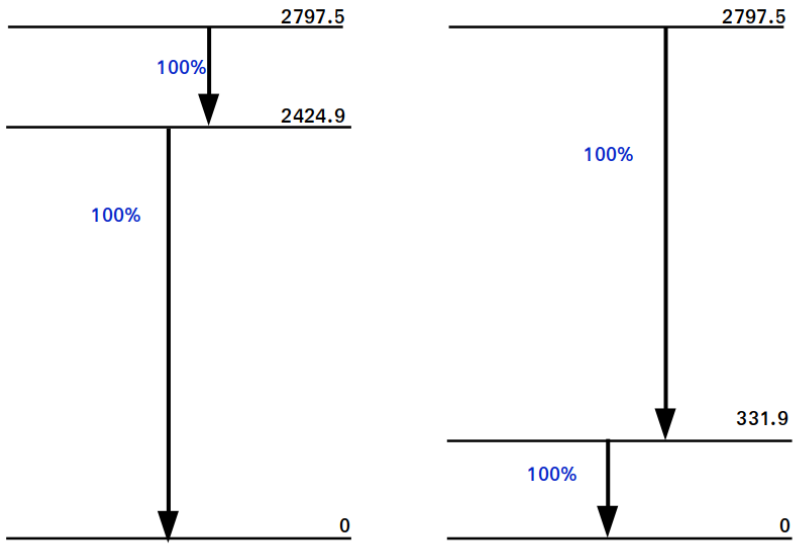

Figure 4.29: Decay scheme for the 2797.5 keV state assumed in the Monte carlo simulations for the straggling corrections.

given by.

$$N_i^{exp,corr} = N_i^{exp} \cdot \frac{N_i^{MC,mono}}{N_i^{MC,dec}} \tag{4.16}$$

where N_i^{exp} are the experimental net counts for a i transition, $N_i^{MC,mono}$ are the net counts for the i transition from the simulated single gamma source and $N_i^{MC,dec}$ the net counts for the i transition from the simulated decay level.

4.5.4 Energy straggling measurements

In this thesis, two different approaches have been considered for the energy straggling corrections. Moreover, the setup adopted for the study of the 366 keV resonance can be used to measure experimentally the energy straggling.
In particular, the location of the two detectors without any internal collimator, allows to see the reaction from two different positions where the effect of the energy straggling is different. The count rate of the detector depends on the detection

efficiency and on the energy straggling which consequently depends on the beam energy. Therefore, the ratio between the count rates of the two detectors is sensible to the beam energy, and hence the position in the chamber.
Given a proper characterization of the detectors ($\eta(E,z)$) it is possible to estimate the expected number of events seen by the two detectors as:

$$N(E_\gamma, \sigma_{\text{stragg}}) = \text{Br} \times \int_{z_{in}}^{z_{fin}} \eta(E_\gamma, z) \frac{1}{\sigma_{\text{stragg}}\sqrt{2\pi}} exp\left(-\frac{(z-z_0)^2}{2\sigma^2_{\text{stragg}}}\right) dz \qquad (4.17)$$

where z_0 is the point where the resonance is populated,z_{in}-z_{in} is the target length, $\eta(E_\gamma, z)$ is the detection efficiency and the second term of the integrand is the count rate of the resonance at a given position characterized by given σ_{stragg}.

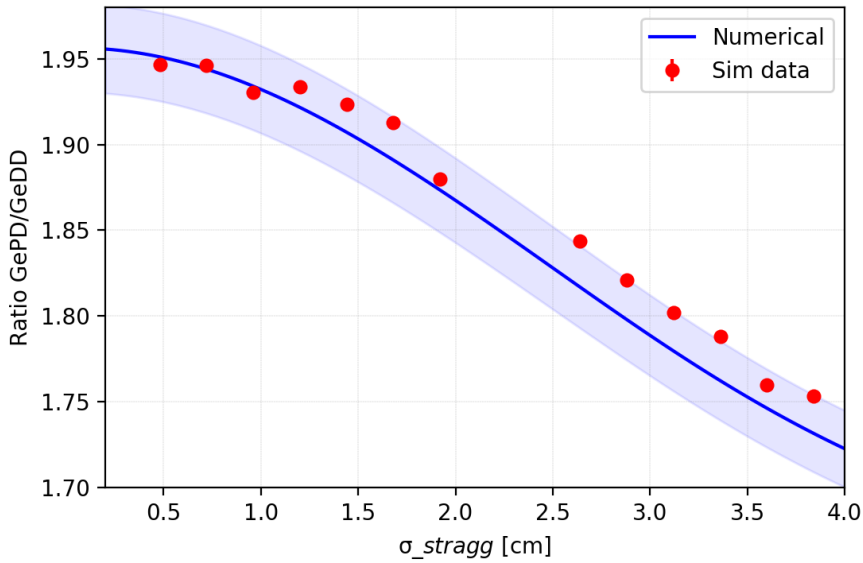

Figure 4.30: Ratio between the counts of the two detectors as a function of the energy straggling for the E_γ = 373 keV. In blue the numerical calculations, in red the simulations. The blue shadow represent the uncertainty if the ratio of the two detectors are measured with 1% uncertainty.

Assuming Eq. 4.17 and knowing the detection efficiency, the ratio of the counts seen by each detector can be determined numerically ($(N_{GePD}/N_{GeDD})_{num}$), and depends only on the energy straggling, σ_{stragg} . This ratio can also be measured experimentally, ($(N_{GePD}/N_{GeDD})_{exp}$). Here, from the resonance scans of ^{20}Ne(p,γ)^{21}Na reaction, for different transitions, the count rate ratio of the two

detectors can be determined.
The σ_{stragg} that meets:

$$\left(\frac{N_{GePD}}{N_{GeDD}}\right)_{num} = \left(\frac{N_{GePD}}{N_{GeDD}}\right)_{exp} \tag{4.18}$$

estimates the beam energy straggling at different beam energies. Figure 4.30 shows the numerical count ratio as a function of the energy straggling. The numerical calculations have been been compared with Monte Carlo simulations where the resonance has been simulated for different energy straggling values. To achieve this energy straggling estimation experimentally, high statistic resonance scan measurements are needed. Nevertheless, considering the resonance scan for the $E_\gamma = 373$ keV (Figure 4.25), and the numerical calculations given in Figure 4.30 a very preliminary results can be given. The energy straggling for 394 keV proton beam (resonance populated in front of the GePD detector), where the count ratio is 1.92, results $\sigma_{stragg} = 0.64^{+0.03}_{-0.04}$ keV.

4.5.5 Resonance strength determination

As was described in Chapter 1, the thermonuclear reaction rate for a resonant reaction is calculated from the resonance strength $\omega\gamma$. The resonance strength is determined from the experimental yield introduced in Section 3.4.5 (Eq. 3.19). The resonance strength is determined inverting Eq. 3.22:

$$\omega\gamma = \frac{2}{\lambda_r^2} Y \epsilon_r \frac{M}{m+M} \tag{4.19}$$

where λ is the de Broglie wavelength defined in Eq. 1.20 and the $\lambda_r^2/2$ can be determined as:

$$\frac{\lambda_r^2}{2} = \left(\frac{m+M}{M}\right)^2 \frac{4.125 \cdot 10^{-18}}{M E_{R,lab}} \tag{4.20}$$

with $E_{R,lab}$ the resonance energy in the laboratory system given in eV while the masses in amu. For the adopted resonance energy in the present work (386.0 keV) the $\lambda_r^2/2 = 1.17 \cdot 10^{-23}$ cm^2.
The yield at the maximum of the excitation function curve has been calculated using Eq. 4.21 for the observed transitions and adopting the branching ratios in Table 4.16:

$$Y = \frac{N_j/\eta(E_j)}{Br_j} \frac{e}{Q} \tag{4.21}$$

The net counts, N_j, has been corrected for the beam energy straggling using the approach given in Section 4.5.3. Summing-in and summing-out corrections have

also been considered using MC simulations previously introduced. The total charge Q has been calculated using the live time of the detectors. For each energy, the deadtime of the detectors has been taken into account: for the CAEN acquisition the deadtime has been calculated using the pulser channel; for the analog multichannel acquisition the deadtime provided by the software was considered. In both DAQ systems, the deadtime of the two detectors was $\sim 1\%$.
The ϵ_r in Eq. 4.19 is the effective stopping power already introduced in Chapter 3. If only one species is present in the target, the effective stopping power is equal to the stopping power given by SRIM for that species.
In the present work, the measurements have been performed by using natural neon gas, therefore the contribution of other isotopes present in the natural neon gas should be considered.
In general, when more than one species is present in the target, the effective stopping is given by:

$$\epsilon_r = \epsilon_{eff} = \epsilon_X + \frac{n_Y}{n_X}\epsilon_Y \tag{4.22}$$

where X is the element of interest, Y is the inactive element, ϵ_X (ϵ_Y) the stopping power for the active (inactive) element, and n_X (n_Y) is the number of active nuclei (inactive) per area.
For active ^{20}Ne atoms in the natural neon gas (90.48 (2.01)% ^{20}Ne, 0.27(1.44)% ^{21}Ne, 9.25(0.72)% ^{22}Ne), $E_{R,lab} = 386.0$ keV, the effective stopping power results:

$$\epsilon_{eff} = \frac{\epsilon_{Ne}}{n_{^{20}Ne}} = \frac{\epsilon_{Ne}}{0.9048} = 12.0\frac{\text{eVcm}^2}{10^{15}\text{atoms}} \tag{4.23}$$

The resonance strength obtained at two different positions in the chamber (corresponding to the maximum of GePD and GeDD detectors) for each detector are given in Table 4.17. Figure 4.31 reports the data of the resonance strengths obtained with GePD at the GePD maximum detection efficiency, GeDD at the GeDD maximum detection efficiency together with the literature data.

Detector	$\omega\gamma$ [meV]
GePD (z = 6 cm)	0.112±0.007
GePD (z = 11 cm)	0.114±0.006
GeDD (z = 6 cm)	0.112±0.006
GeDD (z = 11 cm)	0.122±0.008

Table 4.17: Summary of resonance strengths for the two detectors.

The new resonance values obtained in the present work are in agreement with the data given in [102] and [108] within 2% and ~ 50 %, respectively.

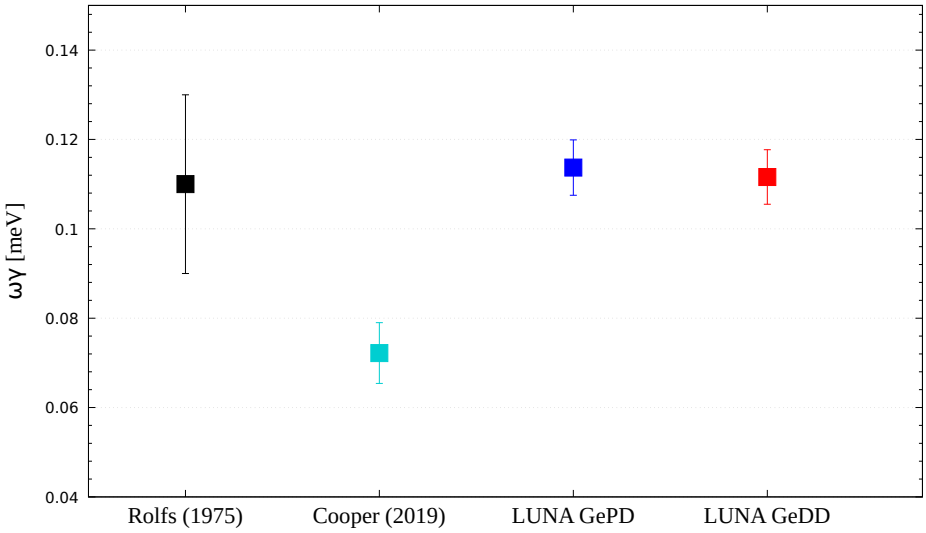

Figure 4.31: Comparison of the 366 keV resonance strength measurements from each detector obtained in the present study with the results given in [102] and [108].

The weighted average of the resonance strength values for the two detectors at their maximum detection efficiency (z = 11 cm for GePD and z = 6 cm for GeDD) is $\omega\gamma$ = 0.113 ± 0.004 meV. This average value is the one adopted for the thermonuclear rate calculation in the next section.

4.5.6 Thermonuclear reaction rate

The total of ^{20}Ne(p,γ)^{21}Na reaction rate is calculated considering the weighted average of the 366 keV resonance strength determined in Section 4.5.5 and using Eq. 3.31. All other resonances are considered as in [83]. The reaction rate in [83] has been calculated assuming the 366 keV resonance properties given in [102].

The present reaction rate normalized to the NACRE data [37] is reported in Figure 4.32 while the contribution of the single resonance to the total reaction rate is given Figure 4.33. The total rate is lightly lower than the rate given in [83] between temperatures of 0.2 GK and 0.4 GK and lightly higher from 0.4 GK to 1 GK. A significant reduction of the uncertainty is shown in the temperature region between 0.2 GK and 1 GK affected by the 366 keV resonance.

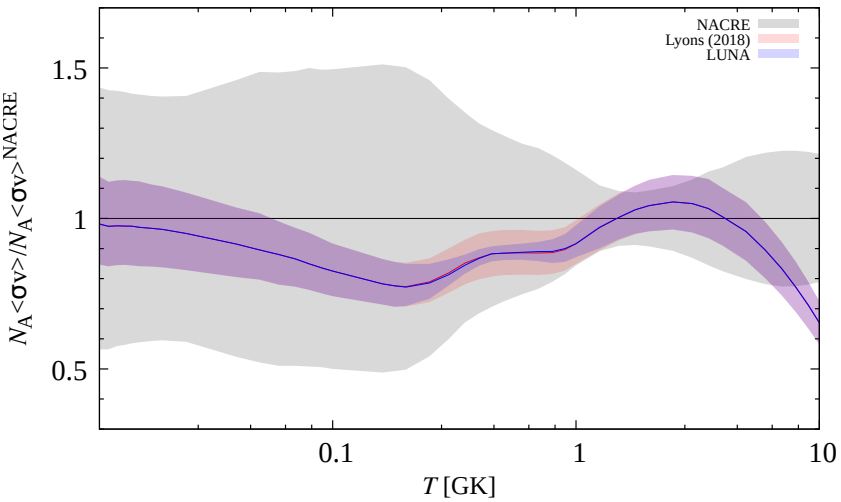

Figure 4.32: LUNA thermonuclear reaction rate of $^{20}\mathrm{Ne}(\mathrm{p},\gamma)^{21}\mathrm{Na}$ reaction, together with the rate given in [83] as a function of temperature T. The data are normalized to the previous NACRE rate [37].

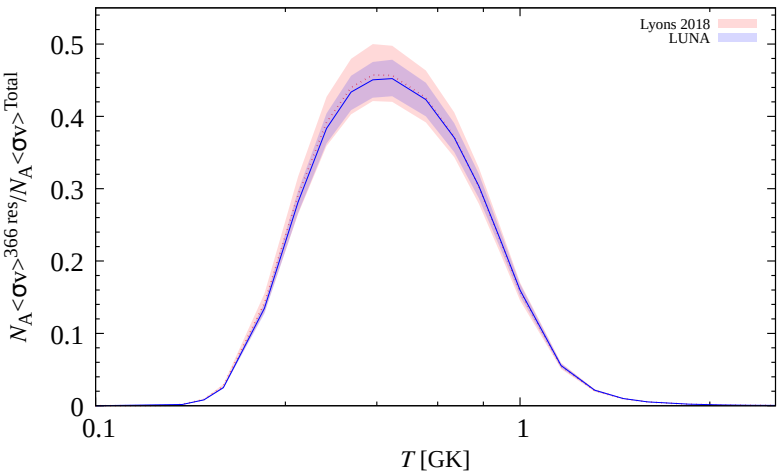

Figure 4.33: Contribution of the 366 keV resonance to the total reaction rate.

4.5.7 Remarks and future perspectives

During the experimental campaigns devoted to the study of the ^{20}Ne(p, γ)^{21}Na reaction, some problems were identified such as the pressure fluctuations during Campaign I, the low statistics in Campaign II which limited the observation of the low intensity γ-rays. Nevertheless, the present results on the 366 keV resonance of ^{20}Ne(p, γ)^{21}Na reaction are very promising and further improvements will be achieved in the next phase of the ^{20}Ne(p, γ)^{21}Na study ongoing at LUNA 400 kV accelerator. In this phase, the resonance scan will be measured with $\sim 1\%$ statistics. The higher statistics might reduce further the uncertainties on the results presented and will allow determining the energy straggling experimentally as discussed in Section 4.5.4.

Thereafter, the experimental campaign will focus on the study of the direct capture component below 400 keV. In the context of this last one, at the end of Campaign II a preliminary measurement of the direct capture component at E_p = 380 keV, using exactly the same experimental conditions (same setup, same pressure in the chamber), was performed.

Based on results given in [102], the cross section at these energies is supposed to be dominated by the direct capture into the 2425 keV state which decays purely to the ground state. The expected γ-rays from ^{20}Ne(p, γ)^{21}Na reaction at E_p = 380 keV are reported in Table 4.18. The choice of this energy was intentional in order do be low enough in energy to avoid the 366 keV resonance presented above. The experimental spectrum acquired with the GePD detector is shown in Figure

Transitions [keV]	E_γ[keV]
DC→ 2425	368.5
DC→ 1716	1077.5
DC→ 332	2461.5
DC→ 0	2793.5
2425→ 0	2425
1716→ 332	1384
1716→ 0	1716
332→ 0	332

Table 4.18: Expected γ-rays from ^{20}Ne(p, γ)^{21}Na *at* E_p = = *380 keV.*

4.34. At this energy, with the present setup the study of the direct capture seems limited by the beam-induced background from the florine contaminants present in the collimator or implanted in the calorimeter.

The energy region which corresponds to the DC → 2425 keV state is completely

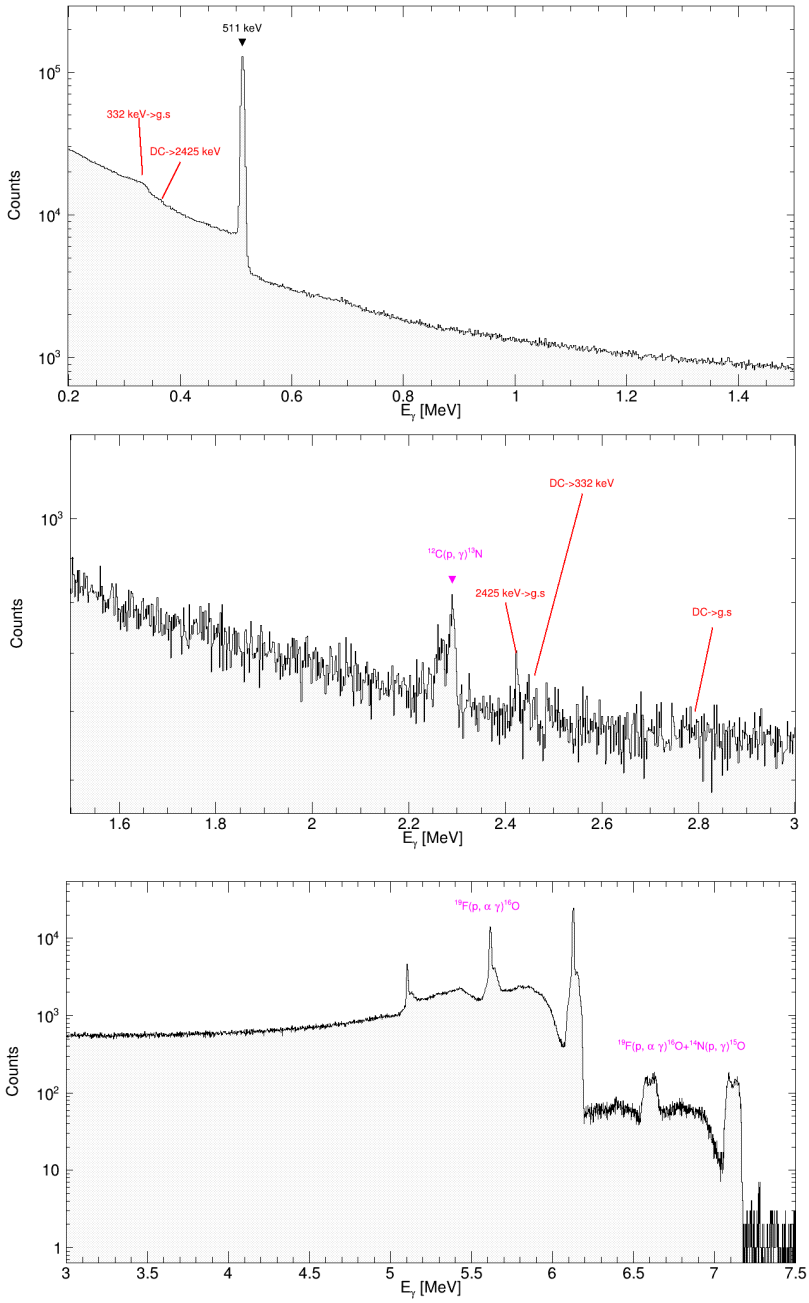

Figure 4.34: Direct capture spectrum of $^{20}\mathrm{Ne}(\mathrm{p},\gamma)^{21}\mathrm{Na}$ *reaction taken at* E_p = *380 keV with GePD detector. The most intense gamma transitions region expected from the DC are labeled in red, while in magenta the main beam-induced background sources.*

covered by the Compton edge. Instead a low intensity signal is observed in the energy region of the secondary transition (2425 $\rightarrow$ 0 keV). From this preliminary measurement it is clear that with the present setup is difficult to study the direct capture at this energy. Nevertheless, this measurement together with some beam-induced background measurements which are under analysis are used as a starting point for some further improvements in the present setup.

Conclusions

The goal of the present PhD thesis was the study of two different nuclear reactions on neon isotopes which are fundamental in several astrophysical environments. Both measurements have been performed at LUNA laboratory. The ^{22}Ne$(\alpha,\gamma)^{26}$Mg reaction has been studied at the resonance energy $E_{cm} = 334$ keV. In literature there are several values reported for this resonance lying in wide range of six orders of magnitude. The goal of the present work is to improve the present data by giving the first direct measurement of the resonance. The measurement has been performed using a windowless gas target filled with enriched ^{22}Ne and a high-efficiency BGO detector. A preliminary campaign was performed before the present work and several improvements have been done to complete the measurement. The experiment determined an upper limit of $4.0 \cdot 10^{-11}$ eV for the resonance strength. Even if the new limit does not exclude most of the previous limits obtained by indirect approaches it is the first direct, model-independent result. Taking into account this result, a new updated ^{22}Ne$(\alpha,\gamma)^{26}$Mg thermonuclear reaction was calculated. The new rate results higher than all recent literature rates and its impact on the AGB stars was investigated by studying the abundances of neutron-rich magnesium isotopes in the pulse-driven convective zone. This study was performed by using a $5M_{\odot}$ AGBs model and a decrease by a factor of 15 of the intershell ^{25}Mg/^{26}Mg ratio was found.
The study of the $E_{cm} = 366$ keV resonance for the ^{20}Ne$(p,\gamma)^{21}$Na reaction has been done with the aim to reduce the resonance strength uncertainty reported in the literature and improve the knowledge on the overall thermonuclear reaction rate. The measurement has been carried out using the windowless gas target of LUNA, filled with natural neon gas, and two high-purity HPGe detectors for the detection of the reaction products. First, a characterization of the setup was performed together with Monte Carlo simulations which were useful to define the best experimental conditions for the study of the resonance. The present measurements at LUNA updated the energy of the resonance from (384 ± 5) keV to (386.0 ± 0.6) keV and

reduced the uncertainty of the resonance strength from 18% to 7 %. The Monte Carlo simulations show that the setup used for the study of the ^{20}Ne(p, γ)^{21}Na reaction and the resonance itself can be used as an alternative method to measure the energy straggling a beam passing through a gas target. Regarding this, a new campaign of the ^{20}Ne(p, γ)^{21}Na reaction is ongoing at LUNA. Moreover, high statistics measurements, further improvements on the setup, and the ongoing analysis on the beam-induced background will allow the measurements of the cross-section below 400 keV where the literature data show several discrepancies.

Appendices

Appendix A

Properties of 10945 keV ^{26}Mg exited state

E_x [keV]	$E_{r,cm}$ [keV]	J^π [keV]	$\omega\gamma$ [eV]	Ref.
10943.0(40)	328.3(40)	$5^-, 6^+, 7^-$	1.72x10^{-17}	[50]
10943.5(23)				[48]
	328.21(200)	7	5.6x10^{-22}	[57]
10943	388(2)	$5^+, 7^-$	$\leq 1.6x10^{-20}$- $\leq 2.3x10^{-20}$	[45]
10944.77		2^+		[43]
	328.21(200)	7	5.6x10^{-22}	[54]
10953(25)		$^*5^-, 6^+, 7^-$		[35]
10945(3)				[121]
10943(2)				[122]

Table A.1: ^{26}Mg *exited state corresponding to the 334 keV resonance. The states corresponding to the* E_x*=10945(3) keV* ($J^\pi = 1^-$) *of NNDC data.*

E_x [keV]	$E_{r,cm}$ [keV]	J^π [keV]	$\omega\gamma$ [eV]	Ref.
10950(20)	334.4(8)	$0^+, 1^-, 2^+$	9.0x10^{-14}	[52]
10949.1(8)	334.4(8)	1^-	9.0x10^{-14}	[50]
10950.0(15)		1^-		[48]
10949(10)		1^-		[46]
10951(21)	336	1^-		[44]
	334.31(10)	1^-		[57]
10949		1^-	8.7x10^{-15}	[45]
10944.77	395.15(18)*	1^-		[43]
	334.31(10)	2^+	3.6x10^{-9}	[107]
10949		1^-		[123]
10949.1(8)		1^-		[39]
10953(25)		1^-		[35]
10953.14	338.4(17)	$7^-, 6^+, 5^-$		[37]
10949(25)	400*	$3^-, 2^+, 4^+$	$\leq 1.4x10^{-13}$	[124]
10950(3)		$3^-, 2^+, 4^+$	1.7x10^{-13}	[125]

* $E_{r,cm}$ is given in the center of mass frame.

Table A.2: ^{26}Mg *exited state corresponding to the 334 keV resonance. The states corresponding to the* E_x*=10949.1(8) keV*$(J^\pi = 1^-)$ *of NNDC.*

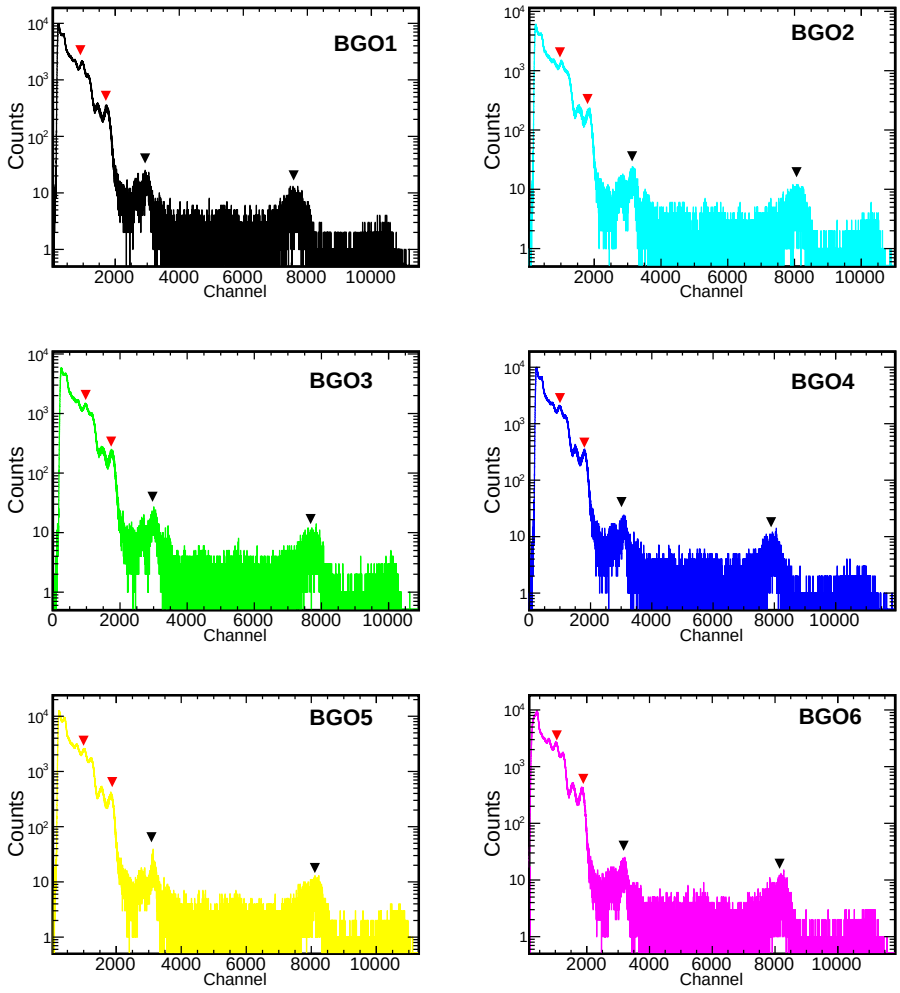

Figure A.1: Spectra of the BGO segments for ^{22}Ne+p run used for the energy calibration above 8 MeV. The peaks used for the linear energy calibration are shown with red markers. The black markers are the gamma lines from the boron contamination used for the quadratic calibration.

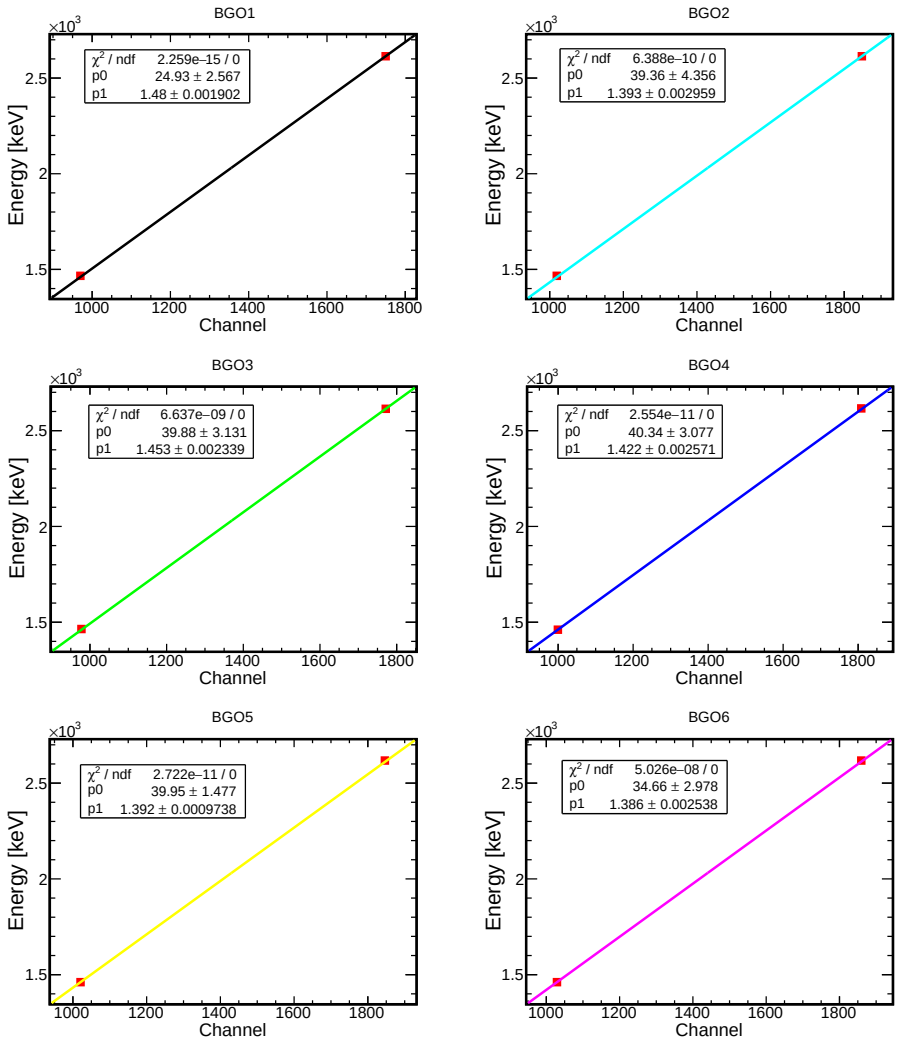

Figure A.2: Linear energy calibration curve of the BGO segments for the run given in Figure A.1.

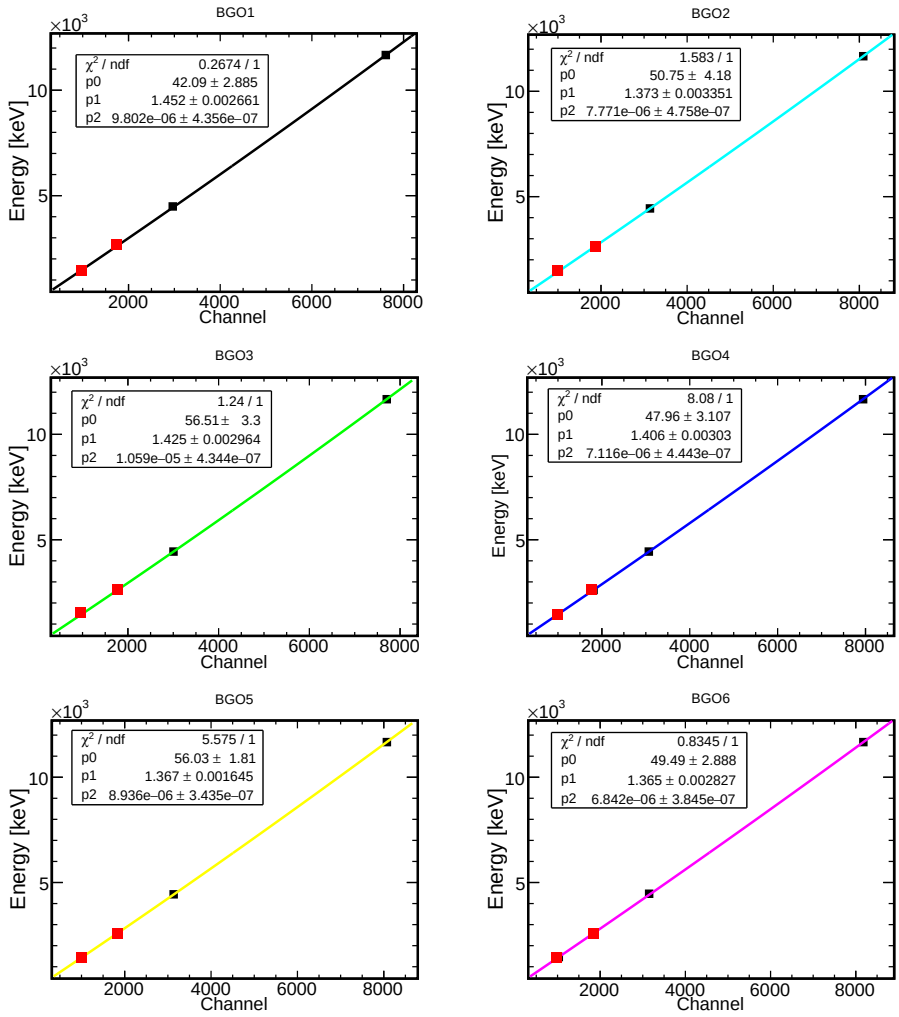

Figure A.3: Quadratic energy calibration curve of the BGO segments for the run given in Figure A.1. The low energy γ-lines present in all spectra taken during the ^{22}Ne+α campaign are shown in red while the added points present only in the ^{22}Ne+p runs used for the study of quadratic energy calibration are shown in black.

Appendix B

$^{20}\mathrm{Ne}(\mathrm{p},\gamma)^{21}\mathrm{Na}$ reaction

B.1 Technical drawings

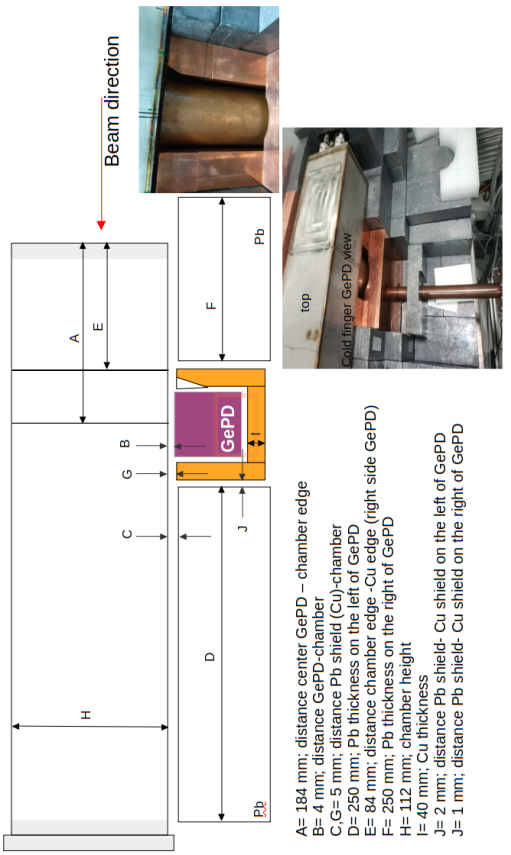

Figure B.1: Drawings and photo of the setup seen from GePD side. The copper shielding around the GePD is well visible.

B.2 Calorimeter calibration

Date	E_p [keV]	W_{el} [W]	W_{cal} [W]
February 2020	51.1	6.5	6.3
	100.6	13.3	13.4
	50.2	20.0	20.4
	199.8	27.1	27.8
	229.5	31.1	31.9
	249.3	33.8	34.7
	249.6	35.0	34.3
	279.3	34.3	35.7
	279.3	38.8	38.5
	298.9	41.8	43.0
	299.2	38.3	40.1
	348.3	48.9	50.7
	348.6	48.6	48.1
	378.0	53.7	55.7
	378.3	52.1	51.7
October 2020	100.2	10.6	10.0
	100.8	21.3	20.4
	101.8	35.8	34.9
	131.6	56.6	55.1
	151.4	67.0	65.4
	199.0	10.5	10.2
	199.4	17.5	16.9
	249.5	34.1	33.5
	249.6	57.8	57.2
	249.8	81.0	79.7
	250.1	102.0	100.5
	277.0	41.1	40.0
	299.6	120.8	119.2
	349.0	141.3	138.7
	377.8	59.2	58.0
	378.6	91.3	89.8
	379.1	166.2	163.9
	391.9	169.7	166.9
	391.9	194.8	192.2

Table B.1: Calorimeter and electrical power as a function of proton beam energy.

B.3 Geant 3 geometry

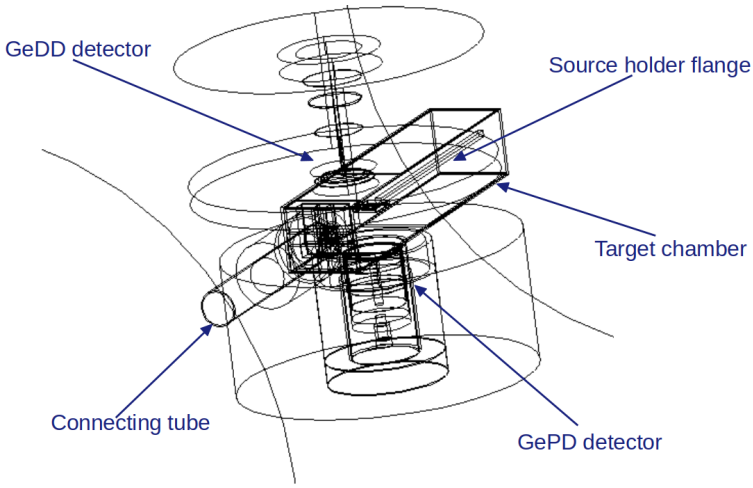

Figure B.2: Side view of the ^{20}Ne(p, γ)^{21}Na *setup geometry simulated with the Geant3 code. The main components are labeled in blue*

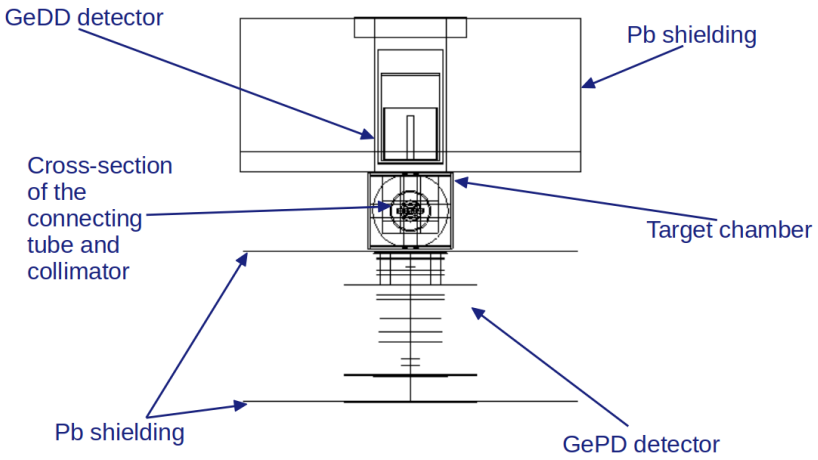

Figure B.3: Beam view of the ^{20}Ne(p, γ)^{21}Na *setup geometry simulated with the Geant3 code. The main components are labeled in blue.*

Bibliography

[1] C. Iliadis, *Nuclear Physics of Stars*. Weinheim: Wiley-VCH, 2nd ed., 2015.

[2] C. Rolfs and W. Rodney, *Cauldrons in the Cosmos*. Chicago: University of Chicago Press, 1988.

[3] D. Prialnik, *An Introduction to the Theory of Stellar Structure and Evolution*. 2009.

[4] C. Iliadis, *Nuclear Physics of Stars*. Weinheim: Wiley-VCH, 2007.

[5] "Luna (laboratory underground for nuclear astrophysics)." http://luna.lngs.infn.it.

[6] F. Cavanna and P. Prati, "Direct measurement of nuclear cross-section of astrophysical interest: Results and perspectives," *International Journal of Modern Physics A*, vol. 33, pp. 1843010–346, Mar. 2018.

[7] C. Broggini, D. Bemmerer, A. Caciolli, and D. Trezzi, "Luna: Status and prospects," *Progress in Particle and Nuclear Physics*, vol. 98, no. Supplement C, pp. 55 – 84, 2018.

[8] U. Greife *et al.*, "LUNA. Laboratory for Underground Nuclear Astrophysics," *Nucl. Inst. Meth. A*, vol. 350, p. 327, 1994.

[9] A. Formicola, G. Imbriani, M. Junker, D. Bemmerer, R. Bonetti, C. Broggini, C. Casella, P. Corvisiero, H. Costantini, G. Gervino, C. Gustavino, A. Lemut, P. Prati, V. Roca, C. Rolfs, M. Romano, D. Schürmann, F. Strieder, F. Terrasi, H.-P. Trautvetter, and S. Zavatarelli, "The LUNA II 400kV accelerator," *Nucl. Inst. Meth. A*, vol. 507, pp. 609–616, July 2003.

[10] C. Casella, H. Costantini, A. Lemut, B. Limata, D. Bemmerer, R. Bonetti, C. Broggini, L. Campajola, P. Cocconi, P. Corvisiero, J. Cruz, A. D'Onofrio, A. Formicola, Z. Fülöp, G. Gervino, L. Gialanella, A. Guglielmetti, C. Gustavino, G. Gyurky, A. Loiano, G. Imbriani, A. P. Jesus, M. Junker, P. Musico, A. Ordine, F. Parodi, M. Parolin, J. V. Pinto, P. Prati, J. P. Ribeiro, V. Roca, D. Rogalla, C. Rolfs, M. Romano, C. Rossi-Alvarez, A. Rottura, F. Schuemann, E. Somorjai, F. Strieder, F. Terrasi, H. P. Trautvetter, A. Vomiero, and S. Zavatarelli, "A new setup for the underground study of capture reactions," *Nucl. Inst. Meth. A*, vol. 489, pp. 160–169, Aug. 2002.

[11] F. Ferraro, M. P. Takács, D. Piatti, V. Mossa, M. Aliotta, D. Bemmerer, A. Best, A. Boeltzig, C. Broggini, C. G. Bruno, A. Caciolli, F. Cavanna, T. Chillery, G. F. Ciani, P. Corvisiero, L. Csedreki, T. Davinson, R. Depalo, G. D'Erasmo, A. Di Leva, Z. Elekes, E. M. Fiore, A. Formicola, Z. Fülöp, G. Gervino, A. Guglielmetti, C. Gustavino, G. Gyürky, G. Imbriani, M. Junker, I. Kochanek, M. Lugaro, L. E. Marcucci, P. Marigo, R. Menegazzo, F. R. Pantaleo, V. Paticchio, R. Perrino, P. Prati, L. Schiavulli, K. Stöckel, O. Straniero, T. Szücs, D. Trezzi, and S. Zavatarelli, "A high-efficiency gas target setup for underground experiments, and redetermination of the branching ratio of the 189.5 kev 22ne(p, $*gamma*$γ)23na resonance," *The European Physical Journal A*, vol. 54, p. 44, Mar 2018.

[12] F. Ferraro, *Direct measurement of the $^{22}Ne(p,\gamma)^{23}Na$ reaction cross section at astrophysical energies.* PhD thesis, Università degli studi di Genova, 2017.

[13] D. Bemmerer, F. Confortola, A. Lemut, R. Bonetti, C. Broggini, P. Corvisiero, H. Costantini, J. Cruz, A. Formicola, Z. Fülöp, G. Gervino, A. Guglielmetti, C. Gustavino, G. Gyürky, G. Imbriani, A. P. Jesus, M. Junker, B. Limata, R. Menegazzo, P. Prati, V. Roca, D. Rogalla, C. Rolfs, M. Romano, C. Rossi Alvarez, F. Schümann, E. Somorjai, O. Straniero, F. Strieder, F. Terrasi, H. P. Trautvetter, and A. Vomiero, "Feasibility of low-energy radiative-capture experiments at the LUNA underground accelerator facility," *Eur. Phys. J. A*, vol. 24, pp. 313–319, 2005.

[14] A. Caciolli, L. Agostino, D. Bemmerer, R. Bonetti, C. Broggini, F. Confortola, P. Corvisiero, H. Costantini, Z. Elekes, A. Formicola, Z. Fülöp, G. Gervino, A. Guglielmetti, C. Gustavino, G. Gyürky, G. Imbriani, M. Junker, M. Laubenstein, A. Lemut, B. Limata, M. Marta, C. Mazzocchi, R. Menegazzo, P. Prati, V. Roca, C. Rolfs, C. Rossi Alvarez, E. Somorjai, O. Straniero, F. Strieder, F. Terrasi, and H. P. Trautvetter, "Ultrasensitive in-beam γ-ray spectroscopy for nuclear astrophysics at LUNA," *Eur. Phys. J. A*, vol. 39, pp. 179–186, 2009.

[15] F.-K. Thielemann, R. Diehl, A. Heger, R. Hirschi, and M. Liebendoerfer, *Massive Stars and Their Supernovae*, vol. 453 of *Astrophysics and Space Science Library*, pp. 173–286. 2018.

[16] M. Lugaro and A. Chieffi, *Low- and Intermediate-Mass Stars*, vol. 453 of *Astrophysics and Space Science Library*, pp. 91–172. 2018.

[17] A. I. Karakas, M. A. Lugaro, M. Wiescher, J. Görres, and C. Ugalde, "The Uncertainties in the ^{22}Ne+α-Capture Reaction Rates and the Production of the Heavy Magnesium Isotopes in Asymptotic Giant Branch Stars of Intermediate Mass," *The Astrophysical Journal*, vol. 643, pp. 471–483, May 2006.

[18] E. M. Burbidge, G. R. Burbidge, W. A. Fowler, and F. Hoyle, "Synthesis of the Elements in Stars," *Rev. Mod. Phys.*, vol. 29, pp. 547–650, 1957.

[19] R. Reifarth, C. Lederer, and F. Käppeler, "Neutron reactions in astrophysics," *J. Phys. G*, vol. 41, p. 053101, May 2014.

[20] M. Busso, R. Gallino, and G. J. Wasserburg, "Nucleosynthesis in Asymptotic Giant Branch Stars: Relevance for Galactic Enrichment and Solar System Formation," *Annu. Rev. Astron. Astroph.*, vol. 37, pp. 239–309, 1999.

[21] M. Busso, R. Gallino, D. L. Lambert, C. Travaglio, and V. V. Smith, "Nucleosynthesis and Mixing on the Asymptotic Giant Branch. III. Predicted and Observed s-Process Abundances," , vol. 557, pp. 802–821, Aug. 2001.

[22] R. Gallino, C. Arlandini, M. Busso, M. Lugaro, C. Travaglio, O. Straniero, A. Chieffi, and M. Limongi, "Evolution and nucleosynthesis in low-mass asymptotic giant branch stars. ii. neutron capture and the s-process," *The Astrophysical Journal*, vol. 497, no. 1, p. 388, 1998.

[23] S. Bisterzo, R. Gallino, F. Käppeler, M. Wiescher, G. Imbriani, O. Straniero, S. Cristallo, J. Görres, and R. J. deBoer, "The branchings of the main s-process: their sensitivity to α-induced reactions on ^{13}C and ^{22}Ne and to the uncertainties of the nuclear network," *Monthly Notices of the RAS*, vol. 449, pp. 506–527, May 2015.

[24] D. Yong, D. L. Lambert, and I. I. Ivans, "Magnesium Isotopic Abundance Ratios in Cool Stars," , vol. 599, pp. 1357–1371, Dec. 2003.

[25] J. Meléndez and J. G. Cohen, "Magnesium Isotopes in Metal-poor Dwarfs: The Rise of AGB Stars and the Formation Timescale of the Galactic Halo," *The Astrophysical Journal Letters*, vol. 659, pp. L25–L28, Apr. 2007.

[26] G. S. Da Costa, E. V. Held, I. Saviane, and M. Gullieuszik, "M22: An [Fe/H] Abundance Range Revealed," *The Astrophysical Journal*, vol. 705, pp. 1481–1491, Nov. 2009.

[27] A. Heger, E. Kolbe, W. Haxton, K. Langanke, G. Martinez-Pinedo, and S. Woosley, "Neutrino nucleosynthesis," *Phys. Lett. B*, vol. 606, pp. 258–264, 2005.

[28] J. Meléndez and J. G. Cohen, "The Rise of the AGB in the Galactic Halo: Mg Isotopic Ratios and High Precision Elemental Abundances in M71 Giants," *The Astrophysical Journal*, vol. 699, pp. 2017–2025, July 2009.

[29] Y. Fenner, B. K. Gibson, H. c. Lee, A. I. Karakas, J. C. Lattanzio, A. Chieffi, M. Limongi, and D. Yong, "The Chemical Evolution of Magnesium Isotopic Abundances in the Solar Neighbourhood," , vol. 20, pp. 340–344, Jan 2003.

[30] P. Adsley, U. Battino, A. Best, A. Caciolli, A. Guglielmetti, G. Imbriani, H. Jayatissa, M. La Cognata, L. Lamia, E. Masha, C. Massimi, S. Palmerini, A. Tattersall, and R. Hirschi, "Reevaluation of the $^{22}\mathrm{Ne}(\alpha,\gamma)^{26}\mathrm{Mg}$ and $^{22}\mathrm{Ne}(\alpha,n)^{25}\mathrm{Mg}$ reaction rates," *Phys. Rev. C*, vol. 103, p. 015805, Jan 2021.

[31] R. Cavanna, F.and Depalo, M. Aliotta, M. Anders, D. Bemmerer, A. Best, A. Boeltzig, C. Broggini, C. G. Bruno, A. Caciolli, P. Corvisiero, T. Davinson, A. di Leva, Z. Elekes, F. Ferraro, A. Formicola, Z. Fülöp, G. Gervino, A. Guglielmetti, C. Gustavino, G. Gyürky, G. Imbriani, M. Junker, R. Menegazzo, V. Mossa, F. R. Pantaleo, P. Prati, D. A. Scott, E. Somorjai, O. Straniero, F. Strieder, T. Szücs, M. P. Takács, D. Trezzi, and LUNA Collaboration, "Three New Low-Energy Resonances in the $^{22}\mathrm{Ne}(\mathrm{p},\gamma)^{23}\mathrm{Na}$ Reaction," *Phys. Rev. Lett.*, vol. 115, p. 252501, Dec. 2015.

[32] The Luna Collaboration, Bemmerer, D., Cavanna, F., Depalo, R., Aliotta, M., Anders, M., Boeltzig, A., Broggini, C., Bruno, C., Caciolli, A., Chillery, T., Corvisiero, P., Davinson, T., Elekes, Z., Ferraro, F., Formicola, A., Fülöp, Zs., Gervino, G., Guglielmetti, A., Gustavino, C., Gyürky, Gy., Menegazzo, R., Mossa, V., Pantaleo, F. R., Prati, P., Scott, D. A., Stöcker, K., Straniero, O., Szücs, T., Takács, M. P., and Trezzi, D., "Effect of beam energy straggling on resonant yield in thin gas targets: The cases $^{22}\mathrm{Ne}(\mathrm{p},\alpha)$ and $^{14}\mathrm{N}(\mathrm{p},\gamma)$," *EPL*, vol. 122, no. 5, p. 52001, 2018.

[33] K. Wolke, V. Harms, H. Becker, J. Hammer, K. Kratz, C. Rolfs, U. Schröder, H. Trautvetter, M. Wiescher, and A. Wöhr, "Helium burning of $^{22}\mathrm{Ne}$," *Zeitschrift für Physik A Atomic Nuclei*, vol. 334, no. 4, pp. 491–510, 1989.

[34] U. Giesen, C. Browne, J. Görres, S. Graff, C. Iliadis, H.-P. Trautvetter, M. Wiescher, W. Harms, K. Kratz, B. Pfeiffer, R. Azuma, M. Buckby, and J. King, "The astrophysical implications of low-energy resonances in 22ne + α," *Nuclear Physics A*, vol. 561, no. 1, pp. 95 – 111, 1993.

[35] C. Ugalde, A. E. Champagne, S. Daigle, C. Iliadis, R. Longland, J. R. Newton, E. Osenbaugh-Stewart, J. A. Clark, C. Deibel, A. Parikh, P. D. Parker, and C. Wrede, "Experimental evidence for a natural parity state in Mg26 and its impact on the production of neutrons for the s process," *Phys. Rev. C*, vol. 76, p. 025802, Aug. 2007.

[36] U. Giesen, C. P. Browne, J. Görres, S. Graff, C. Iliadis, H.-P. Trautvetter, M. Wiescher, W. Harms, K. L. Kratz, B. Pfeiffer, R. E. Azuma, M. Buckby, and J. D. King, "The astrophysical implications of low-energy resonances in ^{22}Ne + α," *Nucl. Phys. A*, vol. 561, pp. 95–111, Aug. 1993.

[37] C. Angulo, M. Arnould, M. Rayet, P. Descouvemont, D. Baye, C. Leclercq-Willain, A. Coc, S. Barhoumi, P. Aguer, C. Rolfs, R. Kunz, J. W. Hammer, A. Mayer, T. Paradellis, S. Kossionides, C. Chronidou, K. Spyrou, S. degl'Innocenti, G. Fiorentini, B. Ricci, S. Zavatarelli, C. Providencia, H. Wolters, J. Soares, C. Grama, J. Rahighi, A. Shotter, and M. Lamehi Rachti, "A compilation of charged-particle induced thermonuclear reaction rates," *Nucl. Phys. A*, vol. 656, pp. 3–187, 1999.

[38] A. I. Karakas, M. A. Lugaro, M. Wiescher, J. Görres, and C. Ugalde, "The Uncertainties in the ^{22}Ne+α-Capture Reaction Rates and the Production of the Heavy Magnesium Isotopes in Asymptotic Giant Branch Stars of Intermediate Mass," , vol. 643, pp. 471–483, May 2006.

[39] R. Longland, C. Iliadis, G. Rusev, A. P. Tonchev, R. J. Deboer, J. Görres, and M. Wiescher, "Photoexcitation of astrophysically important states in Mg26," *Phys. Rev. C*, vol. 80, p. 055803, Nov. 2009.

[40] U. Berg, K. Ackermann, K. Bangert, C. Bläsing, W. Naatz, R. Stock, K. Wienhard, M. Brussel, T. Chapuran, and B. Wildenthal, "Bound state m1 transitions in sd-shell nuclei," *Physics Letters B*, vol. 140, no. 3, pp. 191–196, 1984.

[41] R. Schwengner, A. Wagner, Y. Fujita, G. Rusev, M. Erhard, D. de Frenne, E. Grosse, A. R. Junghans, K. Kosev, and K. D. Schilling, "Dipole transition strengths in ^{26}Mg," *Phys. Rev. C*, vol. 79, p. 037303, Mar. 2009.

[42] R. J. deBoer, M. Wiescher, J. Görres, R. Longland, C. Iliadis, G. Rusev, and A. P. Tonchev, "Photoexcitation of astrophysically important states in ^{26}Mg. ii. ground-state-transition partial widths," *Phys. Rev. C*, vol. 82, p. 025802, Aug 2010.

[43] C. a. Massimi, "Resonance neutron-capture cross sections of stable magnesium isotopes and their astrophysical implications," *Phys. Rev. C*, vol. 85, p. 044615, Apr 2012.

[44] R. Talwar, T. Adachi, G. P. A. Berg, L. Bin, S. Bisterzo, M. Couder, R. J. deBoer, X. Fang, H. Fujita, Y. Fujita, J. Görres, K. Hatanaka, T. Itoh, T. Kadoya, A. Long, K. Miki, D. Patel, M. Pignatari, Y. Shimbara, A. Tamii, M. Wiescher, T. Yamamoto, and M. Yosoi, "Probing astrophysically important states in the ^{26}Mg nucleus to study neutron sources for the *s* process," *Phys. Rev. C*, vol. 93, p. 055803, May 2016.

[45] R. Longland, C. Iliadis, and A. I. Karakas, "Reaction rates for the s-process neutron source ^{22}Ne + α," *Phys. Rev. C*, vol. 85, p. 065809, June 2012.

[46] P. Adsley, J. W. Brümmer, K. C. W. Li, D. J. Marín-Lámbarri, N. Y. Kheswa, L. M. Donaldson, R. Neveling, P. Papka, L. Pellegri, V. Pesudo, L. C. Pool, F. D. Smit, and J. J. van Zyl, "Re-examining the ^{26}Mg$(\alpha, \alpha')^{26}$Mg reaction: Probing astrophysically important states in ^{26}Mg," *Phys. Rev. C*, vol. 96, p. 055802, Nov 2017.

[47] "Neutron spectroscopy of ^{26}Mg states: Constraining the stellar neutron source ^{22}Ne$(\alpha, \mathrm{n})^{25}$Mg," *Physics Letters B*, vol. 768, pp. 1 – 6, 2017.

[48] P. Adsley, J. W. Brümmer, T. Faestermann, S. P. Fox, F. Hammache, R. Hertenberger, A. Meyer, R. Neveling, D. Seiler, N. de Séréville, and H.-F. Wirth, "High-resolution study of levels in the astrophysically important nucleus ^{26}Mg and resulting updated level assignments," *Phys. Rev. C*, vol. 97, p. 045807, Apr 2018.

[49] S. Hunt, C. Iliadis, A. Champagne, L. Downen, and A. Cooper, "New measurement of the E_α^{lab}=0.83 MeV resonance in ^{22}Ne$(\alpha\ ,\gamma\ )^{26}$Mg," , vol. 99, p. 045804, Apr. 2019.

[50] G. Lotay, D. T. Doherty, D. Seweryniak, S. Almaraz-Calderon, M. P. Carpenter, C. J. Chiara, H. M. David, C. R. Hoffman, R. V. F. Janssens, A. Kankainen, T. Lauritsen, R. Wilkinson, P. J. Woods, and S. Zhu, "Identification of γ -decaying resonant states in ^{26}Mg and their importance for the astrophysical s process," *European Physical Journal A*, vol. 55, p. 109, July 2019.

[51] S. Ota *et al.*, "Decay properties of ^{22}Ne + α resonances and their impact on s-process nucleosynthesis," *Physics Letters B*, vol. 802, p. 135256, Mar. 2020.

[52] H. Jayatissa, G. V. Rogachev, V. Z. Goldberg, E. Koshchiy, G. Christian, J. Hooker, S. Ota, B. T. Roeder, A. Saastamoinen, O. Trippella, S. Upadhyayula, and E. Uberseder, "Constraining the ^{22}Ne(α,γ)^{26}Mg and ^{22}Ne(α,n)^{25}Mg reaction rates using sub-Coulomb α-transfer reactions," *Physics Letters B*, vol. 802, p. 135267, Mar. 2020.

[53] M. S. Basunia and A. M. Hurst, "Nuclear Data Sheets for A = 26," *Nuclear Data Sheets*, vol. 134, pp. 1–148, May 2016.

[54] C. Iliadis, R. Longland, A. E. Champagne, and A. Coc, "Charged-particle thermonuclear reaction rates: III. Nuclear physics input," *Nucl. Phys. A*, vol. 841, pp. 251–322, Oct. 2010.

[55] A. L. Sallaska, C. Iliadis, A. E. Champange, S. Goriely, S. Starrfield, and F. X. Timmes, "Starlib: A next-generation reaction-rate library for nuclear astrophysics," *The Astrophysical Journal Supplement Series*, vol. 207, no. 1, p. 18, 2013.

[56] R. Longland, *Investigation of the s-Process Neutron Source* ^{22}Ne + α. PhD thesis, University of North Carolina at Chapel Hill, 2010.

[57] A. L. Sallaska, C. Iliadis, A. E. Champange, S. Goriely, S. Starrfield, and F. X. Timmes, "STARLIB: A Next-generation Reaction-rate Library for Nuclear Astrophysics," *Astrophys. J. Suppl. Ser.*, vol. 207, p. 18, July 2013.

[58] "Starlib." http://starlib.physics.unc.edu/, accessed 30 October 2018.

[59] D. Piatti, *The Study of* ^{22}*Ne*(α,γ)^{26}*Mg and* ^{6}*Li*(p,γ)^{7}*Be Reactions at LUNA*. PhD thesis, Università degli studi di Padova, December 2018.

[60] A. Caciolli, C. Mazzocchi, V. Capogrosso, D. Bemmerer, C. Broggini, P. Corvisiero, H. Costantini, Z. Elekes, A. Formicola, Z. Fülöp, G. Gervino, A. Guglielmetti, C. Gustavino, G. Gyürky, G. Imbriani, M. Junker, A. Lemut, M. Marta, R. Menegazzo, S. Palmerini, P. Prati, V. Roca, C. Rolfs, C. Rossi Alvarez, E. Somorjai, O. Straniero, F. Strieder, F. Terrasi, H. P. Trautvetter, and A. Vomiero, "Revision of the ^{15}N(p,γ)^{16}O reaction rate and oxygen abundance in H-burning zones," *Astron. Astrophys.*, vol. 533, p. A66, Sept. 2011.

[61] C. L. Melcher, "Scintillators for well logging applications," *Nuclear Instruments and Methods in Physics Research B*, vol. 40, pp. 1214–1218, Apr. 1989.

[62] A. Boeltzig, A. Best, G. Imbriani, M. Junker, M. Aliotta, D. Bemmerer, C. Broggini, C. G. Bruno, R. Buompane, A. Caciolli, F. Cavanna, T. Chillery, G. F. Ciani, P. Corvisiero, L. Csedreki, T. Davinson, R. J. deBoer, R. Depalo, A. Di Leva, Z. Elekes, F. Ferraro, E. M. Fiore, A. Formicola, Z. Fülöp, G. Gervino, A. Guglielmetti, C. Gustavino, G. Gyürky, I. Kochanek, R. Menegazzo, V. Mossa, F. R. Pantaleo, V. Paticchio, R. Perrino, D. Piatti, P. Prati, L. Schiavulli, K. Stöckel, O. Straniero, F. Strieder, T. Szücs, M. P. Takács, D. Trezzi, M. Wiescher, and S. Zavatarelli, "Improved background suppression for radiative capture reactions at LUNA with HPGe and BGO detectors," *Journal of Physics G: Nuclear and Particle Physics*, vol. 45, p. 025203, jan 2018.

[63] R. Brun and F. Rademakers, "Root - an object oriented data analysis framework," *Proceedings AIHENP'96 Workshop, Lousanne*, 1996.

[64] R. Brun and F. Rademakers, "Root - an object oriented data analysis framework," *Nucl. Inst. Meth. in Phys. Res. A*, vol. 389, pp. 81–86, 1997.

[65] S. Daigle, K. J. Kelly, A. E. Champagne, M. Q. Buckner, C. Iliadis, and C. Howard, "Measurement of the E_r $^{c.m.}$=259 keV resonance in the $^{14}N(p,\gamma)^{15}O$ reaction," *Phys. Rev. C*, vol. 94, p. 025803, Aug. 2016.

[66] J. F. Ziegler, M. D. Ziegler, and J. P. Biersack, "SRIM - The stopping and range of ions in matter (2010)," *Nucl. Inst. Meth. B*, vol. 268, pp. 1818–1823, 2010.

[67] J. Görres, K. Kettner, H. Kräwinkel, and C. Rolfs, "The influence of intense ion beams on gas target densities," *Nucl. Inst. Meth.*, vol. 177, pp. 295–303, Nov. 1980.

[68] D. Bemmerer, F. Confortola, A. Lemut, R. Bonetti, C. Broggini, P. Corvisiero, H. Costantini, J. Cruz, A. Formicola, Z. Fülöp, G. Gervino, A. Guglielmetti, C. Gustavino, G. Gyürky, G. Imbriani, A. Jesus, M. Junker, B. Limata, R. Menegazzo, P. Prati, V. Roca, C. Rolfs, D. Rogalla, M. Romano, C. Rossi-Alvarez, F. Schümann, E. Somorjai, O. Straniero, F. Strieder, F. Terrasi, and H. P. Trautvetter, "Low energy measurement of the $^{14}N(p,\gamma)^{15}O$ total cross section at the LUNA underground facility," *Nucl. Phys. A*, vol. 779, pp. 297–317, 2006.

[69] F. Cavanna, *A direct measurement of the* $^{22}Ne(p,\gamma)^{23}Na$ *reaction down to the energies of astrophysical interest.* PhD thesis, Università degli studi di Genova, 2015.

[70] R. Depalo, *The neon-sodium cycle: Study of the* ^{22}Ne(p,γ)^{23}Na *reaction at astrophysical energies.* PhD thesis, Università degli studi di Padova, 2015.

[71] M. Marta, F. Confortola, D. Bemmerer, C. Boiano, R. Bonetti, C. Broggini, M. Casanova, P. Corvisiero, H. Costantini, Z. Elekes, A. Formicola, Z. Fülöp, G. Gervino, A. Guglielmetti, C. Gustavino, G. Gyürky, G. Imbriani, M. Junker, A. Lemut, B. Limata, R. Menegazzo, P. Prati, V. Roca, C. Rolfs, M. Romano, C. Rossi Alvarez, E. Somorjai, F. Strieder, F. Terrasi, and H. P. Trautvetter, "Study of beam heating effect in a gas target through Rutherford scattering," *Nucl. Inst. Meth. A*, vol. 569, pp. 727–731, Dec. 2006.

[72] F. Cavanna, R. Depalo, M.-L. Menzel, M. Aliotta, M. Anders, D. Bemmerer, C. Broggini, C. G. Bruno, A. Caciolli, P. Corvisiero, T. Davinson, A. di Leva, Z. Elekes, F. Ferraro, A. Formicola, Z. Fülöp, G. Gervino, A. Guglielmetti, C. Gustavino, G. Gyürky, G. Imbriani, M. Junker, R. Menegazzo, P. Prati, C. Rossi Alvarez, D. A. Scott, E. Somorjai, O. Straniero, F. Strieder, T. Szücs, and D. Trezzi, "A new study of the ^{22}Ne(p, γ)^{23}Na reaction deep underground: Feasibility, setup and first observation of the 186 keV resonance," *Eur. Phys. J. A*, vol. 50, p. 179, Nov. 2014.

[73] J. Osborne, C. Barnes, R. Kavanagh, R. Kremer, G. Matthews, J. Zyskind, P. Parker, and A. Howard, "Low-energy behavior of the ^{3}He$(\alpha,\gamma)^7$Be cross section," *Nucl. Phys. A*, vol. 419, pp. 115–132, 1984.

[74] G. F. Knoll, *Radiation Detection and Measurement.* New York: John Wiley & Sons, 4$^{\text{th}}$ ed., 2010.

[75] R. M. P. D. L. Mason and A. R. Quinton, "Energy straggling of alpha particles through gases," *Nucl. Instr. Methods*, vol. 45, 1966.

[76] J. J. Ramirez, R. M. Prior, J. B. Swint, A. R. Quinton, and R. A. Blue, "Energy straggling of alpha particles through gases," *Phys. Rev.*, vol. 179, pp. 310–314, Mar 1969.

[77] N. B. D. Phil., "Lx. on the decrease of velocity of swiftly moving electrified particles in passing through matter," *The London, Edinburgh, and Dublin Philosophical Magazine and Journal of Science*, vol. 30, no. 178, pp. 581–612, 1915.

[78] D. Bemmerer, F. Confortola, A. Lemut, R. Bonetti, C. Broggini, P. Corvisiero, H. Costantini, J. Cruz, A. Formicola, Z. Fülöp, G. Gervino, A. Guglielmetti, C. Gustavino, G. Gyürky, G. Imbriani, A. P. Jesus, M. Junker, B. Limata, R. Menegazzo, P. Prati, V. Roca, D. Rogalla, C. Rolfs,

M. Romano, C. Rossi Alvarez, F. Schümann, E. Somorjai, O. Straniero, F. Strieder, F. Terrasi, H. P. Trautvetter, and A. Vomiero, "Feasibility of low-energy radiative-capture experiments at the LUNA underground accelerator facility," *European Physical Journal A*, vol. 24, pp. 313–319, May 2005.

[79] G. Gilmore, *Practical γ-ray spectrometry, 2nd edition.* New York: John Wiley and Sons, 2008.

[80] W. A. Rolke and A. M. López, "Confidence intervals and upper bounds for small signals in the presence of background noise," *Nuclear Instruments and Methods in Physics Research A*, vol. 458, pp. 745–758, Feb. 2001.

[81] P. Marigo, A. Bressan, A. Nanni, L. Girardi, and M. L. Pumo, "Evolution of thermally pulsing asymptotic giant branch stars - I. The COLIBRI code," *Monthly Notices of the Royal Astronomical Society*, vol. 434, pp. 488–526, Sept. 2013.

[82] M. Jaeger, R. Kunz, A. Mayer, J. W. Hammer, G. Staudt, K. L. Kratz, and B. Pfeiffer, "^{22}Ne(α,n)^{25}Mg: The Key Neutron Source in Massive Stars," *Phys. Rev. Lett.*, vol. 87, p. 202501, 2001.

[83] S. Lyons, J. Görres, R. J. deBoer, E. Stech, Y. Chen, G. Gilardy, Q. Liu, A. M. Long, M. Moran, D. Robertson, C. Seymour, B. Vande Kolk, M. Wiescher, and A. Best, "Determination of $^{20}\mathrm{Ne}(p,\gamma)^{21}\mathrm{Na}$ cross sections from $E_p = 500 - 2000\,\mathrm{keV}$," *Phys. Rev. C*, vol. 97, p. 065802, Jun 2018.

[84] M. Williams, A. Lennarz, A. M. Laird, U. Battino, J. José, D. Connolly, C. Ruiz, A. Chen, B. Davids, N. Esker, B. R. Fulton, R. Garg, M. Gay, U. Greife, U. Hager, D. Hutcheon, M. Lovely, S. Lyons, A. Psaltis, J. E. Riley, and A. Tattersall, "First inverse kinematics study of the $^{22}\mathrm{Ne}(p,\gamma)^{23}\mathrm{Na}$ reaction and its role in agb star and classical nova nucleosynthesis," *Phys. Rev. C*, vol. 102, p. 035801, Sep 2020.

[85] C. Iliadis, J. M. D'Auria, S. Starrfield, W. J. Thompson, and M. Wiescher, "Proton-induced Thermonuclear Reaction Rates for A=20-40 Nuclei," *Astrophys. J. Suppl. Ser.*, vol. 134, pp. 151–171, 2001.

[86] F. Ferraro, M. P. Takács, D. Piatti, F. Cavanna, R. Depalo, M. Aliotta, D. Bemmerer, A. Best, A. Boeltzig, C. Broggini, C. G. Bruno, A. Caciolli, T. Chillery, G. F. Ciani, P. Corvisiero, T. Davinson, G. D'Erasmo, A. Di Leva, Z. Elekes, E. M. Fiore, A. Formicola, Z. Fülöp, G. Gervino, A. Guglielmetti, C. Gustavino, G. Gyürky, G. Imbriani, M. Junker, A. Karakas,

I. Kochanek, M. Lugaro, P. Marigo, R. Menegazzo, V. Mossa, F. R. Pantaleo, V. Paticchio, R. Perrino, P. Prati, L. Schiavulli, K. Stöckel, O. Straniero, T. Szücs, D. Trezzi, S. Zavatarelli, and LUNA Collaboration, "Direct capture cross section and the $E_p = 71$ and 105 kev resonances in the ^{22}Ne$(p,\gamma)^{23}$Na reaction," *Phys. Rev. Lett.*, vol. 121, p. 172701, Oct 2018.

[87] K. J. Kelly, A. E. Champagne, L. N. Downen, J. R. Dermigny, S. Hunt, C. Iliadis, and A. L. Cooper, "New measurements of low-energy resonances in the ^{22}**Ne**$(p,\gamma)^{23}$**Na** reaction," *Phys. Rev. C*, vol. 95, p. 015806, Jan 2017.

[88] J. B. Marion and W. A. Fowler, "Nuclear Reactions with the Neon Isotopes in Stars.," , vol. 125, p. 221, Jan. 1957.

[89] A. Renzini and M. Voli, "Advanced evolutionary stages of intermediate-mass stars. I - Evolution of surface compositions," *Astron. Astrophys.*, vol. 94, pp. 175–193, Jan. 1981.

[90] R. Gratton, C. Sneden, and E. Carretta, "Abundance Variations Within Globular Clusters," , vol. 42, pp. 385–440, Sept. 2004.

[91] P. Ventura and F. D'Antona, "Does the oxygen-sodium anticorrelation in globular clusters require a lowering of the ^{23}Na(p,α)^{20}Ne reaction rate?," *Astron. Astrophys.*, vol. 457, pp. 995–1001, Oct. 2006.

[92] J. José, M. Hernanz, and C. Iliadis, "Nucleosynthesis in classical novae," , vol. 777, pp. 550–578, Oct. 2006.

[93] J. José and M. Hernanz, "Nucleosynthesis in Classical Novae: CO versus ONe White Dwarfs," *Astrophys. J.*, vol. 494, p. 680, Feb. 1998.

[94] P. A. Denissenkov and F. Herwig, "The Abundance Evolution of Oxygen, Sodium, and Magnesium in Extremely Metal Poor Intermediate-Mass Stars: Implications for the Self-Pollution Scenario in Globular Clusters," *Astrophys. J. Lett.*, vol. 590, pp. L99–L102, June 2003.

[95] R. G. Gratton, E. Carretta, and A. Bragaglia, "Multiple populations in globular clusters. Lessons learned from the Milky Way globular clusters," *Astron. Astrophys. Revs.*, vol. 20, p. 50, Feb. 2012.

[96] J. M. Cesaratto, A. E. Champagne, M. Q. Buckner, T. B. Clegg, S. Daigle, C. Howard, C. Iliadis, R. Longland, J. R. Newton, and B. M. Oginni, "Measurement of the $E_r^{\mathrm{c.m.}} = 138$ kev resonance in the ^{23}Na$(\mathrm{p},\gamma)^{24}$Mg reaction and the abundance of sodium in agb stars," *Phys. Rev. C*, vol. 88, p. 065806, Dec 2013.

[97] N. Prantzos, "The energetics, evolution, and stellar depletion of ^{6}Li in the early galaxy," *Astron. Astrophys.*, vol. 448, pp. 665–675, 2006.

[98] T. Decressin, G. Meynet, C. Charbonnel, N. Prantzos, and S. Ekström, "Fast rotating massive stars and the origin of the abundance patterns in galactic globular clusters," *Astron. Astrophys.*, vol. 464, pp. 1029–1044, Mar. 2007.

[99] N. Tanner, "Direct radiative capture of protons by ^{16}O and ^{20}Ne," *Phys. Rev.*, vol. 114, pp. 1060–1064, May 1959.

[100] C. Van der Leun and W. Mouton, "The reaction $^{20}\mathrm{Ne}(\mathrm{p},\gamma)^{21}\mathrm{Na}$," *Physica*, vol. 30, no. 2, pp. 333–340, 1964.

[101] G. C. Thomas and N. W. Tanner, "The cross section of $^{20}\mathrm{Ne}(\mathrm{p},\gamma)^{21}\mathrm{Na}$," *Proceedings of the Physical Society*, vol. 75, pp. 498–501, apr 1960.

[102] C. Rolfs, W. S. Rodney, M. H. Shapiro, and H. Winkler, "Hydrogen burning of ^{20}Ne and ^{22}Ne in stars," *Nucl. Phys. A*, vol. 241, pp. 460–486, Apr. 1975.

[103] J. Keinonen, M. Riihonen, and A. Anttila, "Absolute resonance strengths in the $^{20,21,22}\mathrm{Ne}(\mathrm{p},\gamma)^{21,22,23}\mathrm{Na}$ and $^{21}\mathrm{Ne}(\mathrm{p},\mathrm{p}_1\gamma)^{21}\mathrm{Ne}$ reactions," *Phys. Rev. C*, vol. 15, pp. 579–586, Feb. 1977.

[104] J. Marion and W. Fowler, "Nuclear Reactions with the Neon Isotopes in Stars.," *Astrophys. J.*, vol. 125, p. 221, Jan. 1957.

[105] A. Mukhamedzhanov, P. Bem, V. Burjan, C. A. Gagliardi, B. F. Irgaziev, V. Kroha, J. Novak, S. R. Piskor, E. Simeckova, R. E. Tribble, F. Vesely, and J. Vincour, "Asymptotic normalization coefficients from the $^{20}\mathrm{Ne}(^{3}\mathrm{He},\mathrm{d})^{21}\mathrm{Na}$ reaction and astrophysical factor for $^{20}\mathrm{Ne}(\mathrm{p},\gamma)^{21}\mathrm{Na}$," 2006.

[106] H. M. Xu, C. A. Gagliardi, R. E. Tribble, A. M. Mukhamedzhanov, and N. K. Timofeyuk, "Overall normalization of the astrophysical s factor and the nuclear vertex constant for $^{7}\mathrm{Be}(p,\gamma)^{8}\mathrm{B}$ reactions," *Phys. Rev. Lett.*, vol. 73, pp. 2027–2030, Oct 1994.

[107] C. Iliadis, R. Longland, A. E. Champagne, A. Coc, and R. Fitzgerald, "Charged-particle thermonuclear reaction rates: II. Tables and graphs of reaction rates and probability density functions," *Nuclear Physics A*, vol. 841, pp. 31–250, Oct. 2010.

[108] A. Cooper, *A Low-Energy Study of the* $^{20}\mathrm{Ne}(\mathrm{p},\gamma)^{21}\mathrm{Na}$ *Reaction with High-Current Proton Beams at LENA*. PhD thesis, University of North Carolina, Chapel Hill, Department of Physics and Astronomy, 2019.

[109] J. Karpesky, *Measuring the neon-20 radiative proton capture rate at dragon.* PhD thesis, Colorado School of Mines, 2020.

[110] C. Rolfs and W. Rodney, "Proton capture by ^{15}N at stellar energies," *Nucl. Phys. A*, vol. 235, pp. 450–459, 1974.

[111] "Several narrow resonances in the proton bombardment of ^{20}Ne, author = Bloch, R and Knellwolf, T and Pixley, R E, abstractnote = , doi = 10.1016/0375-9474(69)90894-X, url = https://www.osti.gov/biblio/4812975, journal = Nucl. Phys., A123: 129-46(1969)., number = , volume = , place = Country unknown/Code not available, year = 1969, month = 1,"

[112] J. Dubois, H. Odelius, and S. O. Berglund, "A Search for a Missing $J^{\pi}=3/2^{+}$ level in ^{21}Na," *Phys. Scr. A*, vol. 5, pp. 163–168, Apr. 1972.

[113] C. Rolfs, R. Kraemer, F. Riess, and E. Kuhlmann, "Study of the low-lying states in ^{22}Mg.," *Nucl. Phys. A191: No. 1, 209-24(1972).*

[114] J. Pronko, R. Lindgren, and D. Bromley, "Structure of ^{21}Na from the ^{24}Mg(p,α) ^{21}Na reaction," *Nuclear Physics A*, vol. 140, no. 2, pp. 465–480, 1970.

[115] G. Christian, D. Hutcheon, C. Akers, D. Connolly, J. Fallis, and C. Ruiz, "Strength of the $E_{\mathrm{c.m.}} = 1113$ kev resonance in $^{20}\mathrm{Ne}(\mathrm{p},\gamma)^{21}\mathrm{Na}$," *Phys. Rev. C*, vol. 88, p. 038801, Sep 2013.

[116] E. L. Brady and M. Deutsch, "Angular correlation of successive gamma-rays," *Phys. Rev.*, vol. 78, pp. 558–566, Jun 1950.

[117] M. Marta, *The $^{14}N(p,\gamma)^{15}O$ reaction studied at low and high beam energy.* PhD thesis, Technische Universität Dresden, Fakultät Mathematik und Naturwissenschaften, 2012.

[118] U. S. Pande and B. P. Singh, "Gamma-gamma-gamma angular correlation method and triple gamma angular correlation studies in ^{133}Cs from the decay of ^{133}Ba," *Nuclear Instruments and Methods*, vol. 97, pp. 123–130, 1971.

[119] C. Casella, H. Costantini, A. Lemut, B. Limata, R. Bonetti, C. Broggini, L. Campajola, P. Corvisiero, J. Cruz, A. D'Onofrio, A. Formicola, Z. Fülöp, G. Gervino, L. Gialanella, A. Guglielmetti, C. Gustavino, G. Gyurky, G. Imbriani, A. P. Jesus, M. Junker, A. Ordine, J. V. Pinto, P. Prati, J. P. Ribeiro, V. Roca, D. Rogalla, C. Rolfs, M. Romano, C. Rossi-Alvarez, F. Schuemann, E. Somorjai, O. Straniero, F. Strieder, F. Terrasi, H. P. Trautvetter, and S. Zavatarelli, "First measurement of the $\mathrm{d}(\mathrm{p},\gamma)^{3}\mathrm{He}$ cross section down to the solar Gamow peak," *Nucl. Phys. A*, vol. 706, pp. 203–216, July 2002.

[120] Mossa, V., Stöckel, K., Cavanna, F., Ferraro, F., Aliotta, M., Barile, F., Bemmerer, D., Best, A., Boeltzig, A., Broggini, C., Bruno, C. G., Caciolli, A., Csedreki, L., Chillery, T., Ciani, G. F., Corvisiero, P., Davinson, T., Depalo, R., Di Leva, A., Elekes, Z., Fiore, E. M., Formicola, A., Fülöp, Zs., Gervino, G., Guglielmetti, A., Gustavino, C., Gyürky, G., Imbriani, G., Junker, M., Kochanek, I., Lugaro, M., Marcucci, L. E., Marigo, P., Masha, E., Menegazzo, R., Pantaleo, F. R., Paticchio, V., Perrino, R., Piatti, D., Prati, P., Schiavulli, L., Straniero, O., Szücs, T., Takács, M. P., Trezzi, D., Zavatarelli, S., and Zorzi, G.

[121] P. M. Endt, "Supplement to Energy Levels of A=21-44 Nuclei (vii)," *Nucl. Phys. A*, vol. 633, pp. 1–220, Apr. 1998.

[122] F. Glatz, S. Norbert, E. Bitterwolf, A. Burkard, F. Heidinger, T. Kern, R. Lehmann, H. Röpke, J. Siefert, C. Schneider, and B. H. Wildenthal, "High-spin states in ^{26}Mg," *Zeitschrift für Physik A Atomic Nuclei*, vol. 324, pp. 187–204, Jun 1986.

[123] R. J. deBoer, J. Görres, G. Imbriani, P. J. LeBlanc, E. Uberseder, and M. Wiescher, "R-matrix analysis of ^{16}O compound nucleus reactions," *Phys. Rev. C*, vol. 87, p. 015802, Jan. 2013.

[124] U. Giesen, C. P. Browne, J. Görres, S. Graff, C. Iliadis, H.-P. Trautvetter, M. Wiescher, W. Harms, K. L. Kratz, B. Pfeiffer, R. E. Azuma, M. Buckby, and J. D. King, "The astrophysical implications of low-energy resonances in ^{22}Ne + α," *Nucl. Phys. A*, vol. 561, pp. 95–111, Aug. 1993.

[125] C. Moss, "Excitation energies of levels in ^{23}Na, ^{24}Mg and ^{26}Mg," *Nuclear Physics A*, vol. 269, no. 2, pp. 429 – 442, 1976.

Acknowledgments

I should start with something like "it takes a long time to write a PhD thesis...", but then I can just imagine my supervisors reading this lines and saying: "yes Eliana, it takes some time, but is not your case since we got the draft of your thesis the week before the deadline. You can be the best definition of the last minute". Unfortunately they are right and I know it, but (probably) I'll still go on with " diamonds are made under pressure".
Until the end I wasn't sure whether to write this last page or not but I don't want to disappoint the readers who will open this thesis just for the acknowledgments.
Il punto è che questo traguardo porta il peso di un percorso prezioso. Io vorrei ringraziare tutti loro che hanno contribuito a questo lavoro ma sopratutto hanno reso questo viaggio un tesoro da non perdere, a prescindere di quello che mi riserva il futuro.
Sono molto grata a Dott.ssa Chiara Mazzocchi e Dot. Ronald Schwengner per tutte le correzioni, i suggerimenti e il loro gentile modo di fare.
Un ringraziamento alla mia prof.ssa Alessandra Guglielmetti. Grazie per tutto! Sappiamo entrambe quanto lei sia speciale per me. Non riesco nemmeno a decidere cosa scrivere, e questa volta non per mancanza di tempo ma veramente non trovo le parole giuste. Lei è parte della famiglia da anni ormai, di quelli che sento la mancanza ancora prima di partire. Le voglio un gran bene!
"Non capita a tutti di avere un relatore come me. Ti porto anche a Parigi. Parigi, Gennaio 2019". Parigi a parte, alla fine di questo percorso (anche molto prima) posso dire con certezza e fiera più che mai che prof. Antonio Caciolli come sempre aveva ragione. Grazie infinite Antonio, per ogni consiglio, suggerimento scientifico e sopratutto umano. Grazie per tutta la fiducia che mi hai trasmesso, per aver sempre dedicato del tempo anche nei momenti più difficili.
Ringrazio di cuore prof. Piero Corvisiero per i suoi modi dolci e il suo prezioso e continuo aiuto. Quando in bel mezzo a tante cose che non tornano ho detto "cosa farei senza di lei" sono sempre stata seria. Grazie per aver risposto a tutte le mie

domande e ansie a qualsiasi ora.
Ringrazio molto Sandra Zavatarelli per tutto il tempo dedicato e l'aiuto continuo per qualsiasi cosa. Nonostante il tuo essere precisa (e ansiosa) e il mio masochismo, siamo riuscite a creare il nostro equilibrio. Grazie Sandra!
Un grazie speciale a Daniel Bemmerer! Tu sei nella lista di quelli che mi ha dato la spinta verso LUNA e dopo quella spinta non hai smesso di insegnarmi ed aiutarmi ogni volta che ne avevo bisogno. Grazie di cuore.
Grazie infinite a Francesca per ogni aiuto e ogni prezioso momento condiviso! Sei in assoluto (senza offendere nessun'altra/o) la mia compagna di turno preferita nonostante tutte le sfortune che ho avuto con i turni con te.
Grazie infinite a Rosanna per tutti i suoi consigli, per tutte le volte che mi ha fatto riflettere e per tutto il tempo dedicato. Sei una persona veramente cara e preziosa e mi dispiace dover lasciare Milano proprio ora che ci sei anche tu.
Non posso non ringraziare Denise! Grazie per non aver mai perso le speranze con neon alpha e per tutto l'aiuto che mi hai dato.
Sono grata a Paola Marigo per il suo contributo e l'aiuto. Grazie a Matthias Junker per la sua disponibilità nei momenti di sfortuna (continua nel mio caso) ai LNGS. Grazie ai ragazzi di chimica e l'ufficio meccanica per aver sopportato le nostre tempistiche. Non posso non essere grata a Donatello che è stato un sostegno continuo durante i turni. Grazie a Giovanni che ha iniziato a chiedere della tesi prima che del dovuto, solo per il gusto di mettere ansia, ma sopratutto grazie per i taralli che sono sempre apprezzati.
Grazie a tutta la collaborazione LUNA e tutti i Lunatici con cui ho condiviso diverse settimane di turno. Magari il mio dottorato a LUNA è stato un piccolo passo per l'umanità però è stato decisamente un enorme per me. Grazie e spero di continuare in questo viaggio che porta solo un futuro migliore.
Grazie ad Andrea Zanzani per la sua super disponibilità. Secondo me se riusciamo a concludere questo percorso è anche grazie a te.
Grazie a tutti i nucleari con cui ho condiviso idee e bei momenti e alla super amica Giulia. Grazie a Letizia con tutto il suo entusiasmo anche nelle giornate grigie.
Grazie a Rosy! Questi tre anni sono stati la prova che anche lontane siamo sempre amiche del cuore. Altro sarebbe inutile e non abbastanza.
Infine, un enorme ringraziamento alla mia super famiglia. Non importano i traguardi che potrei raggiungere nella vita, nulla mi renderebbe più fiera di voi. Papà, mamma, lali, Rudi voi siete il punto fisso indiscusso. Nell'infinità dell'universo non troverò mai stelle più belle di Sofi, Leo e Joel.
La probabilità di aver dimenticato qualcuno è tanta, in ogni caso spero che questi ringraziamenti e tutti quelli persi dell'ansia siano parte di futuri traguardi e viaggi.